Final Report

Dissolution Rate, Weathering Mechanics and Friability of TNT, Comp B and Octol

SERDP Project ER-1482
TR-10-2

FEBRUARY 2010

Bonnie Packer
U.S. Army Engineer Research and Development Center

Susan Taylor
Susan Bigl
Jennifer Fadden
James Lever
Nancy Perron
Marianne Walsh
U.S. Army Engineer Research and Engineering Laboratory

Matthew Curnow
Ronald Spanggord
SRI International

Distribution Statement A: Approved for Public Release, Distribution is Unlimited

Strategic Environmental Research and Development Program

This report was prepared under contract to the Department of Defense Strategic Environmental Research and Development Program (SERDP). The publication of this report does not indicate endorsement by the Department of Defense, nor should the contents be construed as reflecting the official policy or position of the Department of Defense. Reference herein to any specific commercial product, process, or service by trade name, trademark, manufacturer, or otherwise, does not necessarily constitute or imply its endorsement, recommendation, or favoring by the Department of Defense.

Strategic Environmental Research and Development Program

ERDC/CRRELL TR-10-2
February 2010

Dissolution Rate, Weathering Mechanics, and Friability of TNT, Comp B, Tritonal, and Octol

Susan Taylor, PhD, James Lever, PhD, PE, Marianne Walsh, Jennifer Fadden, Nancy Perron, and Susan Bigl

Cold Regions Research and Engineering Laboratory
U.S. Army Engineer Research and Development Center
72 Lyme Road
Hanover, NH 03755-1290

Ronald Spanggord, PhD, and Matthew Curnow

SRI International
333 Ravenswood Ave.
Menlo Park, CA 94025

Bonnie Packer, PhD

U.S. Army Environmental Command
5179 Hoadley Road
Aberdeen Proving Ground, MD 21010-5401

Final report

Approved for public release; distribution is unlimited.

Prepared for Strategic Environmental Research and Development Program (SERDP)
Arlington, Virginia 22203

Under ER 1482

Abstract: The Army needs live-fire training and testing, but residues from such activity can contaminate nearby groundwater and trigger regulatory actions that restrict training or even close bases. Our three-year project measured the dissolution of TNT, Comp B, Tritonal, Octol, and C4, both in the laboratory and outdoors under conditions that mimic what occurs in the field—dissolution of spatially isolated explosives scattered onto range soils. The resulting data and dissolution models provided insight on environmental factors that affect dissolution, the frequency at which explosive chunks split, and the size of explosive loads on existing ranges. Our drop-impingement model indicated we can use rainfall data and average solubility to calculate the dissolution rate and expected lifespan of explosive pieces. Other findings included learning that the crushing strengths of explosives were low and did not significantly change after three years of outdoor exposure. Also, size distributions of the crushed explosives showed power law distributions, as found for blow-in-place, low-order detonations. This similarity suggests that we can crudely estimate particle size distributions on soils from total mass. Range managers can use the work reported here to guide future training and cleanup activities.

DISCLAIMER: The contents of this report are not to be used for advertising, publication, or promotional purposes. Citation of trade names does not constitute an official endorsement or approval of the use of such commercial products. All product names and trademarks cited are the property of their respective owners. The findings of this report are not to be construed as an official Department of the Army position unless so designated by other authorized documents.

DESTROY THIS REPORT WHEN NO LONGER NEEDED. DO NOT RETURN IT TO THE ORIGINATOR.

Table of Contents

List of Figures and Tables v

Preface x

Unit Conversion Factors xi

Terms, Abbreviations, and Acronyms xii

1 Introduction 1

1.1 Background 1
1.2 Objective 4
1.3 Approach 5
1.4 Scope 5
1.5 Report content overview 8

2 Laboratory Dissolution Tests 10

2.1 Materials and methods 10
2.1.1 Sample composition 10
2.1.2 Experimental set-up 10
2.1.3 Analytical methods 11
2.2 Results 12
2.2.1 Appearance of test particles 12
2.2.2 HE mass recovery 15
2.2.3 Dissolution modeling and comparison with dissolved mass time-series 18
2.3 Discussion 26

3 Outdoor Dissolution Tests 28

3.1 Materials and methods 28
3.1.1 Sample composition 28
3.1.2 Experiment set-up 28
3.1.3 Analytical methods 30
3.2 Results 30
3.2.1 Weather conditions 35
3.2.2 Appearance of HE pieces 36
3.2.3 Mass loss of HE chunks 39
3.2.4 Dissolution modeling 44
3.2.5 Validation of dissolution model for TNT and Tritonal 47
3.2.6 Layered dissolution model for Comp B 52
3.2.7 Validation of layered dissolution model for Comp B 58
3.2.8 Population modeling 65
3.3 Conclusions 69

4 TNT Phototransformation Studies 72

4.1 Results 73

4.1.1 TNT loss pathways ... *73*
4.2 Identifying the TNT phototransformation products ... 79

4A Analytical Characterization of Solid-phase TNT Photolysis Products Formed from the Weathering of Tritonal and TNT ... 81
4.3 Materials and methods ... 81
4.3.1 Sample composition ... *81*
4.3.2 HPLC analyses ... *81*
4.3.3 Standard preparation ... *82*
4.3.4 Liquid chromatography mass spectroscopy (LCMS) ... *83*
4.3.5 Nitrite and nitrate ... *85*
4.4 Results ... 85
4.4.1 UV and LC/MS evaluation of CRREL Tritonal sample ... *88*
4.4.2 Investigations into the formation of Red Product 2 ... *94*
4.4.3 Making Red Product 2 ... *96*
4.4.4 Identifying Red Product 2 (RP 2) ... *98*
4.4.5 Preparation of Red Product 1 (RP 1) ... *100*
4.5 Conclusions ... 107

5 Laboratory Crushing Tests ... 108
5.1 Experimental setup ... 108
5.2 Results ... 109
5.2.1 Crushing tests ... *109*
5.2.2 Piece size distribution ... *111*
5.2.3 Appearance of crushed samples ... *113*
5.2.4 Outdoor dissolution ... *115*
5.3 Discussion ... 117

6 Outdoor Friability of HE Chunks ... 119
6.1 Methods ... 119
6.1.1 Holloman Air Force Base, New Mexico ... *119*
6.1.2 Pond 155 at Eagle River Flats, Alaska ... *120*
6.1.3 Low-order residues at Eagle River Flats, Alaska ... *121*
6.2 Results ... 122
6.2.1 Holloman Air Force Base, New Mexico ... *122*
6.2.2 Pond 155 at Eagle River Flats, Alaska ... *123*
6.2.3 Distribution and weathering of LO detonation residue, ERF, Alaska ... *126*
6.3 Discussion ... 136

7 Conclusion ... 138

References ... 141

Appendix A: Bibliography of ER-1482 Publications ... 145

Appendix B: Photos of Control Chunks and Force vs. Displacement Plots ... 147

Report documentation page ... 165

List of Figures and Tables

Figures

Figure 1. Schematic of the drip-impingement model and steady flow model for HE dissolution. Each model contains one unknown, which is parameterized using the measured dissolution data. The drip-impingement model uses the thickness of the wetted layer, whereas the steady flow model uses a surface area factor; both are related to the surface area of the HE chunk and termed area factors. 4

Figure 2. Schematic showing how our study (shown in pink) fits into the bigger picture of mass loading of HE onto range soils and processes that affect the fate of HE. 8

Figure 3. Laboratory setup showing the multiple-syringe pump used to drip water on explosive particles. 11

Figure 4. Photos and initial masses of millimeter-size particles used in the 0.5 and 1.0 mL/hr laboratory tests. 13

Figure 5. Percent mass loss (mg) of HE particles versus time for a 0.5 mL per hour drip rate. The starting masses of the particles were TNT=5.34 mg, Comp B=2.31 mg, Tritonal=1.89 mg, and Octol=6.53 mg. 16

Figure 6. Percent mass loss (mg) of HE particles versus time for a 1.0 mL/hr drip rate. The starting masses of the particles were TNT=9.59 mg, Comp B=9.09 mg, Tritonal=6.40 mg and Octol=17.33 mg. Extraction of frits at end of tests accounted for the final increases seen in the Comp B and Octol records. 17

Figure 7. Percent TNT present in 21 mm-size Tritonal particles. Particles were weighed on a microbalance, extracted, and analyzed. The horizontal black line represents the average percent TNT present; red lines mark the one standard deviation. 17

Figure 8. Cumulative dissolved mass versus time for the TNT test particles (symbols are measured values and smooth curves are modeled values). 21

Figure 9. Cumulative dissolved mass versus time for the Tritonal test particles (symbols are measured values and smooth curves are modeled values). 22

Figure 10. Cumulative dissolved mass versus time for the Comp B test particles (symbols are measured values, smooth curves are modeled values). Dissolution of RDX eventually controls dissolution of TNT (modeled via Equation 3). Independent TNT dissolution would occur much faster. 24

Figure 11. Cumulative dissolved mass versus time for the Octol test particles (symbols are measured values, smooth curves are modeled values). TNT dissolution rate apparently was neither controlled by, nor independent of, HMX dissolution. 25

Figure 12. Outdoor tests showing Buchner funnels used to hold the HE pieces. Any precipitation landing in the funnel moved through the glass frit and into 1-L glass bottles in the wooden boxes. 29

Figure 13. Photos and initial masses of HE particles used in the outdoor dissolution tests. 31

Figure 14. Three years of rainfall and air temperature data at CRREL, May 2006–May 2009. 35

Figure 15. C4-2 photographed May 2008. 36

Figure 16. (a) Photograph of TNT particle and (b) close-up of its surface. 37

Figure 17. (a) Photograph of Comp B particle and (b) close-up of its surface. Note hollows where RDX crystals have de-bonded from the matrix and fallen out. 37

Figure 18. (a) Photograph of Tritonal particle and (b) close-up of its surface showing an incipient crack and the aluminum grains that comprise 20%–30% of its mass by weight. 37

Figure 19. Four of the HE chunks split naturally during the tests: TNT 3, TNT 11, Comp B 6 and C4 5. 38

Figure 20. Number of HE chunks that cracked, spalled off a >1 mm piece, and split into multiple millimeter-size pieces over the three-year test. For example, the circled triangle indicates that 3 of the 34 chunks had split by day 810 of the test. 39

Figure 21. Cumulative mass loss of TNT (mg) versus time. TNT 5 was crushed on day 436 (July 2007) resulting in an increase in mass loss. TNT 3 split a few days later. 40

Figure 22. Cumulative mass loss of TNT and RDX (mg) as a function of time for the 12 Comp B pieces tested. Comp B 11 was crushed on day 436, and you can see an increase in its mass loss starting at that time. 40

Figure 23. Cumulative mass loss of TNT (mg) as a function of time for the Tritonal 5 pieces tested. Tritonal 5 was crushed on day 436 resulting in increased mass loss. 41

Figure 24. Cumulative mass loss of RDX (mg) as a function of time for six C4 pieces tested. None of the C4 chunks were crushed. After the 2008 winter, C4 2 shows a pronounced increase in dissolution and was found to be crumbly-(see Figure 15). The large jumps at the end of the record are the HE mass extracted from the funnels. 41

Figure 25. Dissolved TNT mass measured for TNT 1 and TNT 8 along with predictions from full and linear drop-impingement models. 48

Figure 26. Dissolved TNT mass measured for Tritonal 3 and Tritonal 4 along with predictions from full and linear drop-impingement models. 49

Figure 27. Predicted initial dissolution rate and particle lifespan versus a particle's initial mass. Curves were generated using the linear drop-impingement model (Equations 14 and 16), an average annual rainfall of 100 cm per year, and an average annual temperature of 11 °C. 52

Figure 28. Dissolved mass and dissolution rate as functions of total rainfall, H (mm), for an 80-μm-diameter RDX crystal, based on the small-particle drop-impingement model. 58

Figure 29. Examples of good agreement between measured and modeled Comp B dissolved masses (Comp B 1 and Comp B 9) using default parameters (Table 5). The default parameters provided similarly good agreement for Comp B 5 and Comp B 7. 60

Figure 30. Examples of under-prediction of Comp B dissolved masses (Comp B 2 and Comp B 6) using default parameters (Table 5). Increasing AF_L to ~ 3 yielded good model agreement for these chunks and Comp B 12. 61

Figure 31. Examples of over-prediction of Comp B dissolved masses (Comp B 3 and Comp B 4) using default parameters (Table 5). These were the only chunks warranting $AF_L < 1$. They both possessed dark surface coatings that impeded dissolution. 62

Figure 32. The two cases (Comp B 8 and Comp B 10) where simply adjusting area factor would not substantially improve model agreement. Improving the fit to TNT dissolution would worsen agreement with RDX dissolution. 63

Figure 33. Comparison of measured and predicted dissolution for Comp B 11. The default parameters yielded excellent agreement before the chunk was crushed and the pieces returned outdoors on day 436. 64

Figure 34. The model agreement with Comp B 11 dissolution is quite good using a 5-fold increase in area factor, beginning after the chunk was crushed. The jump in area factor mimics the increase in surface area for the population of smaller pieces, compared with the original chunk. 64

Figure 35. Measured and predicted dissolution for TNT 5, which was crushed and returned outdoors on Day 436. The post- crushing predictions used the measured-size distribution of the daughter particles. 68

Figure 36. Measured and predicted dissolution for Tritonal 5, the chunk which was crushed and returned outdoors on Day 436. The post- crushing predictions used the measured-size distribution of the daughter particles. Note that the largest daughter particle split naturally near Day 800. The model did not include this effect. 68

Figure 37. Mass loss measured by HPLC versus measured mass loss by electronic balance for TNT and Tritonal samples. 72

Figure 38. Analyses of a 12 mg/L solution of TNT placed in the outside sample box as a control for TNT transformation in solution. 74

Figure 39. Note the darkening of TNT 4 between when it was set outside on 2 May 2006 (left) and on 30 May 2006 (right). 76

Figure 40. Tritonal 5 rainwater sample. 76

Figure 41. TNT piece placed in a windowsill. 77

Figure 42. TNT piece embedded in wax and sectioned. Thin layer on edge is responsible for the very dark looking coating in Figure 41. 77

Figure 43. HPLC Chromatogram showing two examples of the pre-solvent peak (arrows). 78

Figure 44. Decrease in TNT concentration is associated with an increase in the peak height of the pre-solvent peak. 79

Figure 45. Typical HPLC profile of explosive standards. 83

Figure 46. Typical ultra HPLC profile of explosives and related compounds. 84

Figure 47. HPLC Profiles of weathered Tritonal, TNT, Comp B, and C4. ADNTs are the aminodinitrotoluenes. 86

Figure 48. Overlay HPLC profile for a low-level and nitrate standard (bottom) and Tritonal sample (top). 87

Figure 49. HPLC profiles for weathered Tritonal, TNT, Comp B, and C4 at 520 nm. 87

Figure 50. HPLC profile of CRREL Tritonal sample. 88

Figure 51. HPLC profiles of photolyzed TNT in 15% acetone solution (top), water solution (middle), and Tritonal from CRREL (bottom). 94

Figure 52. TNT decay plots (left) and RP 1 and RP 2 formation (right). 95

Figure 53. UV spectra of RP 1 (left) and RP 2 (right). 95

Figure 54. RP 1 and RP 2 formation on cloudy days. 96

Figure 55. Band formation and the fractions collected from the strata C18-E column. RP 2 appears in Fraction 7. 97

Figure 56. Red solid resulting from drying the RP 2 fraction. 98

Figure 57. Mass spectrum of RP 2. 98

Figure 58. ^{1}H-NMR spectrum of RP 2 (top) and expanded scale (bottom). 99

Figure 59. Structure for RP 2 that is consistent with mass spectrometer and nuclear magnetic resonance data. 100

Figure 60. Mass spectrum of RP 1. 101

Figure 61. ^{1}H-NMR spectrum of RP 1/TNT mixture, the mass, and NMR data. 102

Figure 62. Possible structure for RP 1. 103

Figure 63. Photochemical formation of RP 1. 104

Figure 64. Formation of RP 2 from RP 1. 104

Figure 65. Analytical scheme used to capture the TNT anion. 105

Figure 66. HPLC profile of the aqueous filter (top) and the dissolved precipitate (bottom). 106

Figure 67. Chromatographic profiles of selected bands obtained from the SPE column. 107

Figure 68. CRREL's Material Testing System (MTS) used to crush explosive particles. 109

Figure 69. Plot of fragment masses from TNT chunks crushed in the MTS machine. Note that all six chunks broke into fragments that can be described by a power law distribution. The best-fits for four of the particles are shown. 112

Figure 70. Plot of fragment masses from Comp B chunks crushed in the MTS machine. Note that all seven chunks broke into fragments that can be described by a power law distribution. The best-fits for three of the chunks are shown in the figure. 112

Figure 71. Plot of fragment masses from Tritonal chunks crushed in the MTS machine. Note that all six chunks broke into fragments that can be described by a power law distribution. The best-fits for four of the chunks are shown in the figure. 113

Figure 72. Appearance of TNT 5, Trit 5, and Comp B11 before (left) and after crushing (center) in July 2007 and in May 2009 (right). 114

Figure 73. Cumulative HE mass loss as a function of time for the three chunks crushed in July 2007, namely TNT 5, Trit 5, and Comp B 11. TNT 7 was not crushed, and is shown as an example of what the mass loss curves might have looked like had the chunks not been broken. 115

Figure 74. Change in the TNT to RDX ratio for Comp B 11. Note the large increase in TNT immediately after the particle was crushed. 116

Figure 75. Changes in the appearance of one chunk of TNT 3 over the course of the experiment. This chunk was not crushed, but split naturally. 117

Figure 76. Tritonal chunks in May 2005 (left) and May 2006 (right). Note in the May 2006 photo that the soil in contact with the chunks is also red. 120

Figure 77. Setting up camera at Pond 155, Eagle River Flats, Alaska. 121

Figure 78. Map showing relative locations of three low-order detonation events on an estuarine salt marsh impact area. The solid red circles correspond to the impact craters and the red outlines delineate the boundaries of the scatter of solid Comp B chunks. The black dots at LO#2 and LO#3 are the locations of discrete points with Comp B residue that were monitored between May 2006 and May 2009. 122

Figure 79. Close-up photographs of Comp B and C4 pieces at Pond 155, Eagle River Flats, Alaska. 124

Figure 80. Comp B and C4 pieces as originally placed in June 2007 and underwater in Aug 2007. 125

Figure 81. Water temperature (°C) and water depth (m) measurements for Pond 155 at Eagle River Flats, Alaska. 126

Figure 82. Crater formed by LO 2 detonation at ERF. On the right is the same area after flooding tides and rainfall in August 2006. 127

Figure 83. Photos of Comp B chunks dispersed by low-order detonation #2, photographed (l-r) in May and August 2006, and May and August 2007. Missing photographs indicate the loss of HE chunk(s). 128

Figure 84. Images documenting the changes over three summers in one chunk of Comp B at LO 2. 133

Tables

Table 1. Dissolution test parameters and the recovered mass for HE particles. 15

Table 2. Model parameters. 20
Table 3. Measured mass losses for 34 HE chunks exposed outdoors for three years. 42
Table 4. Best-fit area factors and RMS prediction errors for the drop-impingement model, and the linear approximation of the drop-impingement model. 49
Table 5. Parameters for layered Comp B dissolution model. 56
Table 6. Particle masses for TNT 5 and Tritonal 5 after crushing. We used average diameter of 200 μm to determine the number of particles from the dust mass. 66
Table 7. Concentrations of standards that yield 1 AU response. 82
Table 8. Explosives ionization 84
Table 9. Compounds identified and quantified in the CRREL samples. 85
Table 10. UV and mass spectral data for lettered components shown in Figure 50. 89
Table 11. ^{1}H-NMR signals resulting from RP 2. 100
Table 12. 1H-NMR Signals Resulting from RP 1. 103
Table 13. Data on explosive chunks crushed in the laboratory. Particles labeled in red were part of our outdoor tests. 110
Table 14. Mass of Tritonal chunks over one-year test. 123
Table 15. Mass of Comp B and C4 chunks set out at Pond 155, Eagle River Flats, Alaska 124
Table 16. Field observations for Comp B chunks dispersed by LO 2 detonation. Chunks were observed on 24 May 2006, 23 Aug. 2006, 22 May 2007, 24 Aug. 2007, 4 June 2008, 25 Aug.2008, and 14 May 2009. 131
Table 17. Field observations for Comp B chunks dispersed by LO #3. Chunks were observed on 24 May 2006, 23 Aug. 2006, 22 May 2007, 24 Aug. 2007, 4 June 2008, 25 Aug.2008, and 14 May 2009. 134

Preface

This report is the result of a three-year study funded through CPSON-01-01, "Range Environmental Fate for Energetic Materials." It was prepared for the Strategic Environmental Research and Development Program (SERDP) under Environmental Restoration Program Project ER-1482. We thank Dr. Andrea Leeson and Dr. Jeffery Maquesee for funding this work.

The work was performed by the Biogeochemical Science Branch (CEERD-RR-N) of the Research and Engineering Division at the U.S. Army Engineer Research and Development Center (ERDC), Cold Regions Research and Engineering Laboratory (CRREL) in Hanover, New Hampshire. The authors wish to acknowledge two students, Pamela Collins and Carey Li, who helped with this work; their dedication and interest was appreciated. The authors also thank Dennis Lambert for his many and varied contributions, Kerry Claffey for obtaining and checking the weather data, and Glen Durrell for operating the Materials Testing System. In addition, Alan Hewitt and Terry Sobecki graciously reviewed the manuscript and provided helpful suggestions.

This report was prepared under the general supervision of Dr. Terrence Sobecki, Biogeochemical Sciences Branch, and Dr. Robert E. Davis, Director, CRREL.

At the time of publication, COL Gary E. Johnston was the Commander and Executive Director of ERDC, and Dr. Jeffrey P. Holland was the Director.

Unit Conversion Factors

Multiply	By	To Obtain
acres	4,046.873	square meters
feet	0.3048	meters
gallons (U.S. liquid)	3.785412 E-03	cubic meters
inches	0.0254	meters
microns	1.0 E-06	meters
miles (U.S. statute)	1,609.347	meters
pounds (mass)	0.45359237	kilograms
square miles	2.589998 E+06	square meters

Terms, Abbreviations, and Acronyms

Term	Spellout
1,3-DNB	1,3-dinitrobenzene
1,3,5-TNB	1,3,5-trinitrobenzene
2-ADNT	2-amino-4,6-dinitrotoluene
4-ADNT	4-amino-2,6-dinitrotoluene
2,2' Azoxy	4,4',6,6'-tetranitro-4,4'-azoxytoluene
2,4' Azoxy	4,2',6,6'-tetranitro-2,4'-azoxytoluene
4,4' Azoxy	4,2',6,6'-tetranitro-2,4'-azoxytoluene
4,4' Azoxy	2,2',6,6'-tetranitro-4,4'-azoxytoluene
2,4-DANT	2,4-diamino-6-nitrotoluene
2,6-DANT	2,6-diamino-4-nitrotoluene
2,4-DNT	2,4-dinitrotoluene
2,6-DNT	2,6-dinitrotoluene
2-HADNT	2-hydroxyamino-2,4-dinitrotoluene
4-HADNT	4-hydroxyamino-2,6-dinitrotoluene
ADNT	amino-dinitrotoluenes
AFB	Air Force Base
AU	absorbance unit; y-axis on chromatograms
C4	Composition 4, a common variety of the plastic explosive known as "C"
Comp B	Composition B, a 39:60 mix of TNT and RDX that contains ~1% wax
CPSON	Call for Proposal Statement of Need
CRREL	Cold Regions Research and Engineering Laboratory
DNX	1,3-dinitroso-5-nitro-1,3,5-triazacyclohexane
ELSD	evaporative light scattering detector
ERDC	Engineer Research and Development Center
ERF	Eagle River Flats (a salt marsh at Fort Richardson, Alaska)
H-NMR	nuclear magnetic resonance measurements that use the spin of hydrogen atom to elucidate structure of molecules.
HE	high explosives- chemical compounds that combust so rapidly that the resulting supersonic shock wave causes the mass to detonate.
HMX	high explosive, 1,3,5,7,-octahydro-1,3,5,7-tetranitrotetrazocine (often a bi-product of RDX production)
HPLC	high performance liquid chromatography
LCMS	liquid chromatography mass spectrum
LO	low-order (detonation)
MNX	1-nitroso-3,5-dinitro-1,3,5-triazacyclohexane
MS	mass spectrum
MTS	Materials Testing Service
m/z	mass-to-charge ratio
NMR	nuclear magnetic resonance

Term	Spellout
Octol	70:30 mix of HMX and TNT
PETN	pentaerythritol tetranitrate
RDX	high energy explosive, 1,3,5-hexahydro-1,3,5-trinitro-1,3,5-triazine
RMS	root mean square
SPE	solid phase extraction
TAT	2,4,6-triaminotoluene-trihydrochloride
TNT	2,4,6-trinitrotoluene, a high energy explosive
TNX	2,6-diamino-4-nitrotoluene
UV	ultra-violet
Tritonal	70:30 or 80:20 mix of TNT and aluminum powder
UPLC	ultra performance liquid chromatogram
U.S. EPA	United States Environmental Protection Agency
UXO	unexploded ordnance

1 Introduction

1.1 Background

Military ranges provide soldiers the opportunity to train with a variety of live munitions. This live-fire training can result in unexploded ordnance (UXO), low-order (LO) detonations, and some high explosive (HE) residues from munitions that detonated as intended. Although all of these outcomes may contaminate the soil and groundwater, LO detonations are thought to be the main source of contamination on ranges today (Jenkins et al. 2001; Taylor et al. 2004a). The LO detonations scatter centimeter- and millimeter-size pieces of explosives such as TNT (2,4,6-trinitrotoluene), and Composition B (a 60:39:1 mixture of RDX [1,3,5-hexahydro-1,3,5-trinitrotriazine], TNT, and wax). Both TNT and RDX are toxic (ATSDR 1995) and have low screening levels in drinking water: 2.2 μgL^{-1} for TNT and 0.6 μgL^{-1} for RDX (U.S. EPA 2008). These pieces may not represent a training hazard, but they can contaminate an entire aquifer. For example, work at Massachusetts Military Reservation estimated that 880 million–1.3 billion gal of water were contaminated by 14–36 kg (30–80 lb) of RDX (Clausen et al. 2004, 2007). It is clear that gram and kilogram pieces of explosives present a significant risk to groundwater.

Dissolution models have indicated that gram to kilogram pieces dissolve slowly (Matyskiela 2003; Lever et al. 2005) and even at high rainfall rates, large chunks of explosives should take many years to dissolve. Anecdotal observations, however, suggest that explosive chunks are friable and may mechanically break down to large numbers of millimeter-size particles which dissolve on a time scale of months rather than years. For example, chunks of explosives appear to be common on desert ranges such as Fort Bliss, Texas, but rare on ranges that experience high rainfalls (defined as greater than 100 cm per year) such as Fort Lewis, Washington.

Only a few studies have measured the persistence of these compounds in the field, and even then, the presence of explosives was determined by analyzing the soil rather than by observing the HE residues (Dubois and Baytos 1991; Radtke et al. 2002). For example, Radtke sampled surface soils at an explosives testing area that had not been used for 50 years and found that the >3 mm soil-size fraction accounted for more than 96% of

the HE contamination. These data suggest that large, millimeter-size pieces remained, while smaller particles have dissolved.

In a different study, powdered explosives were mixed with soils at Los Alamos National Laboratory, New Mexico (Dubois and Baytos 1991). After 20 years, Dubois and Baytos found that RDX, HMX, and PETN persisted, while explosives containing TNT, barium nitrate, or boric acid decreased dramatically in the soils. It should be noted that Los Alamos has a low yearly rainfall that averaged 47.5 cm per year from 1971–2000.

Range characterization studies (Pennington et al. 2006; Hewitt et al. 2003) found HE in surface soils at all military installations that were sampled. HE also was found in groundwater at Fort Lewis (Jenkins et al. 2001) and at three Canadian installations (Martel et al. 1999, 2009; Bordeleau et al. 2008a, 2008b). Dissolution of HE particles by precipitation has to occur before aqueous transport or biodegradation of the HE. The mass transfer of explosives from the solid to liquid phase appears to be the rate-limiting step before aqueous transport or biodegradation. The solubility of pure explosives has been measured (Ro et al. 1996), but it is the dissolution rate as a function of particle size that is needed to predict dissolution rates of explosive compounds on ranges. Researchers have measured the dissolution of explosive particles in laboratory settings (Lynch et al. 2001, 2002a, 2002b; Phelan et al. 2003; Lever et al. 2005) and made some progress modeling their behavior (Matyskiela 2003; Lynch et al. 2003; Lever et al. 2005).

Lynch et al. (2002a) cast TNT and Comp B samples into disks measuring 5.5 cm (diameter) x 0.88 cm (thickness) and measured their initial dissolution rates in a fixed water volume stirred at a constant rate. Using similar methods, they also measured the dissolution rates of pure RDX and TNT dissolved separately and in unbound mixtures in the same proportions as found in Comp B. The experiments measured the initial dissolution rates of TNT and RDX in Comp B but did not track changes as the particles dissolved and varied in size, nor did they track the surface texture and composition of the explosives. The method described by Lynch et al. (2002b) to equate mixing power with rainfall power uses empirical correlations not easily equated with rainfall rates. Their experiments yielded dissolution rates 2 orders of magnitude greater than those reported by Lever et al. (2005). In addition, the Lynch data do not give consistent values when normalized by the calculated surface areas of the constituents exposed on the surface of the samples.

Phelan et al. (2003) layered Comp B particles within a matrix of glass beads in a cylindrical column and subjected them to steady water flow through the porous medium. The particles were manufactured from bulk Comp B and sieved to produce narrow-size distributions centered on 0.1 mm and 1 mm diameters. Micrographs showed HE "dust" adhering to the surface of the particles. The concentration of TNT and RDX in the effluent was measured at regular intervals, and the TNT and RDX residues in the glass-bead matrix were measured at the end of each experiment to check for mass balance. By dissolving particles having a range of sizes and HE dust on their surfaces, Phelan et al. (ibid) blurred the behavior of individual particles, their dissolution sequence, and the time needed for them to dissolve. Also, the HE surface dust probably dissolved rapidly at the onset of each test, accounting for initial concentration spikes that were saturated (at the solubility limit for the compound). Measured mass-balances for TNT were poor, ranging between 35%–89% with most tests falling in the 50%–70% range. The authors could not account for these low values, making it difficult to quantify experiment dissolution times and mass-loss profiles.

Matyskiela (2003) modeled the mass transfer (dissolution) of a "neat" cylindrical block of Comp B that was in direct contact with porous soil. The model included both diffusion and advection of dissolved RDX and TNT through a stagnant boundary layer adjacent to the Comp B block. The advection model derives from Chambre et al. (1982, 1984). It is identical to the slow-percolation model presented by Lever et al. (2005) except Matyskiela assumed the RDX and TNT components dissolved independently. Consequently, the TNT dissolution rate is predicted to be much faster than that of RDX, contrary to measured rates (Lever ibid.). As expected, Matyskiela found that mass loss by diffusion is much slower than that by advection for all test cases modeled. Matyskiela also warned that mass loss, based on annual average flow rather than "burst" rainstorm flow, over-predicts actual loss rates if dissolution rate varies as the square root of rainfall rate.

Lever et al. (2005) were the first to design their experiments to mimic rainfall-driven dissolution of HE residues on surface soils, to use HE residues collected from detonations, and to track changes in individual particles as dissolution proceeded. They dripped water on individual field-collected Comp B particles, and collected and analyzed the effluent to obtain RDX and TNT mass losses versus time. The authors ran four single-particle experiments and used these data to validate two dissolution

models for Comp B that attempted to bracket conditions on training ranges. When the percolation rate of water into the soil is fast, water will not pool on the surface but will disappear quickly into the ground (Figure 1-a). Raindrops impinging nearby will repeatedly wet an exposed HE particle. Between raindrops, the particle will hold a stagnant water layer against its surface, but otherwise the particle will not feel a mean flow velocity. The next raindrop will then wash away the dissolved HE and refresh the stagnant water layer. In contrast, when the percolation rate of water into the soil is slow, water will pool on the surface during a rainstorm (Figure 1-b). The mean flow velocity of water past an exposed HE particle will then approximate the average rainfall rate during the storm. This second conceptual model also simulates dissolution of a particle that experiences constant soil moisture such as one mixed in with the soil (Matyskiela 2003).

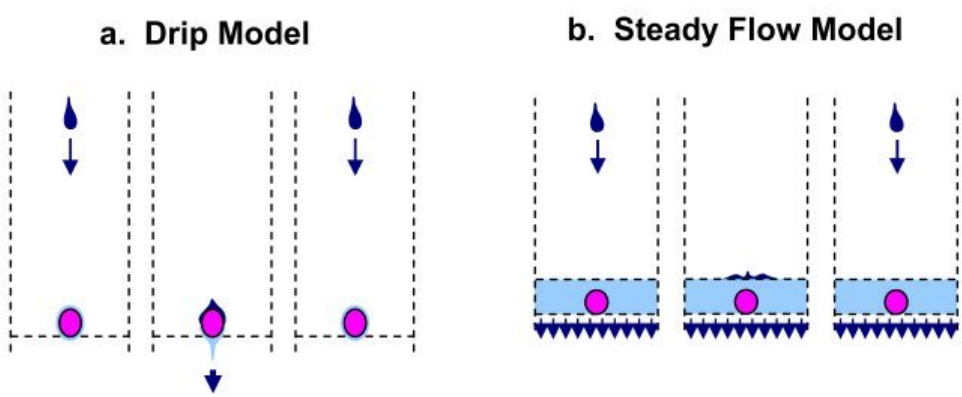

Figure 1. Schematic of the drip-impingement model and steady flow model for HE dissolution. Each model contains one unknown, which is parameterized using the measured dissolution data. The drip-impingement model uses the thickness of the wetted layer, whereas the steady flow model uses a surface area factor; both are related to the surface area of the HE chunk and termed area factors.

1.2 Objective

Our first goal was to obtain the data required to measure and to predict the dissolution rate of explosive residues that result from the commonly used military explosives TNT, Comp B, Tritonal, Octol, and C4. This information is needed to assess the risk to groundwater and to provide range managers a timeframe over which the explosive load on their range will dissolve. Because particle size strongly influences dissolution rate, our second goal was to understand how the energetic compounds weather and break apart in different environments.

1.3 Approach

To achieve these goals we took each of the following steps:

1. Measured dissolution rates of explosives using both laboratory and outdoor tests
2. Used the dissolution data to validate our "drop-impingement" dissolution model;
3. Measured the crushing strength of weathered and un-weathered pieces of TNT, Comp B, and Tritonal; and
4. Documented the appearance, over time, of the HE chunks placed outside for our dissolution tests and for other HE chunks deposited by LO detonations in both semi-arid and salt marsh environments.

We dissolved millimeter-size pieces of TNT, Comp B, Tritonal, and Octol in the laboratory and obtained curves based on mass loss versus time. The particles took several months to dissolve, and we obtained good mass balance (>96%) for the Comp B, TNT, and Tritonal particles. The time series for dissolution from the laboratory experiments were used to validate and expand our previously published drip model (Lever et al. 2005). The generally good agreement between the observed and predicted dissolution data at two simulated rainfall rates indicated that the drop arrival time does indeed scale dissolution rate. The model did not predict well the TNT dissolved-mass time series for the Octol particles. Octol had a poor mass recovery, and although we recovered all the TNT, we did not recover the HMX. We think that the large crystal size and low solubility of HMX relative to the other explosives contributed to our low mass recovery.

1.4 Scope

We have a three-year dissolution record for TNT, Tritonal, Comp B, and C4 from our outdoor tests, in which we collected and analyzed the precipitation interacting with 34 cm-size HE chunks. Because we sought to document changes in the appearance of HE chunks and to check for mass balance, we periodically photographed and weighed the chunks. This revealed two important findings: (1) dissolved TNT mass represented only about one-third of the mass losses from the TNT and Tritonal chunks, and (2) dissolved RDX mass accounted for about half of the original mass. We think the TNT loss is due to phototransformation from the solid into compounds not quantified by Method 8330B. We continue to investigate various pathways that could lead to TNT and RDX loss. Control solutions,

placed outside (next to our outdoor samples) decreased only slightly in concentration, indicating that the explosives did not transform while in solution in the sample bottles. Consequently, our water samples preserved a record of the explosives dissolved from the HE chunks over the three-year experiment and can be used to validate dissolution models.

The drop-impingement model mimics the physical circumstances of HE particles scattered on range soils and wetted by raindrops. It predicts the TNT dissolved-mass time series with remarkably low, root mean square (RMS) prediction errors (12%–13%) for both TNT and Tritonal chunks. The drop-impingement model also forms the basis for modeling rainfall-driven dissolution of Comp B.

However, Comp B, with two HE components dissolving at different rates, requires a more ambitious model. The layered Comp B dissolution model described here simulates the dissolution and recession of TNT and its phototransformation products, the formation of a porous layer from the remaining Comp B crystals, the release of a portion of these crystals and their independent dissolution as small particles, and the impeding effect of the Comp B layer on further TNT dissolution. On average, the model predicts the correct scale of TNT and RDX dissolution for all the chunks studied, with uncertainties of approximately a factor of two. Although this uncertainty is much higher than for single-component TNT and Tritonal chunks, many more processes are modeled.

Our models indicate that the water volume wetting the HE controls the dissolution to first-order, so that we can use yearly rainfall data and average solubility to calculate the dissolution rate and expected lifespan of HE pieces on training ranges across the United States. Indeed, population modeling for two crushed TNT and Tritonal chunks, with known initial-size distributions, produced excellent agreement with measured dissolution data when the populations were returned outdoors.

The frequency at which HE chunks split is not known; it will depend on both the strength of the explosive compound and the environment in which it is deposited. To gauge the importance of this process relative to dissolution, we (1) measured the crushing strengths of HE chunks in the laboratory, and (2) monitored the appearance of HE chunks in three different environments. We found that the crushing strength of TNT, Tritonal, and Comp B were low (generally about 20 lb), and did not significantly change after three years of outdoor exposure. Interestingly,

the size distributions resulting from the crushed HE chunks all show power-law distributions, as was found for blow-in-place, low-order detonations. This similarity suggests that we can crudely estimate particle size distributions on range soils given estimates of total mass.

All TNT-containing explosives that were monitored outside turned red. This coating washed off the Comp B pieces monitored at the Eagle River Flats (ERF), Alaska, salt marsh and stained the soil around the Tritonal particles in the arid environment at Holloman Air Force Base (AFB), New Mexico. The Tritonal chunks appeared to have lost mass by spalling millimeter-size or larger pieces; the explosives at ERF, which were submerged and frozen in saline water for part of the year, crumbled and were quickly dissolved. Of the 34 chunks we monitored in our experiment, 4 split naturally, 9 developed cracks, and 14 spalled millimeter-size pieces. Both the HE chunks' splitting into smaller pieces and the phototransformation of the HE chunks are processes intrinsic to the outdoor weathering of HE. Such processes complicate modeling the dissolution.

In this report we focus on the former, drop-impingement model. It mimics a common condition on training ranges, where HE particles are scattered by LO detonations onto surface soils and exposed to direct impingement by raindrops and to prolonged dry spells. This model predicts the dissolution rate of HE under the action of rainfall as functions of particle size or mass. For saturated systems, the steady-flow model would be more appropriate.

Our goals were to quantify dissolution rates for detonation residues of TNT, Comp B, Tritonal, and Octol and then, to use that data to model their lifespan as a function of particle size. Although researchers have estimated the mass of HE residues in range soils (Jenkins et al. 2001; Pennington et al. 2006) and measured the partitioning coefficients between waters containing dissolved explosives and soils (Morley et al. 2006; Dontsova et al. 2006), these two types of data are linked through the dissolution of the HE particles (Figure 2). Furthermore, we think dissolution of HE particles is the rate-limiting step preceding biodegradation or aqueous transport.

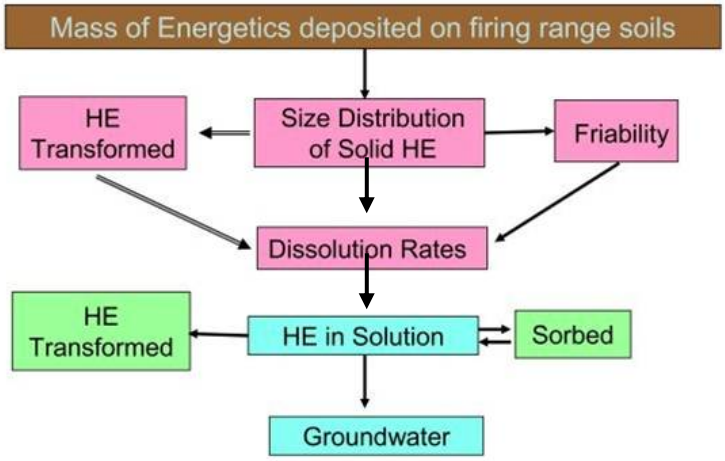

Figure 2. Schematic showing how our study (shown in pink) fits into the bigger picture of mass loading of HE onto range soils and processes that affect the fate of HE.

The dissolution rate of a particle depends on its surface area exposed to rainfall. Consequently, data on the size distribution of the HE particles deposited by detonations and how this distribution changes as a result of particle dissolution and weathering, are also needed to estimate the aqueous-phase influx of HE into range soils. We sought insight into these factors by intentionally crushing HE chunks and returning them outdoors to measure the dissolution rate of known populations of HE particles. We also documented natural splitting, cracking, and spalling of HE chunks during the three-year experiment to estimate the frequency of these population-changing processes.

1.5 Report content overview

We divided this report into chapters that describe the different experiments run to elucidate HE dissolution. Both the laboratory (Chapter 2) and the outdoor dissolution drip tests (Chapter 3) show cumulative mass-loss records of HE with time. We used these mass-loss time series to extend the drip model developed by Lever et al. (2005) and use the explosive concentration in the water. We used either the drip rate or rainfall records to obtain analytical predictions for the dissolution time of explosive pieces as functions of particle size or mass.

In Chapter 4, we investigate the phototransformation of TNT. Because we weighed the HE chunks placed outside at the beginning and end of the experiment, we know that the mass lost from these chunks is not accounted for by the dissolved mass; in fact, between 60%–80% of the HE mass is missing. We have eliminated handling losses, sublimation, and

analytical errors as possibilities for the missing mass. Instead, we think that sunlight is phototransforming TNT and RDX on the surface of the HE chunks into compounds not detected by Method 8330B. If we are correct that TNT phototransforms as a solid, this finding could be very significant since we may not be screening for all potentially harmful compounds in surface and ground waters. Chapter 4 contains Dr. Spanggord's analytical results on the transformation products.

In Chapter 5, we describe the laboratory crushing tests performed on both weathered and unweathered chunks of TNT, Comp B, and Tritonal to help quantify the friability of these compounds. However, since mechanical disaggregation may also depend on environmental factors, in Chapter 6 we document changes to Tritonal chunks found at Holloman AFB (a semi-arid environment) and compare these to Comp B and C4 pieces scattered at ERF (a tidal salt marsh).

2 Laboratory Dissolution Tests

These laboratory tests mimicked field conditions on training ranges, where spatially isolated particles of explosives on the soil surface are dissolved by rainfall. We dripped water onto millimeter-size TNT, Comp B, Tritonal, and Octol and also analyzed the HE mass in the effluent. The particles took several months to dissolve. Two drip rates–0.5mL per hr and 1.0 mL per hr–were used to validate the effect of flow on our drop impingement model. We were able to model the dissolution of TNT, Comp B, and Tritonal well, but with Octol, our mass recovery of the HMX was poor.

2.1 Materials and methods

2.1.1 Sample composition

Our HE particles (TNT, Tritonal, Comp B, and Octol) were all collected from LO field detonations. TNT is a single-explosive compound used by all the services but particularly by the Navy. Comp B is a mixture of 39% TNT, 60% RDX, and 1% wax which is used in mortars and projectiles. Tritonal is an 80% TNT and 20% aluminum mix which is used in Navy bombs. Octol is a mixture of 70% HMX and 30% TNT which is used in penetrators and rockets. The goal of studying pure and mixed compounds was to determine and model how these explosives dissolve and to generalize the results to other explosive compounds.

2.1.2 Experimental set-up

Our laboratory set-up consisted of two, multi-syringe pumps (from Cole Palmer) that allowed us to drip deionized water simultaneously onto eight separate particles. These eight particles consisted of one particle of each of the four HE formulations at two different drip rates. A needle on each syringe dripped water onto an HE particle resting on a 10 mm-diameter glass frit at the base of a Buchner funnel that drained into a 20- or 40-mL scintillation vial (Figure 3). The vials were replaced daily, and the volume and HE concentration of the effluent analyzed. These data provided dissolved HE mass as a function of time for each of the eight particles. At the end of the tests, we extracted each frit and funnel with acetonitrile and analyzed the solutions for HE mass.

Figure 3. Laboratory setup showing the multiple-syringe pump used to drip water on explosive particles.

The two pumps were programmed to flow at 0.5 and 1.0 mL per hour. We measured the actual flow rates and number of drops per hour for each syringe. These flow rates averaged 0.47 ± 0.06 mL per hour with 26 drops per hour, and 0.95 ± 0.09 mL per hour with 56 drops per hour at the two programmed rates. For reference, these flow rates corresponded to rainfall rates of 5.9 and 12.0 mm per hour based on the cross-sectional area of each glass frit. The average volume of the arriving drops was larger than that expected for the natural rainfall at the same flow rates (Pruppacher and Klett 1997), and each arriving drop wetted the particle on the frit. The deionized water used for the tests was at room temperature, and the latter was fairly constant throughout the tests at 22 °C ± 1 °C. Tests were normally stopped over the weekends, and the particles allowed to dry out.

2.1.3 Analytical methods

Explosive concentrations were determined following SW-846 Method 8330B (U.S. EPA 2006). A quantity of 1 mL of the effluent was added to 2 mL of deionized water and 1 mL of acetonitrile, and then filtered through a 0.45 µm syringe filter (from Millipore). High Performance Liquid Chromatography (HPLC) separated TNT, RDX, HMX, and their co-contaminants and breakdown products (1,3,5-TNB, 1,3-DNB, 2,4-DNT, 2,6-DNT, 2-ADNT and 4-ADNT) in the water samples. We used a column (3.9 x 150 mm; Waters NovaPak C8), eluted at 1.4 mL per minute (28 °C), with an 85:15 ratio of water to isopropanol mix, and detected by UV at 254 nm. A commercially available standard (from Restek, Bellefonte, PA) was used for calibration. We prepared 1 ppm and 10 ppm dilutions of these standards. The 1 ppm standards were run every 10 samples, and blanks

were run before and after each standard run. The 10 ppm standards were interspersed with the samples as internal checks, with blanks after each to prevent carryover. Based on the concentrations of the standards and the precision of the effluent volumes, we estimated that the cumulative, dissolved HE masses have uncertainties of about ±1%.

2.2 Results

2.2.1 Appearance of test particles

Figure 4 shows photographs of the 8 particles taken at the beginning and partway through the dissolution tests, at 30 days for the 0.5 mL per hour tests, and at 21 days for the 1.0 mL per hour tests. The TNT particles became smoother and smaller but retained their original shapes. The Tritonal particles became smaller and slightly bumpier as TNT dissolved exposing the aluminum grains. The Comp B particles, on the other hand, became noticeably bumpier and "sugary-looking" as dissolution of the surface TNT revealed the larger (~ 0.1 mm), slower-dissolving RDX crystals. The Octol particles disaggregated completely when their TNT matrix dissolved leaving large (~ 1 mm) HMX crystals (see Figure 4, Octol 2 at 21 days).

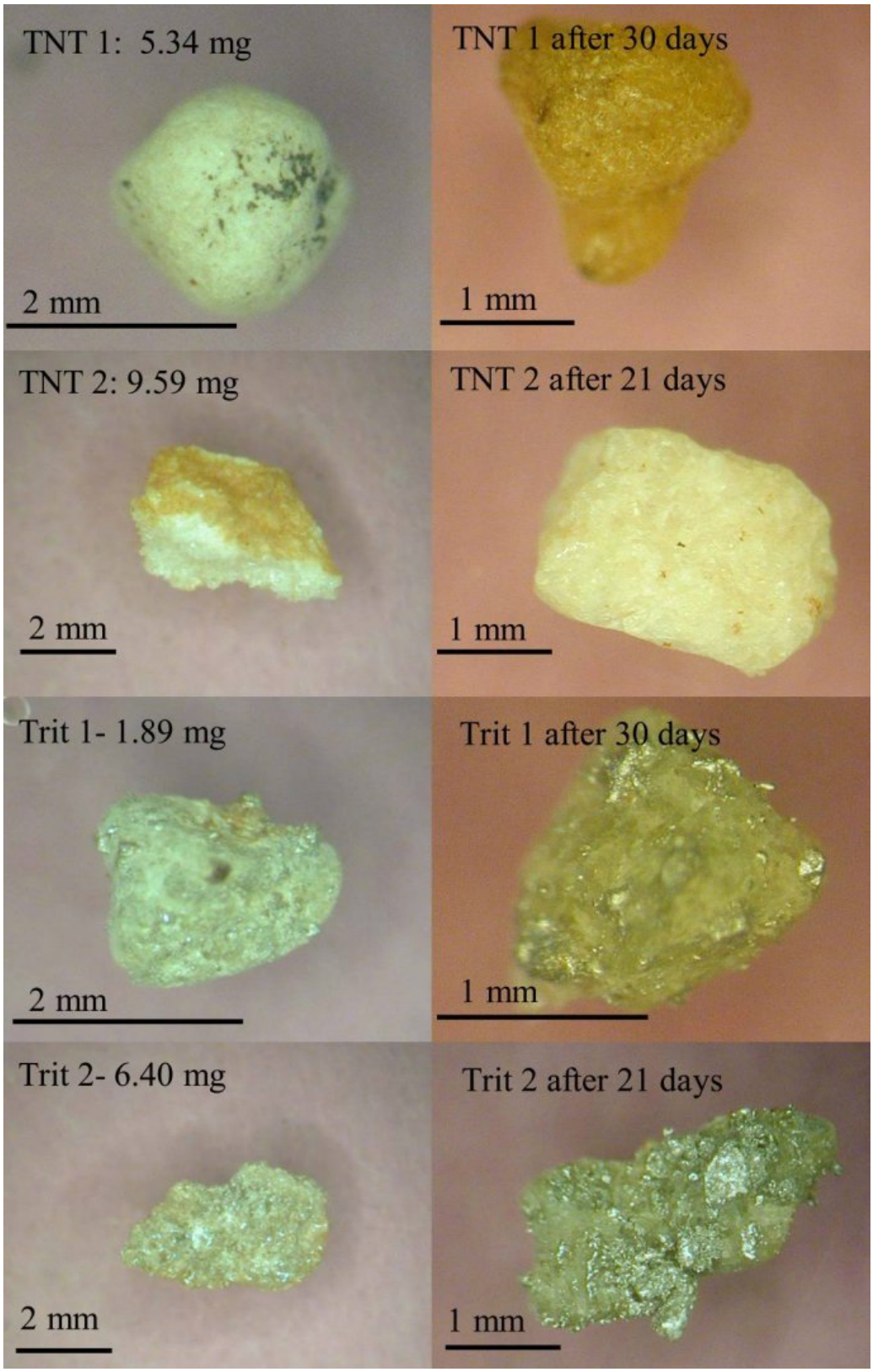

Figure 4. Photos and initial masses of millimeter-size particles used in the 0.5 and 1.0 mL/hr laboratory tests.

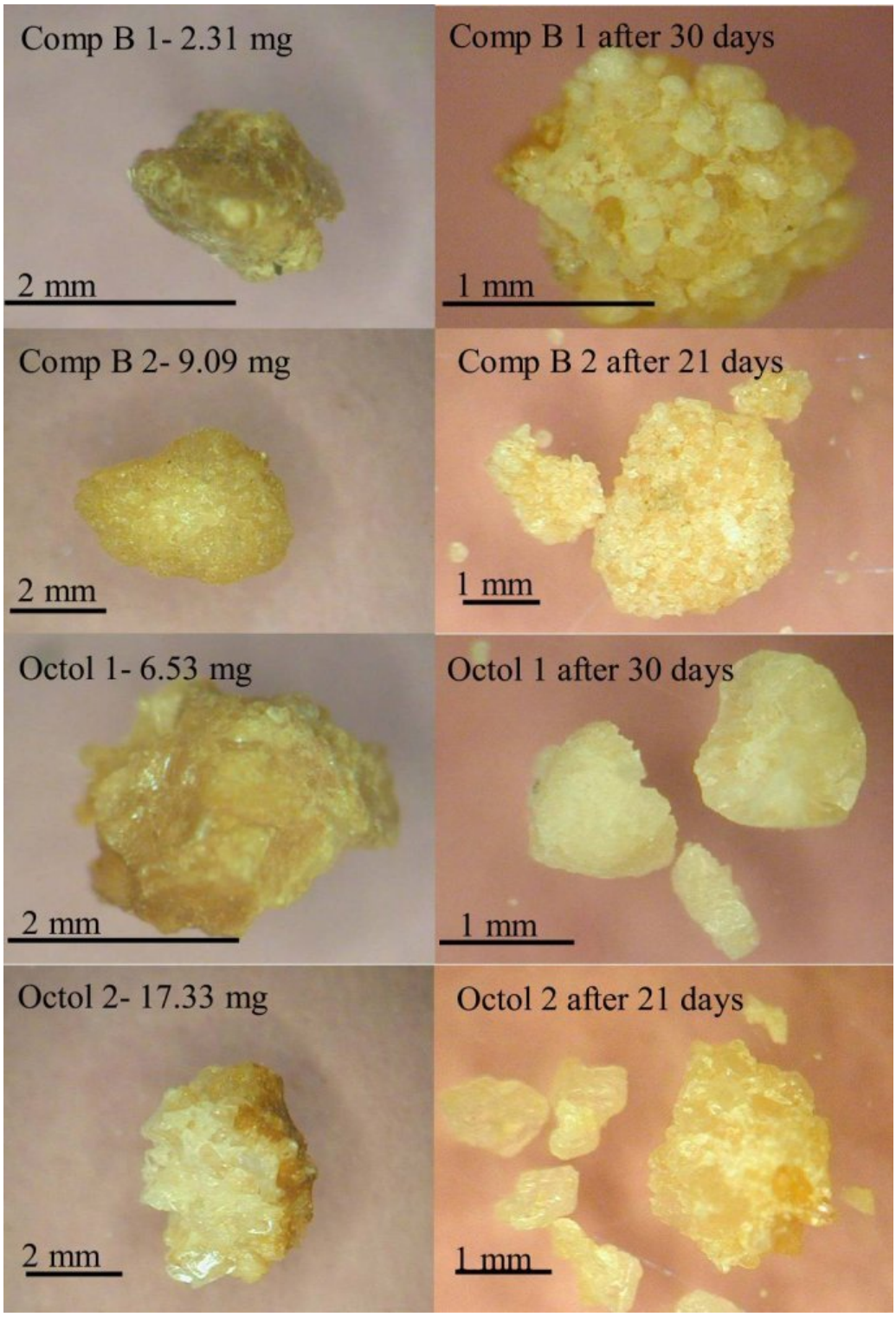

Figure 4 (cont.). Photos and initial masses of millimeter-size particles used in the 0.5 and 1.0 mL/hr laboratory tests.

2.2.2 HE mass recovery

Table 1 lists the dissolution test parameters and the recovered mass for the eight drip-test particles. The "1" and "2" particle designations refer to the nominal 0.5 mL/hr and 1.0 mL/hr drip rates, respectively. We recovered essentially 100% of the mass for the two TNT particles and for Comp B 2 (Figure 2.3 and 2.4). The recovered HE mass for Comp B 1 (96.5%) was close to the average (96% ± 1%) found by Lever et al. (2005) for 30 individual Comp B particles obtained from the same low-order detonation. The two particles dissolved here had RDX:TNT ratios of 1.69 and 1.87, similar to the average ratio obtained by Lever et al. (2005) of 1.74 ± 0.28. We measured less than 1% HMX, an impurity in RDX, in these Comp B particles.

Table 1. Dissolution test parameters and the recovered mass for HE particles.

Particle	Drip Rate mLh^{-1}	Initial Mass (mg)	Dissolved Mass (mg)	Time (days)	Mass Recovered %
TNT 1	0.5	5.34	5.33	201	99.9
TNT 2	1.0	9.59	9.70	98	101
Tritonal 1	0.5	1.89	1.28	72	67.8*
Tritonal 2	1.0	6.40	5.02	73	78.5*
Comp B 1	0.5	2.31	2.23	200	96.5
Comp B 2	1.0	9.09	9.03	141	99.4
Octol 1	0.5	6.52	2.15	101	33.9*
Octol 2	1.0	17.33	9.92	140	57.2*

* All the TNT mass.

For Tritonal 1 and 2, the recovered TNT mass was 67.8% and 78.5% of the initial mass (Figure 5 and Figure 6). This included TNT extracted from the frits. Both particles fell within 2σ of the nominal Tritonal composition. To check the compositional heterogeneity of millimeter-size Tritonal particles, we weighed, dissolved, and analyzed 21 such particles (Figure 7). The percentage of TNT by weight ranged from 52% to 84% of particle mass and averaged 77.5% ± 6.6%. Thus, the average of the 21 particles fell well within 1 standard deviation of the nominal composition of Tritonal (80% TNT).

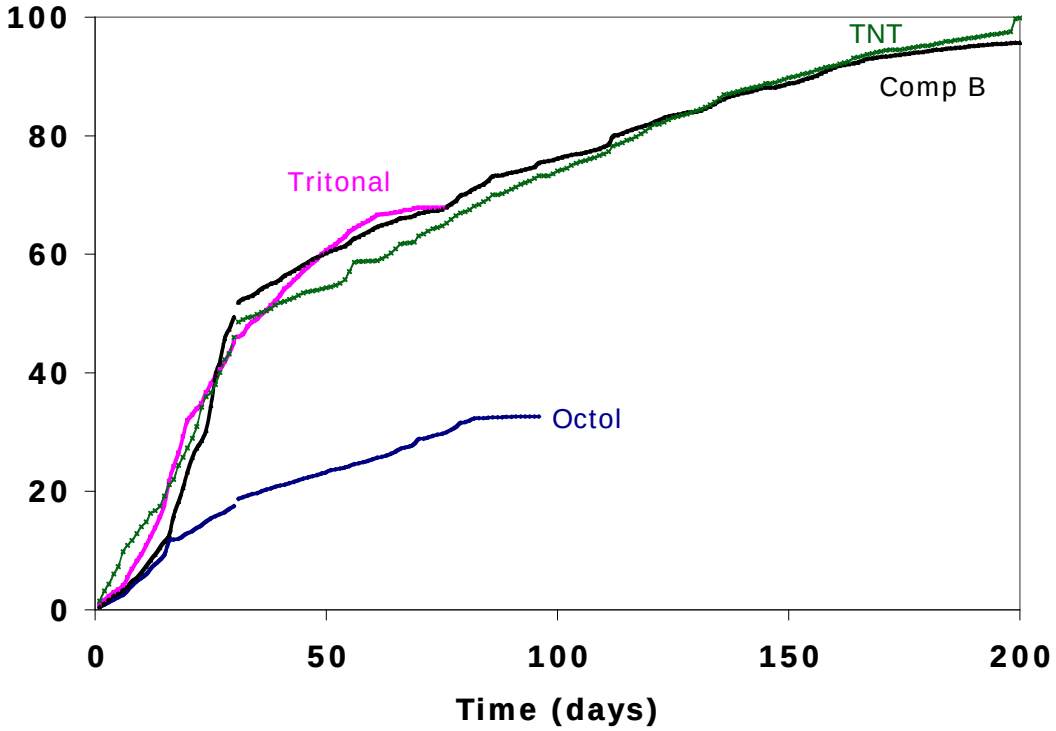

Figure 5. Percent mass loss (mg) of HE particles versus time for a 0.5 mL per hour drip rate. The starting masses of the particles were TNT=5.34 mg, Comp B=2.31 mg, Tritonal=1.89 mg, and Octol=6.53 mg.

For Octol 1 and Octol 2, we recovered 1.86 mg and 3.61 mg of TNT, representing 28.4% and 20.8% of the initial particle masses, respectively (Figure 5 and Figure 6). Octol nominally contains 30% TNT, but we would expect millimeter-size particles to vary significantly from this value owing to the large (~ 1 mm) crystals of HMX present in the TNT matrix. Both dissolution tests continued for many days with no measurable TNT in the water samples, and we found no additional TNT in a series of acetonitrile extractions of the funnels and frits at the end of the tests. Thus, we think the dissolution tests recovered all the TNT initially present in the two Octol particles.

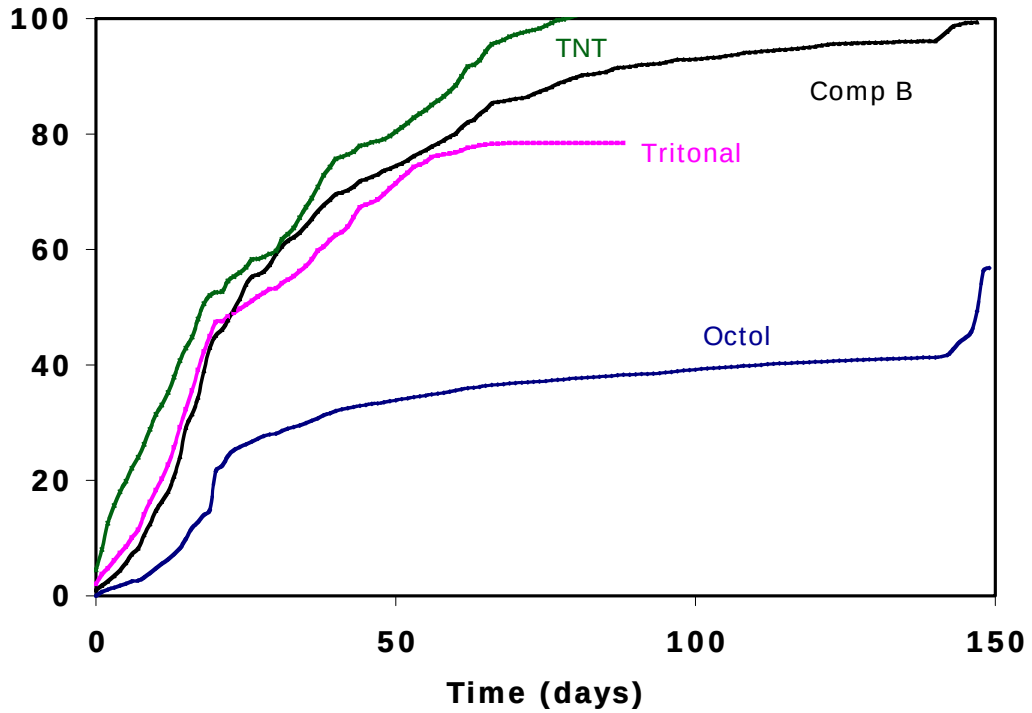

Figure 6. Percent mass loss (mg) of HE particles versus time for a 1.0 mL/hr drip rate. The starting masses of the particles were TNT=9.59 mg, Comp B=9.09 mg, Tritonal=6.40 mg and Octol=17.33 mg. Extraction of frits at end of tests accounted for the final increases seen in the Comp B and Octol records.

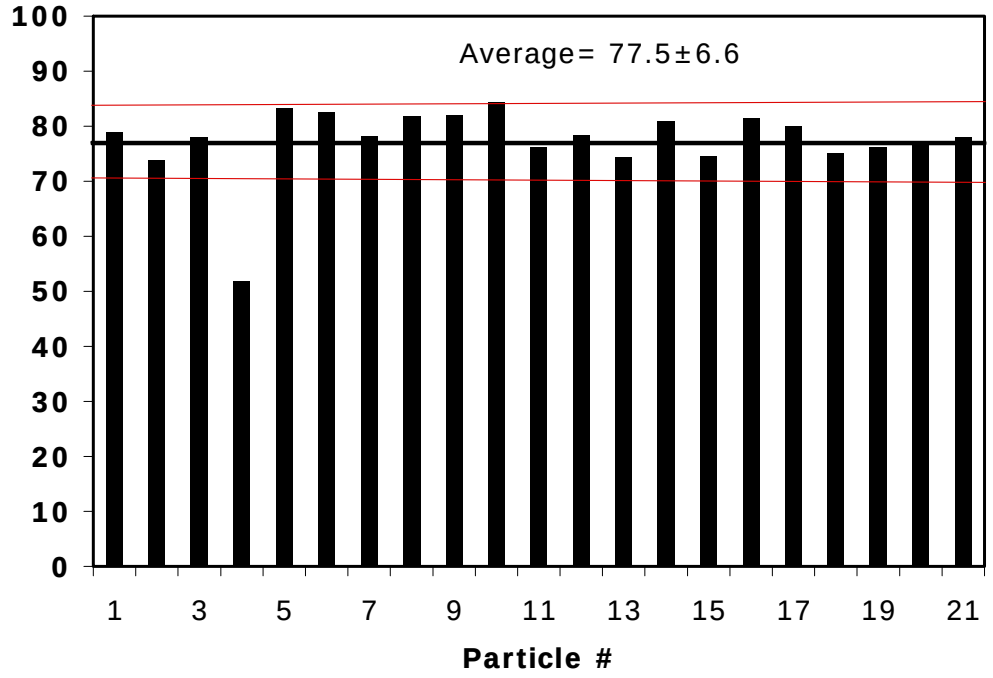

Figure 7. Percent TNT present in 21 mm-size Tritonal particles. Particles were weighed on a microbalance, extracted, and analyzed. The horizontal black line represents the average percent TNT present; red lines mark the one standard deviation.

2.2.3 Dissolution modeling and comparison with dissolved mass time-series

Lever et al. (2005) developed and validated a drop-impingement model for the rainfall-driven dissolution of millimeter-size Comp B particles. It pertains to the practical case where spatially isolated HE particles reside on well-draining surface soils and thus are exposed to direct impingement by raindrops. The present experiments simulated these circumstances. With rare exceptions, water quickly drained through the glass frits so that impinging drops interacted directly with the HE particles. The present experiments offer additional data to validate this model for other HE formulations and for two simulated rainfall rates.

The drop-impingement dissolution model assumes that raindrops hit and wet an HE particle. Between raindrops, the particle holds a stagnant water layer against its surface, which saturates, via diffusion, with HE. Arrival of the next raindrop washes away the dissolved HE and refreshes the stagnant layer. The dissolution rate, m_j (g/s) of HE species j, averaged over a drop-arrival interval, t_d (s), is thus

$$m_j = \frac{S_j V_l}{t_d} \tag{1}$$

where:

S_j = solubility of species j in water (g/cm^3)
V_l = water-layer volume (cm^3)

For a spherical particle, a water layer of thickness h (cm) will effectively saturate (average concentration > $0.9S_j$) provided that

$$t_d > \frac{h^2}{D_j} \equiv t_s \tag{2}$$

where:

D_j = diffusion coefficient of species j into water (cm^2/s)
t_s = layer saturation time

Additionally, for Equation 1 to apply, the volume of an arriving water drop, V_d, must be larger than the volume of the stagnant water layer. This

generally limits the applicability of Equation 1 to millimeter-size and smaller particles.

Each HE species in a particle could dissolve independently, following Equation 1, if it is in contact with the water layer and has a sufficiently high diffusion coefficient to satisfy Equation 2. However, Comp B and Octol particles consist of low-solubility crystals (RDX and HMX, respectively) embedded in higher-solubility TNT matrixes. Initially, TNT on the surface of these particles can dissolve independently into the water layer, leading to high initial TNT dissolution rates. However, the lower-solubility crystals eventually restrict the pathways for TNT molecules to diffuse into the water layer. TNT diffusion into the water layer then becomes analogous to molecular diffusion through a porous medium, where porosity and tortuosity combine to reduce significantly the effective diffusion coefficient (Bear 1972; Chambre et al. 1982; Chambre and Pigford 1984). Consequently, TNT will not saturate the water layer between drops, and its effective dissolution rate will decrease.

Lever et al. (2005) observed this effect during laboratory drip tests of Comp B particles. They implemented the limiting case where RDX dissolution controls the dissolution of TNT by using Equation 1 for RDX and assuming that TNT dissolves at a rate that maintains the bulk RDX:TNT mass ratio:

$$m_{TNT} = m_{RDX} \frac{\rho_{TNT}}{\rho_{RDX}} \tag{3}$$

where:

ρ_{TNT} and ρ_{RDX} are the mass densities of each species in the original Comp B particle.

This approach ensured that the time scale for RDX dissolution controlled the predicted TNT dissolution rate. We applied this approach for both Comp B and Octol particles, substituting ρ_{HMX} for ρ_{RDX} in Equation 3 for Octol.

We implemented the drop-impingement model for the eight test particles by treating each particle as a sphere of equivalent mass, so that the water-layer volume is simply

$$V_l = \frac{4}{3}\pi\left[(a+h)^3 - a^3\right] \tag{4}$$

where:

a = sphere radius (cm)

Because we could not measure the water-layer thicknesses, we determined h by fitting the predictions to the measured dissolved-mass time series for the slower-dissolving species in each particle. Effects of non-spherical particle shape are thereby folded into h. Table 2 summarizes the parameters needed to run the drop-impingement model and to check its validity ($t_d > t_s$, $V_d > V_l$).

Table 2. Model parameters.

Particle	ρ (gcm^{-3})	S_j(gcm^{-3})	D_j(gcm^{-3})	t_d (s)	h (mm)	t_s (s)	V_d/V_l
TNT 1	1.65	1.17E-04	6.71E-06	138	0.075	8.4	21
TNT 2	1.65	1.17E-04	6.71E-06	64	0.095	13	10
Tritonal 1	1.89	1.17E-04	6.71E-06	138	0.090	12	35
Tritonal 2	1.80	1.17E-04	6.71E-06	64	0.082	10	17
Comp B 1	1.65	4.02E-05	2.20E-06	138	0.092	38	28
Comp B 2	1.65	4.02E-05	2.20E-06	64	0.110	55	9.1
Octol 1	1.80	3.64E-06	1.50E-04	138	0.12	1.0	12
Octol 2	1.80	3.64E-06	1.50E-04	64	0.19	2.4	3.5

Densities of the explosive compounds are from Army Materiel Command (1971). Aqueous solubilities are from Lynch et al. (2001) at 22 °C and diffusion coefficients are from Lynch et al. (2002b) at 25 °C; listed are TNT values for TNT and Tritonal, RDX values for Comp B, and HMX values for Octol. The two densities for Tritonal reflect the different TNT/aluminum ratios of the two particles.

Figure 8 and Figure 9 compare the measured and predicted dissolved masses for the TNT and Tritonal particles, respectively. These particles contain only TNT, so Equation 1 applies directly. The model predicts the dissolution of all four particles quite well. The average layer thicknesses for the TNT and Tritonal particles were essentially the same at 0.085 ± 0.014 mm and 0.086 ± 0.006 mm, respectively. Note that for the particles, the drop-arrival times were longer than the water-layer saturation times, and the drop-volumes were larger than the water-layer volumes (Table 2) as required by Equation 1.

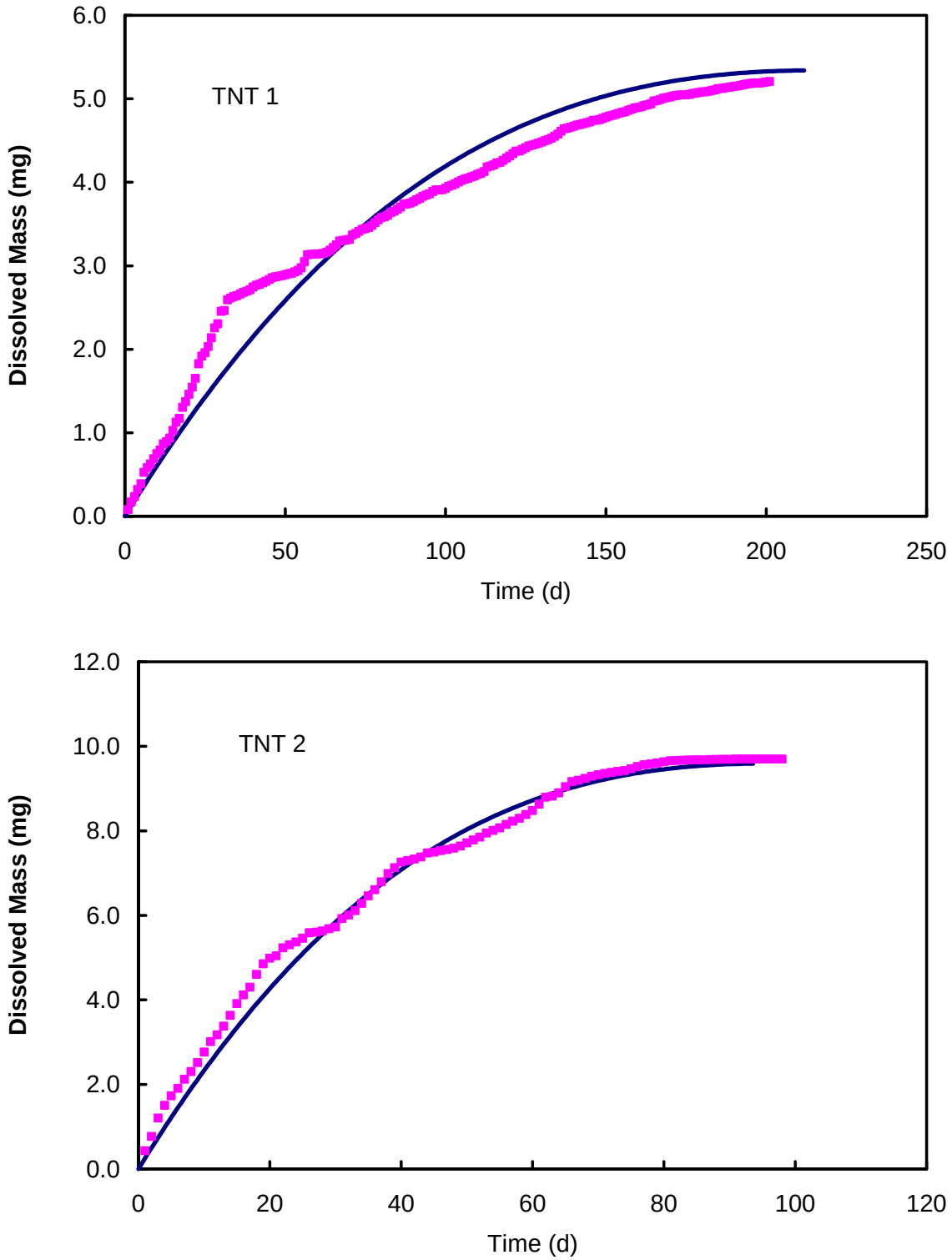

Figure 8. Cumulative dissolved mass versus time for the TNT test particles (symbols are measured values and smooth curves are modeled values).

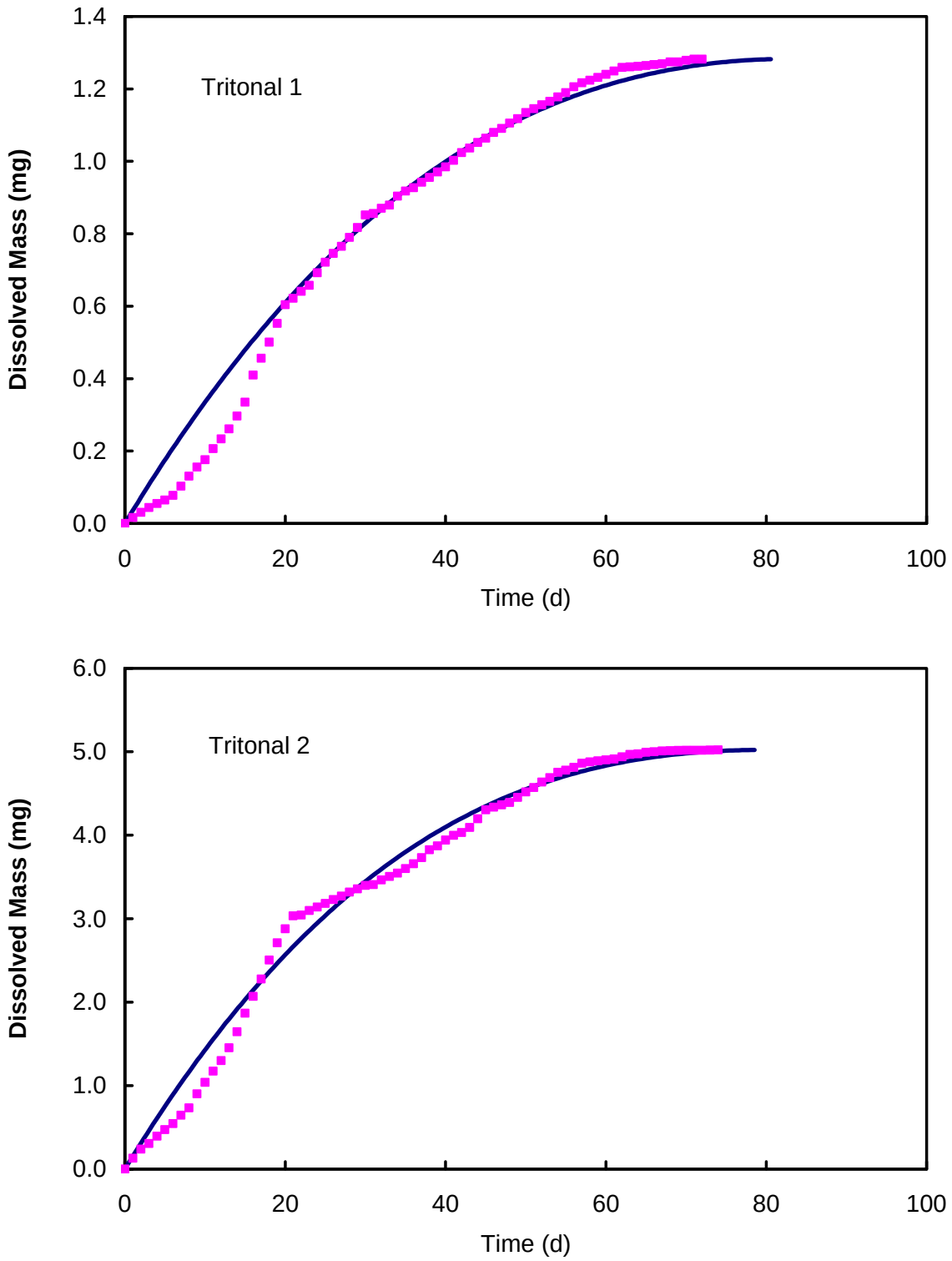

Figure 9. Cumulative dissolved mass versus time for the Tritonal test particles (symbols are measured values and smooth curves are modeled values).

Figure 10 shows the measured and predicted dissolved-masses for the two Comp B particles. The predicted RDX dissolution agrees quite well with

the measured results for both particles. In both tests, TNT initially dissolved quickly but eventually was controlled by the slower dissolution of RDX. The model predicts this behavior reasonably well using the limiting case of RDX control of TNT dissolution (Equation 3). By comparison, it predicts much faster dissolution under the assumption that TNT dissolves independently of RDX. Interestingly, the fastest dissolution rates observed near the beginning of the tests do approximate those for independent TNT dissolution. The transition from independent TNT dissolution to RDX-controlled dissolution probably reflects restriction of TNT diffusion into the water layer by the porous medium of RDX crystals.

The fitted water-layer thicknesses averaged 0.101 ± 0.013 mm for the two Comp B particles (Table 2). This compares well with the average value (0.13 ± 0.05 mm) obtained for the four Comp B particles tested by Lever et al. (2005). For both Comp B particles, the drop volumes were larger than the water-layer volumes, and the drop arrival times were longer than the RDX saturation times (Table 2). TNT saturation times must increase to account for eventual RDX control of TNT dissolution.

Figure 11 shows the measured and predicted dissolved masses for the two Octol particles. As with Comp B, measured TNT dissolution initially proceeded quickly, with maximum dissolution rates approaching the predicted rates for independent TNT dissolution. Unlike Comp B, however, the larger HMX crystals did not eventually control TNT dissolution, and all the TNT dissolved from both particles, which left HMX crystals. We terminated both tests after many days with no TNT in the water samples. The fitted water-layer thicknesses averaged 0.155 ± 0.049 mm, much larger than those for the other particles (Table 2). Nevertheless, the calculated saturation times (Equation 2) based on either TNT or HMX diffusion were less than the drop arrival times, and the water-film volumes were less than the drop volumes, as required by the model.

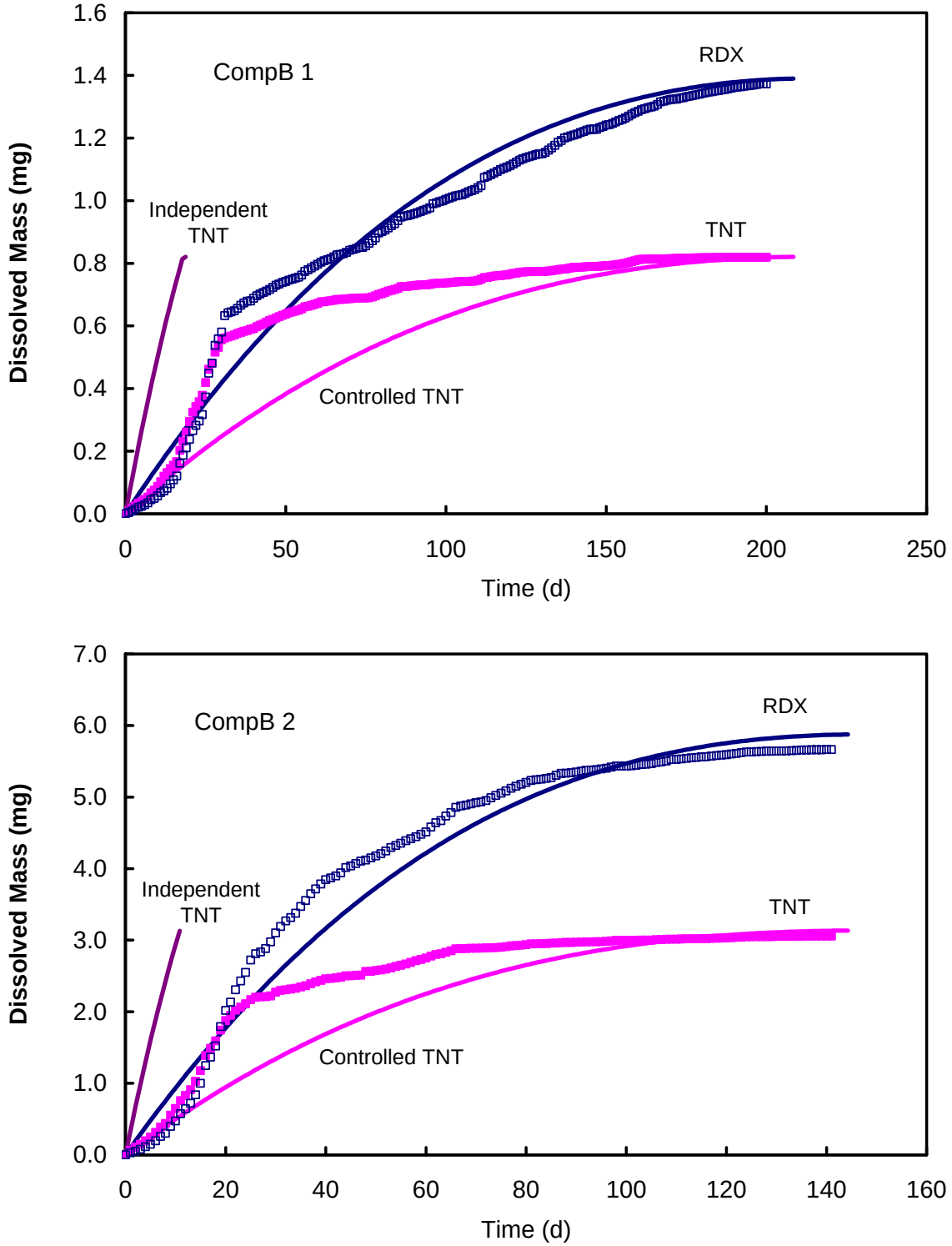

Figure 10. Cumulative dissolved mass versus time for the Comp B test particles (symbols are measured values, smooth curves are modeled values). Dissolution of RDX eventually controls dissolution of TNT (modeled via Equation 3). Independent TNT dissolution would occur much faster.

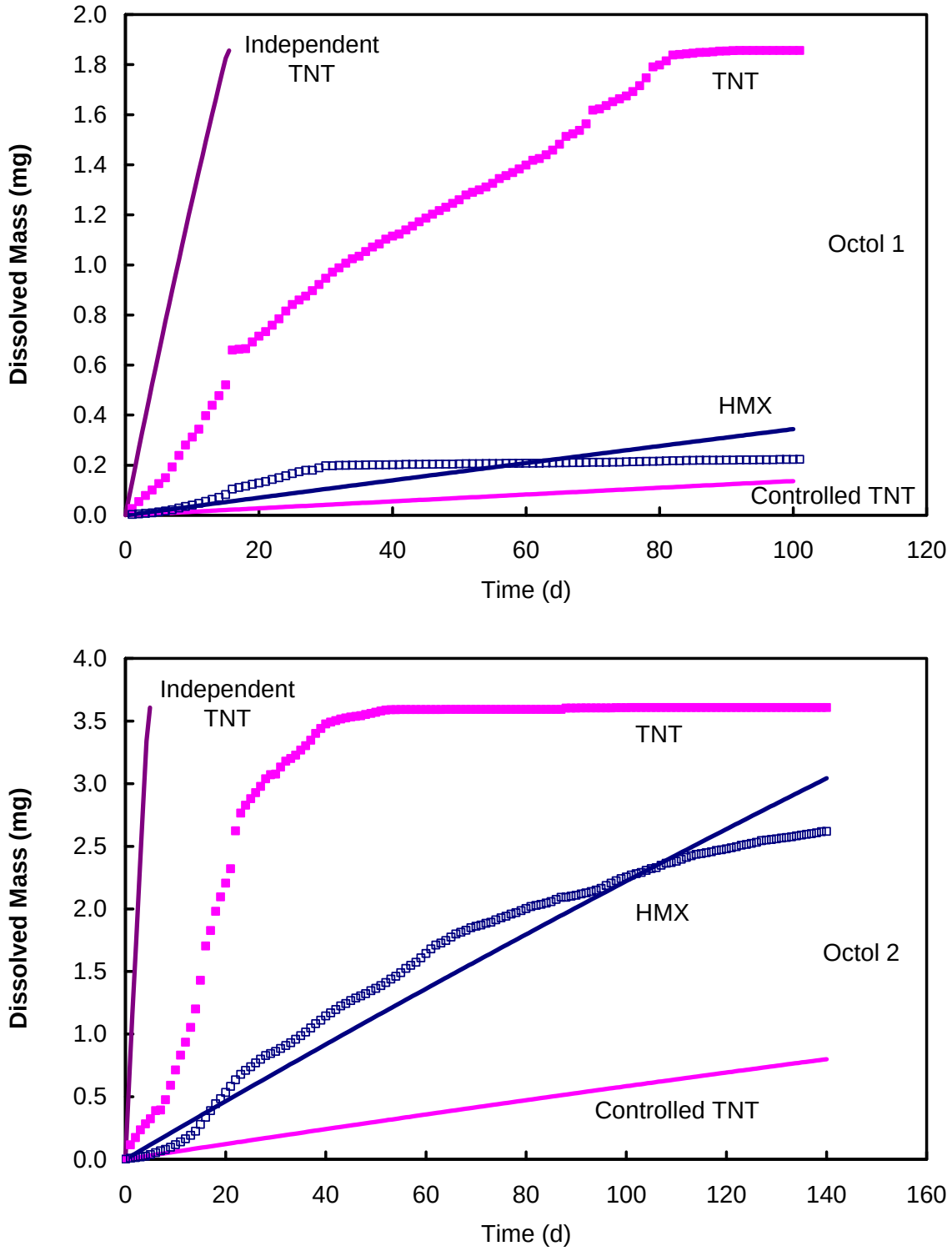

Figure 11. Cumulative dissolved mass versus time for the Octol test particles (symbols are measured values, smooth curves are modeled values). TNT dissolution rate apparently was neither controlled by, nor independent of, HMX dissolution.

2.3 Discussion

The laboratory tests dripped water on individual HE particles collected from field detonations. They more closely simulate the physical circumstances of HE particles exposed to rainfall on surface soils than do stirred-bath (Lynch et al. 2002a, 2002b) or glass-bead column experiments (Phelan et al. 2003). They yield estimates of aqueous HE influx to surface soils as functions of particle size, particle composition and rainfall rate while avoiding the complexity of aqueous-phase HE-soil interactions that occur during soil-column experiments (Pennington et al. 2006; Morley et al. 2006). TNT and RDX mass recoveries from all particles were very good; HMX mass recovery was complicated by its low solubility and disaggregation of the Octol particles following complete TNT dissolution.

Changes in the appearance of the particles provided insight into their dissolution mechanics. The two single HE-species particles, TNT and Tritonal, essentially retained their original morphologies as they dissolved, and their dissolution time series are fairly simple curves. The concentration of aluminum grains in Tritonal is apparently too low to disrupt dissolution of the TNT. By comparison, the Comp B and Octol particles quickly became lumpy as surface TNT dissolved to reveal underlying RDX and HMX crystals. Subsequently, the Comp B particles became smaller conglomerations of RDX crystals shielding internal TNT, while the Octol particles lost all their TNT and disaggregated into collections of HMX crystals.

We do not understand the reasons for discontinuities in the measured dissolution rates for some particles (e.g., TNT 1, Tritonal 2, and Comp B 1). The discontinuities did not coincide with either the dates of particle removal for photographing or observed splitting of the particles. The good mass balances confirm that the particles did not lose pieces during handling, and several particles did not display discontinuities beyond random fluctuations.

The drop-impingement dissolution model predicts very well the dissolved-mass time series of the TNT and Tritonal particles. The single-tuning parameter, water-layer thickness (h) was reasonably consistent among the four particles, averaging 0.086 ± 0.009 mm. The model also predicts well the overall dissolution behavior of the Comp B particles and provides insight into the governing processes. Initially, TNT dissolves independently of RDX, but increasing restriction of TNT diffusion by the

RDX crystals eventually causes TNT dissolution to be controlled by RDX dissolution. Additional work is needed to quantify this effect by modeling TNT diffusion within a changing porous RDX medium.

The model does not predict well the TNT dissolved-mass time series for the Octol particles. The large, low-solubility HMX crystals appeared to impede but not control TNT dissolution. That is, neither limiting model case (independent or HMX-controlled dissolution) fits the observed TNT data. The reduced influence of HMX on TNT dissolution, compared with the controlling role of RDX in Comp B, is consistent with less constraint of TNT diffusion into the surrounding water layer. The higher fitted values of layer thickness (0.155 ± 0.049 mm) could reflect the creation of surface area as the Octol particles disaggregated following TNT loss. These values give reasonable agreement to the limited HMX dissolution data, but the impeding effect of HMX crystals on TNT dissolution in Octol has yet to be quantified.

The drop-impingement model accounts for differences in rainfall rates via differences in average drop-arrival time (t_d) in Equation 1. The generally good agreement between the observed and predicted dissolution data at two simulated rainfall rates suggests that t_d does indeed scale dissolution rate. The model predicts quite well the dissolution of millimeter-size TNT, Tritonal and Comp B particles. This provides confidence it also will work well when applied to the rainfall-driven, outdoor dissolution of these HE materials.

3 Outdoor Dissolution Tests

We conducted dissolution tests using centimeter-size chunks of HE that were placed outside to weather under natural conditions at the Cold Regions Research and Engineering Laboratory (CRREL) facility in Hanover, New Hampshire. These tests closely simulated the dissolution of isolated HE pieces on range soils and provided a realistic validation of the drop-impingement model described in Chapter 2. We developed a "large-particle" extension of the model to eliminate the restriction that raindrop volume would be greater than water-film volume.

3.1 Materials and methods

3.1.1 Sample composition

We used TNT, Comp B, Tritonal, and C4 because they are widely used HE. Because we could not obtain centimeter-size pieces of Octol, we used C4 instead. C4 is a plastic explosive primarily composed of RDX (92%) with added plasticizers (8%). Chunks of C4, collected on a demolition range, were rolled into six different diameter balls. Our HE particles and chunks were all collected from LO field detonations.

3.1.2 Experiment set-up

In May 2006, we placed 11 TNT, 5 Tritonal, and 12 Comp B chunks outside in 4 cm diameter Buchner funnels (Figure 12). We added 6 C4 chunks to the tests in September 2006. The funnels are attached to 1-L bottles with a #4 rubber stopper that was fitted with two holes–one for the funnel stem and the other for air exchange. The bottles fitted snuggly into an insulated wooden box. The box kept the bottles from tipping over or being damaged and also helped to keep them cool in summer and warm in winter. Although we tracked evaporation using a vented bottle with 50 mL of deionized water, evaporation does not affect dissolved mass data collected during the tests. Also, at no time did the collection bottles overflow with rainwater.

Figure 12. Outdoor tests showing Buchner funnels used to hold the HE pieces. Any precipitation landing in the funnel moved through the glass frit and into 1-L glass bottles in the wooden boxes.

At 14 months into the project, we crushed three of the chunks (TNT5, Comp B11, and Tritonal5) and weighed each of the resulting fragments. The fragments were then returned to their funnels. Change in the dissolved masses from these three samples provided us data, which we used to model the effect of particle size on dissolution rate. Chapter 5 details how we crushed the chunks, but we describe their dissolution here.

Rainwater or snowmelt that interacted with the HE was collected in the bottles. Every other week, we exchanged the bottles for clean ones and measured the volume and HE concentration in the water. During the winter months, the bottles were placed in plastic bags to save the sample even if the bottle should break from ice formation. About 7 mL of solution was archived in a scintillation vial. The needed quantity of sample was prepared for HPLC analyses, and the remaining water was placed in a waste jug. The sample bottle was then rinsed with a small amount of water, which was also poured into the waste jug, and the bottle was rinsed two more times. The HE mass in the first rinse contained less than 1% of the mass present in the sample, and the two additional rinses ensured that we introduced less than 1% error from reusing the sample bottles.

Monthly, we photographed the pieces of HE in situ to document changes in their appearance and size. This set-up allowed the explosives to be exposed to conditions similar to those experienced by explosives on a range–where rain, snow, sun and freeze thaw cycles weather the HE–while

allowing us to collect and analyze the dissolved HE and monitor changes in their appearance.

Our experiment was set up in an enclosed, locked site next to a dedicated rain gauge and near the CRREL weather station, which records rainfall totals, temperature, and solar irradiance. We calibrated the rain gauge (HOBO Weather Station, Part S-RGA-M00X) before setting it up outside in April 2006. The rain data was downloaded monthly and checked against the CRREL rain gauge every few months to ensure it was operating well.

3.1.3 Analytical methods

Explosive concentrations were determined following SW-846 Method 8330B (U.S. EPA 2006). A total of 1 mL of the effluent was added to 2 mL of deionized water and 1 mL of acetonitrile, then filtered through a 0.45 µm syringe filter (from Millipore). HPLC analysis separated TNT, RDX, HMX, 1,3,5-TNB, 1,3-DNB, 2,4-DNT, 2,6-DNT, 2-ADNT and 4-ADNT. We used a Waters NovaPak C8 column (3.9 x 150 mm) eluted at 1.4 mL per minute (28 °C) with 85:15 ratio of water:isopropanol mix, which was detected by UV at 254 nm. A commercially available standard (by Restek, Bellefonte, PA) was used for calibration. We prepared 1- and 10-ppm (mg/L) dilutions of these standards. The 1 ppm standards were run every 10 samples, and blanks were run before and after each standard run. The 10-ppm standards were interspersed with the samples as internal checks, with blanks after each to prevent carryover. Based on the concentrations of the standards and the precision of the effluent volumes, we estimated that the cumulative, dissolved HE masses have uncertainties of about ±1%.

3.2 Results

We have 36 months of data from our TNT, Comp B, and Tritonal samples; (61 water samples for each chunk). We have 32 months of data for the C4 chunks (48 samples), which were placed outdoors in September 2006. Figure 13 shows photographs and masses of the 34 HE pieces tested. All of the HE pieces experienced similar precipitation conditions. The volume of water collected during the 36-month tests averaged 7,238 mL ± 803 mL.

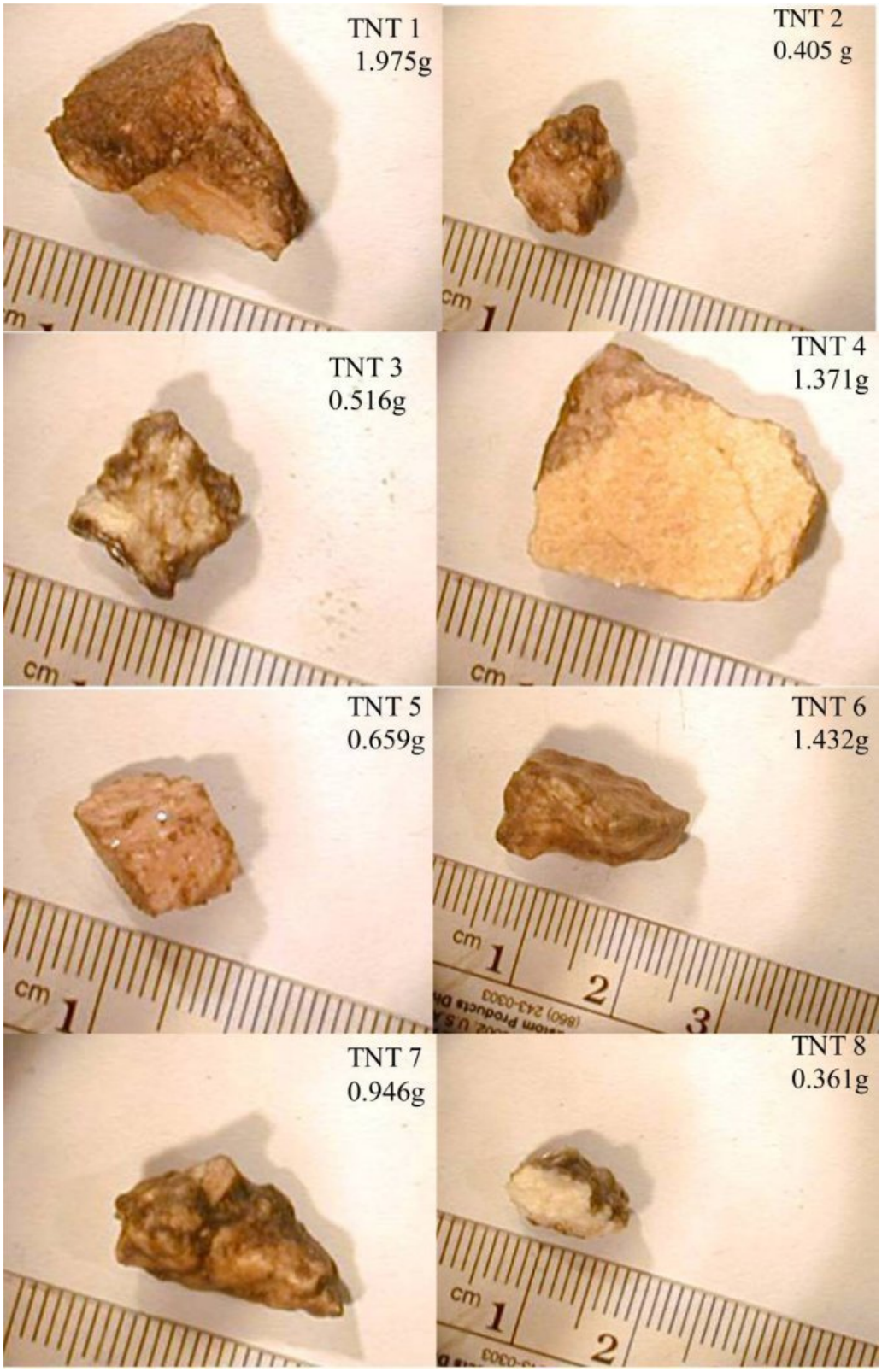

Figure 13. Photos and initial masses of HE particles used in the outdoor dissolution tests.

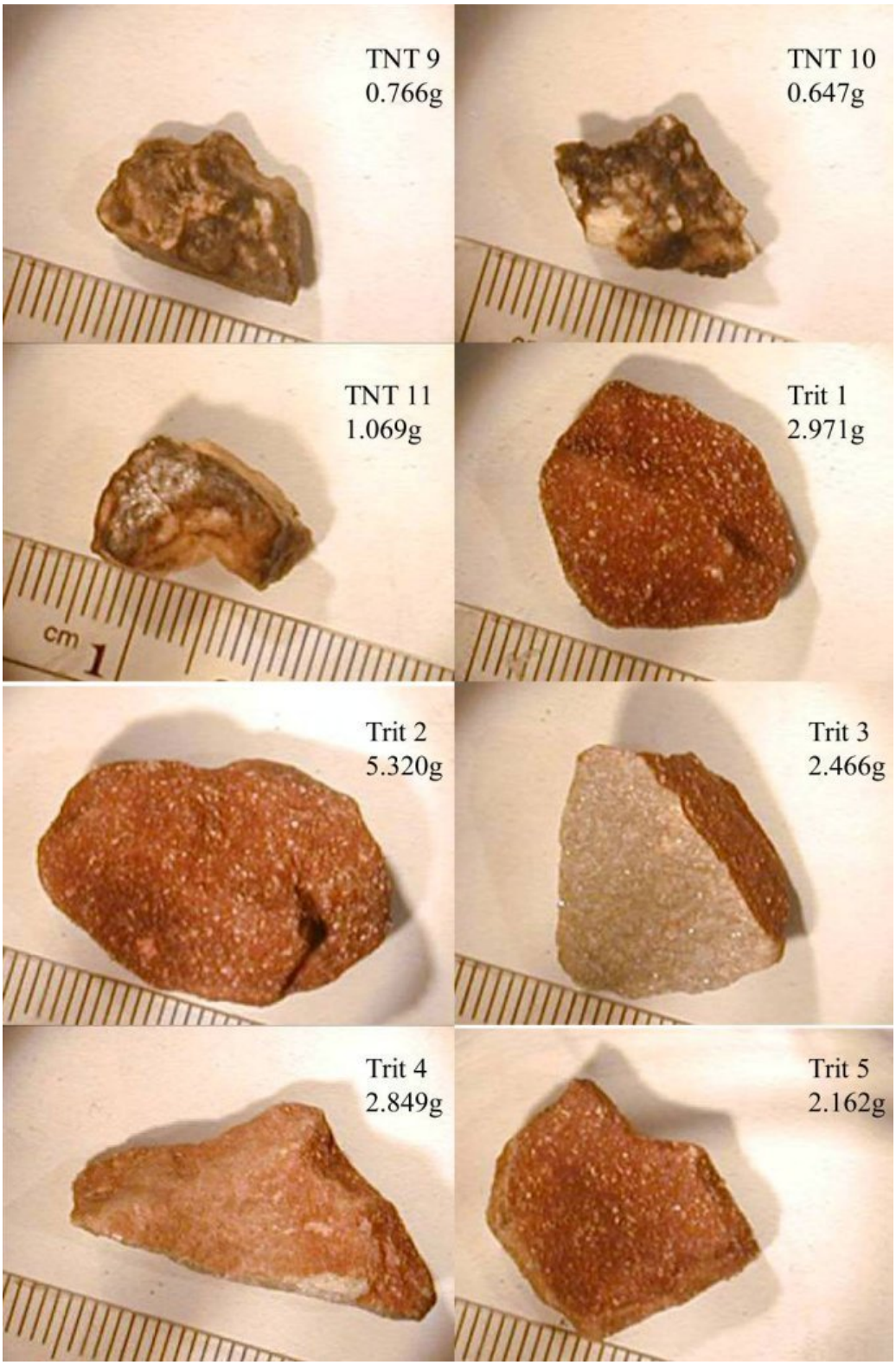

Figure 13 (cont.). Photos and initial masses of HE particles used in the outdoor dissolution tests.

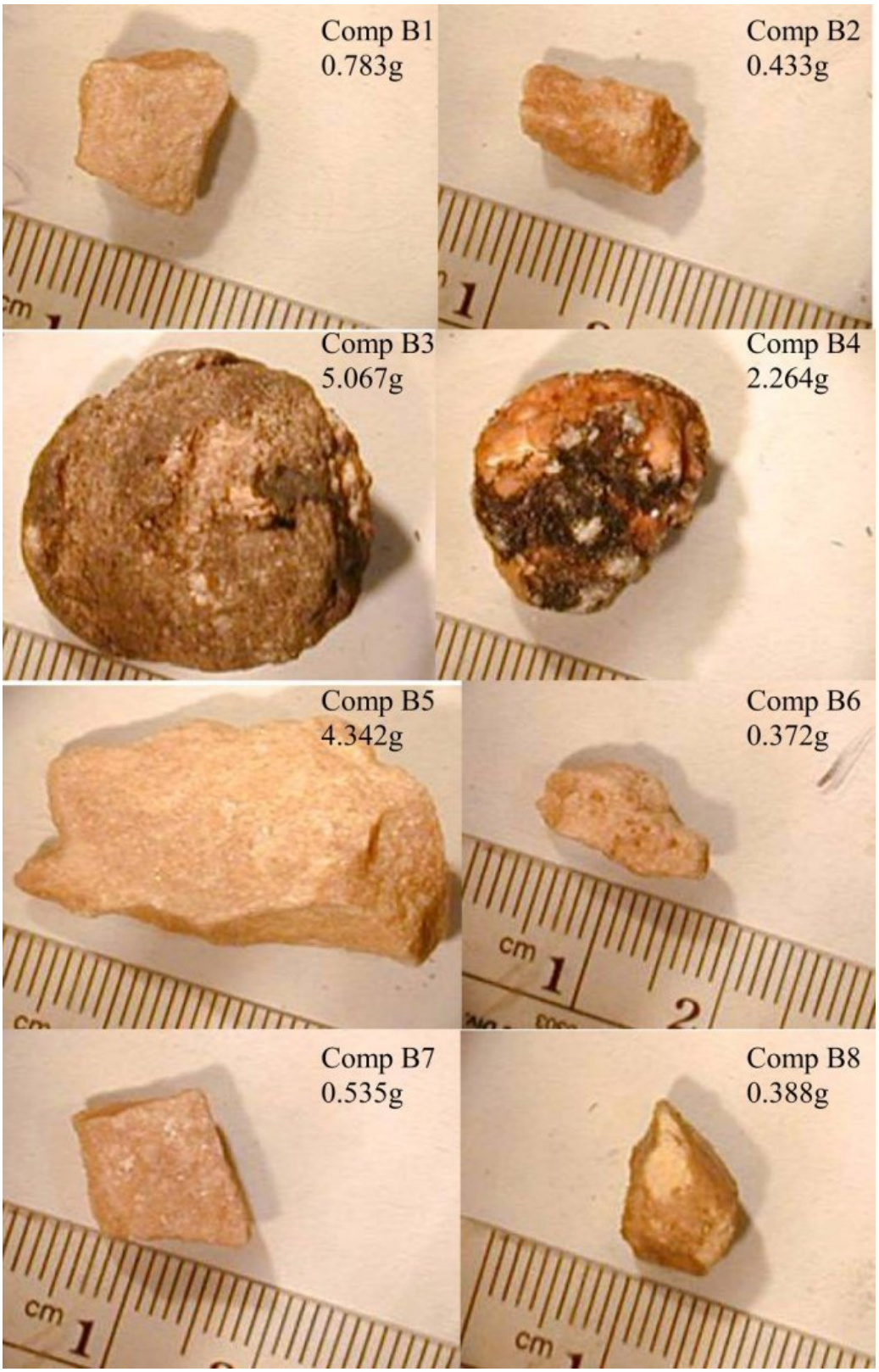

Figure 13 (cont.). Photos and initial masses of HE particles used in the outdoor dissolution tests.

Figure 13 (cont.). Photos and initial masses of HE particles used in the outdoor dissolution tests.

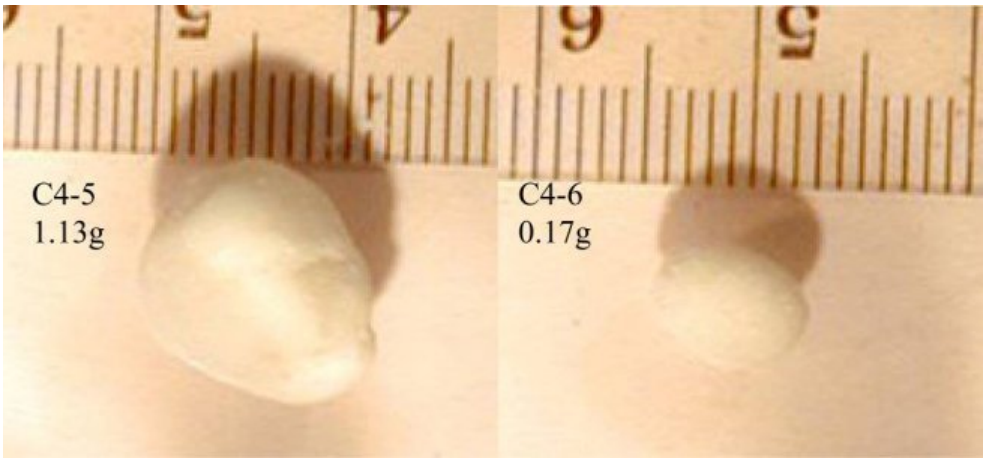

Figure 13 (cont.). Photos and initial masses of HE particles used in the outdoor dissolution tests.

3.2.1 Weather conditions

Figure 14 shows hourly average air temperature and rainfall rates recorded at the CRREL test site during the three years. Total rainfall was 3,156 mm, with annual rainfall decreasing slightly each year (1,226 mm, 1,030 mm, and 900 mm, respectively). The experiment was typically snow-covered during winter (about mid-January through mid-April), although winter 2008 included rainfall on several occasions. Rain fell 8.2% of the time and 55% of the rain fell at rates below 3 mm per hour. The maximum hourly rainfall rate was 20 mm per hour. The average air temperature was 7.2 °C; the maximum and minimum temperatures recorded were 35.5 °C and –30.8 °C, respectively.

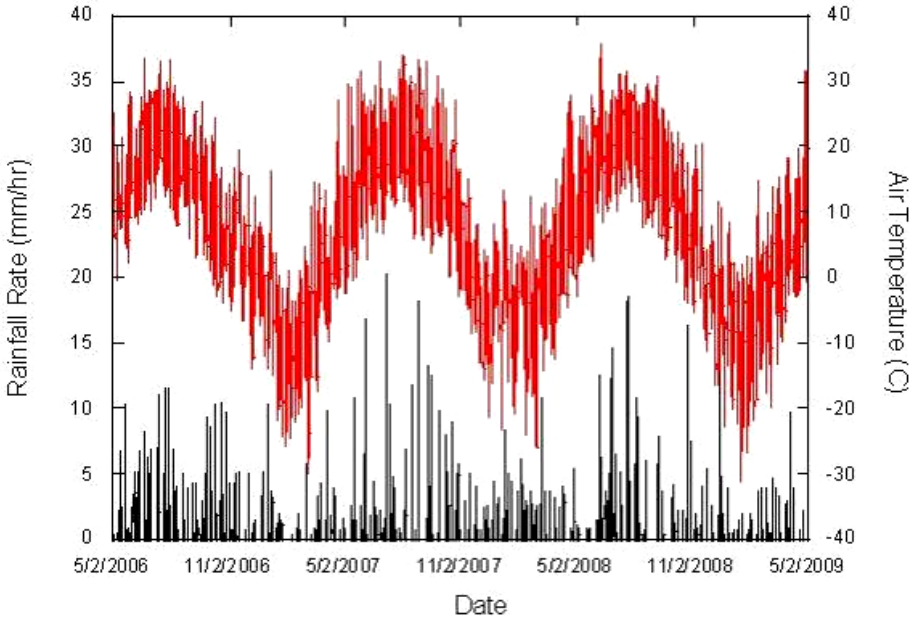

Figure 14. Three years of rainfall and air temperature data at CRREL, May 2006–May 2009.

3.2.2 Appearance of HE pieces

Observations of the HE pieces show the C4 balls did not change color, but their surfaces become powdery over time (Figure 15). In contrast, the TNT-bearing Comp B, Tritonal, and TNT particles turned rust red with occasional shiny, almost iridescent, black patches. Following heavy rains, the reddish product washed off some surface areas, exposing the lighter-colored HE. After snow melt only, the glass frit in contact with the TNT was reddish in color. However, over the course of the summer, more of the frit became red, probably due to water that contained dissolved TNT evaporating on the surface of the frit.

Figure 15. C4-2 photographed May 2008.

The TNT particles became smoother with time, whereas both the Comp B and Tritonal became rougher from loss of surface TNT (Figure 16, Figure 17, Figure 18). In the case of Comp B, loss of TNT exposed RDX crystals (Figure 17); for Tritonal, loss of TNT exposed aluminum grains (Figure 18). The Comp B pieces also lost RDX crystals from their surfaces. Close-up images of Comp B show RDX crystals protruding from the surface and hollows where RDX crystals de-bonded from the TNT and fell off the particle (Figure 17). The result is that numerous ~100 μm RDX crystals were exposed on the frit to dissolve independently of RDX embedded in the main chunk. We included this process to model the dissolution of the Comp B chunks. This process was less pronounced for millimeter-size Comp B particles tested in the lab, where the RDX crystals armored the surface of the particle and fewer independent crystals were present on the frit (Lever et al. 2005).

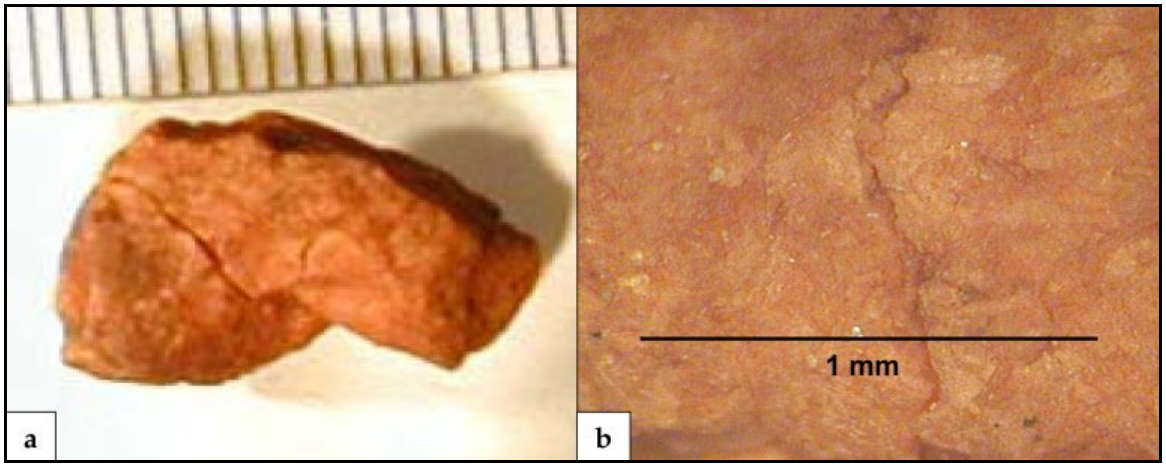

Figure 16. (a) Photograph of TNT particle and (b) close-up of its surface.

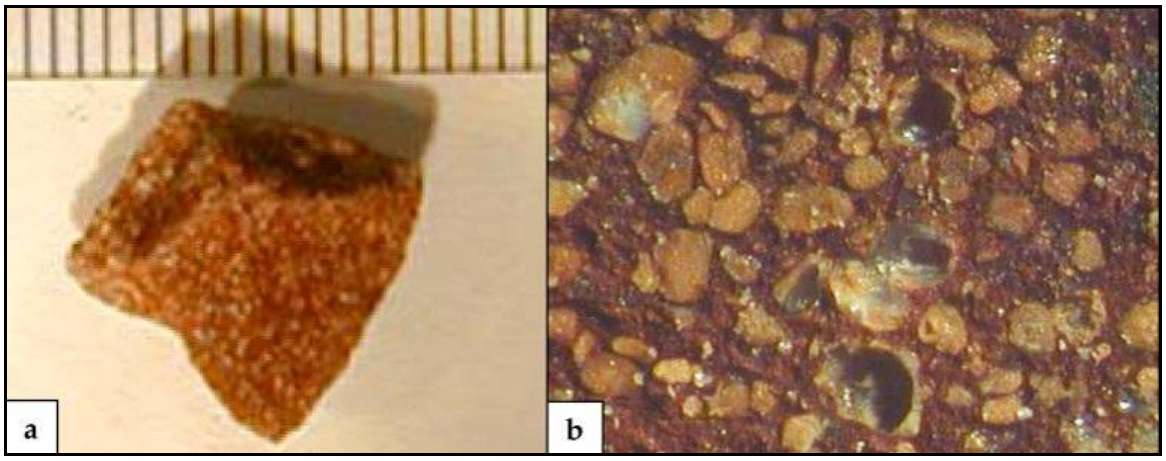

Figure 17. (a) Photograph of Comp B particle and (b) close-up of its surface. Note hollows where RDX crystals have de-bonded from the matrix and fallen out.

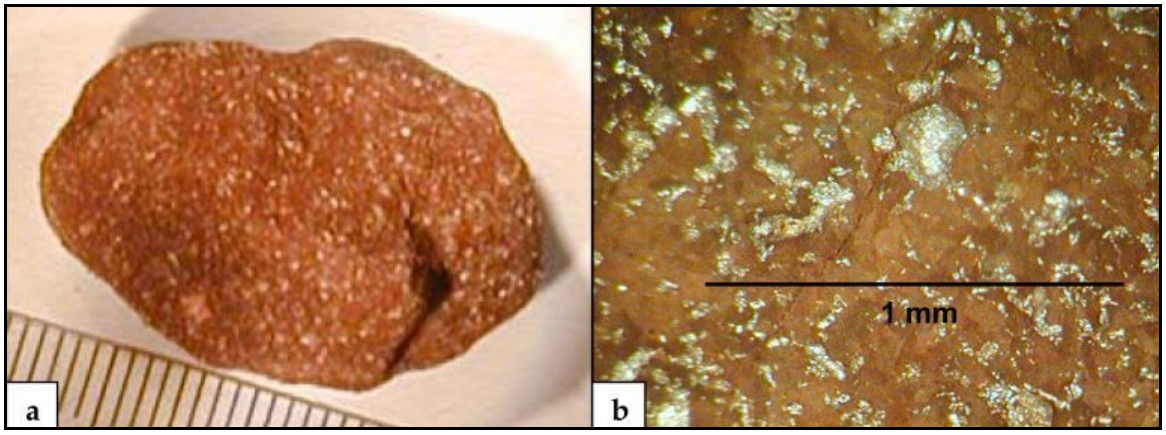

Figure 18. (a) Photograph of Tritonal particle and (b) close-up of its surface showing an incipient crack and the aluminum grains that comprise 20%–30% of its mass by weight.

Four of the HE chunks split naturally during the tests: TNT 3, TNT 11, Comp B 6, and C4 5 (Figure 19). Cracks appeared in 4 TNT chunks, in 2 Tritonal chunks, and in 3 Comp B chunks. The C4 chunks were weathering

along zones introduced when the balls were rolled into balls. On multiple occasions small particles (>1 mm across) broke off from 8 TNT chunks, 2 Tritonal, 3 Comp B, and one of the C4 chunks (Figure 20). Over three years, the TNT and C4 chunks generated more small flakes (<1 mm) than either the Tritonal or Comp B chunks.

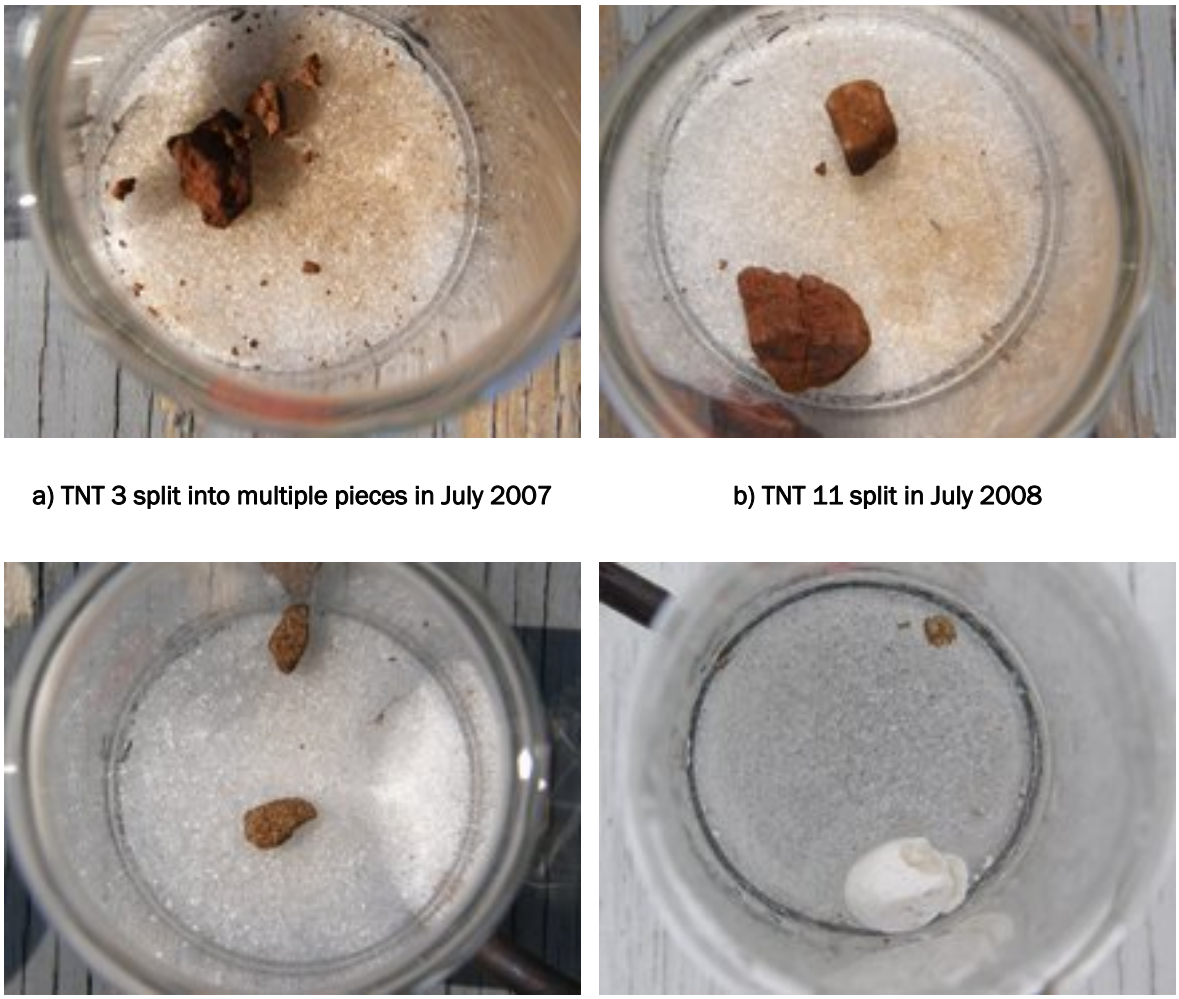

a) TNT 3 split into multiple pieces in July 2007

b) TNT 11 split in July 2008

c) Comp B 6 split in July 2008

d) C4 5 split over the 08-09 winter; the second piece is partially covered by the larger piece

Figure 19. Four of the HE chunks split naturally during the tests: TNT 3, TNT 11, Comp B 6 and C4 5.

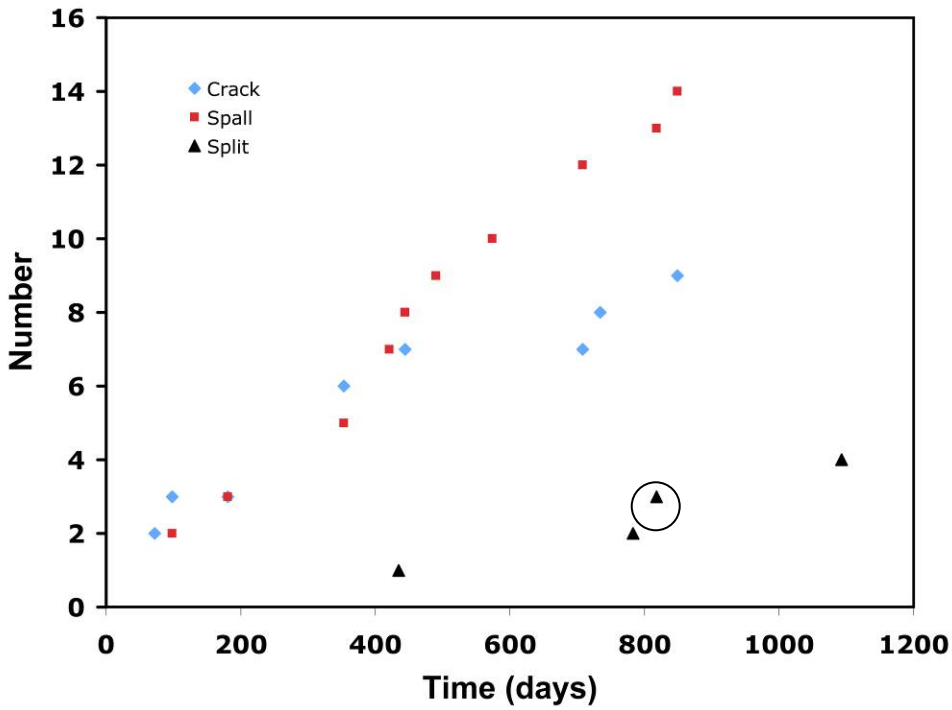

Figure 20. Number of HE chunks that cracked, spalled off a >1 mm piece, and split into multiple millimeter-size pieces over the three-year test. For example, the circled triangle indicates that 3 of the 34 chunks had split by day 810 of the test.

3.2.3 Mass loss of HE chunks

The cumulative mass loss for the TNT, Comp B, Tritonal and C4 pieces measured by HPLC are shown in Figure 21, Figure 22, Figure 23, and Figure 24. Except for the chunks that split or were crushed the shapes of the cumulative mass loss curves are similar among all the chunks. (TNT 3, and TNT 5, Comp B 11, and Tritonal 5 that were crushed are all examples of HE chunks whose split is easily seen in the records.) Although the largest chunks lost the most mass, (e.g., Comp B 3 and B 5), the small HE chunks lost a larger percentage of their initial mass (Figure 22) due to a larger ratio of surface area to mass.

Comp B was the only explosive in the outdoor tests that contained two HE compounds (60:39:1 ratio of RDX:TNT:wax). As we found from the indoor dissolution tests on small Comp B particles (Lever et al. 2005; Taylor et al. 2009), initially TNT dissolved more rapidly than RDX. Eventually, however, the RDX mass loss exceeded that of TNT. For the Comp B chunks, the TNT and RDX mass-loss curves crossed over relatively quickly, between day 35 and day 129. That is, shielding by RDX crystals impeded the TNT dissolution rate for Comp B during most of the experiment.

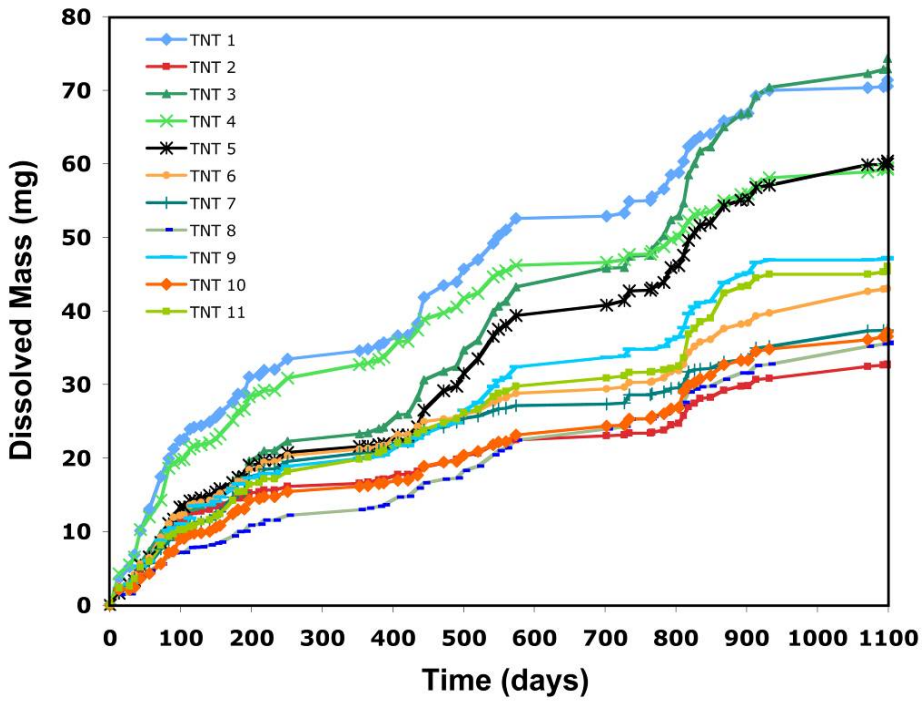

Figure 21. Cumulative mass loss of TNT (mg) versus time. TNT 5 was crushed on day 436 (July 2007) resulting in an increase in mass loss. TNT 3 split a few days later.

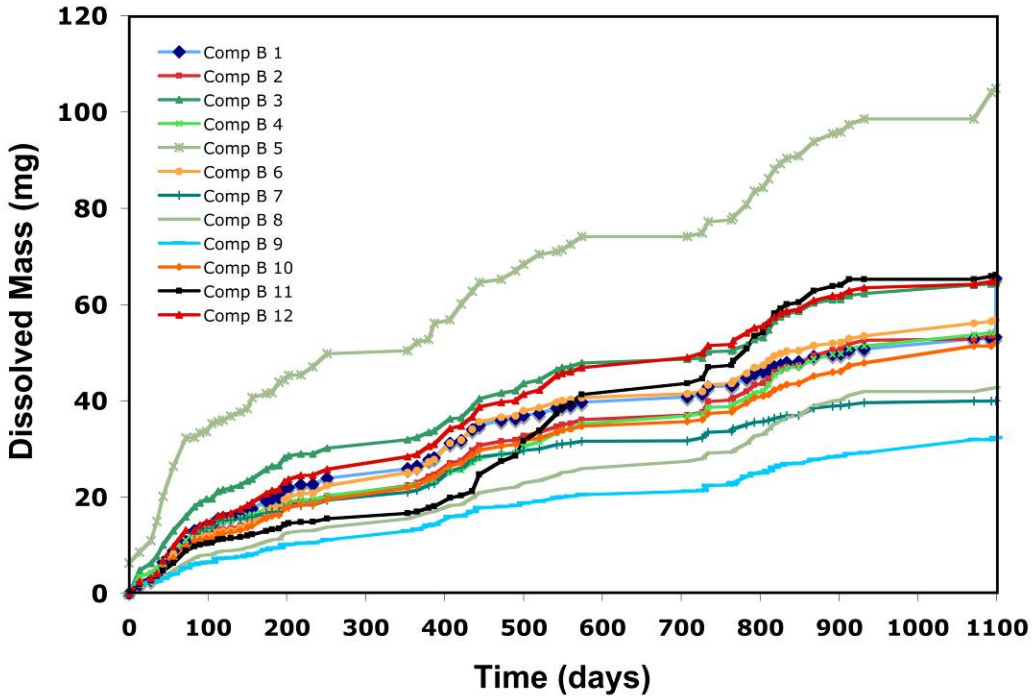

Figure 22. Cumulative mass loss of TNT and RDX (mg) as a function of time for the 12 Comp B pieces tested. Comp B 11 was crushed on day 436, and you can see an increase in its mass loss starting at that time.

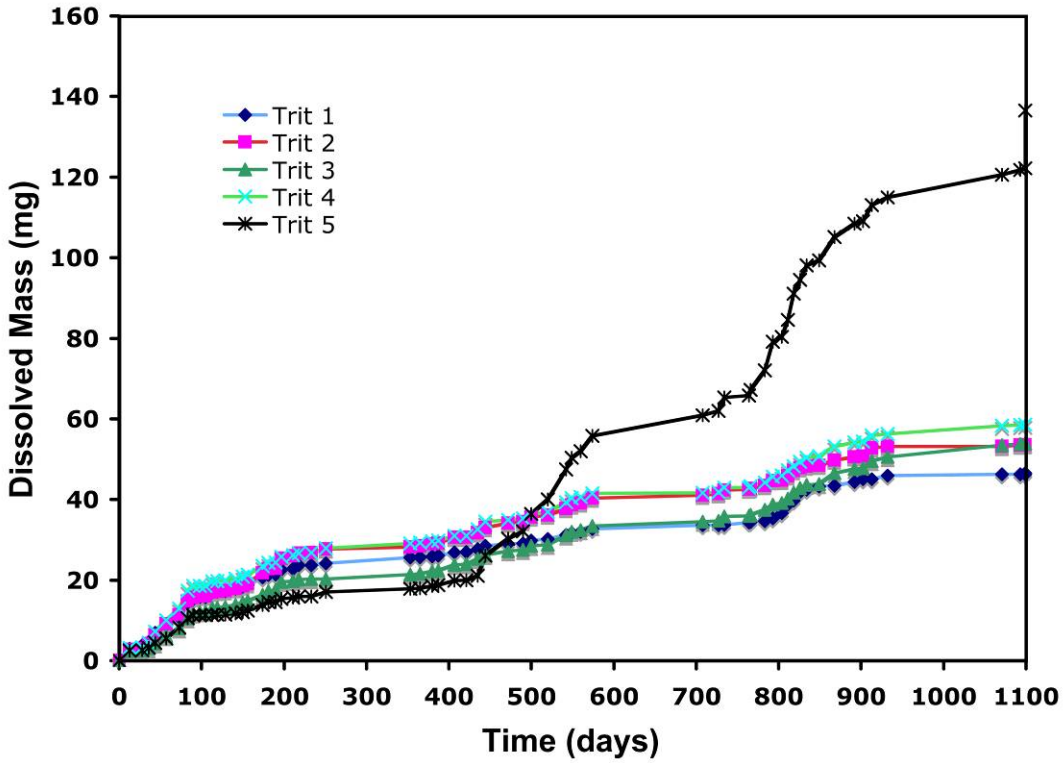

Figure 23. Cumulative mass loss of TNT (mg) as a function of time for the Tritonal 5 pieces tested. Tritonal 5 was crushed on day 436 resulting in increased mass loss.

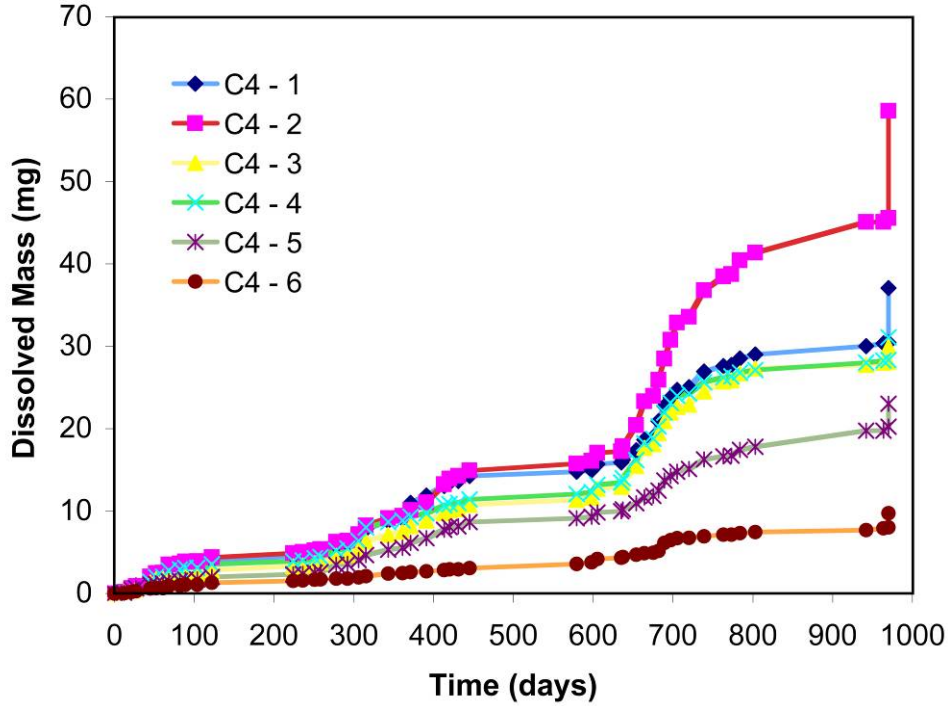

Figure 24. Cumulative mass loss of RDX (mg) as a function of time for six C4 pieces tested. None of the C4 chunks were crushed. After the 2008 winter, C4 2 shows a pronounced increase in dissolution and was found to be crumbly-(see Figure 15). The large jumps at the end of the record are the HE mass extracted from the funnels.

Table 3 summarizes the mass loss for each HE chunk after three years. Note that two types of measurements are included: mass loss measured by electronic balance, and cumulative dissolved mass obtained via HPLC analysis. Mass losses measured with the electronic balance were larger than dissolved masses, and the losses grew with time. These results were unexpected because the two measurement methods had low uncertainties, and there was very good mass balances for TNT, Tritonal, and Comp B in the laboratory tests (Lever et al. 2005, Taylor et al. 2009).

Table 3. Measured mass losses for 34 HE chunks exposed outdoors for three years.

Particle	Electronic Balance			HPLC Dissolved Mass (mg)
	Initial Mass (mg)	Final Mass (mg)	Total Loss (mg)	
TNT 1	1974.80	1751.94	222.86	71.41
TNT 2	404.80	308.66	96.14	32.74
TNT 3	515.50	279.77	235.73	74.34
TNT 4	1371.20	1169.55	201.65	59.45
TNT 5	659.50	459.53	199.97	60.37
TNT 6	1432.20	1293.35	138.85	43.06
TNT 7	945.80	824.65	121.15	37.39
TNT 8	361.40	251.50	109.90	35.71
TNT 9	766.40	629.22	137.18	47.19
TNT 10	646.70	536.47	110.23	37.12
TNT 11	1068.80	913.28	155.52	46.03
Trit 1	2971.20	2769.41	201.79	46.53
Trit 2	5320.40	4985.67	334.73	53.60
Trit 3	2465.50	2224.70	240.80	53.96
Trit 4	2848.70	2589.88	258.82	58.60
Trit 5	2161.70	1509.61	652.09	136.49
Comp B1	782.80	653.20	129.60	65.41
Comp B2	432.50	313.30	119.20	56.37
Comp B3	5066.60	4848.05	218.55	65.60
Comp B4	2263.50	2126.33	137.17	56.68
Comp B5	4342.20	3974.75	367.45	135.67
Comp B6	372.10	251.73	120.37	58.31
Comp B7	534.70	445.56	89.14	41.09
Comp B8	388.00	296.36	91.64	47.20
Comp B9	343.00	277.33	65.67	32.47
Comp B10	1088.30	963.99	124.31	52.18
Comp B11	384.50	193.05	191.45	69.19

Particle	Electronic Balance			HPLC Dissolved Mass (mg)
	Initial Mass (mg)	Final Mass (mg)	Total Loss (mg)	
Comp B12	483.80	343.18	140.62	67.19
C4 - 1	4930.00	4619.80	310.20	37.10
C4 - 2	3970.00	3642.87	327.13	58.59
C4 - 3	2300.00	2098.11	201.89	29.99
C4 - 4	1950.00	1772.75	177.25	31.12
C4 - 5	1130.00	1015.00	115.00	23.05
C4 - 6	170.00	134.24	35.76	9.75

Total HE mass loss is via electronic balance (Tritonal is corrected for aluminum content), dissolved HE mass is via HPLC analysis (including measurable transformation products). Uncertainties are ± 0.005 g in total mass loss, ± 0.001 g in dissolved TNT mass.

We think phototransformation of TNT to compounds not quantified by Method 8330B is the dominant TNT mass-loss pathway. This process is inherent to outdoor weathering of TNT-based explosives, and we discuss it in Chapter 4. We have investigated other TNT mass-loss pathways (aqueous-phase transformation in sample bottles, sublimation, and handling of chunks when we weighed them) and found that they negligibly influenced the TNT mass balances (Taylor et al. 2009). Consequently, the water samples preserved a record of the TNT dissolved from the HE chunks over the three-year experiment and thus, can be used to validate dissolution models. In addition, about twice as much TNT phototransformed on the surface of the chunks (possibly moderated by the presence of water) and this phototransformation product dissolved independently into the samples. To date, these unknown compounds have escaped HPLC analysis. On training ranges, these transformation products likely constitute additional HE-based contaminant influx into range soils.

Solid-phase RDX does phototransform to other compounds (Bedford et al. 1996). However, anecdotal accounts suggest that RDX is much more stable in sunlight than TNT, so that the rate may not be high enough to account for missing mass. We plan to investigate this pathway further.

A possible RDX mass-loss pathway was loss of crystals from the main chunks as TNT receded, and their transport through the frits before they completely dissolved. The outdoor frits were ~2 mm thick, spun-glass filters with 145 – 175 μm openings. The indoor frits were of similar construction but had 25–50 μm openings. We used the larger openings outside to avoid the openings becoming plugged by dust and pollen. RDX

crystals in Comp B and C4 are ~ 100 μm and <1 μm across, respectively. That is, these crystals (especially from C4) could be washed through the outdoor frits without dissolving. Because RDX dissolves slowly in water, these crystals may not have completely dissolved before the water samples were analyzed by HPLC. Unfortunately, we analyzed only water samples and did not filter and analyze for crystals in the sample bottles. We have placed Comp B and C4 chunks outside again to test if this is the dominant RDX mass-loss pathway. Meanwhile, we have approximated this RDX mass-loss pathway and used the outdoor data to validate a two-component model for the dissolution of Comp B.

3.2.4 Dissolution modeling

Lever et al. (2005) developed a "drop-impingement" model to predict the dissolution of millimeter-size Comp B particles. Chapter 2 shows that it also worked well for small TNT and Tritonal particles dissolved in the lab (Taylor et al. 2009). The model pertains to the practical case where spatially isolated HE particles reside on well-draining surface soils and thus are exposed to direct impingement by raindrops. This model assumes that a particle holds a thin (~ 0.1 mm) water film against its surface, which saturates with HE between impinging raindrops. For particles weighing less than a few milligrams, the volume of typical raindrops exceeds the volume of this water film, and each raindrop refreshes the entire film when it impinges on the particle. In this case, the dissolution rate (grams per second) is

$$m_j = \frac{S_j V_f}{t_d} \tag{5}$$

where:

S_j is the solubility limit of species j in water (g/cm^3),
V_f is the water-film volume (cm^3) and
t_d is the drop-arrival time (s).

Lever et al. (2005) formulated the model with V_f evaluated for a film of thickness h against a spherical particle of equivalent mass as the particle of interest:

$$V_f = \frac{4}{3}\pi\left[(a+h)^3 - a^3\right] \tag{6}$$

where:

a is particle radius.

They found that a value of h = 0.13 ± 0.05 mm produced good agreement with the measured-dissolution time series for four Comp B particles. Recent laboratory tests showed that the model gave excellent agreement with dissolution data for milligram TNT and Tritonal particles, with h averaging 0.086 ± 0.009 mm and reasonable agreement for two Comp B particles with h = 0.101 ± 0.013 mm (Taylor et al. 2009). These studies showed that TNT and RDX in Comp B do not dissolve independently. After a brief period of high-rate TNT dissolution, shielding by exposed RDX crystals reduced the rate of TNT dissolution.

To model the dissolution of the outdoor chunks we must extend the drop impingement model to the larger HE chunks and natural rainfall of the outdoor tests. For particles larger than a few milligrams, the volume of the water film against the particle exceeds typical raindrop sizes. We may assume that, in steady-state conditions, each impinging drop causes an equal volume of HE-saturated water to drip off the particle. In this case, the dissolution rate m_j is

$$m_j = \frac{S_j V_d}{t_d} \tag{7}$$

where:

V_d is the raindrop volume (cm^3).

The drop-arrival time for either small- or large-particle regime is related to the volumetric flow rate of rainfall impinging on the particle, $A_c q$:

$$t_d = \frac{V_d}{A_c q} \tag{8}$$

where:

A_c is the rainfall-capture area of the particle (cm^2) and
q is rainfall rate (cm/s).

We again model the particle as a sphere of equivalent mass and assume that drops touching its cross-section will wet it. That is,

$$A_c = \pi(a + D_{om})^2 \tag{9}$$

where:

a is the particle radius and

D_{0m} is the mass-weighted mean diameter for the raindrops.

Pruppacher and Klett (1997) indicated that no single spectrum fits all measurements of raindrop sizes, but an exponential drop-size spectrum has frequently been used and provides reasonable fit. In this case

$$D_{0m} = 0.98R^{0.21} \tag{10}$$

where:

D_{0m} is in mm for rainfall rate R in mm per hour.

Drops sizes thus show a weak dependence on rainfall rate, with D_{0m} ~ 1–2 mm for R ~ 1–30 mm per hr.

We may then combine Equations 3–5 to obtain the dissolution rate for the drop-impingement model in the large-particle regime:

$$m_j = S_j \pi(a + D_{0m})^2 qAF \tag{11}$$

Following Lever et al. (2005), we included an area factor, AF, in Equation 11. In principle, area factor ~ 2 should account for HE chunks with capture areas larger than a sphere of equivalent mass (AF = 1). In reality, AF is a parameter to be obtained by best-fit to dissolution data for actual particles.

The transition between the small- and large-particle regimes of the model occurs when V_f exceeds V_d, where V_f is given by Equation 8, and $V_d = \pi/6 D_{om}^3$. The median rainfall rate during the first year of outdoor tests was about 3 mm per hour, corresponding to D_{om} ~ 1.2 mm. Lab tests (Lever et al. 2005; Taylor et al. 2009) suggested h ~ 0.1 mm for small HE particles. For these conditions, the large-particle regime would apply for HE particles larger than about 5 mg. All HE chunks studied here far exceeded this size.

Equation 11 has an important physical interpretation: all the rainfall intercepted by the particle flows off it fully saturated with HE. This can only be true if the average time raindrops reside within water film, t_r =

$V_f/A_c q$, is longer than the time required to saturate the film with HE via diffusion, t_s. Lever et al. (2005) argued that the water layer will saturate for $t_s > h^2/D_j$. For D_{TNT} ~ 4.6 x 10^{-6} cm²/s and D_{RDX} ~ 1.5 x 10^{-6} cm²/s at 10.5 °C (the one-year average air temperature weighted by rainfall) and h ~ 0.1 mm, saturation time is t_s ~ 20–60 seconds for TNT and RDX, respectively, independent of particle size. At the large-particle boundary of 5 mg, raindrop residence time is t_r ~ 70 seconds and it exceeds 200 seconds for the smallest chunk studied here (0.36 g). That is, there was sufficient time for raindrops impinging on the chunks to saturate with TNT and RDX before dripping off, as required.

3.2.5 Validation of dissolution model for TNT and Tritonal

The drop-impingement model was straightforward to implement and to validate for TNT and Tritonal chunks. These chunks contained only one dissolving component (TNT) and the water samples preserve the TNT dissolved-mass time series for each chunk. Additional mass loss via production and independent dissolution of phototransformation products had only a minor effect of slightly decreasing the chunk radius and hence capturing area at each time step. We may account for this effect by scaling the calculated TNT dissolved mass by the ratio of the measured total per dissolved TNT mass loss for each chunk (Table 3). This ratio averaged 3.2 ± 0.2 for TNT chunks and 3.9 ± 0.6 for Tritonal chunks.

We ran the drop-impingement model for the TNT and Tritonal chunks by using their initial masses and measured rainfall and temperature data. The starting time was 10 a.m. on 2 May 2006, the end time was three years later, and the time step was one hour. Over this period, we collected and analyzed 61 sets of effluent samples for each of the 16 HE chunks and used these results to validate the model.

The predicted dissolution rate (Equation 11) requires S_{TNT}, which varies with temperature. We assumed that the raindrops and the water film on the particle are at the measured air temperature and used the temperature correlation developed by Lynch et al. (2002b):

$$S_{TNT} = \exp\left(16.981 - \frac{3607.5K}{T}\right) \tag{12}$$

where:

S_{TNT} has units mg/L and

T is air temperature in K. (Note that for $T < 0°C$, we set S_{TNT} to zero.)

Figure 25 compares predicted and measured TNT dissolved mass for chunks TNT 1 and TNT 8 over the three years. The model shows good agreement by using independent values of area factor best-fit to the measurements. Figure 26 shows similarly good agreement for Tritonal 3 and Tritonal 4. The flat sections on both plots reflect near-zero dissolution during winter, as expected. Figure 25and Figure 26 are typical of the agreement achieved by the model with the measurements for all TNT and Tritonal chunks, excluding one of each type that were intentionally crushed and returned outdoors at the end of the first year (see Chapter 5).

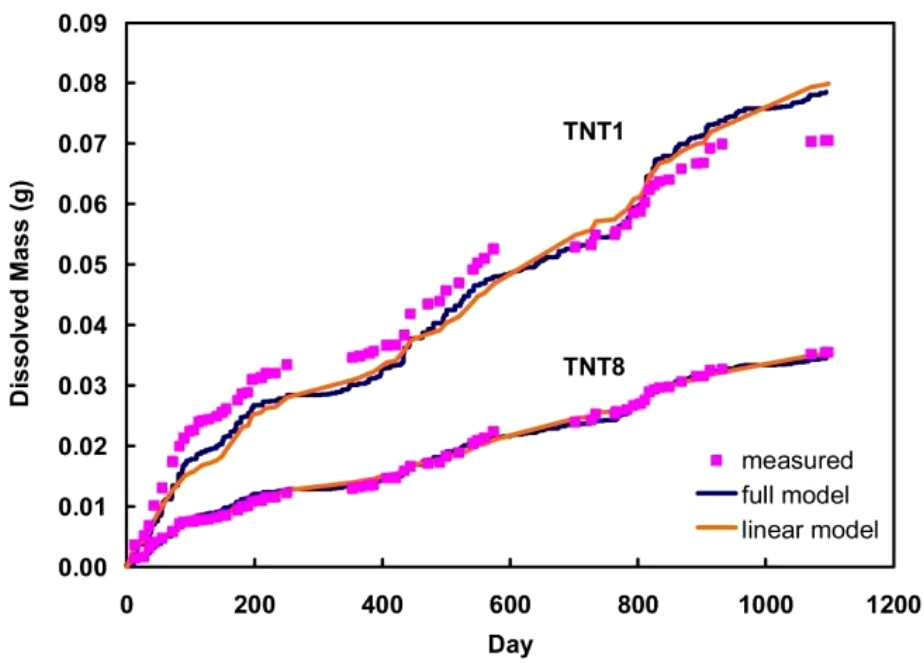

Figure 25. Dissolved TNT mass measured for TNT 1 and TNT 8 along with predictions from full and linear drop-impingement models.

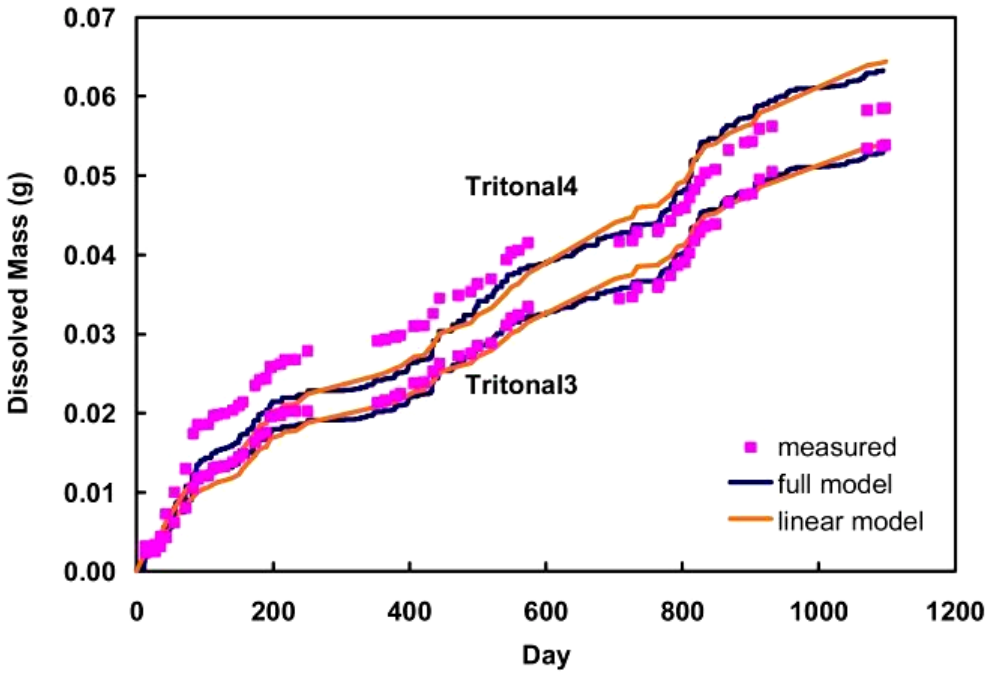

Figure 26. Dissolved TNT mass measured for Tritonal 3 and Tritonal 4 along with predictions from full and linear drop-impingement models.

Table 4. Best-fit area factors and RMS prediction errors for the drop-impingement model, and the linear approximation of the drop-impingement model.

HE Chunk	Full Model		Linear Model		Notes
	AF	RMS error	AF_L	RMS error	
TNT 1	1.81	0.14	1.77	0.17	
TNT 2	1.94	0.20	1.82	0.22	
TNT 3	3.49	0.18	3.29	0.18	chunk split naturally
TNT 4	1.94	0.19	1.88	0.20	
TNT 5	2.59	0.08	2.47	0.10	chunk crushed at the end of Year 1
TNT 6	1.23	0.16	1.20	0.18	
TNT 7	1.42	0.15	1.37	0.17	
TNT 8	2.04	0.08	1.91	0.06	
TNT 9	1.93	0.07	1.85	0.10	
TNT 10	1.58	0.09	1.51	0.11	
TNT 11	1.51	0.09	1.46	0.09	
average	*1.71*	*0.13*	*1.64*	*0.14*	excludes split and crushed chunks
st. dev.	*0.28*		*0.26*		
Tritonal 1	0.99	0.19	0.98	0.21	
Tritonal 2	0.82	0.14	0.82	0.16	
Tritonal 3	1.12	0.06	1.10	0.09	
Tritonal 4	1.23	0.15	1.22	0.18	
Tritonal 5	1.07	0.07	1.08	0.09	before crushing
Tritonal 5c	4.48	0.07	4.31	0.09	after crushing

HE Chunk	Full Model		Linear Model		Notes
	AF	RMS error	AF_L	RMS error	
average	*1.05*	*0.12*	*1.04*	*0.15*	excludes crushed chunk
st. dev.	*0.16*		*0.15*		

Table 4 summarizes the best-fit values of area factor determined for each chunk and the resulting prediction errors. RMS errors averaged 12%–13% of measured dissolved masses over the three-year test. First-year results (Taylor et al. 2009b) had lower RMS errors (8%–9%), probably because none of the chunks had split and their shapes were reasonably consistent throughout the year.

The area factor does not appear to vary systematically with particle mass for either TNT or Tritonal chunks. However, the *AF* values were substantially higher for TNT compared with Tritonal. These area factors include the effect of minor flaking of HE crystals from the main chunks onto the glass frits, which increased the chunk's exposed surface area. The more common flaking observed for TNT chunks probably accounted for their larger area factors.

The drop-impingement model has a linear relationship between dissolution rate and rainfall rate (Equation 11) ignoring the small effect of rainfall rate on drop diameter. That is, cumulative mass loss is approximately proportional to cumulative rainfall:

$$\begin{aligned} M_{lossj}(t) &= \int_0^t m_j\,dt = \pi AF \int_0^t S_j \left(a + D_{0m}\right)^2 q\,dt \\ &\approx \pi AF\,\overline{S_j}\left(a_0 + \overline{D_{0m}}\right)^2 H(t) \end{aligned} \tag{13}$$

where:

H(t) is cumulative rainfall (cm) and

$\overline{S_j}$ and $\overline{D_{0m}}$ are the average values, weighted by rainfall, of solubility and drop size, respectively.

Because particle mass and thus radius change slowly, Equation 13 uses the initial radius, a_0. We implemented this linear model because it offers a simple approach to estimate HE influx into range soils and is based on local climatology (rather than rain and temperature time series). The rainfall-weighted average temperature during the study's three years was 11 °C, so $\overline{S_{TNT}}$ = 7.3 x 10^{-5} g/cm^3 (via Equation 12). About 55% of total

rainfall fell at rates below 3 mm per hour, and 90% fell at rates below 10 mm per hour. These rates produced mean drop sizes of 0.12–0.16 cm via Equation 13. We selected $\overline{D_{0m}}$ = 0.16 cm because it enters Equation 13 squared and gives area factors that are very similar to the full model.

Figure 25 and Figure 26 show the linear model's predicted TNT dissolved mass alongside the full model's predictions. Table 4 includes the resulting area factors, termed AF_L, and the RMS prediction errors, which averaged only slightly larger than those for the full model. The linear model did not follow the seasonal variations in measured dissolution as well as the full model did because it uses a constant solubility. Nevertheless, its simplicity is a distinct advantage.

The linear drop-impingement model also allowed us to estimate lifespan of HE particles on ranges by allowing particle radius to vary but retaining average solubility and drop size. Equation 11 thus becomes

$$m_j = -\frac{dM_j}{dt} = -4\pi\rho_j a^2 \frac{da}{dt} \approx \pi AF\overline{S_j}\left(a + \overline{D_{0m}}\right)^2 q \tag{14}$$

Rearranging Equation 14 yields

$$\int_{a(t)}^{a_0} \frac{a^2 da}{\left(a + \overline{D_{0m}}\right)^2} \approx \frac{AF\overline{S_j}}{4\rho_j} H(t) \tag{15}$$

The rainfall needed to dissolve the particle completely, H_0, is thus

$$H_0 \approx \frac{4\rho_j}{AF\overline{S_j}}\left\{\overline{D_{0m}} + a_0 - 2\overline{D_{0m}}\ln\left(1 + \frac{a_0}{\overline{D_{0m}}}\right) - \frac{\overline{D_{0m}}^2}{\overline{D_{0m}} + a_0}\right\} \tag{16}$$

We may divide H_0 by annual average rainfall, $\overline{H}$, to estimate the lifespan of the particle, t_0 in years. Figure 27 shows initial dissolution rate and lifespan versus initial particle mass for annual average temperature of 11 °C and annual rainfall of 100 cm/yr. The results scale linearly with rainfall rates and solubility. Roughly speaking, 1 g chunks of TNT or Tritonal will require approximately 100 years to dissolve at annual rainfall of 100 cm per year and 200 years at 50 cm per year. Note that these estimates do not include the effect of natural splitting of the chunks, which would increase the dissolution rate and decrease the lifespan.

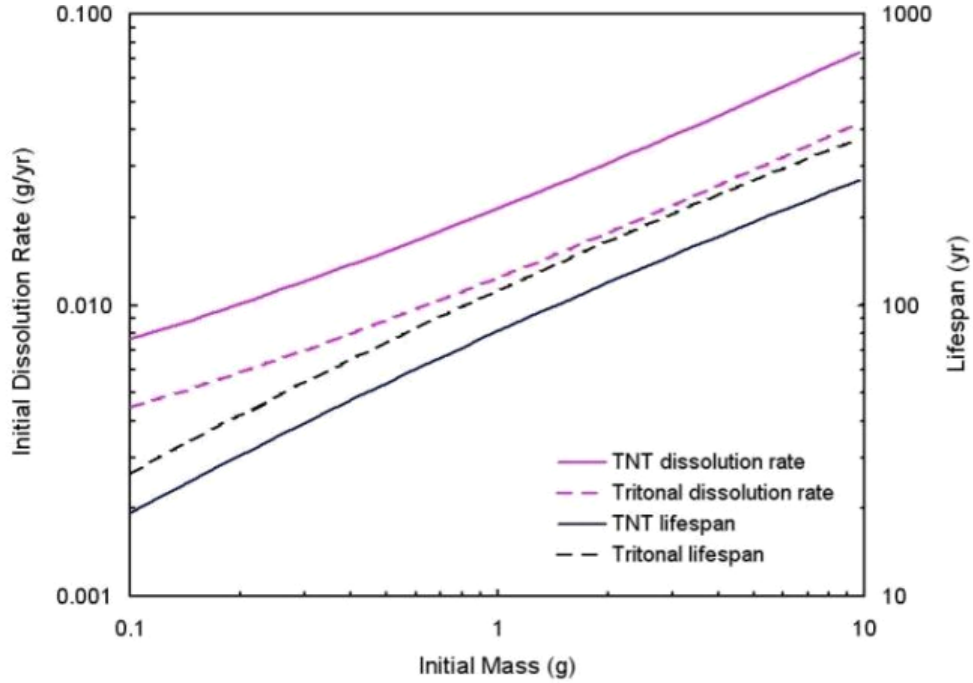

Figure 27. Predicted initial dissolution rate and particle lifespan versus a particle's initial mass. Curves were generated using the linear drop-impingement model (Equations 14 and 16), an average annual rainfall of 100 cm per year, and an average annual temperature of 11 °C.

3.2.6 Layered dissolution model for Comp B

Comp B consists of low-solubility (~ 100 μm) RDX crystals embedded in a higher-solubility TNT matrix. This composition complicates modeling its dissolution. Here, we first describe the main processes operating during outdoor dissolution of centimeter-size Comp B chunks, then we introduce a layered-dissolution model to account for these processes.

The solubility of TNT is about three times higher than that of RDX, and the TNT phototransformation products appear to have even higher solubility. Consequently, TNT exposed on the surface of a Comp B particle initially dissolved rapidly to expose RDX crystals (Figure 17). As the TNT face receded, RDX crystals could fall off the main chunk and dissolve as independent small particles to substantially boost the dissolution rate of RDX. Eventually, TNT receded sufficiently that the surrounding porous layer of RDX crystals controlled its dissolution. Diffusion of TNT through this porous layer was slower and the exposed TNT area was lower, so that TNT dissolution rate decreased substantially. An equilibrium was reached, and RDX and TNT then dissolved at rates that essentially preserved the bulk composition of the chunk.

This equilibrium stage quickly occurred for millimeter-size Comp B particles tested in the lab (Lever et al. 2005; Taylor et al. 2009). In addition, a model that implemented RDX control of TNT dissolution, by preserving the bulk TNT:RDX ratio, gave quite good agreement with the data. Here, we expanded the model to track the transition from rapid TNT dissolution to RDX control of TNT dissolution as a shielding layer of RDX crystals developed.

Lynch et al. (2003) identified a layered model of this type for multi-component HE formulations with components that dissolve at different rates. Using Octol as an example, the authors speculated that the porous layer of HMX crystals would probably disintegrate as TNT receded but lacked observations to confirm this process. They also noted that the thickening layer of HMX crystals would reduce the TNT dissolution rate, although their model was based on a stirred-bath dissolution concept.

Listed below are the key features and equations for our layered dissolution model for Comp B chunks. So far, we have only implemented it using the linear drop-impingement model. Its implementation using the full model would follow the same steps.

TNT initially dissolves at a rate given by independent dissolution from the chunk (Equation 13):

$$\Delta M_{TNT} = \overline{S}_{TNT}\pi\left(a_{RDX} + \overline{D_{0m}}\right)^2 AF_L \Delta H \tag{17}$$

where the rainfall-capture area of the chunk is governed by the outer radius of the RDX layer, a_{RDX} (cm). The dissolution of TNT phototransformation products boosts the total TNT loss rate, $\Delta M'_{TNT}$:

$$\Delta M'_{TNT} = \Delta M_{TNT} R_{TNT} \tag{18}$$

where:

R_{TNT} is the measured ratio of total TNT mass loss to HPLC-derived dissolved mass (~ 3:1).

As noted, creation and dissolution of TNT phototransformation products is inherent to outdoor dissolution of TNT-based explosives. It must be included here to track the receding TNT layer.

The equivalent radius of TNT remaining in the chunk, a_{TNT}, relates to the remaining mass of TNT, M_{TNT}, via:

$$a_{TNT} = \left(\frac{M_{TNT}}{\frac{4}{3}\pi\rho\gamma_{TNT}} \right)^{1/3} \tag{19}$$

where:

ρ is the density of Comp B (1.65 g/cm3) and
γ_{TNT} is the mass fraction of TNT in Comp B (0.39).

RDX dissolves from the main chunk independently of TNT:

$$\Delta M_{RDX_chunk_diss} = \overline{S}_{RDX}\pi\left(a_{RDX} + \overline{D_{0m}}\right)^2 AF_L \Delta H \tag{20}$$

In addition, the receding TNT exposes a layer of RDX crystals whose mass relates to the TNT mass loss via the ratio of mass fractions:

$$\Delta M_{RDX_layer} = \Delta M'_{TNT} \frac{\gamma_{RDX}}{\gamma_{TNT}} \tag{21}$$

where:

γ_{RDX} is the mass fraction of RDX in Comp B (0.60).

This layer consists of $\Delta N_{crystals}$ of RDX:

$$\Delta N_{crystals} = \Delta M_{RDX_layer} / M_{crystal} \tag{22}$$

where:

$M_{crystal}$ is the average mass of an RDX crystal.

Without TNT available to bind them, some fraction of these exposed crystals, f_{fall} (say ~ 0.5), fall off the chunk to dissolve independently. This adds

$$\Delta N_{fall} = f_{fall}\Delta N_{crystals} \tag{23}$$

to the number of crystals on the ground (or frit in the case of the outdoor experiments), N_{ground}. These crystals dissolve as independent small particles (Equation 5). The number of independent crystals lost from the

Comp B chunk can quickly rise to several thousand. Rather than track their change in size and dissolution rate with time, we may use an average dissolution rate times the number of crystals to approximate the dissolved mass of the group:

$$\Delta M_{RDX_crystals_diss} = N_{ground}\,\overline{m}_{crystal}\,\Delta H \tag{24}$$

where:

$\overline{m}_{crystal}$ is the average dissolution rate (g/cm-rainfall) for an RDX crystal.

We may then approximate the decrease in number of RDX crystals on the ground as

$$\Delta N_{ground} = \Delta M_{RDX_crystals_diss} \big/ M_{crystal} \tag{25}$$

The total dissolution rate for RDX is the sum of dissolution from the main Comp B chunk plus that from the independent RDX crystals:

$$\Delta M_{RDX_diss} = \Delta M_{RDX_chunk_diss} + \Delta M_{RDX_crystals_diss} \tag{26}$$

This constitutes the RDX influx into range soils. The contribution from the numerous independent RDX crystals can exceed RDX dissolution from the main Comp B chunk.

The mass of RDX in the Comp B chunk is reduced by the dissolved mass from the chunk plus the mass of the fallen crystals. That is:

$$\Delta M_{RDX_chunk} = \Delta M_{RDX_chunk_diss} + f_{fall}\,\Delta M_{RDX_layer} \tag{27}$$

The outer radius of the chunk (equivalent to the radius of the RDX layer) is then given by the mass of RDX remaining in the chunk:

$$a_{RDX} = \left(\frac{M_{RDX}}{\frac{4}{3}\pi\rho\gamma_{RDX}} \right)^{1/3} \tag{28}$$

As TNT recedes, the exposed layer of Comp B crystals, $b = a\text{RDX} - a\text{TNT}$, grows in thickness. This porous layer of RDX crystals impedes the dissolution of TNT from the chunk (Lever at al. 2005; Taylor et al. 2009).

At present, we do not know the functional form of this impeding effect. Here, we model it via an exponential attenuation of TNT solubility based on the thickness of the porous RDX layer:

$$S'_{TNT} = \overline{S}_{TNT} \exp\left(-b / D_a\right) \tag{29}$$

where:

D_a is an attenuation depth.

This depth is probably similar to the average RDX crystal size. Equation 29 coupled with Equation 17 will reduce the TNT dissolution rate as the RDX porous layer develops.

Table 5 lists the parameters needed to implement the layered Comp B dissolution model. Most parameters derived from the underlying drop-impingement model or are physical constants (solubility, drop size, area factor, density, mass fraction). Parameters unique to this model (crystal mass, crystal dissolution rate, fall fraction, attenuation depth) are constrained within limited ranges. We comment here on those constraints.

Table 5. Parameters for layered Comp B dissolution model.

Parameter	Description	Value	Comment
$\overline{S}_{TNT}$	average TNT solubility	7.4 x 10^{-5} g/cm^3	at 11°C
$\overline{S}_{RDX}$	average RDX solubility	2.3 x 10^{-5} g/cm^3	at 11°C
$\overline{D}_{0m}$	average raindrop size	0.16 cm	
R_{TNT}	total TNT loss/TNT dissolution	3.3	3.1 – 3.6 for TNT and Tritonal chunks, to account for phototransformation products
ρ	Comp B density	1.65 g/cm^3	
γ_{TNT}	TNT mass fraction	0.39	
γ_{RDX}	RDX mass fraction	0.60	
AF_L	area factor	1.5	average 1.0–1.6 for TNT and Tritonal chunks
$M_{crystal}$	average RDX crystal mass	4.4 x 10^{-7} g	for 80 μm RDX sphere
$\overline{m}_{crystal}$	average RDX crystal dissolution rate	6.0 x 10^{-9} g/cm	for 80 μm RDX sphere

Parameter	Description	Value	Comment
f_{fall}	fraction of exposed RDX crystals that fall off layer	0.5	owing to receding TNT, likely range 0.3–0.7
D_a	TNT solubility exponential attenuation depth	80 μm	impeding effect of RDX crystal layer, likely range 60–120 μm

Solid TNT will phototransform when exposed to sunlight, and the phototransformation products are not detected by HPLC analysis. As TNT dissolved in Comp B, we accounted for the missing TNT mass via R_{TNT} (Equation 19) and constrained its value to the range (3.1–3.6) found for TNT and Tritonal chunks. It is possible that the porous layer of RDX crystals shielded TNT from sunlight and reduced phototransformation, but for now, we ignored this possibility.

The area factor accounts for rainfall-capture areas for non-spherical chunk shapes. It should range between 1–2, with 1.6 and 1.0 found as average values for TNT and Tritonal chunks (Table 4).

The RDX crystals in Comp B varied in size and shape. We used 80 μm as an average diameter, which yielded an average crystal mass of 4.4×10^{-7} g. To determine a crystal's average dissolution rate, we applied the small-particle form of the drop-impingement model (Equations 5–6, 8–10) and used the same values for RDX solubility and drop size as for the Comp B chunk (Table 5). Figure 28 shows the predicted results. Dissolution rate decreased slowly with particle mass until quite near the end. It required about 740 mm of rainfall to dissolve the crystal completely, for an average dissolution rate of 6.0×10^{-9} g per centimeter of rainfall.

The Comp B chunks clearly developed outer surfaces of exposed RDX crystals as TNT receded (Figure 17b). We also saw evidence of RDX crystal loss. These observations constrained f_{fall} to a range $0 < f_{fall} < 1$ with a practical range probably closer to 0.3 – 0.7.

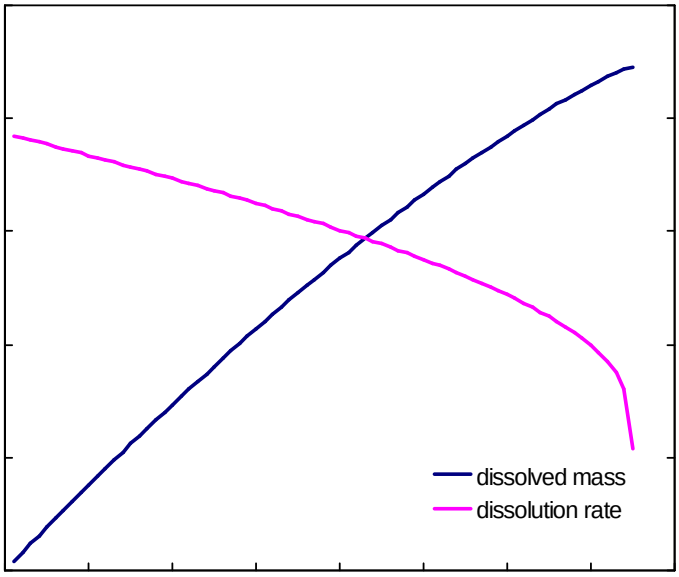

Figure 28. Dissolved mass and dissolution rate as functions of total rainfall, H (mm), for an 80-µm-diameter RDX crystal, based on the small-particle drop-impingement model.

3.2.7 Validation of layered dissolution model for Comp B

We wished to use the outdoor dissolution data to validate the layered Comp B dissolution model. Unfortunately, we did not obtain 100% mass balances for the chunks (Table 3). As mentioned, we recovered via HPLC analysis about one-third of the TNT mass loss from outdoor TNT and Tritonal chunks, and we expect that phototransformation accounts for the other two-thirds. If we applied $R_{TNT} \sim 3$ to the Comp B chunks, we found that we recovered only about 50% of the RDX mass though HPLC analysis of the water samples.

Solid-phase RDX does phototransform to other compounds (Bedford et al. 1996). However, anecdotal evidence suggested that RDX is more stable in sunlight than TNT, so that the rate may not be high enough to account for the missing mass. We plan to investigate this pathway further but have not accounted for it here.

A likely RDX mass-loss pathway was transport of free RDX crystals through the frits before their complete dissolution. The frit openings (145–175 µm) were larger than RDX crystal sizes (<100 µm). We are currently attempting to verify this pathway by filtering new outdoor-dissolution water samples and analyzing the filters for RDX. Meanwhile, we may account for this pathway by assuming that a fraction, f_{thru}, of the RDX crystals present on the frit between sample intervals would pass through it. It appeared that a small pass-through fraction, $f_{thru} \sim 0.05$, is sufficient

to account for the missing RDX mass. Note that this pathway is an artifact of the experiment and would not be present for Comp B exposed to rainfall on training ranges. We included it here to compare model predictions with our existing three-year data record for Comp B chunks.

We generated model predictions for all Comp B chunks using the default parameter values given in Table 5. We could best-fit the data by tuning some parameters, in keeping with adjusting area factors to fit TNT and Tritonal data (Table 4). However, several model parameters besides AF_L could be adjusted (e.g., R_{TNT}, $M_{crystal}$, f_{fall}, D_a), plus we have postulated that an unknown fraction of RDX crystals passed through the frit, f_{thru}. We preferred to present results using the default parameter values rather than adjust them all to achieve better fits. Used this way, the model does provide some insight into the differences in Comp B dissolution behavior.

Figure 29 shows two examples of good agreement between measured and modeled dissolved masses, for Comp B1 and Comp B9, using the default model parameters (Table 5). Model results for Comp B5 and Comp B7 were similarly in good agreement with measured data. The model agreement is not as good as that for the single-component TNT and Tritonal chunks (Figure 24, Figure 25, Table 4) but the layered Comp B model is attempting to simulate more processes than unimpeded dissolution of TNT.

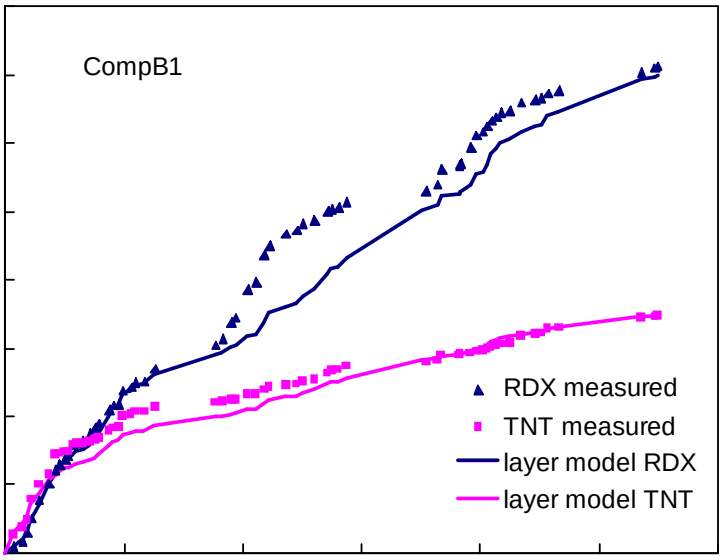

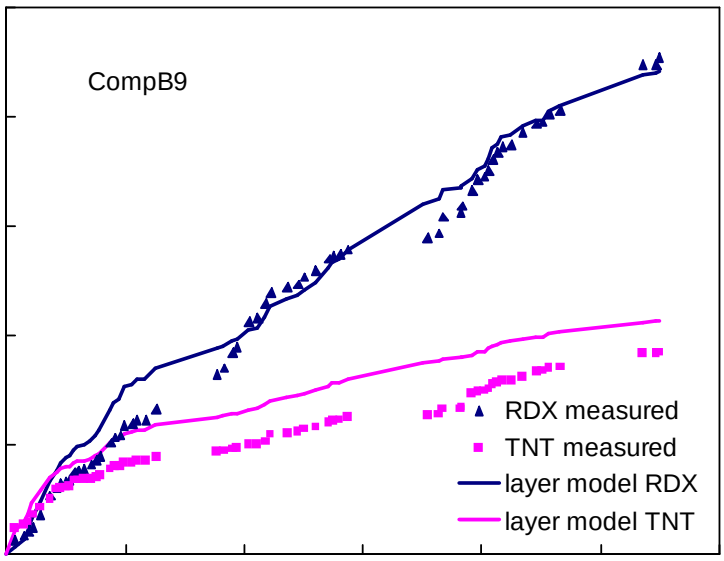

Figure 29. Examples of good agreement between measured and modeled Comp B dissolved masses (Comp B 1 and Comp B 9) using default parameters (Table 5). The default parameters provided similarly good agreement for Comp B 5 and Comp B 7.

Figure 30 shows two examples of under-prediction using the default model parameters (Comp B 2 and Comp B 6). Both RDX and TNT in these chunks dissolved faster than predicted. Simply increasing area factor from 1.5 to ~ 3 substantially improves the agreement for these two chunks and for Comp B 12.

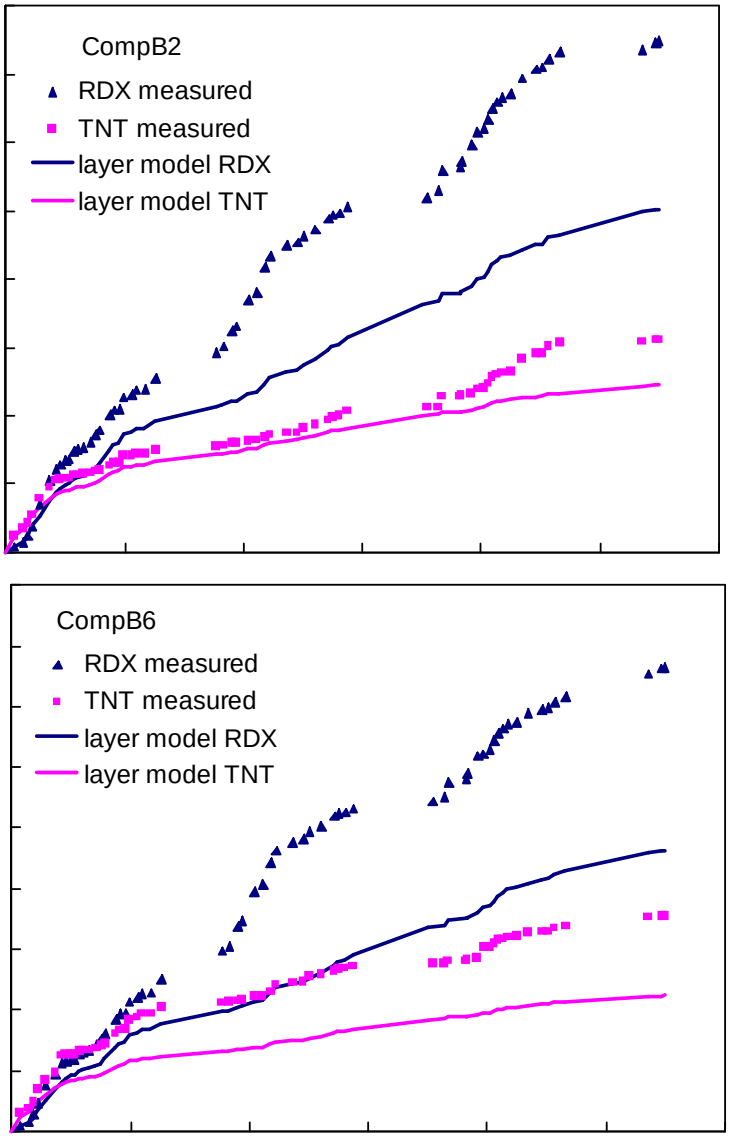

Figure 30. Examples of under-prediction of Comp B dissolved masses (Comp B 2 and Comp B 6) using default parameters (Table 5). Increasing AF_L to ~ 3 yielded good model agreement for these chunks and Comp B 12.

Figure 31 shows two examples of over-prediction using the default model parameters (Comp B 3 and Comp B 4). Both RDX and TNT in these chunks dissolved slower than predicted. These were the only two chunks warranting $AF_L < 1$ ($AF_L \sim 0.5–0.7$ needed). Interestingly, these chunks had a dark surface coating (Figure 13) that persisted over the course of the tests. They were collected from the same partial detonation as the other Comp B chunks, but were coated with material from the detonation that impeded dissolution. They were included in the outdoor tests to assess how materials that adhered to explosives during detonations would affect the dissolution of the explosive.

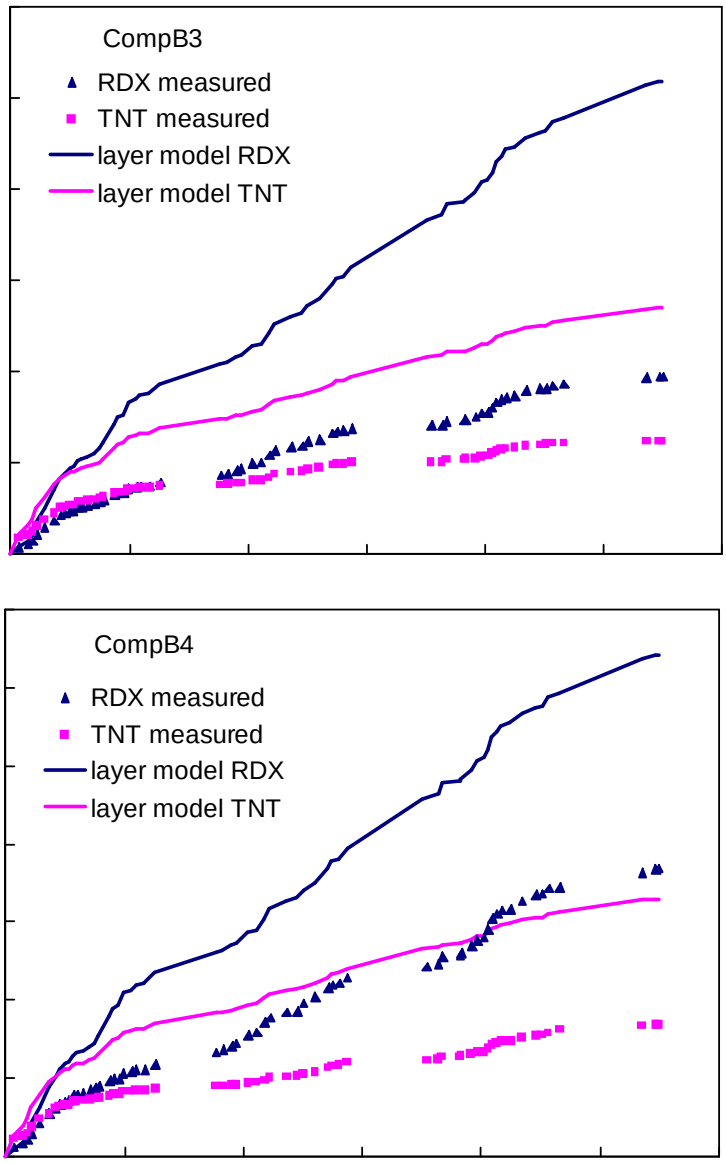

Figure 31. Examples of over-prediction of Comp B dissolved masses (Comp B 3 and Comp B 4) using default parameters (Table 5). These were the only chunks warranting $AF_L < 1$. They both possessed dark surface coatings that impeded dissolution.

Figure 32 shows the two sets of model predictions (Comp B 8 and Comp B 10) that cannot be improved by simply changing area factors. The default parameters caused the model to over-predict TNT and under-predict RDX dissolution. Smaller RDX crystal size, higher crystal fall fraction or lower crystal through-frit fraction would all improve the predictions, but we have no basis to justify these changes.

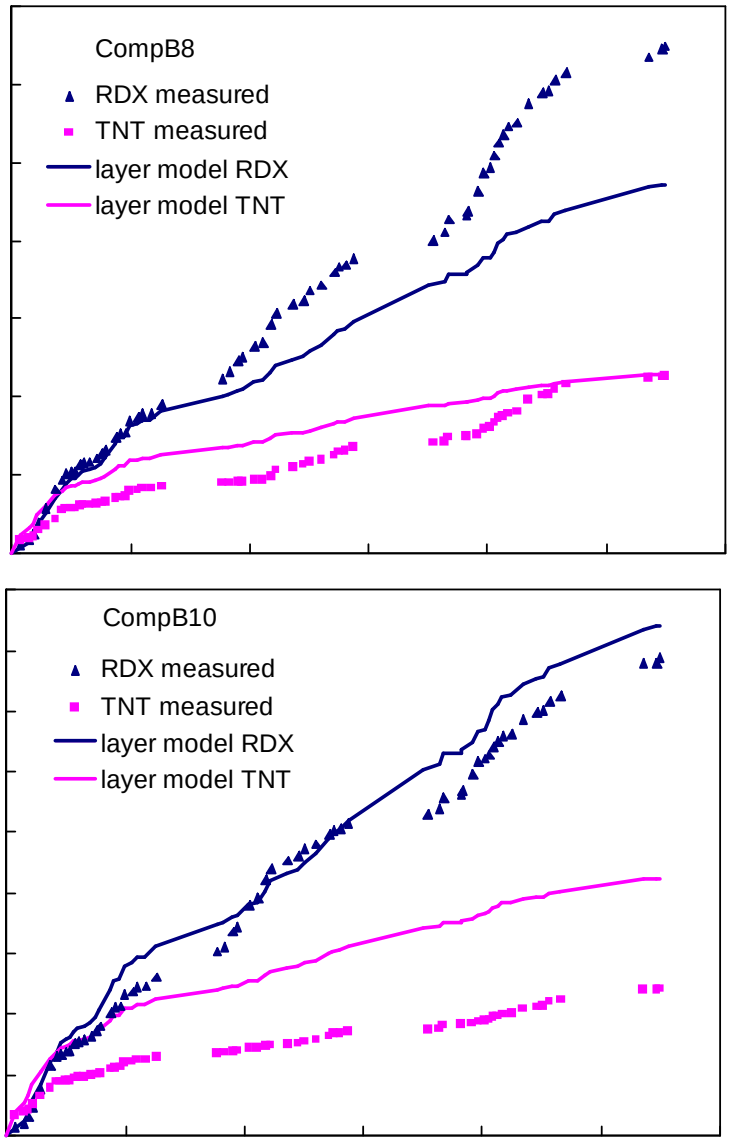

Figure 32. The two cases (Comp B 8 and Comp B 10) where simply adjusting area factor would not substantially improve model agreement. Improving the fit to TNT dissolution would worsen agreement with RDX dissolution.

The results from Comp B 11, which was crushed and returned outdoors on day 436, provided strong support for the basic structure of the layered Comp B model. Figure 33 shows the predictions using default parameters.

The agreement is excellent until the chunk was crushed, at which point the model significantly under-predicts dissolution of both TNT and RDX. Figure 34 shows the predictions if we boosted *AF* by 5-fold after Day 436, to mimic the increased surface area of the population of daughter particles after crushing. All other parameters were held constant. The simple increase in AF_L captured most of the measured dissolution behavior of the population of daughter particles.

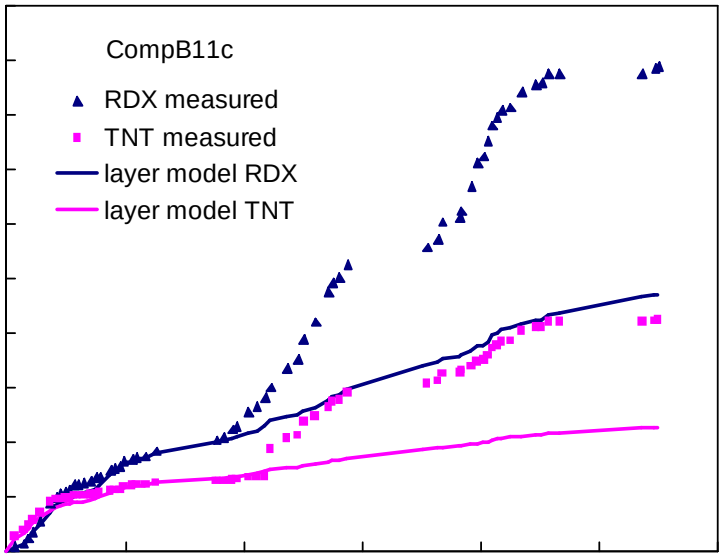

Figure 33. Comparison of measured and predicted dissolution for Comp B 11. The default parameters yielded excellent agreement before the chunk was crushed and the pieces returned outdoors on day 436.

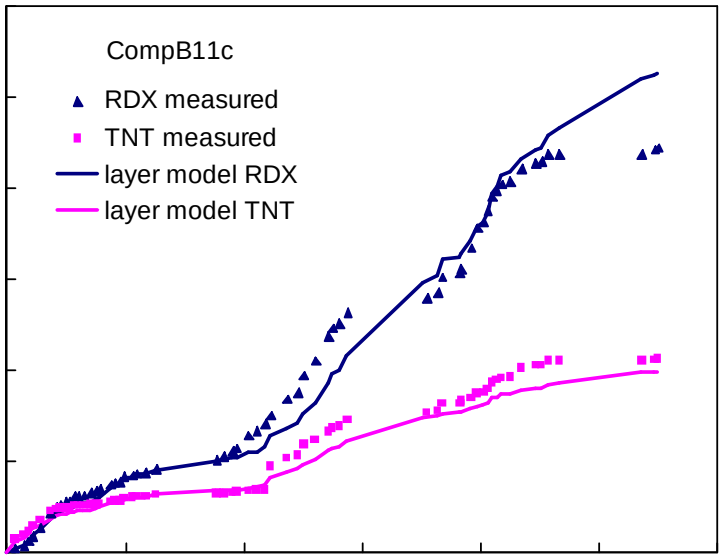

Figure 34. The model agreement with Comp B 11 dissolution is quite good using a 5-fold increase in area factor, beginning after the chunk was crushed. The jump in area factor mimics the increase in surface area for the population of smaller pieces, compared with the original chunk.

3.2.8 Population modeling

Three HE chunks, TNT 5, Tritonal 5 and Comp B 11 were crushed after ~ 14 months of outdoor exposure and the daughter particles weighed and returned to their funnels on Day 436 (Chapter 5). These daughter particles continued to weather and dissolve, and we collected the water samples from each population at the same intervals as the remaining uncrushed HE chunks. So far, we have implemented a population model to simulate dissolution of the crushed TNT and Tritonal chunks. The Comp B model was more complex to implement in population form, but we followed the same approach as used for the HE chunks.

Table 6 shows the population distributions for TNT 5 and Tritonal 5. The larger Tritonal 5 produced many more individual pieces when crushed. Both chunks produced dust particles that were too small to weigh individually. We assumed that the dust averaged about 200 μm in diameter in calculating the number of these particles from the total mass of dust. These data constituted the starting populations on Day 436 for continued dissolution modeling.

Table 6. Particle masses for TNT 5 and Tritonal 5 after crushing. We used average diameter of 200 μm to determine the number of particles from the dust mass.

TNT 5	Mass (g)	Tritonal 5	Mass (g)
1	0.3217	1	1.1485
2	0.2123	2	0.2141
3	0.0404	3	0.1024
4	0.0087	4	0.0894
5	0.0062	5	0.0685
6	0.0057	6	0.0671
7	0.0006	7	0.0655
dust	6.912E-06	8	0.0521
		9	0.0356
		10	0.0271
		11	0.0237
		12	0.0171
		13	0.0165
		14	0.0134
		15	0.0131
		16	0.0104
		17	0.0080
		18	0.0077
		19	0.0066
		20	0.0062
		21	0.0040
		22	0.0029
		23	0.0021
		24	0.0018
		25	0.0013
		26	0.0007
		dust	7.494E-06

Both populations included particles smaller than 5 mg, the approximate lower bound for the large-particle drop-impingement model. Also, particles close to the boundary could pass into the small-particle regime as they dissolved. Thus, the model tested for this condition and used the appropriate version of the drop-impingement model. The large- and small-

regime predictions converged at the boundary and were very similar close to it. Consequently, the predictions are not highly sensitive to the exact boundary value.

Each version of the model has a tuning parameter: (a) water-film thickness, h, for the small-particle version and (b) area factor, AF, for the large-particle version. We used h = 0.009 cm for all small TNT and Tritonal pieces. This was the average value determined from laboratory dissolution tests for milligram pieces of TNT and Tritonal (Taylor et al. 2009). This approach removed it as a tuning parameter for the population models. We then best-fit AF to the measured dissolution data and examined whether the resulting values were consistent with the pre-crushing values.

Figure 35 compares measured and modeled dissolution for TNT 5. The full model (using hourly rainfall and temperature data) fit the measured dissolution data extremely well (3.5% RMS error). The best-fit area factor dropped from 2.4 to 1.4 after crushing. This compares with a value of AF = 2.6 (with 8% RMS error) if we model the entire three-year record as a single chunk (Table 4). The pre-crushing AF reflected the exposed area of small TNT crystals that commonly flaked off the main chunk. The population model explicitly included the increase in area from the post-crushing daughter particles and dust. The linear drop-impingement population model also fit the dissolution data well (8.6% RMS error) and showed similar best-fit area factors (2.3 and 1.3, before and after crushing, respectively).

Figure 36 compares measured and modeled dissolution for Tritonal5. Again, the full model provided excellent agreement before and after crushing, in this case without changing area factor (AF = 1.07). When modeled as a single chunk, AF = 4.5 was needed to track the post-crushing dissolution data (Table 4). Explicitly modeling the population of daughter particles eliminated the need to boost area factor after crushing. Note that the largest daughter particle of Tritonal 5 split naturally into three similar-size pieces near Day 800 (determined by photographs). The measured dissolution rate jumped at this point. Because we did not alter the population data to account for this natural splitting, the model under-predicted dissolution of the population after Day 800, as expected.

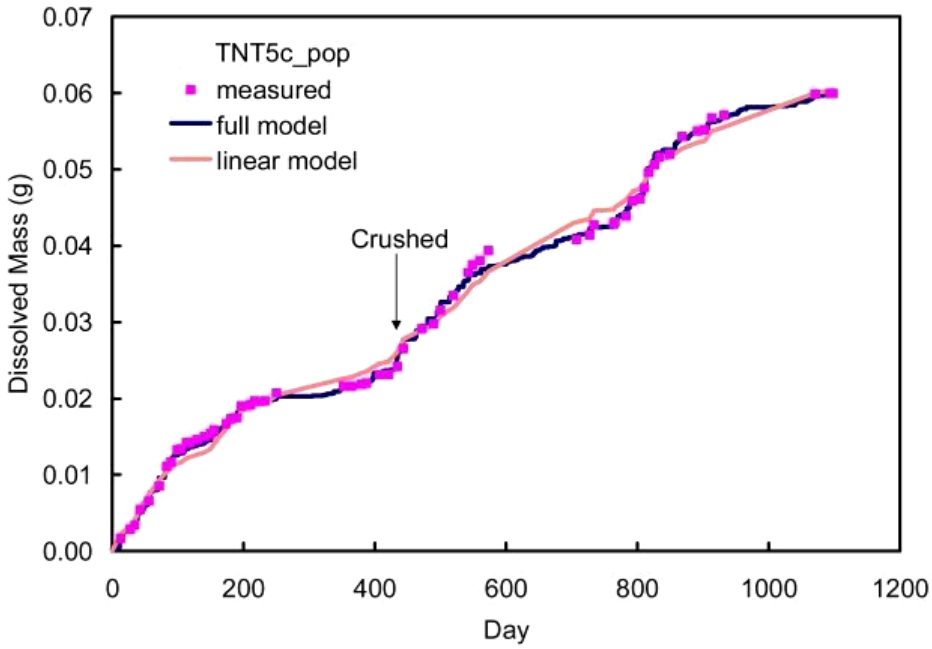

Figure 35. Measured and predicted dissolution for TNT 5, which was crushed and returned outdoors on Day 436. The post- crushing predictions used the measured-size distribution of the daughter particles.

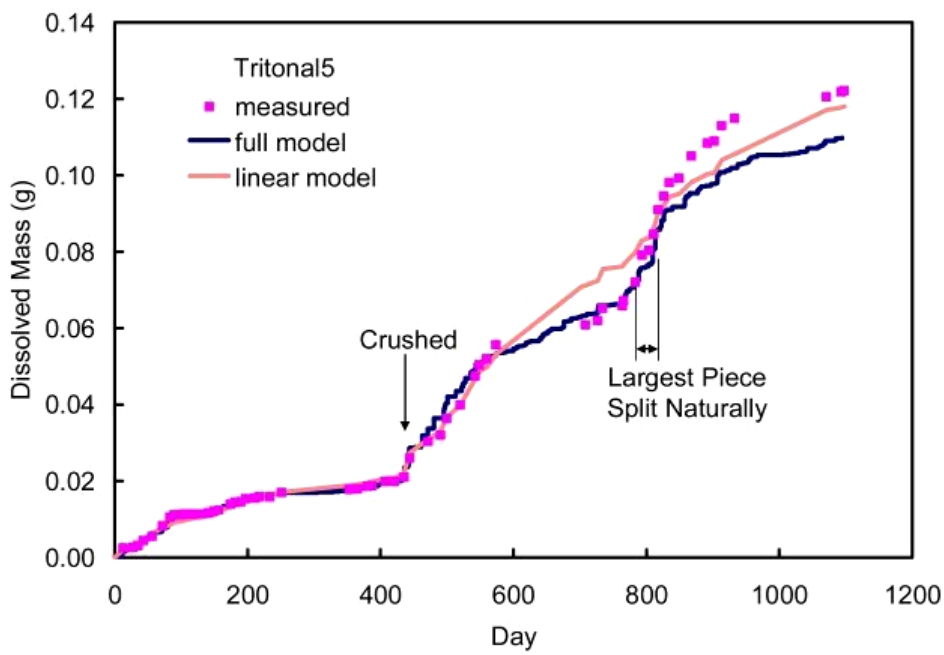

Figure 36. Measured and predicted dissolution for Tritonal 5, the chunk which was crushed and returned outdoors on Day 436. The post- crushing predictions used the measured-size distribution of the daughter particles. Note that the largest daughter particle split naturally near Day 800. The model did not include this effect.

The model-validation work presented here indicates that, at least for TNT, Tritonal, and Comp B, the drop-impingement model can provide reasonable estimates for the dissolution rate of a known population of HE chunks. More work is needed to estimate the starting HE population distributions on training ranges, and the evolution of those populations caused by natural splitting of the chunks.

3.3 Conclusions

To our knowledge, the experiments described here are the first to measure dissolution of individual HE chunks exposed to natural weather conditions. The tests mimicked conditions on military ranges where surface-deposited HE chunks from LO detonations weather and dissolve under the action of rainfall, sunlight, and temperature variations. Our sample bottles captured all rainwater that interacted with HE present in the funnels, namely the main chunks and any pieces that split off as a result of weathering. Once in the sample bottle, dissolved TNT and RDX in the water samples were minimally affected by phototransformation, so that the HPLC-measured concentrations accurately reflected the TNT and RDX dissolved from each chunk over the three-year test. They thus represented important datasets to validate dissolution models for HE chunks on training ranges.

Because we sought to document changes in the appearance of HE chunks and to check for mass balance, we periodically photographed and weighed the chunks. This revealed an important finding: dissolved TNT mass represented only about one-third of the mass losses from the TNT and Tritonal chunks. Formation and dissolution of solid-phase phototransformation products, or “red products” on the surface of TNT containing HE, can account for the missing two-thirds mass losses. Whether these products occurred solely due to radiation or are mediated by moisture on the particle surface is not yet known. The identities of these red products are also unknown as are their health risks, if any. The formation, dissolution, and transport of TNT phototransformation products are processes inherent to outdoor exposure of TNT-based explosives. The influx of these products into range soils can exceed that for TNT itself and thus clearly warrants more attention.

The drop-impingement model predicted the TNT dissolved-mass time series with remarkably low RMS prediction errors (12%–13%) for both TNT and Tritonal chunks. The model had a simple physical interpretation: all rainfall captured by the particle flowed off it fully saturated in HE. The

linear relationship between dissolution rate and rainfall rate made it possible to link average annual HE influx to average annual rainfall. This approximation predicted dissolved mass with only 14%–15% RMS errors and can be applied easily to ranges across the country by using readily available rainfall and temperature climatology. Slightly larger uncertainties existed in area factors for individual HE particles (± 15 – 30%), reflecting unknown differences in particle shapes and surface friability.

The drop-impingement model also formed the basis for modeling rainfall-driven dissolution of Comp B. However, Comp B, with two HE components dissolving at different rates, required a more ambitious model. Considering its scope, the layered Comp B dissolution model described here works remarkably well. It modeled the dissolution and recession of TNT and its phototransformation products, the growth of a porous layer of Comp B crystals, the release of a portion of these crystals and their independent dissolution as small particles, and the impeding effect of the Comp B layer on further TNT dissolution. We set the default model parameters using physical arguments, and on average, the model predicted the correct scale of TNT and RDX dissolution for all the chunks studied. Uncertainties are about a factor of two for an arbitrary Comp B chunk. Although this uncertainty is much higher than for single-component TNT and Tritonal chunks, many more processes are modeled and more natural variability probably existed in these processes. We have resisted the urge to fit the many model parameters to the data until we understand these processes better.

The layered model can account for several subtle but important dissolution characteristics of Comp B chunks. Dissolution of RDX was initially quite low and then accelerated. This reflected an increase in exposed RDX surface area. The model captured this effect as the release of RDX crystals from the receding TNT and their independent dissolution as small particles. The porous outer layer of RDX crystals impeded and eventually controlled the dissolution of TNT in Comp B. The model captured the timing and scale of this impeding effect reasonably well with a simple exponential attenuation of TNT solubility with increasing RDX-layer thickness, using average crystal size as the attenuation depth. As with the simpler single-component model, cumulative rainfall plays a predominant role; good predictions are possible by using constant solubilities and ignoring the role of temperature variations. That is, the

model can use annual rainfall and average temperature to predict Comp B dissolution on training ranges.

The drop-impingement model worked very well to model the dissolution of populations of daughter particles following crushing (TNT 5 and Tritonal 5). This provided some confidence that it would work well when the population of HE particles on a training range would be given as input. The linear drop-impingement model, because it can use local rainfall and temperature climatology, most easily lends itself to population modeling and provides dissolution estimates nearly as good as the full, hourly model calculations. However, several large uncertainties remain to produce reliable range-wide HE dissolution estimates.

Large cracks appeared in several of the HE chunks and several chunks split off pieces naturally during the three-year test. Thus, splitting is probably common during the decades-long lifespans of gram-size chunks of HE. As we observed, splitting into multiple, centimeter-size particles can produce a several-fold increase in exposed surface area and thus, total dissolution rate. For reasonable estimates of HE influx into range soils, this process must be better understood. Key parameters needed are the rate of splitting, its dependence on weather conditions, and the size distribution of the resulting group of “daughter” particles.

Probably the largest source of uncertainty to estimate HE aqueous influx into range soils resulted from the poorly quantified starting population distribution of the HE particles on a range of interest. The number and size distribution of these particles depends on many factors including the munitions used, their firing rates, their detonation probabilities (high-order, low-order, or dud) and weathering and mechanical disaggregation (Taylor et al. 2004a). It is likely that poor constraint of the initial number and size distribution of HE particles on a given range could cause an order-of-magnitude uncertainty in predicted annual HE dissolution.

4 TNT Phototransformation Studies

Our outdoor tests showed that the dissolved TNT mass measured via HPLC analysis averaged about one-third of the TNT mass loss determined by electronic balance measurements (Figure 37). This result was surprising because HE mass-closure was excellent for our laboratory dissolution experiments (Lever et al. 2005; Taylor et al. 2009) and measurement uncertainties were small relative to the unaccounted mass losses. We found that the unaccounted losses scaled closely with surface area and so were smaller for TNT than for the larger Tritonal chunks over the three years (157 ± 49 mg versus 338 ± 182 mg). To assess whether the lack of mass closure revealed defects in the experiment design, we investigated many possible pathways for TNT mass to leave the particle yet escape HPCL measurement. These included TNT phototransformation in solution, handling losses during the first year of the tests when we regularly moved chunks to weigh and photograph them, sublimation of the HE, and phototransformation of the solid phase explosive. By elimination, we concluded that phototransformation on the solid HE is the dominant mass-loss mechanism.

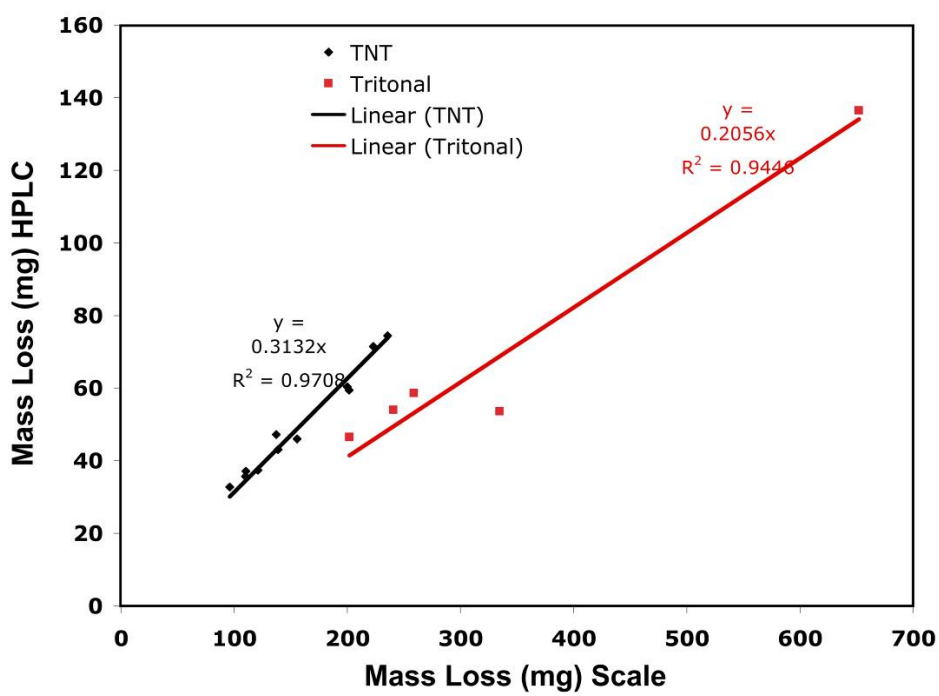

Figure 37. Mass loss measured by HPLC versus measured mass loss by electronic balance for TNT and Tritonal samples.

While much is known about the microbial biotransformation of TNT in soil (Kaplan and Kaplan 1982), and that TNT quickly photodegrades in aqueous solution (Burlinson 1980; Spanggord et al. 1980), the products generated from the solid-phase photochemical transformation of TNT have not been investigated. The formation and dissolution of solid-phase HE phototransformation products on the chunks is intrinsic to the outdoor weathering and dissolution of explosives. Although we did not design our outdoor experiments specifically to investigate phototransformation, we found that this pathway may be the dominant mass-loss mechanism, as previously stated. This finding is significant because the compounds produced on solid chunks are unknown and have the potential to leach into groundwater.

4.1 Results

4.1.1 TNT loss pathways

Phototransformation of the solid HE is a processes intrinsic to the outdoor weathering and dissolution of explosives. However, phototransformation of the HE once in solution is an experimental design problem. To minimize phototransformation of the HE solutions the 1 L bottles catching the rainfall interacting with the HE chunks were kept in a box that excluded light. Nevertheless, because aqueous-phase TNT is known to phototransform quickly to form reddish products in water (Spanggord et al. 1980) we wondered if phototransformation could have occurred in our sample solutions before we analyzed them. To assess this, we measured the TNT concentration of two ~10 mg per liter control samples, and one of our previously analyzed samples. Five-day residence of these solutions in the sample box (the average time between rainfall and sample collection) reduced the TNT concentration by less than 0.5% (Figure 38). Additional tests revealed that 5-minute exposures to direct sunlight (more than sufficient time to swap the collection bottles for analysis) reduced TNT concentrations by less than 2%. Also, day-long exposure of the control samples to indoor laboratory lighting produced undetectable changes in the TNT concentrations. Thus, the measured TNT concentrations represent, within 2%–3 %, the concentrations of TNT in the effluent that interacted with each HE chunk.

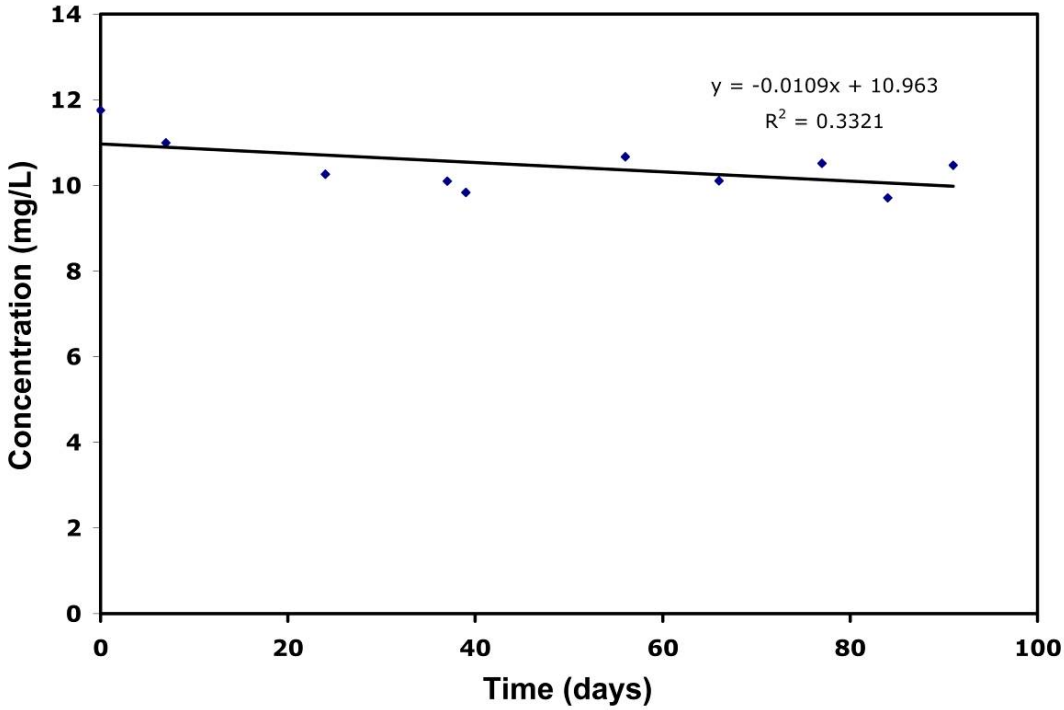

Figure 38. Analyses of a 12 mg/L solution of TNT placed in the outside sample box as a control for TNT transformation in solution.

Other pathways for TNT loss are linked to weathering and increased friability of the HE chunks. As noted in Chapter 3, weathering produced 0.1–1 mm particles on the frits near many of the chunks. Provided the particles remained in the funnels, they eventually contributed to the measured dissolved mass of the chunk. We estimated that these small particles would dissolve within a couple of months after flaking from the main chunk (Lever et al. 2005). Because we only weighed the main chunks on the electronic balance, the mass of these small particles would be unaccounted for until they dissolved. However, their individual masses were small (~ 1 mg for a 1 mm particle; 0.001 mg for a 0.1 mm particle) and could not account for the missing TNT mass even if they did not dissolve. Also, at the end of the experiment we rinsed the funnels twice with 10 mL of acetonitrile to extract and measure all of the remaining HE.

We also assessed whether we inadvertently lost small particles while handling the HE chunks to weigh and photograph them, a procedure conducted seven times during the first year. Each chunk was carefully moved three times (out of the funnel onto weigh-paper on the balance, from there to a glass dish to be photographed, and then back to the funnel) for a total of 21 transfers per HE chunk. To simulate this process, we selected and weighed two HE chunks collected on training ranges but not used for the outdoor tests: 1,933.7 ± 0.5 mg TNT and 6,147.2 ± 0.5 mg

Tritonal. We then transferred them 30 times between two aluminum boats. All four boats contained small particles by the end of the test. The TNT chunk decreased in mass by 1.9 mg and the Tritonal chunk by 7.6 mg. Scaling the mass losses by chunk mass, these handling losses would account for less that 5% of the unaccounted TNT mass losses. This is a conservative estimate because we returned to the funnels any particles that we observed to flake off the chunks during weighing and photographing. These control tests indicated that sample collection and particle handling would not account for the missing TNT mass in the HPLC measurements.

Sublimation of solid-phase TNT is a mass-loss pathway intrinsic to outdoor exposure of the HE chunks. However, the vapor pressure of TNT is low, about 1.6×10^{-4} Pa at 20 °C (Leggett et al. 1977; Dionne et al. 1986), and drops exponentially with decreasing temperature. We estimated the sublimated mass by assuming 1-D diffusion of TNT, from equilibrium concentration at the base of the funnel to zero at the top, a distance of 6 cm (Skelland 1974; Parmeter et al. 1996). This predicted ~ 0.1 mg of TNT lost over the year through sublimation for each TNT or Tritonal particle. Using vapor pressure at 20 °C made this estimate conservative, but air exchange within the funnels would increase diffusion rates. Nevertheless, sublimation would not be a significant pathway for TNT mass loss from the chunks even at ten times the estimated rate. Sublimation of aqueous-phase TNT from the sample bottles would be even smaller, due to the small diameter of the vent tubes.

Formation and dissolution of reddish phototransformation products is also an intrinsic mass-loss pathway for TNT-based explosives exposed outdoors. As noted, the HE chunks quickly turned reddish after being placed outdoors (Figure 39) and the effluent from our outdoor tests usually appeared reddish with visual intensities that correlated with TNT concentrations (Figure 40). Rainfall frequently reduced the reddish appearance of the chunks. Because transformation of the dissolved TNT was found to be small within our sample bottles, rainfall apparently dissolved, at least partially, the surface red layers into the captured effluent.

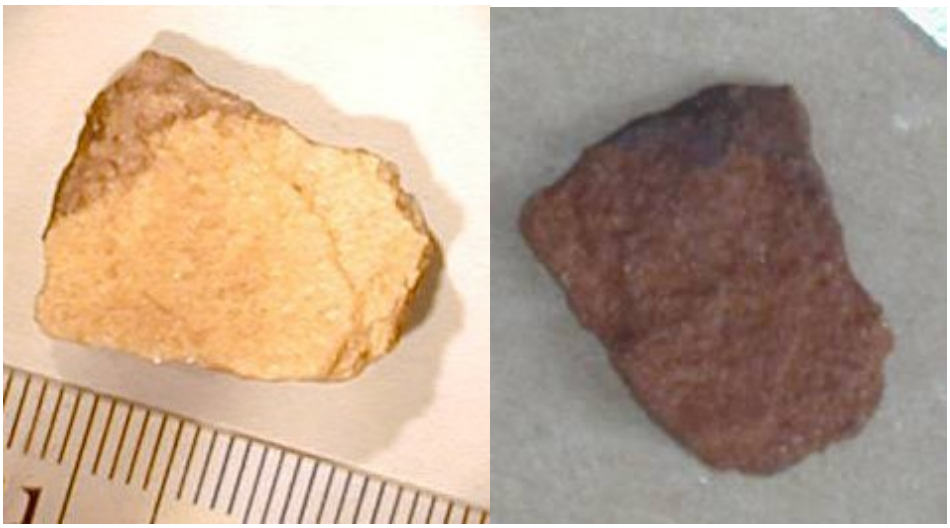

Figure 39. Note the darkening of TNT 4 between when it was set outside on 2 May 2006 (left) and on 30 May 2006 (right).

Figure 40. Tritonal 5 rainwater sample.

Unfortunately, these "red products" have not been unambiguously identified, and no analytic methods exist to quantify their aqueous concentrations. To account for the missing TNT mass, red-product layers only 2–3 μm thick would need to form and be dissolved by rainfall between sample collections. To determine whether this was likely, we placed fresh TNT particles in a lab window for several days and then sectioned them. The brick-red phototransformation product was clearly visible on the exteriors of the particles (Figure 41). Sectioning revealed the

red layer to be ~ 2 μm thick, although layer thicknesses are highly variable (Figure 42). Furthermore, the red products appear to be more soluble in water than TNT (see Section 4A).

Figure 41. TNT piece placed in a windowsill.

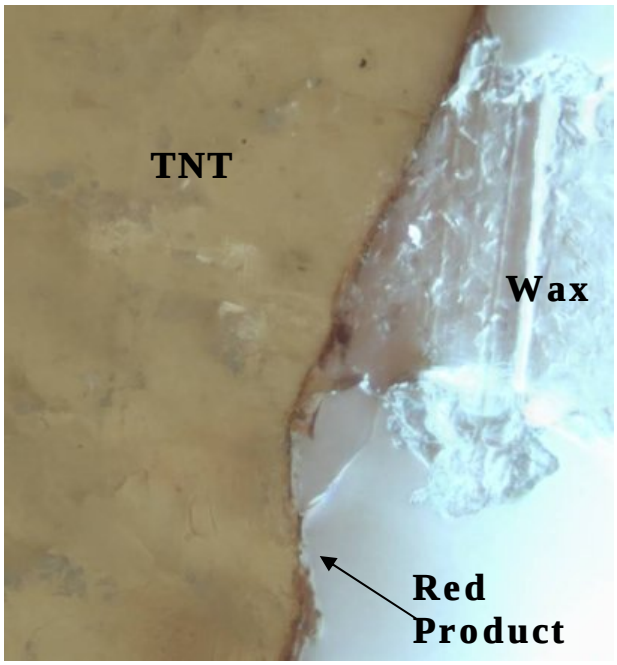

Figure 42. TNT piece embedded in wax and sectioned. Thin layer on edge is responsible for the very dark looking coating in Figure 41.

Interestingly, we found a pre-solvent peak in the HPLC chromatogram positively correlated with red color of the samples (Figure 43). A similar pre-solvent peak was produced when we photo-degraded a TNT solution. As the TNT in the solution decreased, the height of this pre-solvent peak increased (Figure 44). This result suggested that highly polar compounds are formed from both the solid and aqueous phototransformation of TNT.

We hypothesized that solid-phase TNT phototransformed into soluble compounds that are dissolved by rainfall, and that this process probably accounted for the missing TNT mass. This pathway is intrinsic to the problem under study here–the outdoor weathering and dissolution of TNT-based explosives. For conditions similar to those of our study site, aqueous-phase red-product influx into range soils would be twice as large as the influx of HE itself. Depending on local climate conditions, this pathway could produce the dominant aqueous-phase HE influx into soils on training ranges.

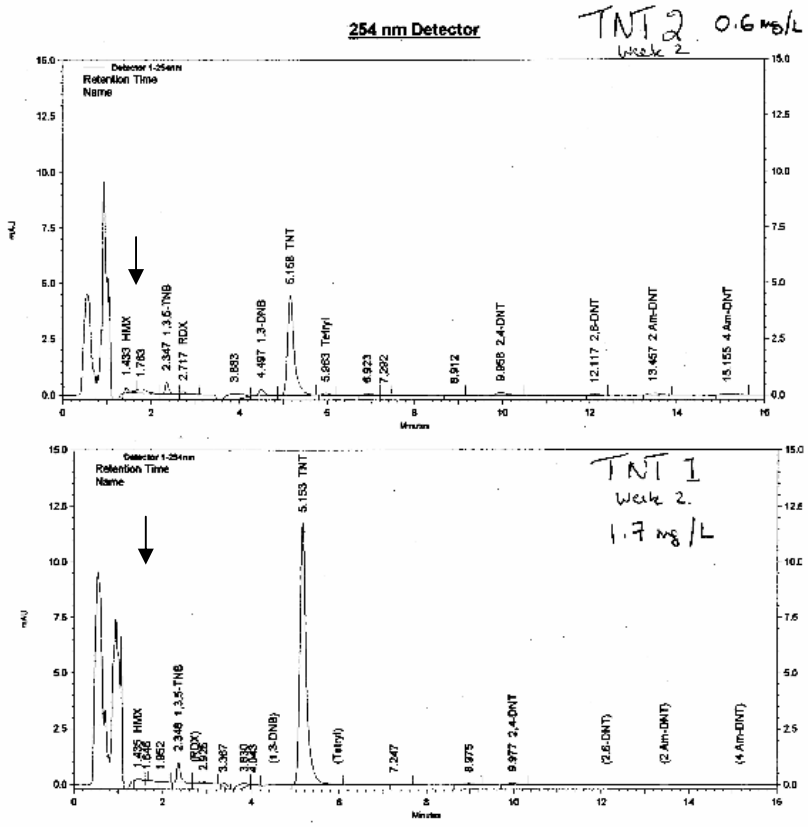

Figure 43. HPLC Chromatogram showing two examples of the pre-solvent peak (arrows).

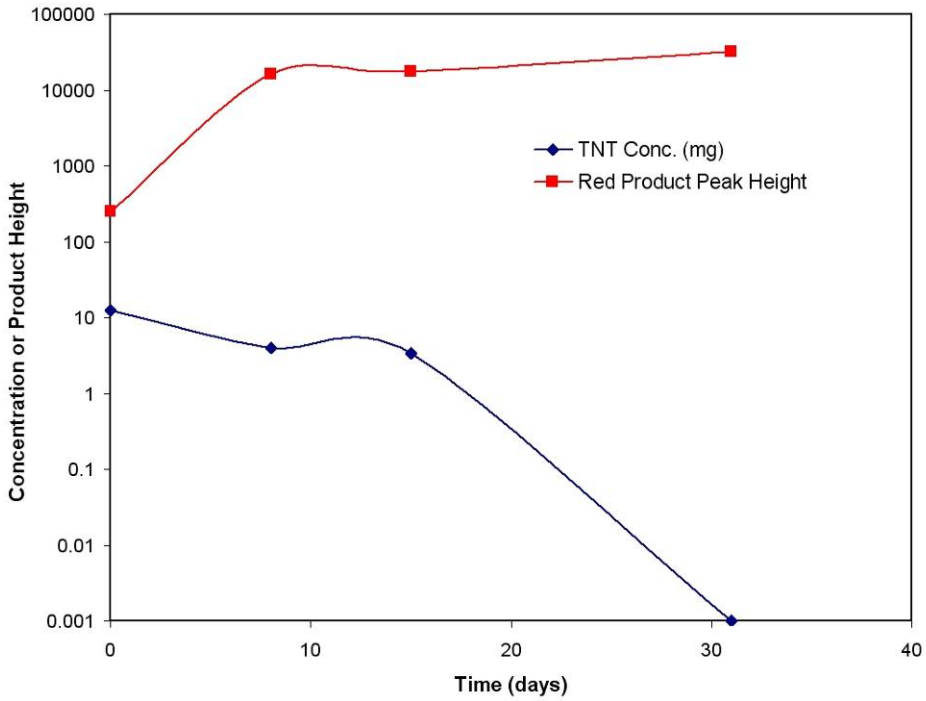

Figure 44. Decrease in TNT concentration is associated with an increase in the peak height of the pre-solvent peak.

4.2 Identifying the TNT phototransformation products

We sent water samples from our outdoor tests to Dr. Ronald Spanggord at SRI International in Menlo Park, California, for characterization. These samples contained compounds washed off the HE chunks that we hoped to separate, isolate, and identify. His report appears in this report as Section 4A, but we summarize his results below.

In addition to compounds quantified by Method 8330B, the outdoor water samples contained 2-amino-4, 6-dinitrobenzoic acid and nitrate. Because the nitrate concentrations were high and were similar in all samples, they are not thought to be related to the explosives. The 2-amino-4, 6-dinitrobenzoic acid, on the other hand, is a known transformation product of TNT. Furthermore, its concentration was similar to, or larger than, the TNT concentration in these samples suggesting it could account for the missing TNT mass. This compound was very polar, was not quantified by Method 8300B, and eluted in the pre-solvent peak area of the chromatogram.

Exposure of TNT to outdoor conditions produced two red-colored, polar products that were highly acidic and water-soluble; we labeled them red

product 1 (RP 1) and red product 2 (RP 2). The majority of the mass eluted chromatographically in the pre-solvent peak where 2-amino-dinitrobenzoic acid was measured. Results presented in Section 4A indicated RP 1 and RP 2 form in the following way. When the outdoor TNT chunks become damp or wet, TNT dissolves on the surface. The acid-form of TNT was generated photo chemically in this solution, and the TNT then condensed with itself to form RP 1. RP 1 is not stable and can convert back to TNT. However, by eliminating water from its structure, RP 1 can form RP 2. RP 2 is very stable and is the compound found in the CRREL Tritonal and TNT water samples. Moisture is key to its formation; outdoor photolysis studies of solid TNT conducted in the absence of water showed no RP 2.

These results are significant because they suggest that solid TNT readily phototransforms in the presence of moisture. Some of the resulting compounds are unstable, but 2-amino-4, 6-dinitrobenzoic acid and RP 2 appear to be stable and highly soluble. More work is needed to measure their production rates, to determine if they can account for the missing mass and are the “end products” of a cascade of chemical transformations.

4A Analytical Characterization of Solid-phase TNT Photolysis Products Formed from the Weathering of Tritonal and TNT

Researchers at SRI performed a number of analytical tests on leachates from HE chunks exposed outside to weather (sunlight, rain, snow, etc). Analyses of the leachates found a number of new components, as well as previously reported compounds, resulting from the photolysis of 2,4,6-trinitrotoluene (TNT). Because chunk explosives are commonly found on military training ranges, it is important to identify these transformation products and evaluate their environmental impact.

The test objectives were to produce, isolate, and characterize the photo-generated components formed on TNT chunks using chromatographic and spectrometric methods.

4.3 Materials and methods

4.3.1 Sample composition

We received water samples from the outdoor CRREL tests, a sample each of the leachate from Tritonal 5, Comp B 4, TNT 5 as well as residues remaining after the leachates from the Tritonal, Comp B, TNT, and C4 samples were left to dry. We also prepared and photolyzed TNT solutions made in our lab.

4.3.2 HPLC analyses

Leachates from the Tritonal, TNT, Comp B, and C4, outdoor samples were centrifuged and filtered through 0.45µm nylon syringe tip filters before analysis. Quantitative analysis of the leachates were performed by high-performance liquid chromatography (HPLC) using a reverse phase gradient. Separations were performed using a Waters 600E Pump, 717 Autosampler, 960 PDA, and a Zorbax SB-CN 250 x 4.6 mm, 5µ-column. The mobile phases were (A) 10mM ammonium formate aqueous and (B) 100% acetonitrile. The gradient method consisted of a flow 1.0 mL per minute at 12%–70% B in 28.5 minutes, followed by a column wash to 100% B at 33.5 minutes, and a return to the initial conditions. The total run time was 43.5 minutes. Chromatography was monitored at 230 nm. Samples were injected from 20-40 µL depending on concentration.

4.3.3 Standard preparation

We prepared a variety of analytical standard solutions to identify and quantify peaks in the chromatographs of the leachates. The standards were prepared in two groups to eliminate the interference of peaks that closely elute. The first standard solution contains TNX, 2,4-DANT, MNX, HMX, and 4-ADNT. The second standard solution contains 2,6-DANT, DNX (~55% with impurities of TNX and MNX), RDX, 2-ADNT, and TNT. Because the DNX reference standard has impurities of TNX and MNX, TNX and MNX were calibrated using a separate standard. Standards of 2,2'-Azoxy, 2,4'-Azoxy, and 4,4'-Azoxy were also calibrated separately using single-point calibrations. The 2-amino-4, 6-dinitrobenzoic acid (2-ADNT) was prepared at SRI and quantified separately by single-point calibration.

There are three highly unstable TNT metabolites, TAT, 2-HADNT and 4-HADNT. The 2-HADNT and 4-HADNT condense to form the azoxy-dimmers. These two must be calibrated separately as they closely elute. As TAT oxidizes in air within a few hours, it is prepared immediately before injection, and is calibrated by a single point. All of the standards, except for TAT, were prepared in 100% acetonitrile. TAT comes as a hydrochloric salt, and must be prepared in 100% water. Standards were made to yield around 1 absorbance unit (AU) at the highest level. Standard concentrations that yield ~ 1 AU of absorbance by this HPLC method are shown in Table 7. A typical HPLC profile of standards appears in Figure 45.

Table 7. Concentrations of standards that yield 1 AU response.

Standard	Abbreviation	MW	Conc. mg/L
2-amino-4,6-dinitrobenzoic acid	2ADNBA	227.13	330
2,4,6-triaminotoluene-trihydrochloride	TAT (TAT-HCL)	137.18 (246.57)	82 (147)
1,3,5-trinitroso-1,3,5-triazacyclohexane	TNX	174.12	191
2,6-diamino-4-nitrotoluene	2,6DANT	167.17	151
2,4-diamino-6-nitrotoluene	2,4DANT	167.17	154
1,3-dinitroso-5-nitro-1,3,5-triazacyclohexane	DNX	190.12	169
1-nitroso-3,5-dinitro-1,3,5-triazacyclohexane	MNX	206.12	159
1,3,5-trinitro-1,3,5-triazacyclohexane	RDX	222.12	194
2-hydroxyamino-4,6-dinitrotoluene	2-HADNT	213.15	120
4-hydroxyamino-2,6-dinitrotoluene	4-HADNT	213.15	110
1,3,5,7-Tetranitro-1,3,5,7-tetraazacyclooctane	HMX	296.16	100
2-amino-4,6-dinitrotoluene	2-ADNT	197.15	68

Standard	Abbreviation	MW	Conc. mg/L
4-amino-2,6-dinitrotoluene	4-ADNT	197.15	65
2,4,6-trinitrotoluene	TNT	227.13	94
4,4’,6,6’-tetranitro-4,4’-azoxytoluene	2,2'Azoxy	406.27	63
4,2’,6,6’-tetranitro-2,4'-azoxytoluene	2,4'Azoxy	406.27	69
2,2',6,6'-tetranitro-4,4'-azoxytoluene	4,4'Azoxy	406.27	78

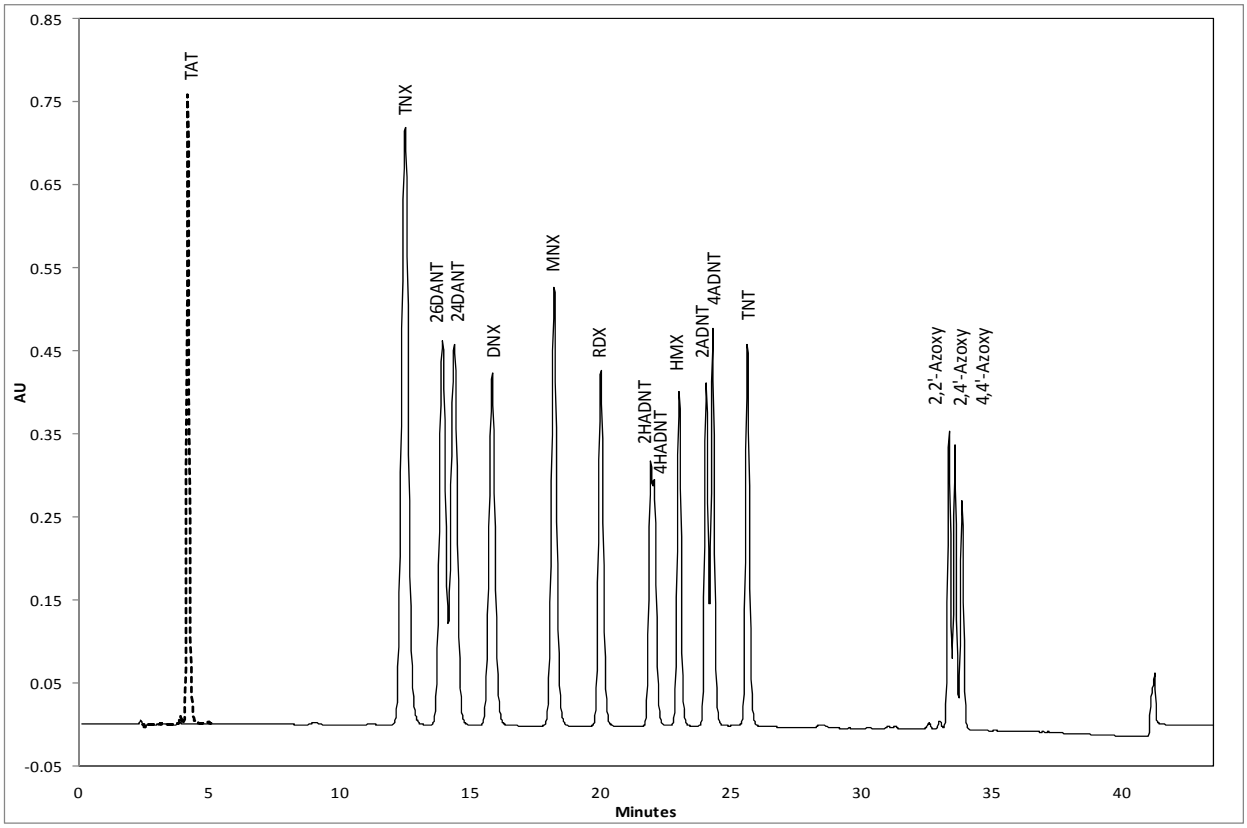

Figure 45. Typical HPLC profile of explosive standards.

4.3.4 Liquid chromatography mass spectroscopy (LCMS)

Liquid chromatography mass spectroscopy (LCMS) analysis was performed using a Waters Aquity Ultra Performance Liquid Chromatogram (UPLC) system equipped with an Aquity BEH-C18, 50 x 2.1 mm, 1.7 µm column. The mobile phases were (a) 10 mm ammonium formate and (b) 100% acetonitrile. The gradient method consisted of 5% B to 70% B in 6.1 minutes at a flow 0.208 mL/min, followed by a column wash to 100% B at 7.1 minutes and held to 8.1 minutes and return to the initial conditions. The total run time was 10.1 minutes. Chromatography was monitored at 230 nm. Samples were injected from 1–2 µL. The mass spectrometer was equipped with an electro-spray probe (from ESI) that

can operate in either the positive or negative mode. In the positive mode, the ionization parameters were generally 3.2 kV probe voltage and 50 V for the cone voltage. For the negative mode, the parameters were generally 3.2 kV probe voltage and the cone voltage was varied between 10–50 V to observe or express certain fragments. The majority of the products were detectable in the negative mode. RDX- and HMX-related products are detectable as formate adducts in the negative mode. Ionization conditions for various explosive components are shown in Table 8. A typical total UV chromatographic profile appears in Figure 46.

Table 8. Explosives ionization.

Chemical	Ionization Mode	MW	with Formate	Peaks	Major Peak	Difference
TAT	ES+	137.1	182.1	138.1	138.1	1.0
DANT	ES+	167.1	212.1	153.9, 167.9, 183.9, 208.9	167.9	0.8
HADNT	ES-	213.0	258.0	211.8, small 257.8	211.8	-1.24
ADNT	ES-	197.0	242.0	195.9, small 241.83	195.9	-1.14
TNT	ES-	227.0	272.0	211.8, 225.8, 266.8	225.8	-1.22
Azo	ES-	390.1	435.1	389.8	389.8	-0.26
Azoxy	ES-	406.1	451.0	404.91	404.9	-1.14
TNX	ES-	174.1	219.0	218.9	218.9	44.85
DNX	ES-	190.0	235.0	234.8, 251.8	234.8	44.75
MNX	ES-	206.0	251.0	250.8, 267.8	250.8	44.76
RDX	ES-	222.0	267.0	266.8, 283.8	266.8	44.77
HMX	ES-	296.0	341.0	340.84, 357.82	340.8	44.79

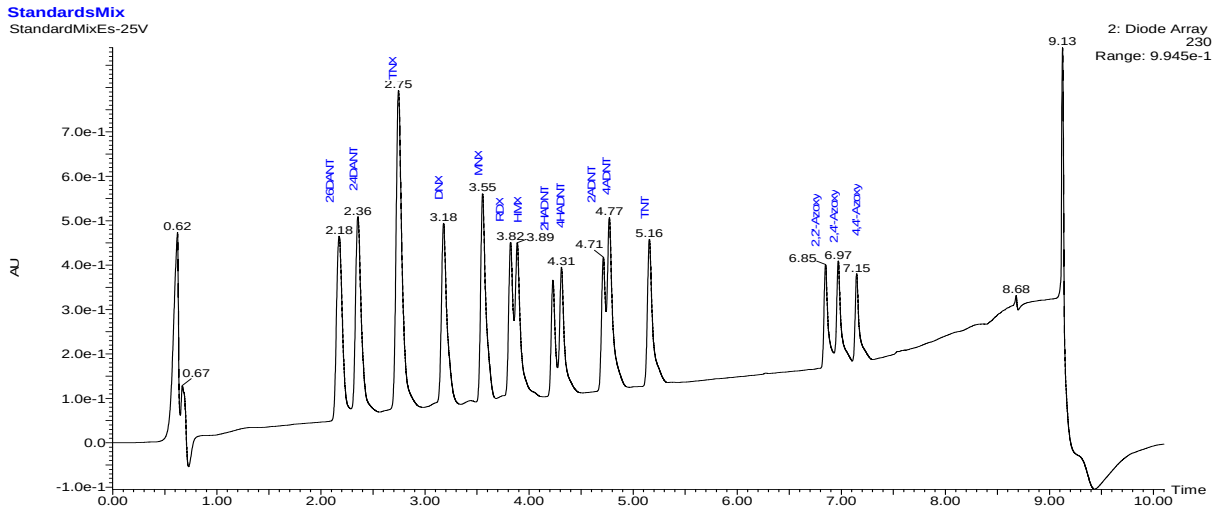

Figure 46. Typical ultra HPLC profile of explosives and related compounds.

4.3.5 Nitrite and nitrate

Nitrate and nitrite are determined by HPLC, using ultra-violet detection according to the method of Thayer and Huffacker (1980). Chromatography is performed on a 10 SAX 250 x 4.6mm column (Whatman Partisil PN 4226-001). The mobile phase is a 50 mm phosphate buffer at pH level of 3–3.5, with an isocratic flow of 1.0 mL/minute. A 10 µL sample volume is injected and monitored at 210nm over 15 minutes. All samples were filtered through a 0.45 µm nylon syringe tip filter before analysis. The linear range of the method is from 0.02–9.8mm for nitrite, and 0.01–3.2 mm for nitrate. Samples outside this range were analyzed by reducing the injection volume.

4.4 Results

Our HPLC results of the HE chunk leachates are listed in Table 9, and the chromatograms are shown in Figure 47. Of note is the large amount of 2 amino 4,6- dinitrobenzoic acid found in the TNT containing explosives. Spanggord et al. (1983) identified 2 amino 4,6- dinitrobenzoic acid in munition wastewaters and is found in groundwater near ammunition facilities (Grummt et al. 2006). Of interest is its high concentration, which is similar to that of TNT. Perhaps some large portion of the missing TNT mass transforms to 2 amino 4,6- dinitrobenzoic acid.

Table 9. Compounds identified and quantified in the CRREL samples.

Compounds / Samples	Nitrate mg/L	2A46DN-Benzoic Acid mg/L	MNX mg/L	RDX mg/L	RP 2* mg/L	HMX mg/L	2ADNT mg/L	4ADNT mg/L	TNT mg/L
Tritonal	468.1	125.97	N/D	N/D	21	N/D	7.76	4.04	138.74
TNT	801.1	165.25	N/D	N/D	9	N/D	8.12	4.63	159.64
Comp B	833.3	49.85	N/D	58.02	N/D	0.45	14.48	25.58	33.60
C4	830.2	N/D	0.62	68.75	N/D	6.47	N/D	N/D	N/D

N/D = Not Detected (TAT, DANTs, HADNTs, Azoxys, TNX and DNT were also not detected.)

* Calculated based on the response factor of RP 1 which was determined from its conversion to TNT

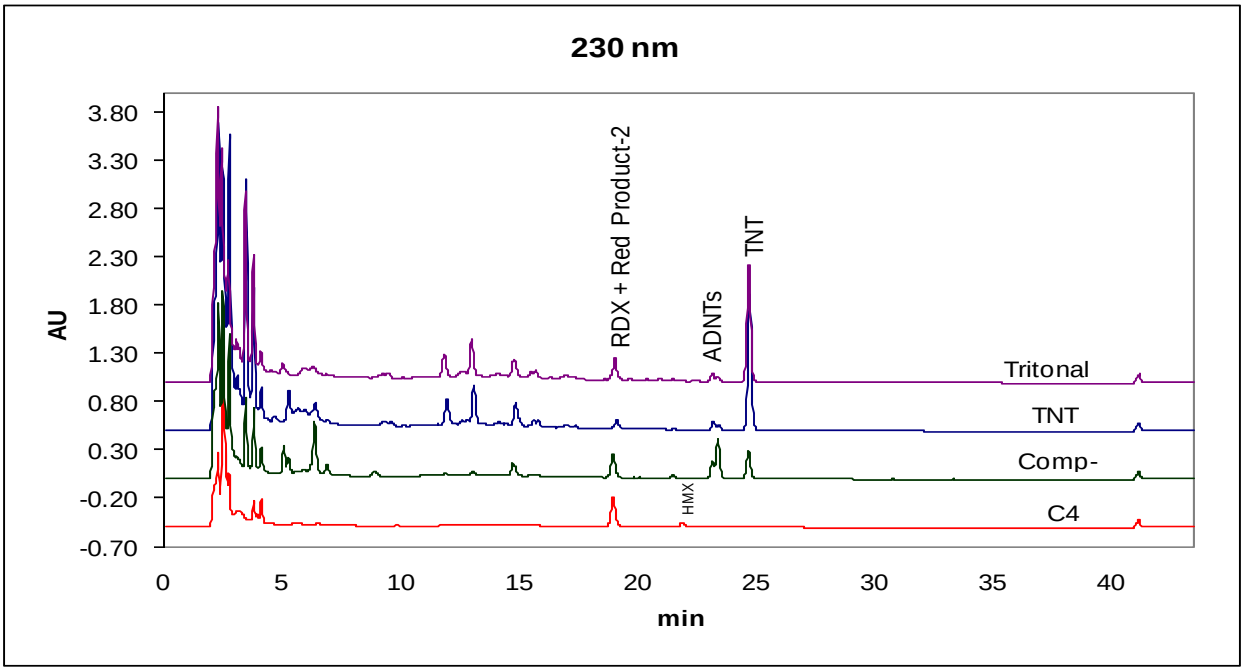

Figure 47. HPLC Profiles of weathered Tritonal, TNT, Comp B, and C4. ADNTs are the aminodinitrotoluenes.

Nitrate concentrations are also high in all samples. We analyzed for the nitrate and nitrite because these nitrogen-containing explosives could form these compounds when degraded. Although the Tritonal sample shows a large signal for nitrate (Figure 48), the consistent nitrate concentration in all samples suggests its origin may not be related to the explosives but to the transformation of nitrogen oxides in the air. Low concentrations of an unidentified red product (RP 2) and of amino-dinitrotoluenes (ADNTs) are also present in these samples. Although there was no HE-soil interaction the presence of ADNTs suggests the some microbial transformations occurred.

The Tritonal, TNT, and Comp B solutions were red in color, and we worked to characterize these components, especially the component labeled RP 2. Figure 46 shows that RDX co-elutes with RP 2 in the Comp B and C4 samples when monitored at 230 nm. We eliminated the RDX response by monitoring at 520 nm, the wavelength maxima for RP 2 (Figure 49). Although TNT is a component of Comp B, no RP 2 was observed in the TNT sample.

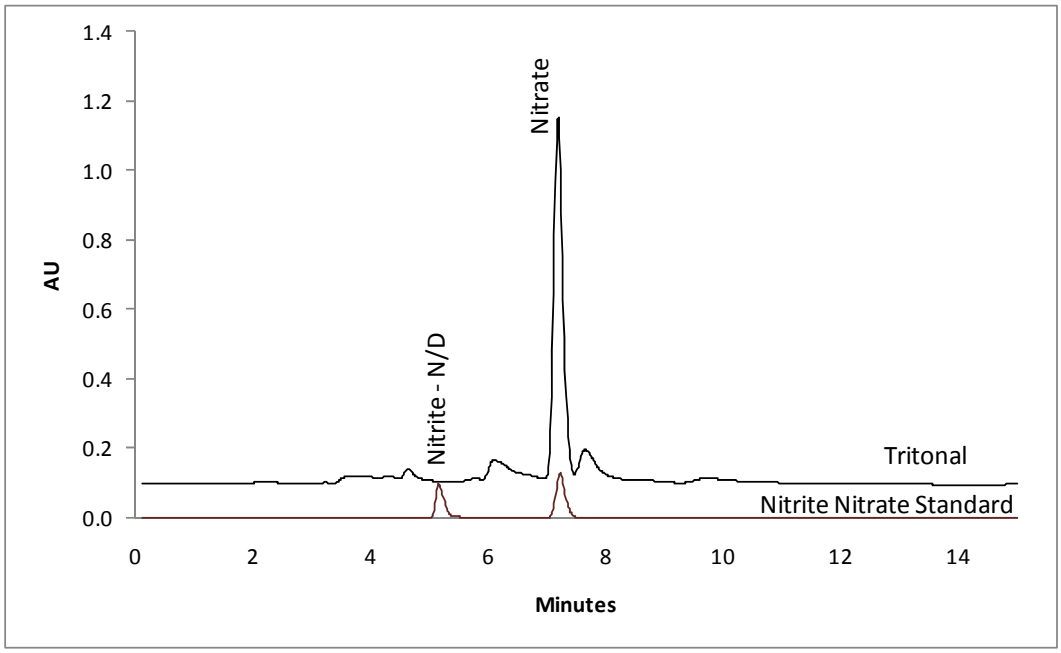

Figure 48. Overlay HPLC profile for a low-level and nitrate standard (bottom) and Tritonal sample (top).

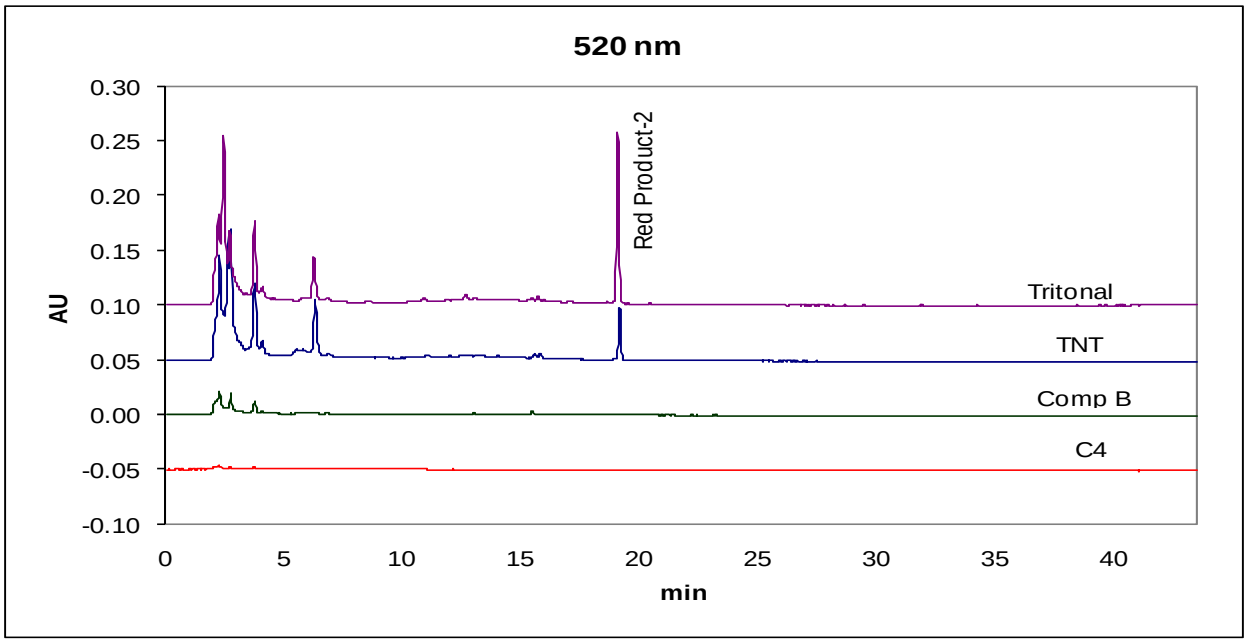

Figure 49. HPLC profiles for weathered Tritonal, TNT, Comp B, and C4 at 520 nm.

Although there were a great number of peaks, many of which eluted at the same location as known TNT metabolites, their UV spectra were not consistent with known degradation products. Those components in the

outdoor samples that could be confirmed by UV and quantified are shown in Table 9.

4.4.1 UV and LC/MS evaluation of CRREL Tritonal sample

The HPLC profile for the Tritonal sample appears in Figure 50, and the individual components are identified by a letter. The UV and mass spectral data for these components appear in Table 10. Although the majority of these components could not be identified, their spectral properties suggested multiple transformations and condensations of TNT derivatives.

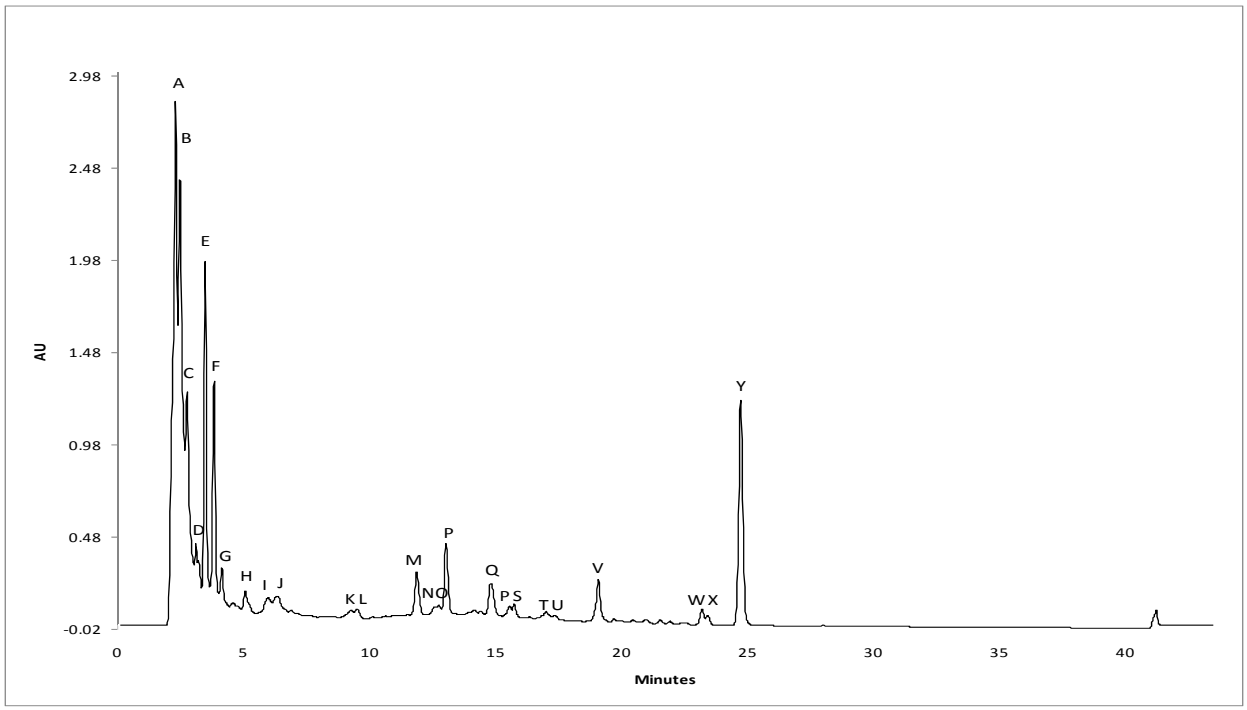

Figure 50. HPLC profile of CRREL Tritonal sample.

Table 10. UV and mass spectral data for lettered components shown in Figure 50.

Peak	UV Data (200-600 nm)	MS Data	Notes
A	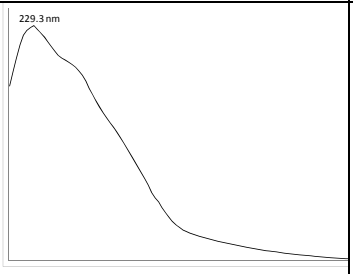		Contains nitrate, although UV data is not consistent with nitrate.
B	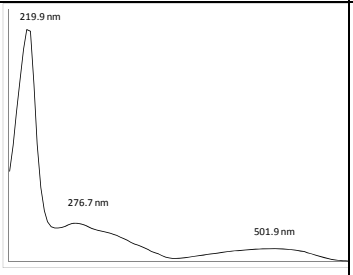		
C	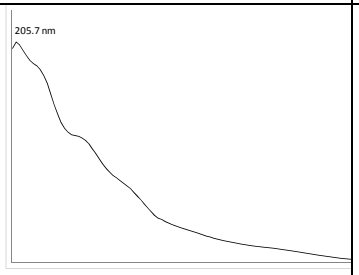		
D	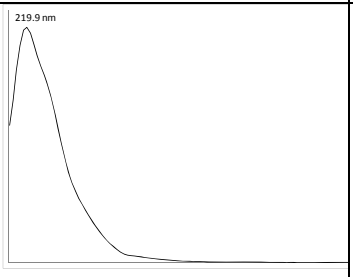		
E	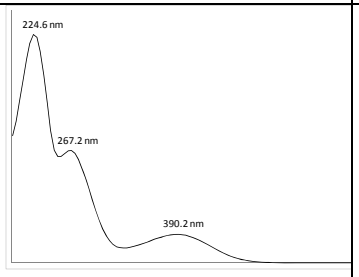	226 = M-1 182 = M-COOH 453 = 2M-1 MSMS on 453: 226, 182	2-amino-4,6-dinitro-benzoic acid Structure confirmed with an authentic standard. 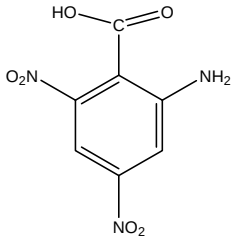

Peak	UV Data (200-600 nm)	MS Data	Notes
F	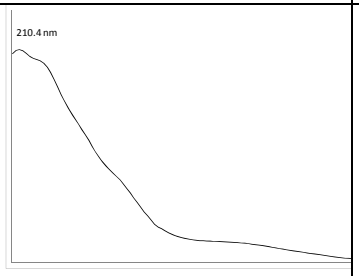	389 433 MSMS on 433 389 Small 344, 315, 257, 239	Possibly m/z = 434; C14H6N6O11 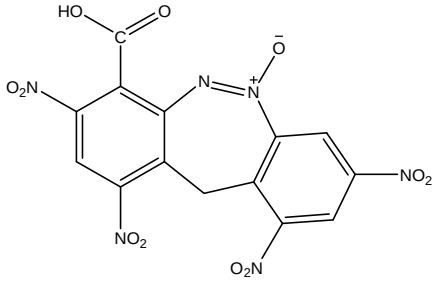
G	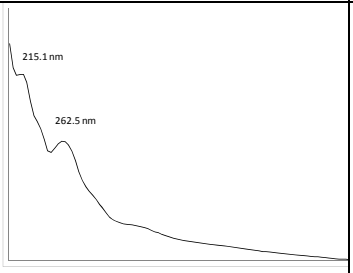		
H	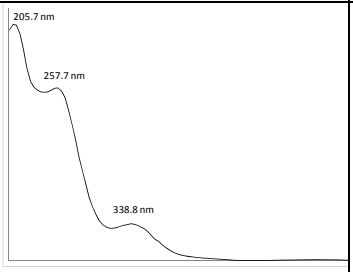		
I	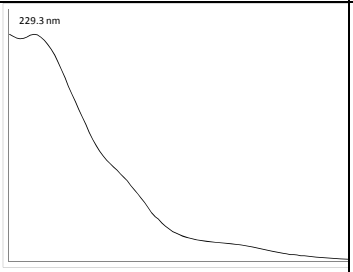		
J	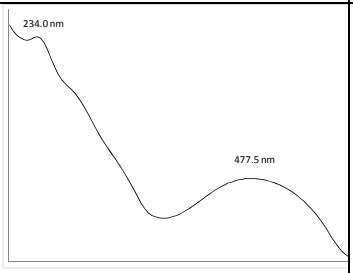		

Peak	UV Data (200-600 nm)	MS Data	Notes
K	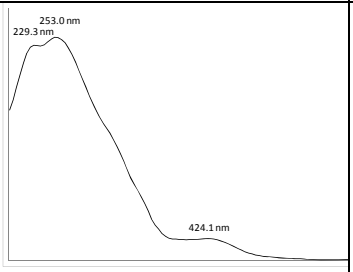		
L	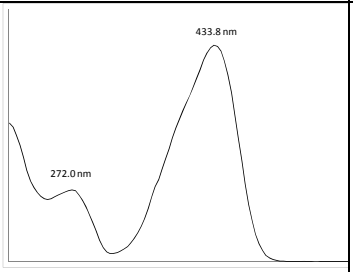	276, 182	
M	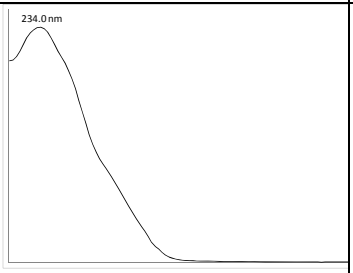	377 451 228 MSMS of 377 377, 301, 285, 257, 243, 226, 213, 198	
N	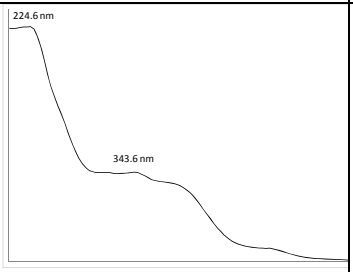		
O	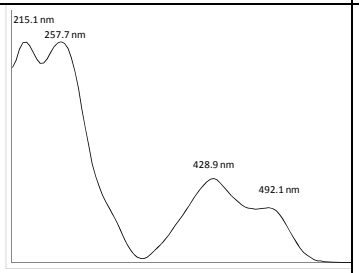		

Peak	UV Data (200-600 nm)	MS Data	Notes
P	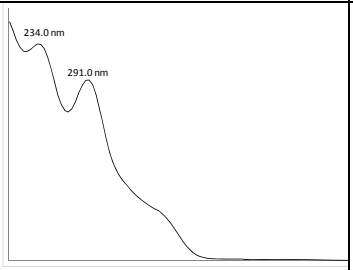	373 Small 391, 419, 435, 531 MSMS 373 373, 342, 315, 301, 296, 255, 224, 214, 191, 164, 134	Possibly m/z = 373; $C_{14}H_7N_5O_b$ 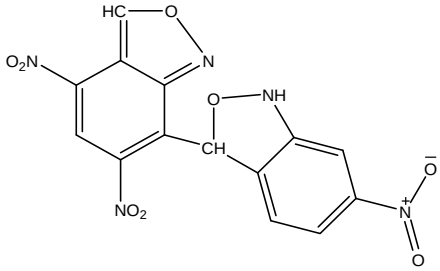
Q	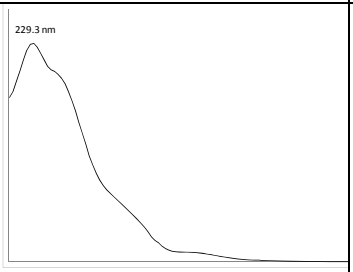	435, 391, 375, 549 MSMS of 465 391, 364,348, 344, 314, 397, 371, 242, 208, 182, 151. 182 is major peak	
R	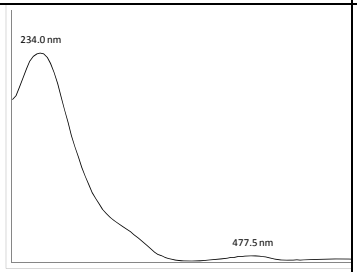	465 MSMS of 465 212 Small 374, 347, 299, 272	
S	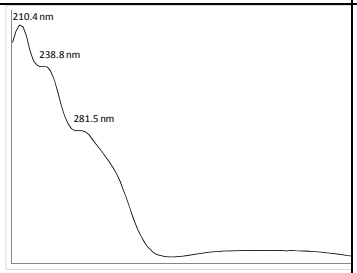	419 451 MSMS of 419 419, 401, 372, 358, 343, 327	Possibly m/z = 420; $C_{14}H_8N_6O_{10}$ 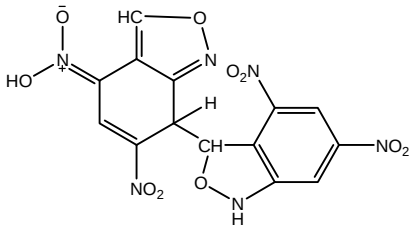
T	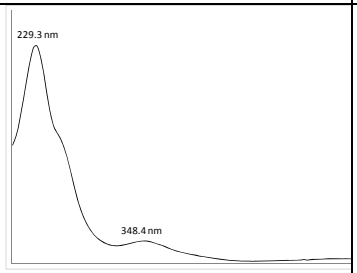		

Peak	UV Data (200-600 nm)	MS Data	Notes
U	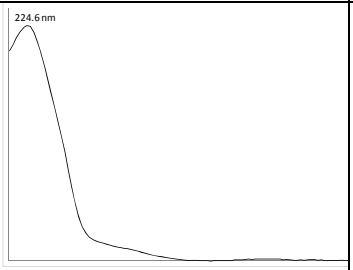		
V	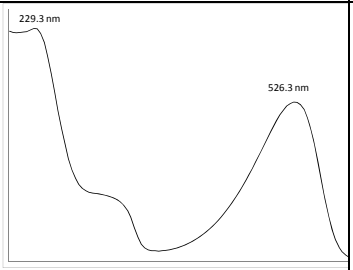	435, 404, 357, 226 MSMS of 435 226, 341	Red Product 2; m/z=436; $C_{14}H_7N_6O_{11}$ 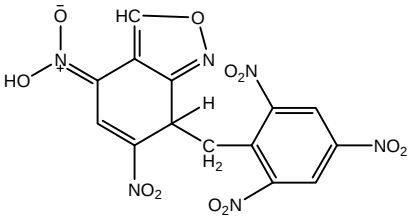
W	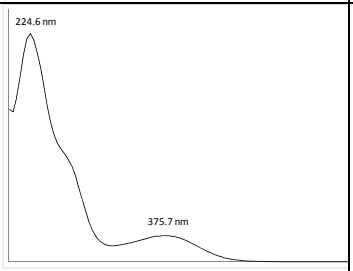	197 = M-1 242 = M+Formate(45) 439 = 2M+Formate(45)	2-amino-4,6-dinitrotoluene confirmed with authentic standard
X	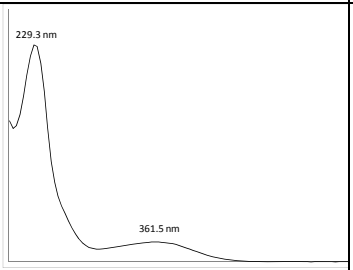	197 = M-1 242 = M+Formate(45) 439 = 2M+Formate(45)	4-amino-2,6-dinitrotoluene confirmed with authentic standard
Y	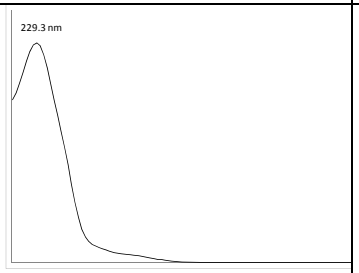	226 = M-1	2,4,6-trinitrotoluene confirmed with an authentic standard

4.4.2 Investigations into the formation of Red Product 2

As stated previously, TNT phototransformation studies in our laboratory using artificial and natural sunlight showed that in the initial photolysis of TNT, two red products (RP) are formed, identified as RP 1 and RP 2. These two products were separated by our HPLC conditions. TNT in aqueous solution and in 15% acetone solution (a triplet sensitizer that would enhance the reactions) were photolyzed under controlled laboratory light using a mercury lamp (~>310 nm) (Figure 51). The TNT-acetone solution showed little RP 1, but some RP 2. Some of the peaks observed in these photolyzed solutions were also present in the outdoor Tritonal sample we examined. A complex series of additional components were formed.

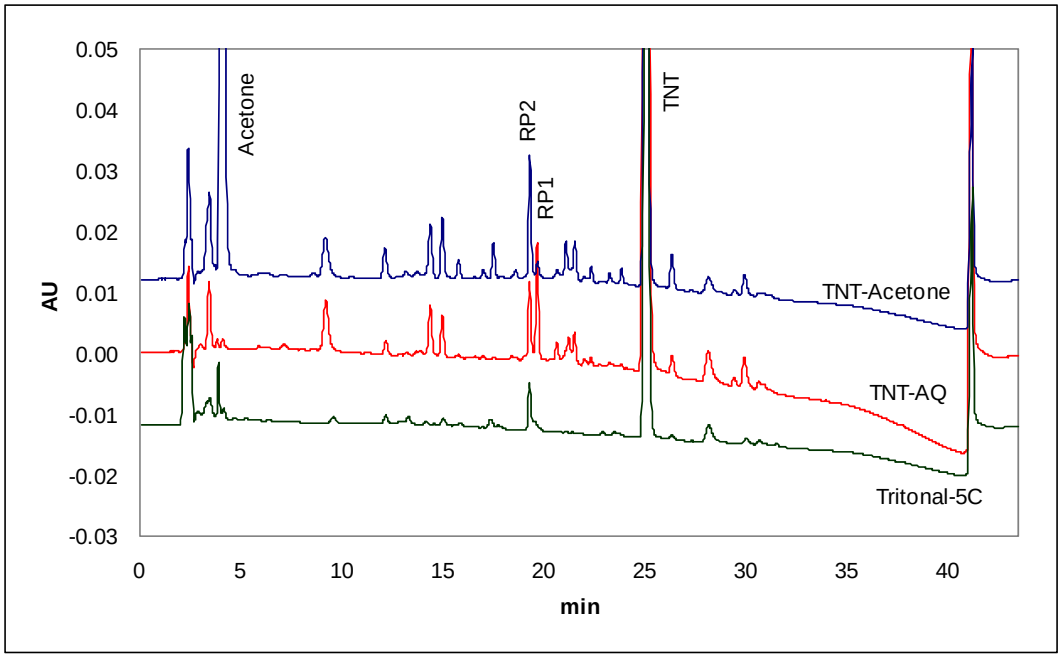

Figure 51. HPLC profiles of photolyzed TNT in 15% acetone solution (top), water solution (middle), and Tritonal from CRREL (bottom).

Figure 52 shows a linear plot of TNT loss and the formation of RP 1 and RP 2. RP 1 forms initially, builds to a steady state concentration, and RP 2 forms later. TNT appeared to decay as a zero order process indicating that light exposure, not concentration, controls the rate of reaction. There was little difference in the rates of TNT decay in water and acetone. UV spectra for RP 1 and RP 2 appear in Figure 53. Both compounds show long wavelength absorptions at 521 nm.

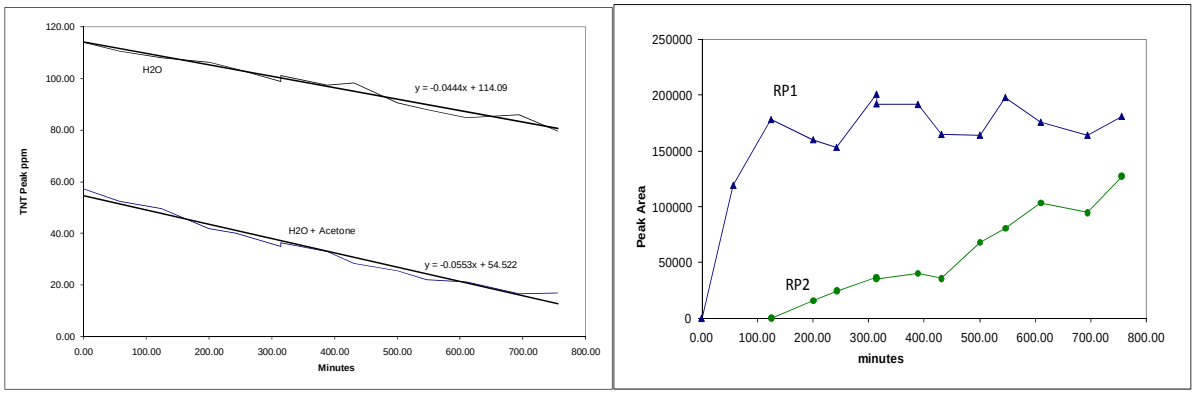

Figure 52. TNT decay plots (left) and RP 1 and RP 2 formation (right).

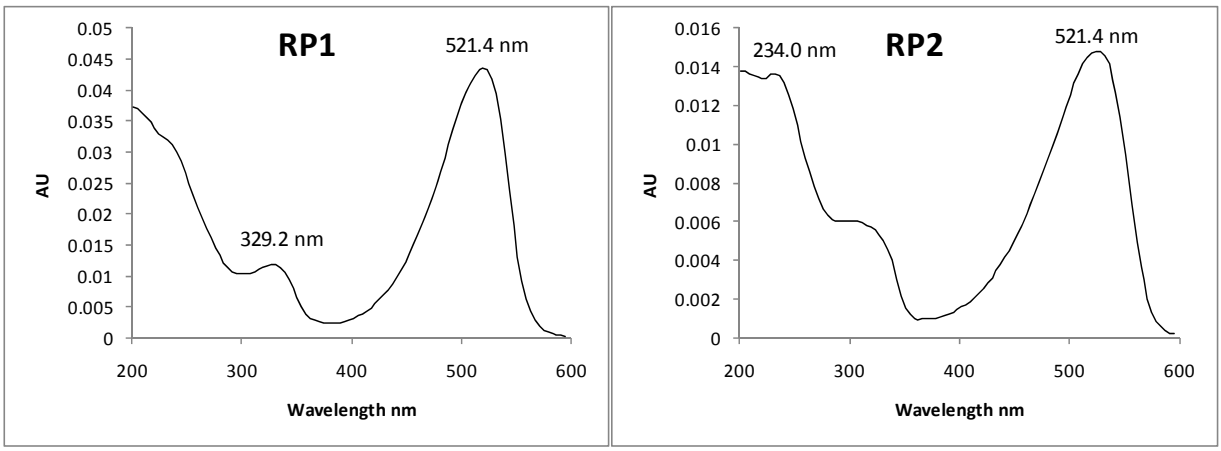

Figure 53. UV spectra of RP 1 (left) and RP 2 (right).

Because a large volume of TNT solution was needed to prepare enough RP 2 for identification, we made a solution and set it outside to phototransform. Rate differences in TNT loss were found to depend on the light intensity and the thickness of the glass vessels. A high dependence on light intensity is also consistent with the zero-order decay of TNT observed under laboratory conditions. The formations of RP 1 and RP 2 were similar in sunlight as compared to artificial light, as shown in Figure 54.

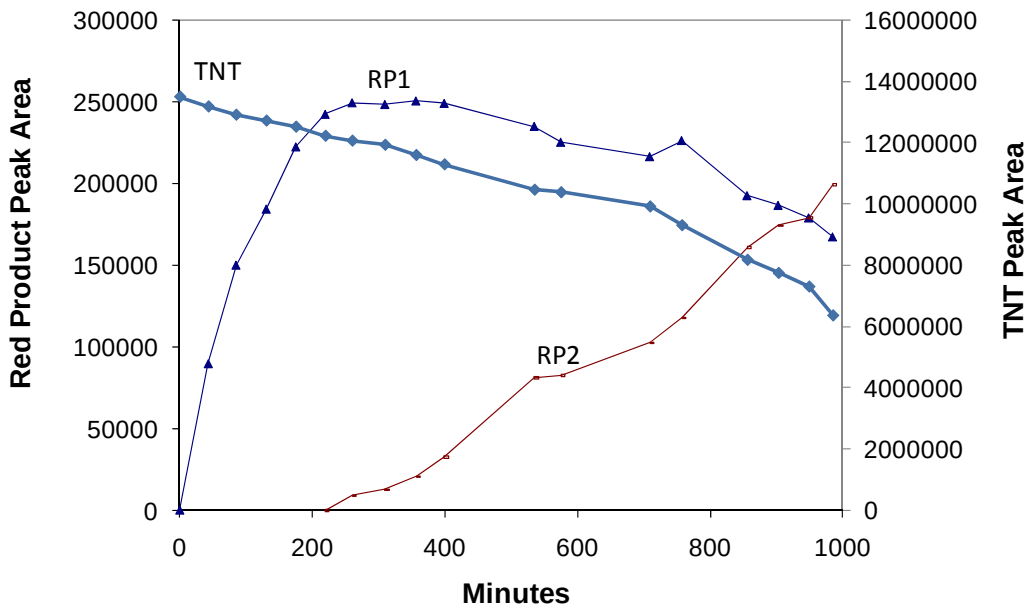

Figure 54. RP 1 and RP 2 formation on cloudy days.

4.4.3 Making Red Product 2

The component identified as RP 2 was isolated from a solid-phase extraction (SPE) column, lyophilized, and characterized by ^{1}H-NMR and mass spectrometry. To prepare RP 2, approximately 1 L of 130 ppm TNT solution was placed into 33 30-mL vials closed with Teflon caps. These vials were placed on the roof in direct sunlight for 6 hours. After exposure, the vials were combined and 0.65 gm of ammonium formate was added. The pH of the solution was adjusted to 8.5 using ammonium hydroxide. Adjusting the pH eliminated RP 1, which was found to degrade at elevated pH, while RP 2 was stable.

We activated a Phenomenex Strata C18-E 70g/150mL SPE column by flushing it with acetonitrile to remove air from the column bed. The column was then washed with 100% water to equilibrate it. Solvents were passed through the column by vacuum. Care was taken throughout the process to ensure the column did not dry out. The photolyzed TNT solution was then loaded onto the column and initially eluted with 100% water. Each observable band that came off the column was collected. RP 2 began to elute down the column slowly, and by the half-way point, band broadening was significant. Because there were no observable bands near RP 2, the eluent was changed to 10% acetonitrile. This increased the rate at which RP 2 traversed the column, however it still eluted from the

column in ~200mL of solution. Photographs of the columns at various stages, and the colors of the fractions collected are shown in Figure 55.

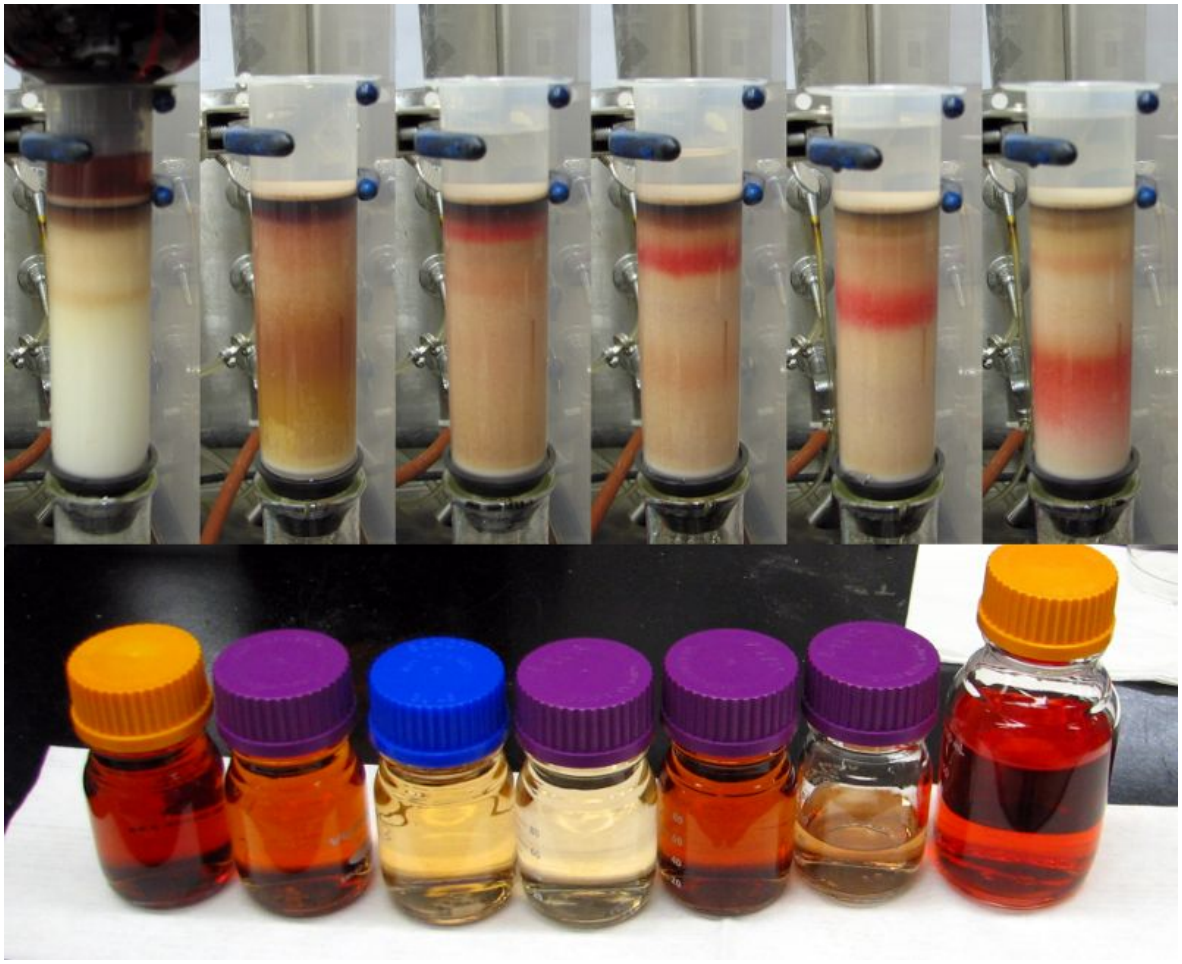

Fraction 1 2 3 4 5 6 7

Figure 55. Band formation and the fractions collected from the strata C18-E column. RP 2 appears in Fraction 7.

To concentrate RP 2, it was loaded into a clean Strata C18-E SPE column that had half of its packing removed in an earlier experiment. Once loaded, RP 2 was eluted with 60% acetonitrile and came off the column in ~20 mL into a 100 mL round-bottom flask. The elution into the round-bottom flask was done with positive pressure from the column opening, rather than with vacuum. The solution was frozen by placing the flask in a dry ice/acetone bath, and then placing it on a lyophilizer to freeze dry. This yielded a dry, low-density, red solid that was estimated to be about 5 mg (Figure 56) or about 4% of the TNT originally in the solution.

Figure 56. Red solid resulting from drying the RP 2 fraction.

4.4.4 Identifying Red Product 2 (RP 2)

The isolated fraction of RP 2 was analyzed by HPLC and determined to be 86% pure. LCMS data showed a 435 peak by the electrospray negative ionization mode, indicating a mass of 436, and a base peak of 226 (TNT). The mass spectrum is shown in Figure 57.

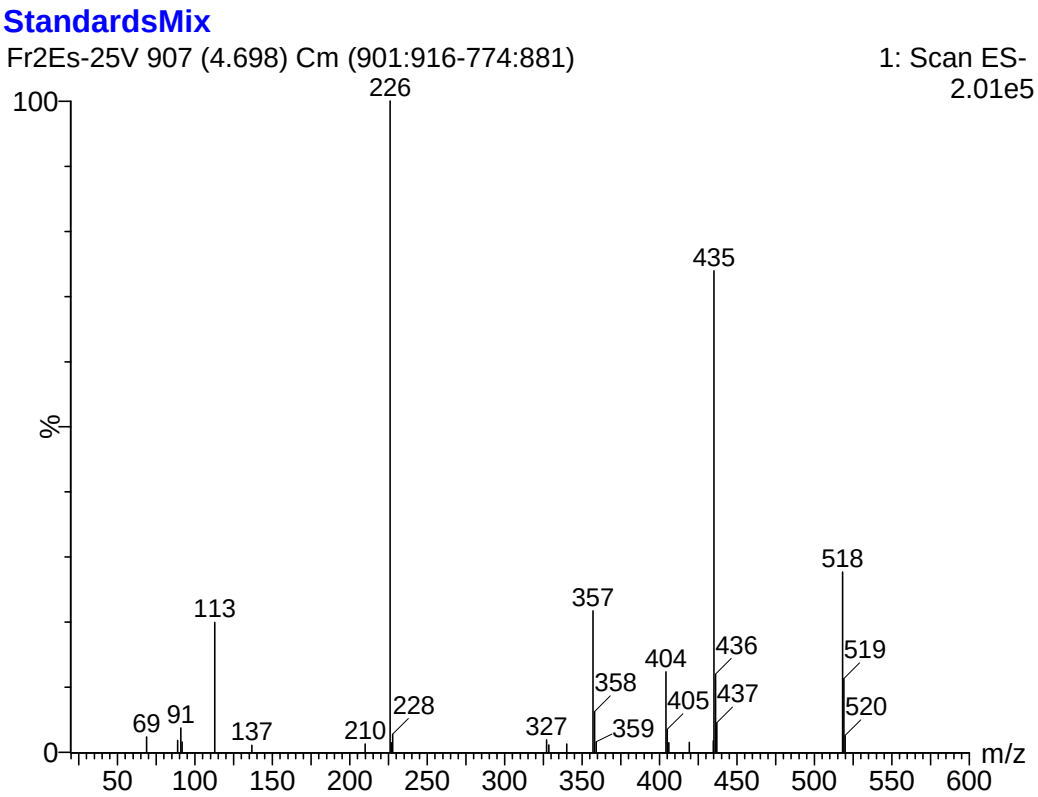

Figure 57. Mass spectrum of RP 2.

NMR analysis was performed using a Varian 300MH instrument with the sample dissolved in deuterated acetonitrile. The ^{1}H-NMR spectrum appears in Figure 58. From right to left, acetonitrile background signals resonated from 1.9–2.2 ppm. A small signal from the TNT methyl group impurity appears at 2.5 ppm.

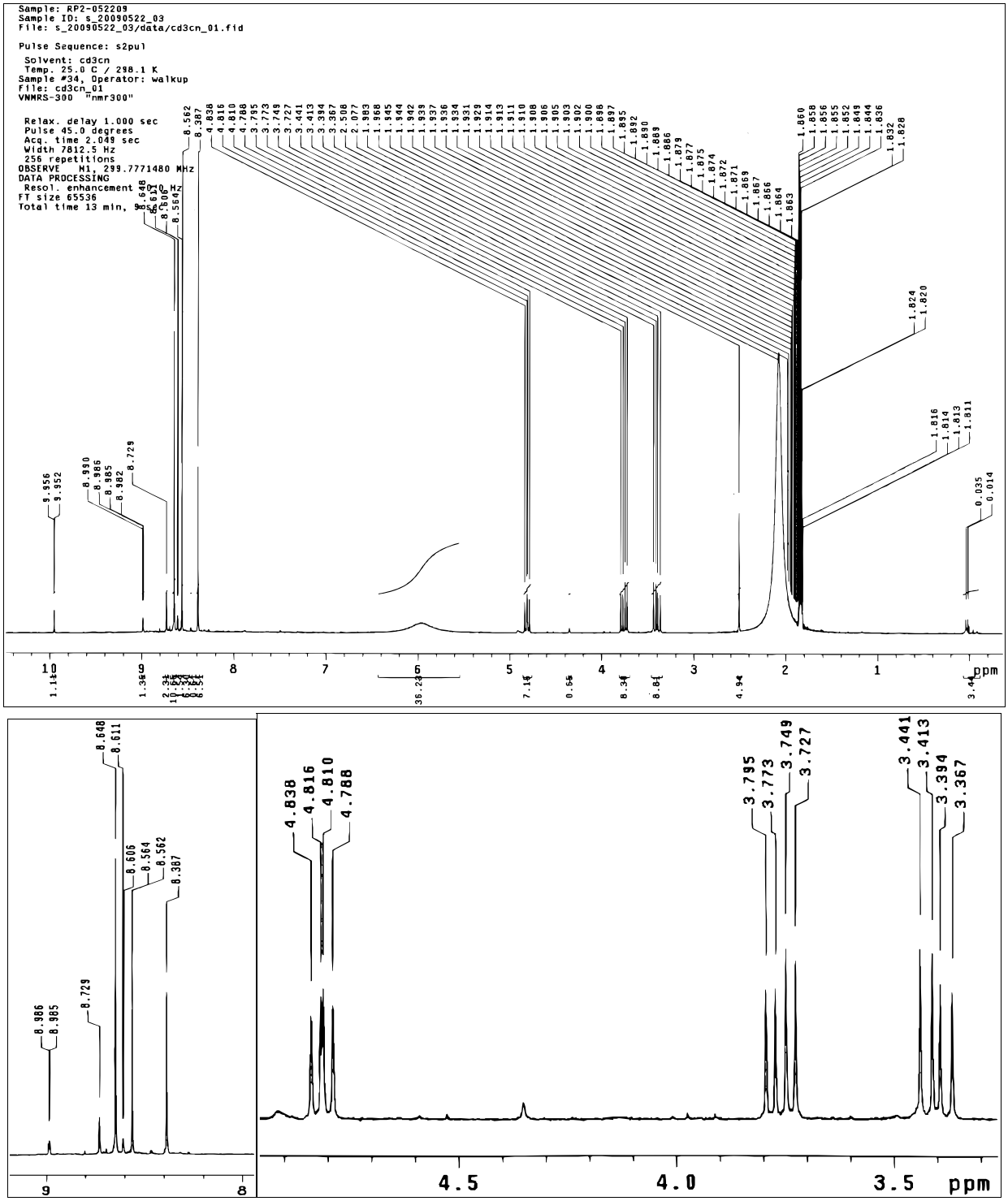

Figure 58. ^{1}H-NMR spectrum of RP 2 (top) and expanded scale (bottom).

RP 2 signals are shown in Table 11. Based on the nuclear magnetic resonance (NMR) results, a structure that is consistent with the mass spectrum (MS) and NMR results is shown in Figure 59. This product is mostly likely formed from a photochemically generated TNT anion attacking itself at the aromatic 3-position, followed by the loss of water between the methyl group and an ortho nitro group. Because RP 2 forms from RP 1, we wanted to prepare RP 1 to elucidate the transformation pathway.

Table 11. ^{1}H-NMR signals resulting from RP 2.

Resonance, PPM	Coupling	J Value	Assignment	Proton
3.367-3.442	Doublet of Doublets	J = 13.8, 8.4	Methylene C-H	a
3.727-3.3.795	Doublet of Doublets	J = 13.8, 8.4	Methylene C-H	b
4.785-4.838	Doublet of Doublets	J = 8.4	Ring Aliphatic	c
5.6-6.4	Broad singlet		Acid,HON-O	
8.387	Singlet		Anil H-C-O	d
8.564-8.562	Doublet	J = 0.6	Ring Alkene	e
8.648	Singlet		Aromatic C-H	f, f

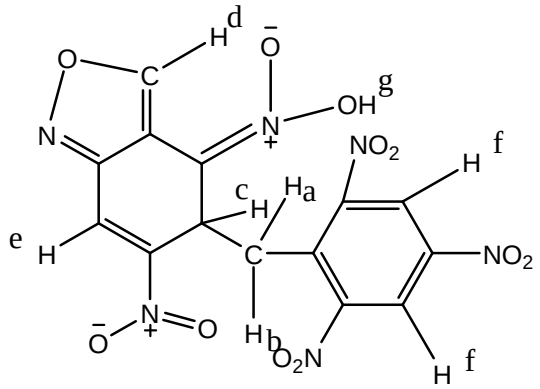

Figure 59. Structure for RP 2 that is consistent with mass spectrometer and nuclear magnetic resonance data.

4.4.5 Preparation of Red Product 1 (RP 1)

Around 600 mL of 65 ppm TNT was placed into 20 mL scintillation vials and exposed to overcast sunlight for 45 minutes. The shortened exposure time and intensity ensured only RP 1 would be produced. The samples were immediately loaded onto a Phenomenex Strata C18-E 70g/150mL SPE column that had been activated as described previously. RP 1 required 20% acetonitrile in water to move a broad red band down the column, eluting in ~100 mL. This volume was too large to be lyophilized, so the acetonitrile was rotary evaporated, and the sample was loaded onto a 6 mL

SPE column until saturated and then removed with 100% acetonitrile. This took several loading/removal steps as the column would only load ~10 mL before saturation. The sample was reduced to ~20 mL of mostly acetonitrile, frozen in an acetone/dry ice bath, and lyophilized to dryness.

We found that RP 1 rapidly degrades to TNT. We therefore set up elution conditions so that RP 1 elutes, while TNT is held on the column. Nevertheless, significant amounts of TNT were observed in the RP 1 eluant that was assayed 5 minutes after column elution. When TNT is present in a high ratio, the degradation appears to slow. This makes obtaining a pure sample of RP 1 difficult, and the resulting isolate contained significant amounts of TNT. HPLC analysis of the RP 1 solution showed that the solution was 29.99% RP 1 and 65.38% TNT by peak area. LCMS analysis yielded a mass-to-charge ratio (m/z) = 453 in the negative ion mode, indicating a mass of 454 (twice the mass of TNT, where m/z = 227). The mass spectrum is shown in Figure 60.

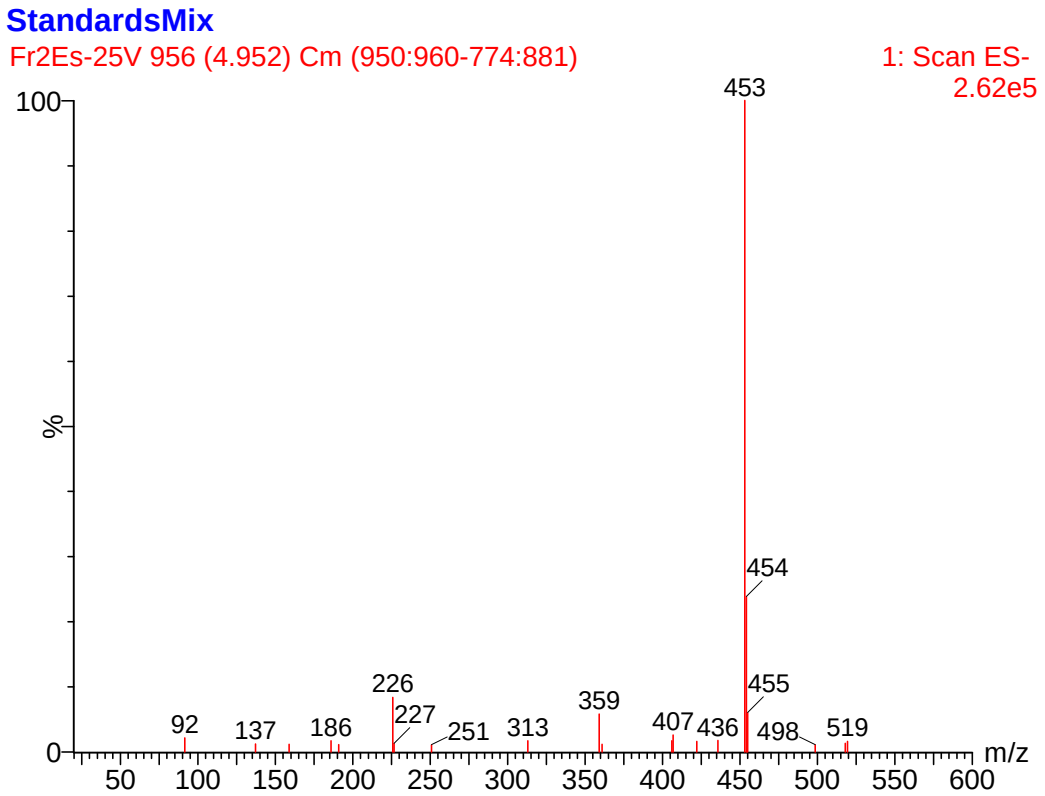

Figure 60. Mass spectrum of RP 1.

The ^{1}H-NMR spectrum for this mixture was obtained in d_6-acetone, and the spectrum appears in Figure 61. The TNT signals are readily eliminated, and the signals resulting from RP 1 are shown in Table 12.

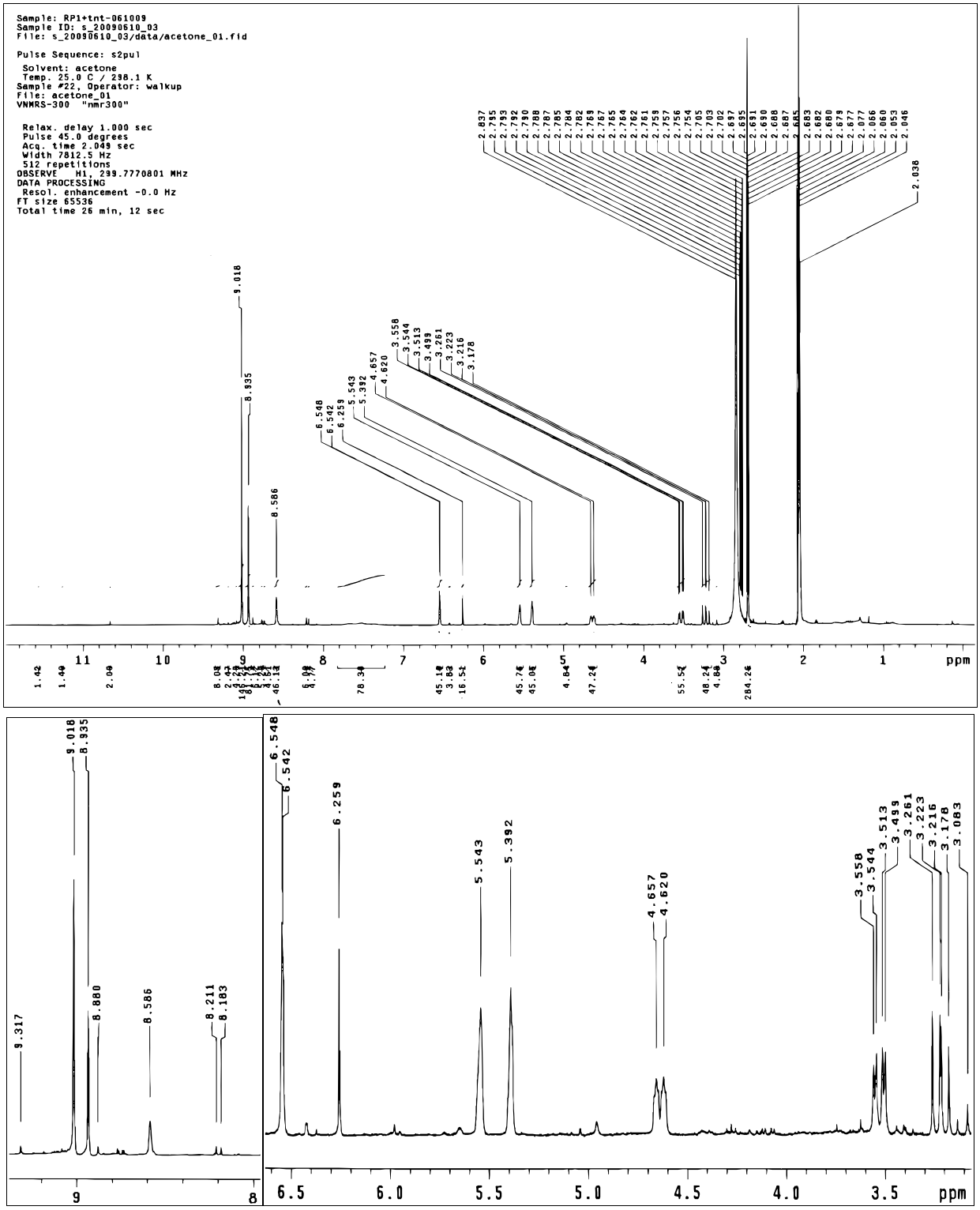

Figure 61. ^{1}H-NMR spectrum of RP 1/TNT mixture, the mass, and NMR data.

Table 12. 1H-NMR Signals Resulting from RP 1.

Resonance, PPM	Coupling	J Value	Assignment	Proton
3.178-3.261	Doublet of Doublets	J = 13.5, 11.4	Methylene C-H	a
3.727-3.3.795	Doublet of Doublets	J = 13.5, 4.2	Methylene C-H	b
4.657-4.620	Doublet of multiplets	J = 11.1, 3.0	Ring Aliphatic	c
5.543	Broad singlet		Methine	d
5.392	Broad Singlet		Methine	e
6.548-6.542	Doublet	J = 1.8	Alkene =C-H	f
8.586	Broad Singlet		HO-N-O	h
8.935	Singlet		Aromatic C-H	g, g

Based on this information, the structure in Figure 62 is consistent with the mass and the NMR data. Figure 62 also shows that proton c has an interactive coupling with protons a, b, and f, a finding quite different from that observed with proton c in RP 2. Based on the magnitude of the coupling constants, proton c is trans- to proton b, and cis- to proton a, suggesting there is little free rotation about the C-3 – methylene group (CH_aH_b) bond.

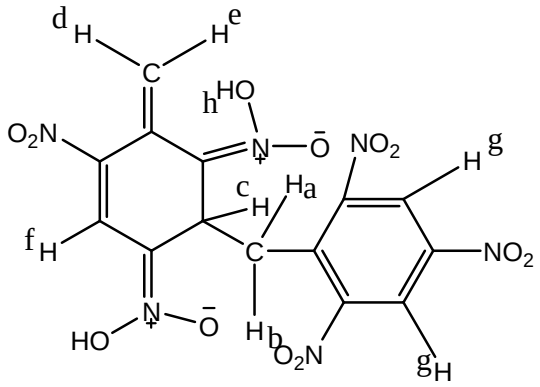

Figure 62. Possible structure for RP 1.

Thus, it appears that as the outdoor TNT chunks become damp, the surface TNT dissolves. The aci-form of TNT is generated photochemically from this TNT solution and a TNT molecule then condenses with itself to form RP 1, as shown in Figure 63. As noted in our isolation process, RP 1 is less stable than RP 2 and can be converted back to TNT. However, once formed, RP 1 can eliminate water to form RP 2 (Figure 64), which is very stable. It is RP 2 that we found in the CRREL Tritonal and TNT water samples.

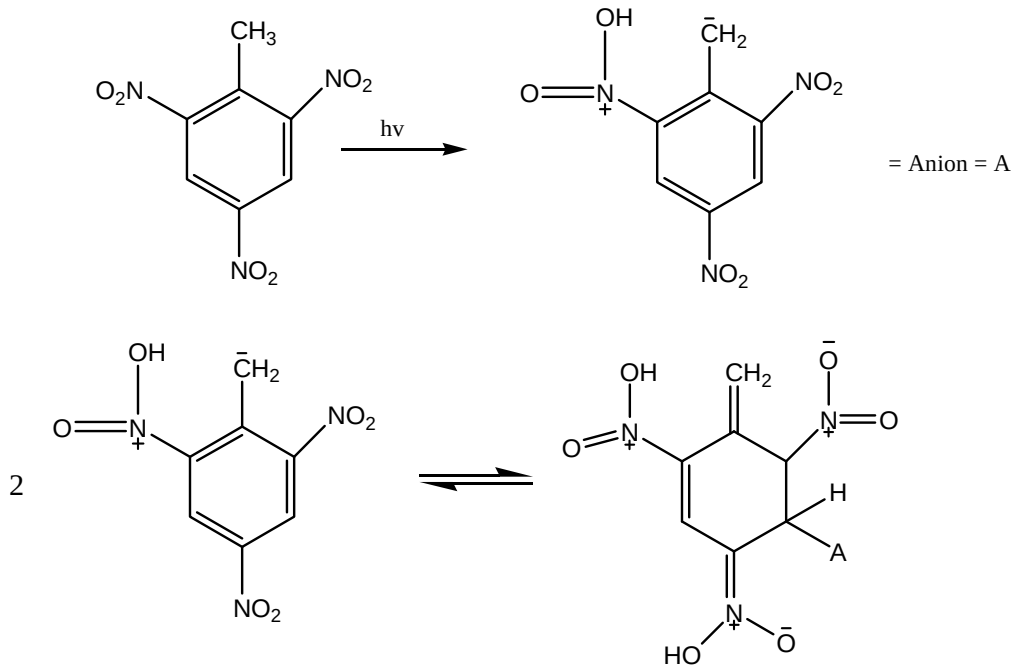

Figure 63. Photochemical formation of RP 1.

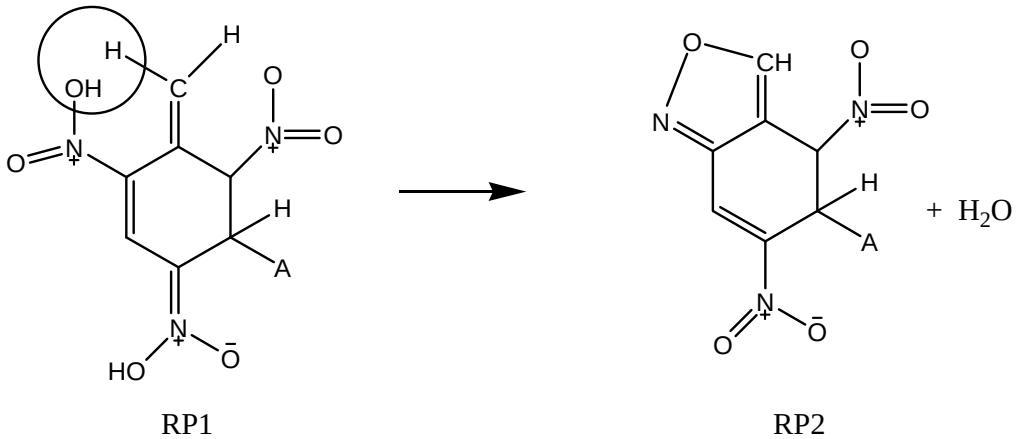

Figure 64. Formation of RP 2 from RP 1.

Formation of the TNT anion

For a TNT dimer consistent with RP 1 to form, we hypothesize that a TNT-anion is formed, which then attacks another TNT molecule to form RP 1. Since no peaks are seen by our chromatographic data that would be consistent with a TNT anion, its existence is either short-lived, or it is unstable under our HPLC conditions. Burlenson et al. (1979) described the formation of the anion form of TNT exposed to light. The anion can be

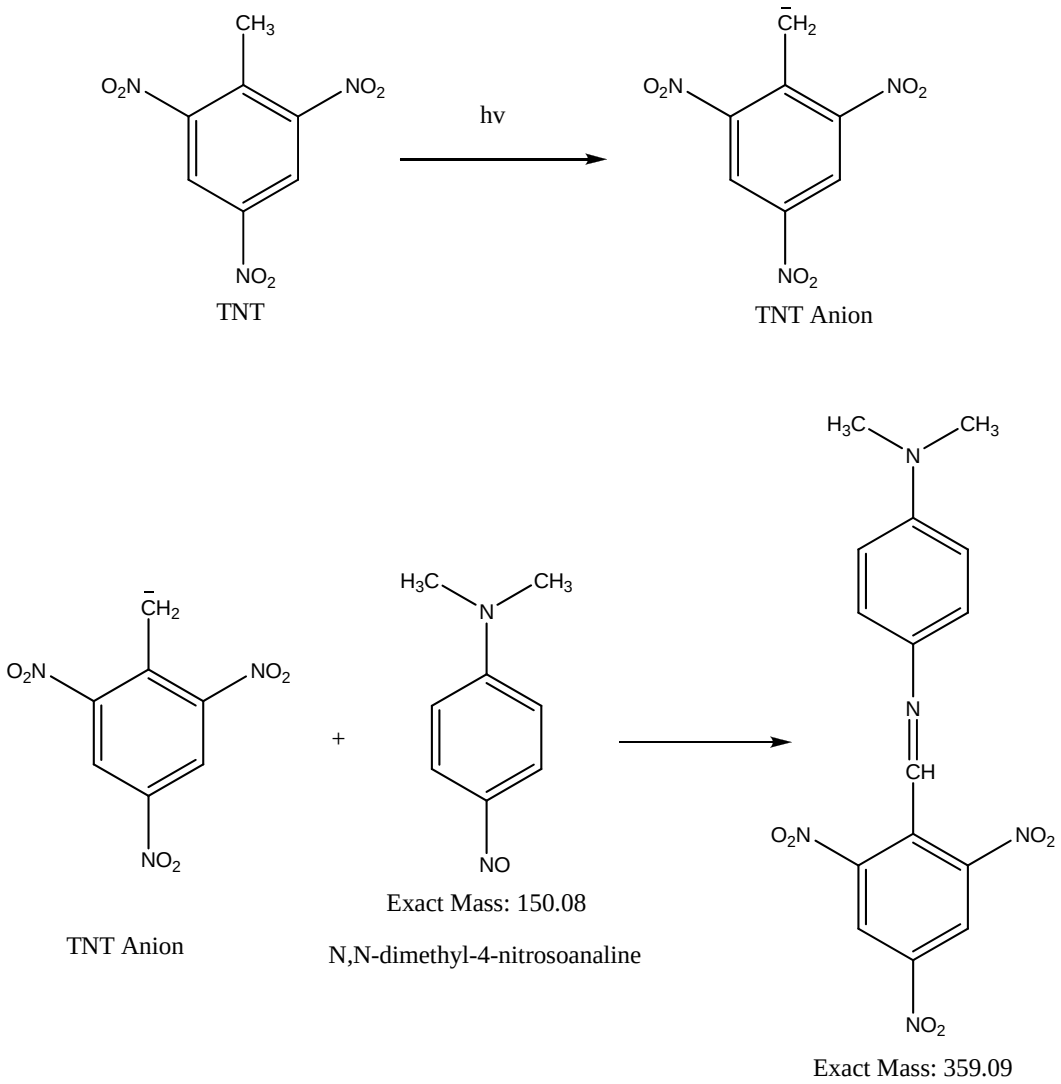

Figure 65. Analytical scheme used to capture the TNT anion.

identified by reaction with N, N-dimethyl-4-nitrosoanaline under aqueous conditions to form an adduct as shown in Figure 65.

A 4 mL aqueous solution of 458 µM TNT and 4.59 mm N, N-dimethyl-4-nitrosoanaline was exposed to daylight for 45 minutes. A dark precipitate was observed to form. The sample was filtered through a 0.45 µm nylon filter membrane, removing the precipitate. Then 4 mL of acetonitrile was passed through the filter slowly to dissolve the precipitate. The aqueous filtrate and the acetonitrile-filtered solution were analyzed by HPLC and LCMS. Figure 66 shows a chromatographic profile of the two filtrates.

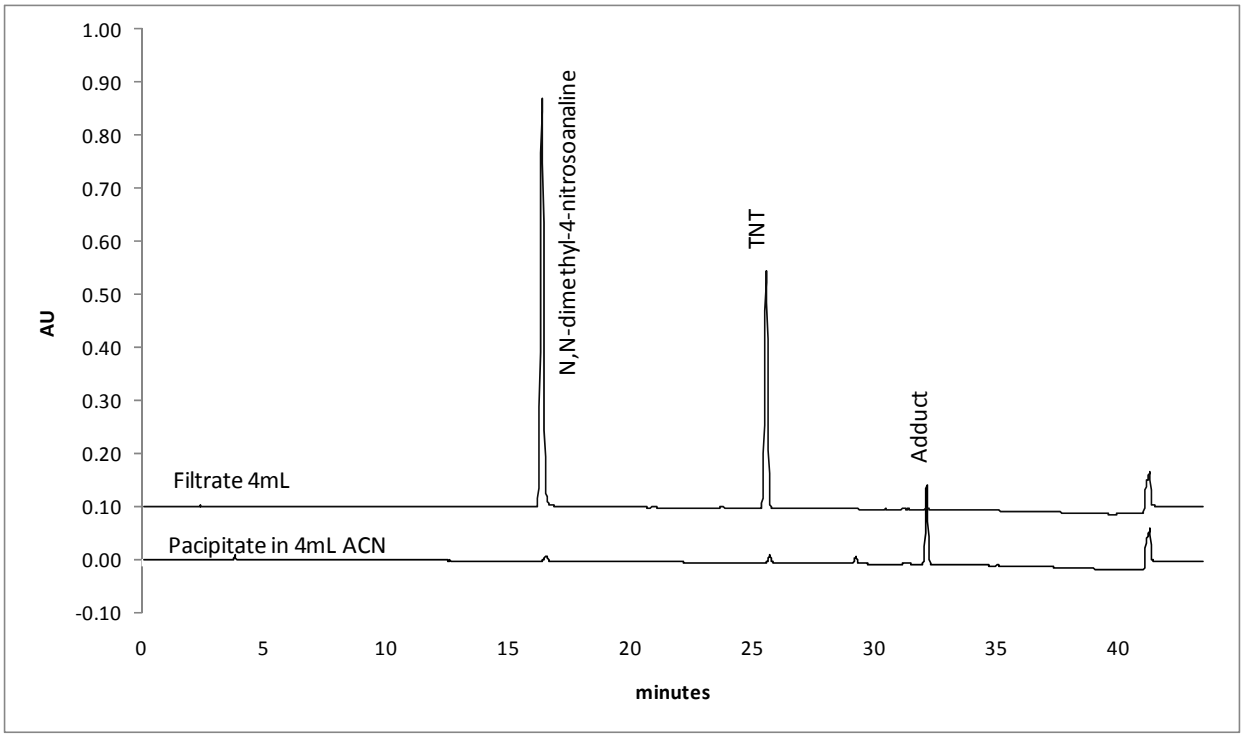

Figure 66. HPLC profile of the aqueous filter (top) and the dissolved precipitate (bottom).

The HPLC data showed that the precipitate had a UV maximum at 521.4 nm and that the initial aniline reagent had a maximum at 443.5 nm. LCMS was performed on the samples, and under the positive ionization mode, the aniline-derivative starting material gave a m/z = 151 (M+1) ion. The adduct peak gave a m/z = 360 (M+1) which is consistent with the TNT-aniline adduct as described in the literature. Thus, the TNT anion can be generated in aqueous solution, confirming the potential to form the RP 1 and RP 2 adducts through an anionic mechanism.

Other unknowns from light studies

During the purification of RP 2, additional bands were collected off the column. Many of these were not sufficient purity for ^{1}H-NMR analyses. Band 5 was brown and did not produce a good chromatograph. Band 10 was dark brown, and came off the SPE column at the solvent front with a 60% acetonitrile wash to remove TNT from the column. Both showed broad peaks that did not produce good chromatographs by our HPLC or UPLC/MS methods. These bands appear similar to some of the broad baseline disturbances seen in samples from CRREL but are observable, being concentrated ~10x from the starting solutions. These peaks may account for a significant amount of the mass balance, but are easily missed, or interpreted as many smaller, co-eluting peaks as shown in

Figure 67. Neither band yielded interpretable mass spectral data in either the positive or negative mode.

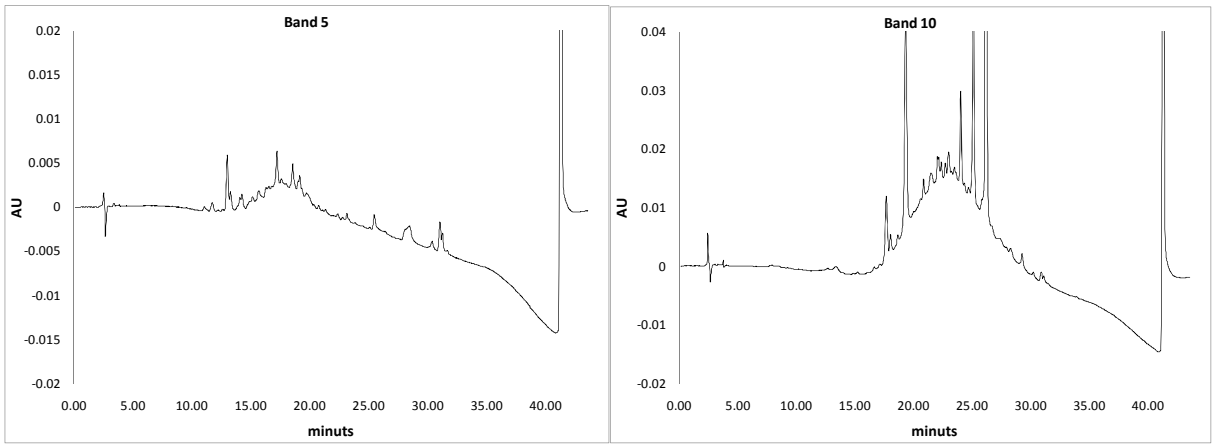

Figure 67. Chromatographic profiles of selected bands obtained from the SPE column.

4.5 Conclusions

The results of this investigation showed that exposure of TNT and TNT-containing explosives to outdoor conditions can produce an extremely complex mixture of components including highly polar, condensed TNT derivatives. Previous studies dealt mainly with those products extractable with benzene. In this study, condensations of the TNT anion resulted in polar products highly acidic in nature, leading to increased water solubility. The majority of mass appeared to chromatographically elute near the pre-solvent peak (dead volume), where we identified 2-amino-4,6-dinitrobenzoic acid. Although the red products we identified can be separated chromatographically, they are subject to further condensations, potentially leading to trimers and tetramers of high polarity because of the poly-acid nature of functional groups. We would expect these transformations to occur on a TNT surface exposed to water and light. We recommend additional studies using an evaporative, light-scattering detector (ELSD) for a better mass assessment, using derivatization techniques to improve chromatography and the isolation of other major components for spectral evaluations.

5 Laboratory Crushing Tests

We used a Materials Testing System (MTS) machine to crush both weathered and un-weathered pieces of TNT, Tritonal and Comp B. The chunks were photographed before and after crushing, and we weighed the individual fragments produced by the tests to obtain a size distribution for the fragments. We compared the crushing strength and the size distribution of the unweathered "control" chunks to pieces of TNT, Tritonal, and Comp B that were crushed after being outside for 14 months (May 2006–July 2007) and for 36 months (May 2006–May 2009). The outdoor samples that were crushed 14 months into this project were returned to their funnels. Changes in the dissolved masses from these three samples allowed us to model the effect of particle size on dissolution rate.

5.1 Experimental setup

The MTS is a closed-loop, electro-hydraulic, uni-axial testing system (Figure 68). The system can be programmed to move the piston at a specified rate to a given height. We attached a 90 kg (200-lb) load cell and controlled the system with a 0.5-inch full-scale displacement transducer. We programmed the piston to move 1 mm at 10 mm per second into the explosive piece. Because particle shapes affect the load at which pieces break, we tried to test chunks of similar size and shape but were limited to the samples on hand.

Figure 68. CRREL's Material Testing System (MTS) used to crush explosive particles.

5.2 Results

5.2.1 Crushing tests

We crushed six TNT chunks in the MTS machine. Four of those (TNT 12–15) acted as weathering "control" samples as they were not placed outside. TNT 5 was crushed on 11 July 2007, after being outdoors for 14 months and TNT 9 was tested in May 2009 after 36 months of outdoor exposure as part of our dissolution tests (Chapter 3). The TNT chunks had initial masses that ranged between 0.52–0.96 g (Table 13). Peak forces measured for these chunks averaged 7.5±3.0 lbs. Each chunk broke into around 7±1 fragments plus dust. Photos of the control chunks before and after crushing, along with the force versus displacement plots, are shown in Appendix B (Figures B1–B5).

Table 13. Data on explosive chunks crushed in the laboratory. Particles labeled in red were part of our outdoor tests.

Sample ID	Mass (g)	Peak force (lbs)	Resulting# pieces	Mass of largest piece (g)
TNT 12	0.5223	8	7	0.4021
TNT 13	0.9588	7	7	0.5473
TNT 14	0.6585	8	7	0.1421
TNT 15	0.5168	3	10	0.2134
TNT#5 (2007)	0.6004	8	6	0.3217
TNT #9 (2009)	0.6292	12	7	0.2947
Comp B 13	0.386	21	13	0.1123
Comp B 14	0.1752	4	5	0.0495
Comp B 15	0.276	6	12	0.073
Comp B 16	0.3787	24	11	0.1066
Comp B 17	0.3911	24	18	0.0659
Comp B #11 (2007)	0.3377	15	7	0.1761
Comp B #1 (2009)	0.6532	20	12	0.2906
Trit 6	2.1265	54	13	1.0672
Trit 7	1.6854	29	17	0.7141
Trit 8	1.0186	26	16	0.5142
Trit 9	0.7221	13	10	0.3454
Trit #5 (2007)	2.0592	110	28	1.1485
Trit #1 (2009)	2.7694	76	3	0.8987

Seven chunks of Comp B were crushed, five of these controls (Comp B 13 to 17). Comp B 11 and Comp B 1 were outdoors for 14 and 36 months, respectively. Initial masses for the Comp B chunks ranged from 0.18 to 0.65g (Table 13). Peak forces measuring during the test were 15.9 ± 8.0 lb. The average number of fragments generated was 11 ± 4. In Section 4A, Figures A6–A 11 show the before and after crushing photos and the force versus displacement plots for the Comp B chunks.

Six Tritonal chunks were crushed; of these, four (Tritonal 6 to 9) were control samples and two (Trit 5 and 1) outdoor chunks were crushed after 14 and 36 months, respectively. The Tritonal chunks were larger than the TNT or Comp B samples and ranged from 0.72 to 2.77g (Table 13). Peak forces measured for these samples were variable and ranged between 13 and 110 lbs (Table 13). The average number of fragments produced was 14

± 8. Photos of the control chunks and the force versus displacement plots are shown in Appendix B.

Average failure peak loads increase from TNT (7.5 ± 3.0 lb), to Comp B (15.9 ± 8.0 lb) to Tritonal (54 ± 27 lb) suggesting that the formulations with two components, Comp B, and Tritonal may be stronger than the single-component TNT. However, peak loads also were positively correlated with the mass of the initial chunk, $R^2 = 0.77$. Therefore, we think it more likely that the higher values measured for Tritonal resulted because they were bigger pieces.

Compared with the control pieces, failure loads of HE chunks exposed outside appear to be higher for TNT 9 (36 months) and possibly for Tritonal 1 and Tritonal 5. The Comp B samples are within the range seen for the unweathered pieces. We initially thought the chunks might become less competent with time, but our data indicate that the pieces do not become weaker.

5.2.2 Piece size distribution

We weighed all the particles generated by the crushing tests to obtain a daughter particle size distribution for each chunk. Figure 69, Figure 70, and Figure 71 show these results plotted as the cumulative probability versus the fragment size. Masses of the daughter particles follow similar, power law distributions with the largest fragments being approximately half the mass of the original chunk (also see Table 13). The fits of these power laws to the data were generally good, with an $R^2 = 0.9$ or higher. The data points for the Comp B and TNT fragments were more dispersed than those for the Tritonal chunks.

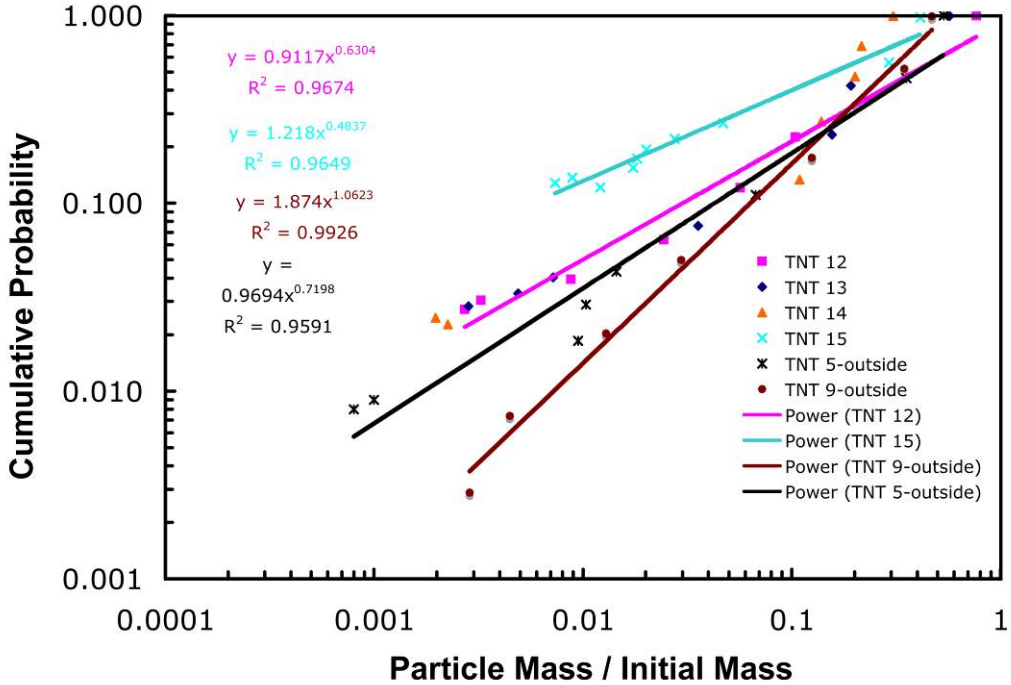

Figure 69. Plot of fragment masses from TNT chunks crushed in the MTS machine. Note that all six chunks broke into fragments that can be described by a power law distribution. The best-fits for four of the particles are shown.

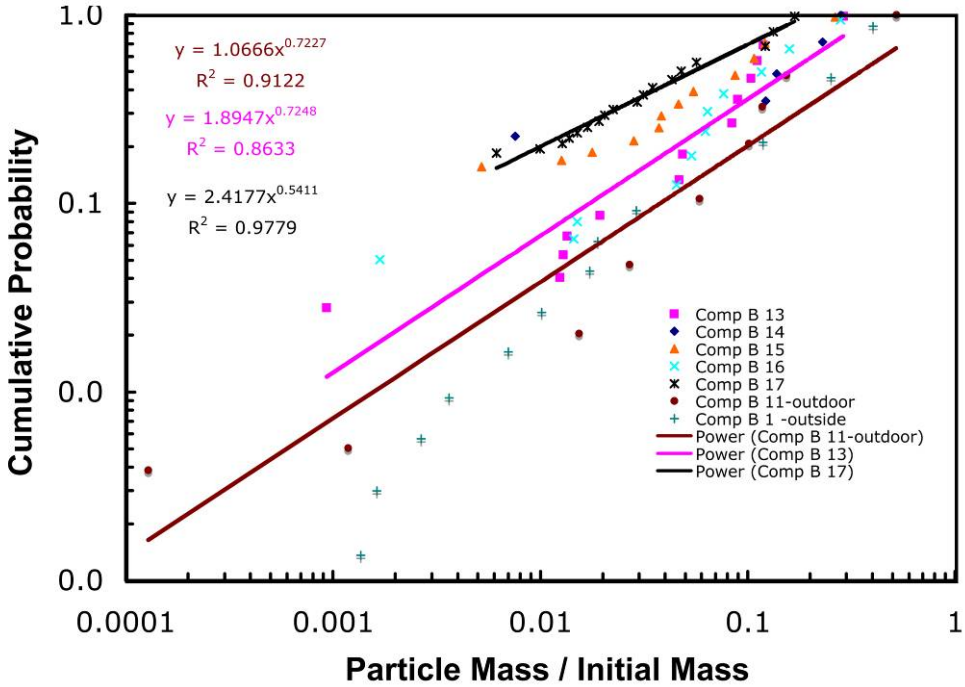

Figure 70. Plot of fragment masses from Comp B chunks crushed in the MTS machine. Note that all seven chunks broke into fragments that can be described by a power law distribution. The best-fits for three of the chunks are shown in the figure.

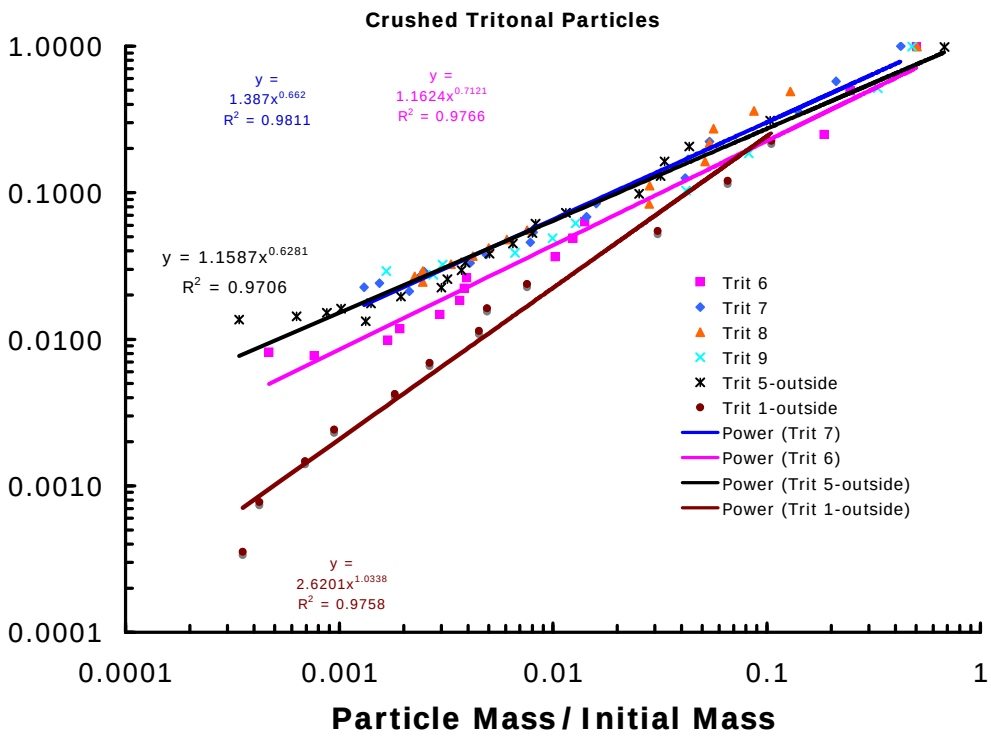

Figure 71. Plot of fragment masses from Tritonal chunks crushed in the MTS machine. Note that all six chunks broke into fragments that can be described by a power law distribution. The best-fits for four of the chunks are shown in the figure.

We had two reasons for weighing the fragments that resulted from the crushing tests. First we returned the samples crushed in July 2007 to their outside funnels and continued measuring their dissolution. The resulting data allowed us to test our model's to predict increased dissolution from the disaggregated chunks. Second, previous studies of the particle size distributions of residues deposited by low-order detonations also were best described by power-law distributions (Taylor et al. 2004b, 2006). We wondered if explosives fractured in a predictable way allowing us to estimate the particle size distribution deposited by a LO detonation by finding the largest chunk. No other means are available to obtain or estimate this variable, and the sizes of the HE particles may control the flux of dissolved HE into the soil.

5.2.3 Appearance of crushed samples

Figure 72 shows photographs of TNT 5, Tritonal 5 and Comp B 11 before and after crushing in July 2007 and at the end of the dissolution tests in May 2009. TNT 5 broke into two comparable size 100 mg pieces, a 10 mg piece, four >1 mg pieces, and 4.8 mg of dust. In May 2009, only the two 100 mg pieces remained; they weighed 14% less than in 2007.

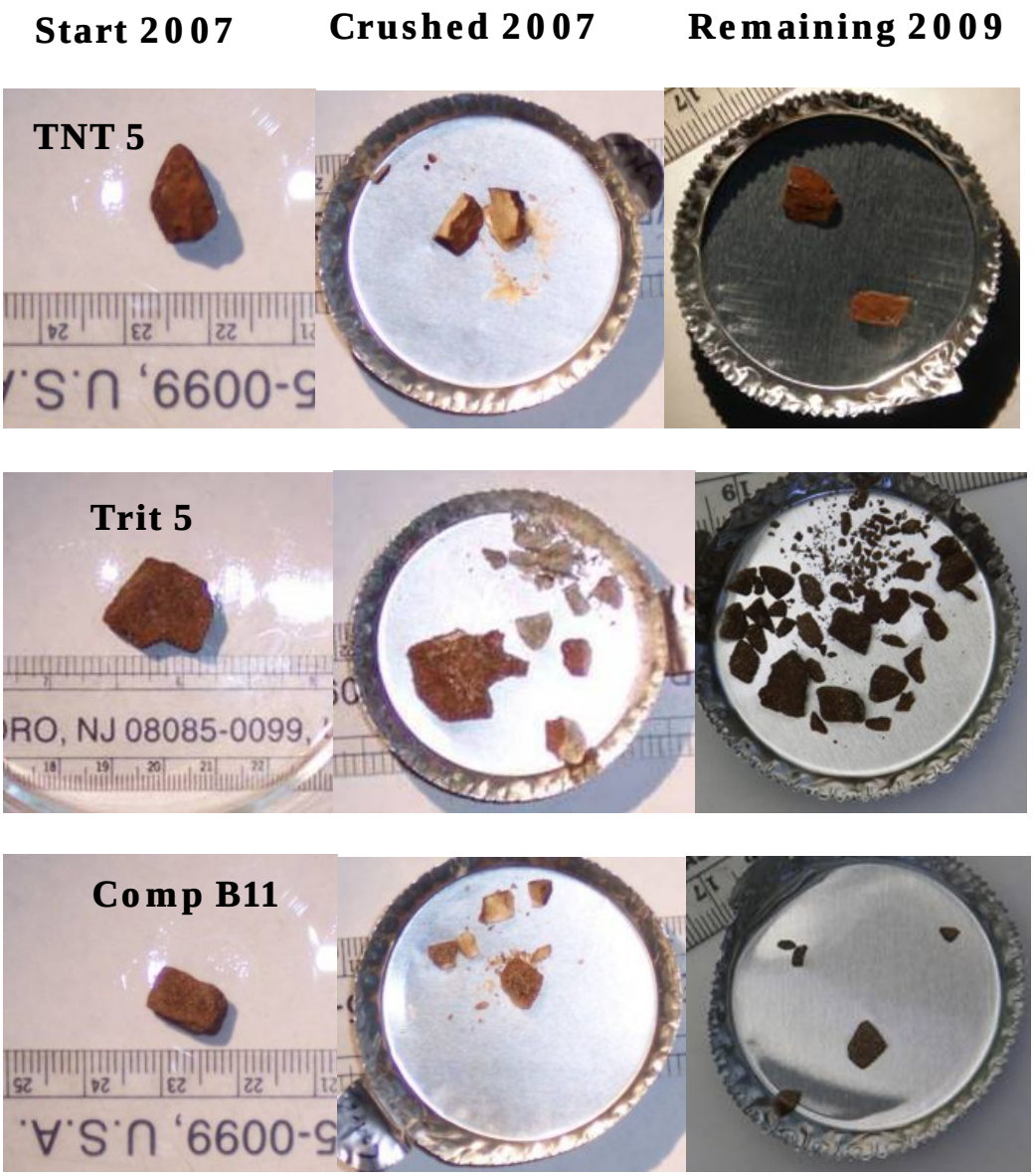

Figure 72. Appearance of TNT 5, Trit 5, and Comp B11 before (left) and after crushing (center) in July 2007 and in May 2009 (right).

Tritonal 5 broke into 1 piece >1 g, 1 100-mg piece, 9 pieces that weighed over 10 mg, 10 pieces that weighed between 1–10 mg, and 27 mg of dust. In May 2009, there were 3 100-mg pieces, 17 pieces >10-mg, 9 pieces weighing 1–10 mg, ~60 particles 0.1–1 mg, and 14 mg of dust. Clearly, the large fragment broke to form at least two of the 100 mg fragments and other fragments must also have split, because there are more particles in May 2009 than in July 2007, a total of 34 particles compared with 21 earlier.

Comp B 11 broke into the following distribution of particles: 1 >100 mg, 4 >10 mg, 2 >1 mg, 1 >0.1 mg, and 1.3 mg of dust. In May 2009, only 5 pieces remained: 1 >100mg, 2 >10 mg, and 2 >1 mg. The masses for all these samples are listed in a Table B-1 in Appendix B. Also listed are the masses of the fragments produced during the May 2009 crushing tests (Table B-2) and photos of the particles before and after crushing.

5.2.4 Outdoor dissolution

After crushing TNT 5, Tritonal 5, and Comp B 11 in July 2007 (day 436 of the test) and returning the particles to their outdoor funnels, we observed two expected effects. The first was an increase in the amount of HE dissolved for these samples; the second was an increase in the TNT dissolution relative to that of RDX for the Comp B chunk. Figure 73 shows the mass loss versus time record for these chunks. One can clearly see a large increase in HE mass loss in the dissolution time-series for all the crushed samples compared to TNT 7, which was not crushed. After crushing the TNT/RDX ratio for Comp B 11 also jumps noticeably (Figure 74). This ratio approaches its initial value, ~3, reflecting a large increase in newly exposed TNT surface area.

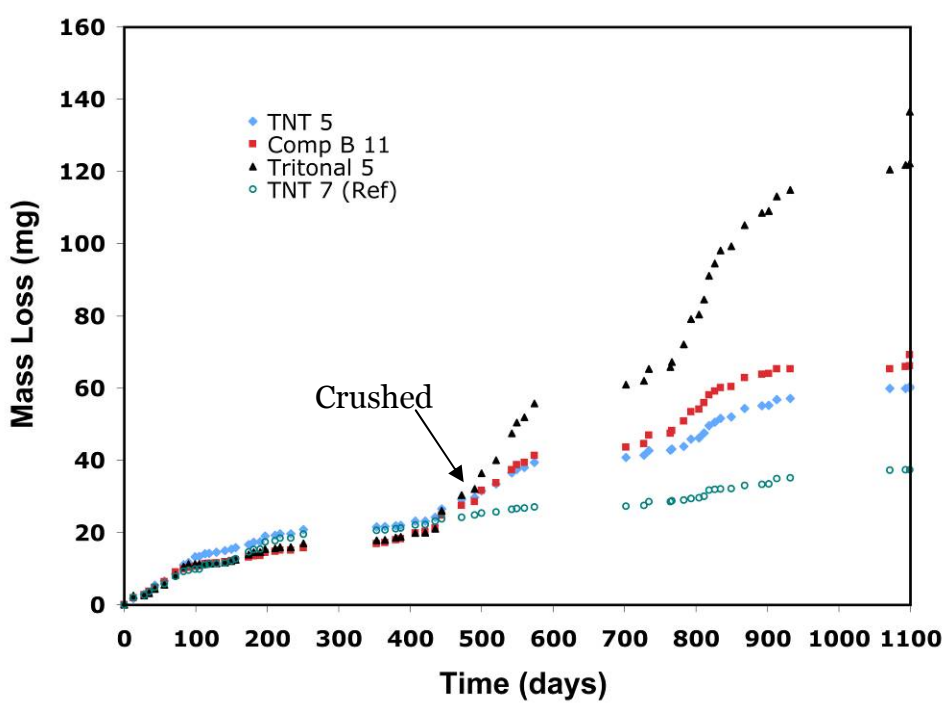

Figure 73. Cumulative HE mass loss as a function of time for the three chunks crushed in July 2007, namely TNT 5, Trit 5, and Comp B 11. TNT 7 was not crushed, and is shown as an example of what the mass loss curves might have looked like had the chunks not been broken.

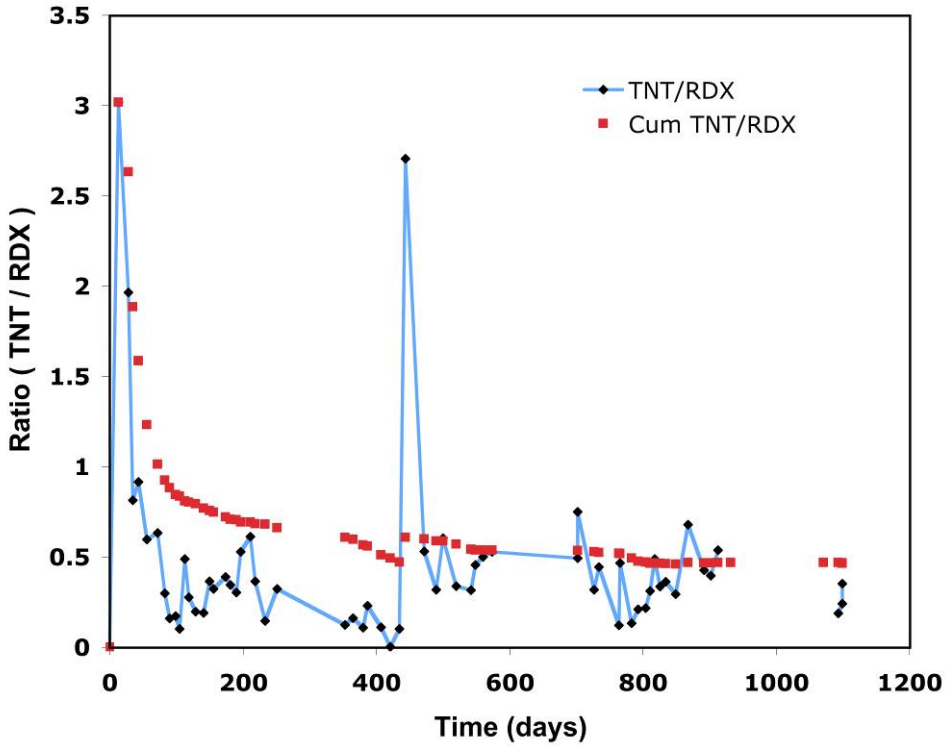

Figure 74. Change in the TNT to RDX ratio for Comp B 11. Note the large increase in TNT immediately after the particle was crushed.

We used the measured size distributions of TNT 5 and Tritonal 5 as input to continue modeling their dissolution after they were crushed (Chapter 3). The drop-impingement model is able to predict the dissolution of a split chunk extremely well, given the size distribution of the daughter particles. However, what happens if the size distribution of the daughter particles is not known? Four of our outdoor samples split naturally during the three-year experiment. TNT 3, for example, shed a millimeter-size piece in July 2007, broken apart into one large chunk and multiple millimeter-size pieces in Sept 2007, and shed several more millimeter-size pieces in May 2008. A visual record of how this particle changed over the three-year test is shown in Figure 75. Although the size distribution of the daughter particles was not measured, we were able to fit the cumulative mass curves by increasing the area factor from 2.6 to 3.5. High area factors, therefore, indicate particle splitting.

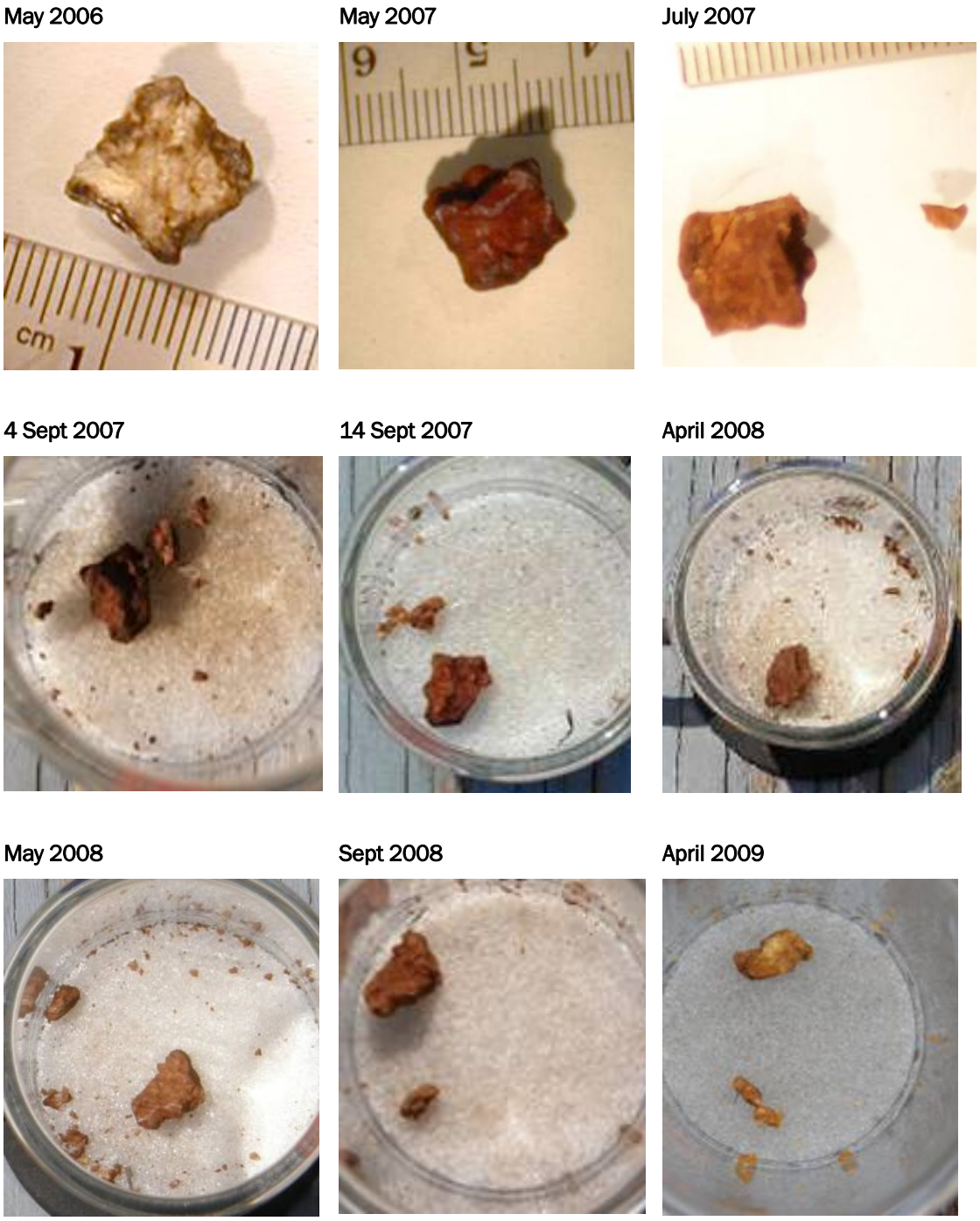

Figure 75. Changes in the appearance of one chunk of TNT 3 over the course of the experiment. This chunk was not crushed, but split naturally.

5.3 Discussion

The geometry and size of the HE chunk appeared to control the crushing strength of these pieces. For example, flat pieces tended to fail at higher loads than irregularly shaped chunks because bumps on the surface

focused the load. Consequently, the data from the crushing tests provided only an estimate of the force needed to break these HE materials. Nevertheless, the needed forces were generally small, ~10 to 20 lb.

HE chunks on training ranges likely experience some jostling from wind, vehicle and animal traffic, and from nearby detonations if the range is active. The role of such mechanical agitation on splitting of HE chunks is essentially unknown and could be an important factor governing the dissolution of HE. Observations during our three-year test indicated that natural splitting from weathering is relatively common. Both processes significantly increased HE surface area and thus, dissolution rates.

The piece size distribution resulting from the crushed HE chunks showed a power-law distribution. If explosives systematically break in this way, we can at least constrain the shape of population distributions on training ranges. However, to reliably estimate the total HE influx on a range will require a better understanding of splitting rates caused by weathering or mechanical agitation.

6 Outdoor Friability of HE Chunks

To ensure long-term use of military training lands, we need to understand the accumulation and persistence of energetic compounds deposited from live-fire training. Several studies have shown that HE detonations of mortar and artillery projectiles normally leave very little energetic residue in the impact area (Hewitt et al. 2005; Walsh 2007). Occasionally, a malfunction will produce either unexploded or partially (LO) detonated ordnance that scatters pieces of the projectile body and chunks of the HE filler up to tens of meters from the impact point. As part of our work, we documented the appearance and persistence of Tritonal and Comp B residues deposited at two live-fire training range over several years.

We monitored Tritonal chunks at Holloman AFB along with Comp B and C4 chunks at ERF. These two ranges experience very different climatic conditions, and they were chose so that we could understand the effect of moisture on the long-term integrity of HE chunks. Holloman is an arid region that receives less than 30 cm of rainfall a year and has over 280 days of sunshine. Eagle River Flats, on the other hand, is an impact area in an estuarine salt marsh on Cook Inlet, Alaska. ERF is periodically inundated by tides and is ice-covered from November until April each year. During these weather cycles, it experiences drying and wetting cycles and freeze-thaw cycles.

6.1 Methods

6.1.1 Holloman Air Force Base, New Mexico

In May 2005, we collected 12 Tritonal chunks, deposited from the LO detonation of a 500-lb bomb. After weighing and photographing the pieces, we set them in a non-trafficked site near where they had been collected. Upon our return in December 2005, the pieces had been disturbed and only 10 were found (Figure 76). Based on the weights of the recovered pieces, we first matched them to the original pieces, then weighed and photographed them again before placing them in a nearby but more protected location (flat area on a hillside protected by three concrete blocks). In May 2006, the Tritonal chunks were where we had left them. The site was not visited again until March 2009, at which time we were not able to find any of the pieces.

Figure 76. Tritonal chunks in May 2005 (left) and May 2006 (right). Note in the May 2006 photo that the soil in contact with the chunks is also red.

6.1.2 Pond 155 at Eagle River Flats, Alaska

At the ERF site, we set out HE chunks of known weight at a location with monitoring instrumentation (Figure 77). We selected five Comp B chunks from a LO detonation (LO 5), a piece of C4 whose history is not known from Demolition Site 3, and 11 pieces of C4 from a demolition block. We set them out in Pond 155 where there was a tripod for mounting instruments, a data logger, a water depth sensor, and a web camera (http://www.crrel.usace.army.mil/erf/webcamera/). To this, we added a water-temperature sensor, a water-flow meter, and a dedicated camera. The water flow, depth, and temperature measurements were made every 15 minutes and downloaded via satellite every morning. The camera photographed the particles every 90 minutes, recording 16 photos daily; these were downloaded manually every other month. The camera was attached to one of the tripod legs directly over the explosive pieces. This placement had advantages and disadvantages. The advantages were that the explosive pieces and the camera were somewhat protected from birds and wolves. The disadvantage was that the tripod might have protected the particle from some rainfall. We collected one season's data (May–October 2007) from this site.

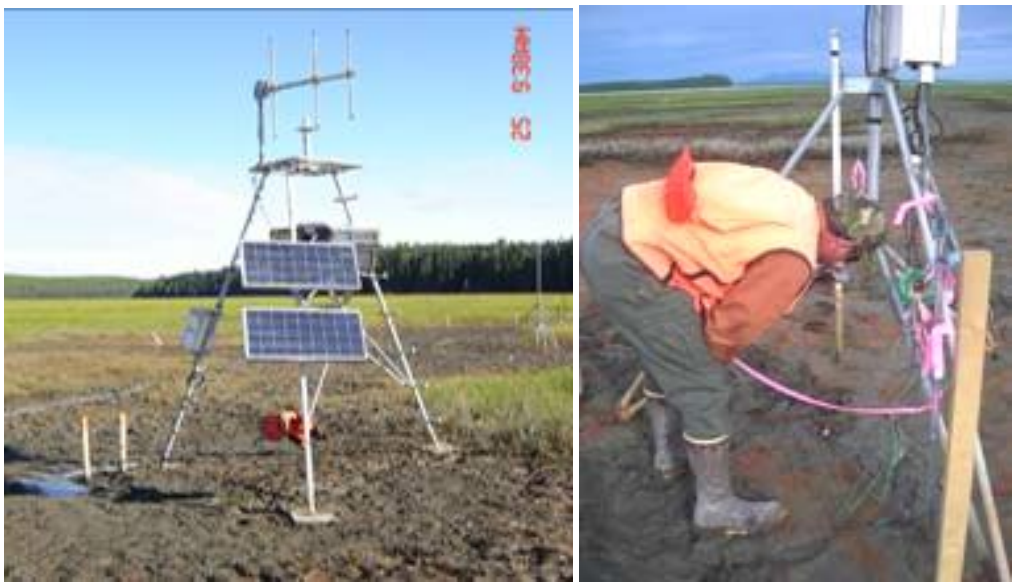

Figure 77. Setting up camera at Pond 155, Eagle River Flats, Alaska.

6.1.3 Low-order residues at Eagle River Flats, Alaska

The Comp B residues were deposited by two live-fire training events at ERF with 120-mm HE M933 point-detonating mortar projectiles. The first event, designated as LO 1 (Figure 78), occurred in February 2005. At this test, a total of 160 projectiles were fired, of which 8 of the120-mm mortars did not detonate, and 4 others produced LO detonations. In May 2005, we located a crater that contained an incompletely fragmented projectile with Comp B adhered to the remains of the projectile and discrete particles of Comp B within and around the crater. We mapped the distribution of Comp B chunks outside the crater. Then we collected them to obtain an estimate of the mass of macroscopic Comp B scattered outside the crater.

In March 2006, another live-fire exercise using 120-mm projectiles produced additional LO detonations near LO 1. We mapped the distribution of macroscopic Comp B residues around two additional LO detonation craters, designated as LO 2 and LO 3 (Figure 78). At each site, we photographed 14 discrete Comp B chunks in May and August of 2006. Any visible residues were also photographed in May and August of 2007, and in June and August of 2008. We did not touch the residues; we monitored them in situ.

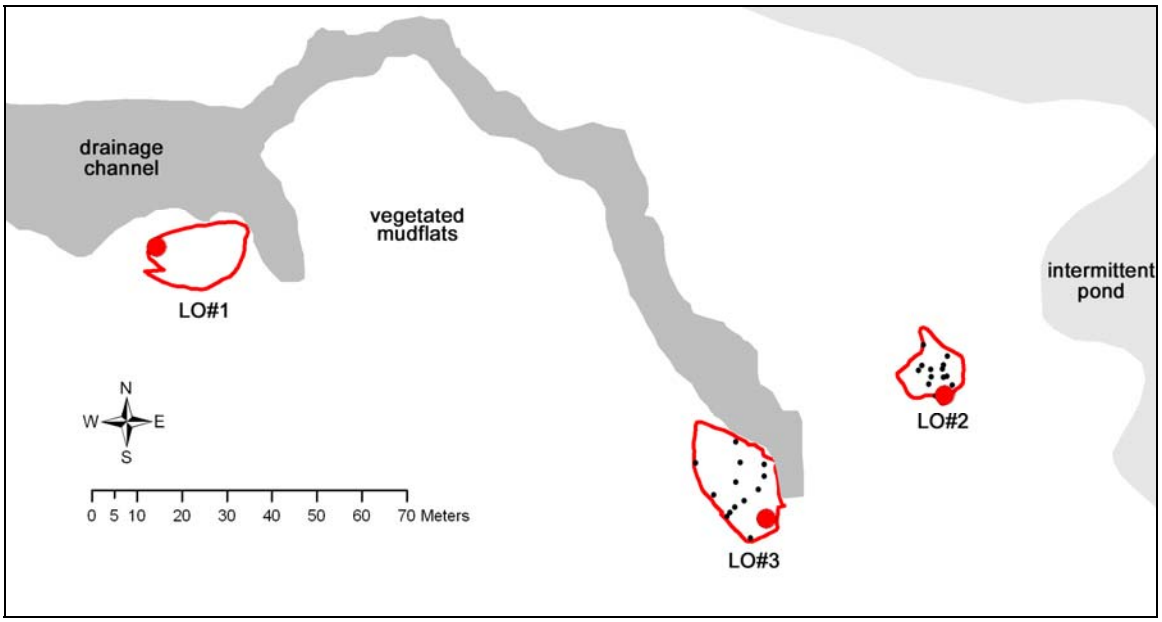

Figure 78. Map showing relative locations of three low-order detonation events on an estuarine salt marsh impact area. The solid red circles correspond to the impact craters and the red outlines delineate the boundaries of the scatter of solid Comp B chunks. The black dots at LO#2 and LO#3 are the locations of discrete points with Comp B residue that were monitored between May 2006 and May 2009.

6.2 Results

6.2.1 Holloman Air Force Base, New Mexico

The exposed surfaces of all the Tritonal pieces were rust red in color with greenish specks, the latter caused by oxidized aluminum flakes. The undersides of the Tritonal pieces were grey and the soil underneath the pieces was stained red in all cases. When we picked up pieces to photograph and weigh them, red dust from the coating adhered to our gloves and also left a fine dust on the weigh paper used to place them on the scale.

Table 14 lists the masses of the initial 12 Tritonal chunks set out in May 2005, the masses of the 10 chunks recovered in December 2005, and the masses of the same chunks in May 2006. The mass losses measured between May and December 2005 were high, ranging from 2.5%–33% of the initial chunk mass. In the cases of chunks 7, 9, and 11, we may have paired them incorrectly or the original chunk may have spalled. Most of the 10 cm (4 in.) rainfall between May 2005 and December 2005 occurred during a heavy rain in June. During this downpour, the HE pieces could have been moved and abraded.

Table 14. Mass of Tritonal chunks over one-year test.

Chunk	Mass (g)			Mass loss (g)	Mass loss (%)	
	May 05	Dec 05	May 06	One year	One year	6 Month
1	0.4					
2	0.6	0.56	0.56	0.04	6.67	0
3	0.65	0.64	0.63	0.02	3.08	1.6
4	0.5					
5	1.95	1.89	1.88	0.07	3.59	0.5
6	2.35	2.22	2.21	0.14	5.96	0.5
7	1.1	0.76	0.73	0.37	33.64	3.9
8	1.2	1.1	1.08	0.12	10.00	1.8
9	6.2	5.47	5.44	0.76	12.26	0.5
10	4	3.92	3.9	0.1	2.50	0.5
11	5.7	5.26	5.21	0.49	8.60	1.0
12	3.15	3.02	3.01	0.14	4.44	0.3

The samples did not lose as much mass between December 2005 and May 2006 with losses ranging from 0%–3.9%. Only 6 mm of rain fell at Holloman AFB during that time period and, as the chunks had not moved, they were not abraded by physical transport.

6.2.2 Pond 155 at Eagle River Flats, Alaska

Images from our camera showed the HE pieces stayed in place from the date they were set out–6 pieces on 6 June 2007 (pieces A–F in Figure 79a) and 11 pieces on 22 June 2007 (pieces 1–11 in Figure 79a)–until July 19, 2007. Paw prints indicated that, on the morning of 19 July 2007, a wolf tilted our camera and disturbed the HE pieces. Between the June and July dates, a large desiccation crack formed in the sediment and "swallowed" our Comp B particle E (Figure 79b). As shown, desiccation is a mechanism that can bury particles in the subsurface.

We reweighed the HE chunks on 27 August 2007 (Table 15). The C4 piece F was too fragile to handle, but the rest of the pieces were either the same weight or in some cases weighed more; we suspect the now-heavier pieces contained moisture.

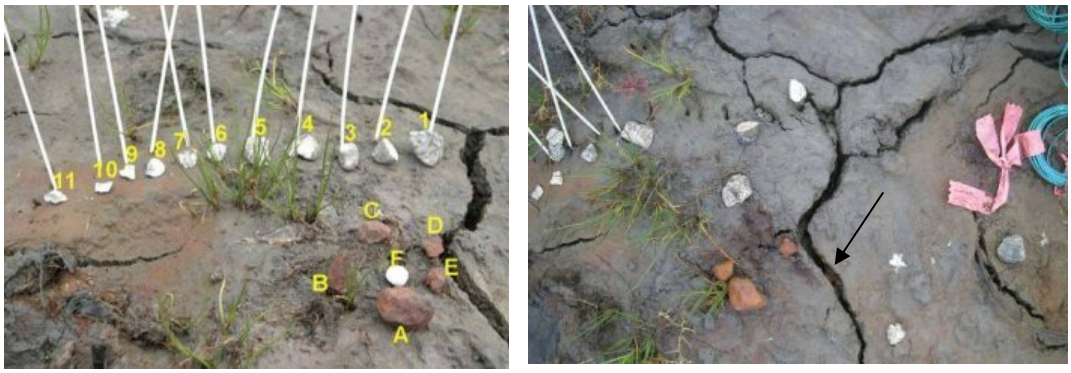

a. Comp B pieces (A–E) and C4 piece (F) set out on the 6 June, 2007 plus additional C4 pieces (1–11) set out on 22 June 2007 at Pond 155, Eagle River Flats, Alaska.

b. A large desiccation crack opened before 19 July 2007 and "swallowed" Comp B particle E, which is now about 1 cm below the surface (see arrow pointing to new location of particle E).

Figure 79. Close-up photographs of Comp B and C4 pieces at Pond 155, Eagle River Flats, Alaska.

Table 15. Mass of Comp B and C4 chunks set out at Pond 155, Eagle River Flats, Alaska.

HE Chunk	Mass (g)	
Comp B	6 June 07	27 Aug 07
A	34.5	34.8
B	16.1	15.9
C	4.7	4.5
D	2.3	2.2
E	2.1	In crack
C4	22 June 07	27 Aug 07
F	3.2	Too friable
1	14.6	14.9
2	6.5	6.6
3	6.7	6.2 +piece
4	11.5	11.7
5	9.9	10.0
6	3.0	2.9
7	2.5	2.6
8	1.6	1.6
9	0.8	0.8
10	0.9	0.9
11	0.9	0.9

Until the end of August 2007, the HE chunks we placed in Pond 155 did not experience wetting by tidal waters. The site flooded on 31 August–2 September, and again from 29 September–3 October of 2007 (Figure 80). Water depth decreased between flooding events, but remained around 30 cm until freeze-up occurred. Water depth reached a maximum of 1.1 m on 2 October 2007. Our temperature measurements showed a diurnal cycle and water temperatures decreasing with time during the fall (Figure 81). Note that the large variations in the temperature signal before flooding were a record of air, not water, temperatures. Despite testing and calibrating the water flowmeter before placing it at the site, it did not work correctly. Observations suggested that tidal waters moved slowly in these ponds; the usable data from our flowmeter indicated flow velocities of 1–2 cm per second.

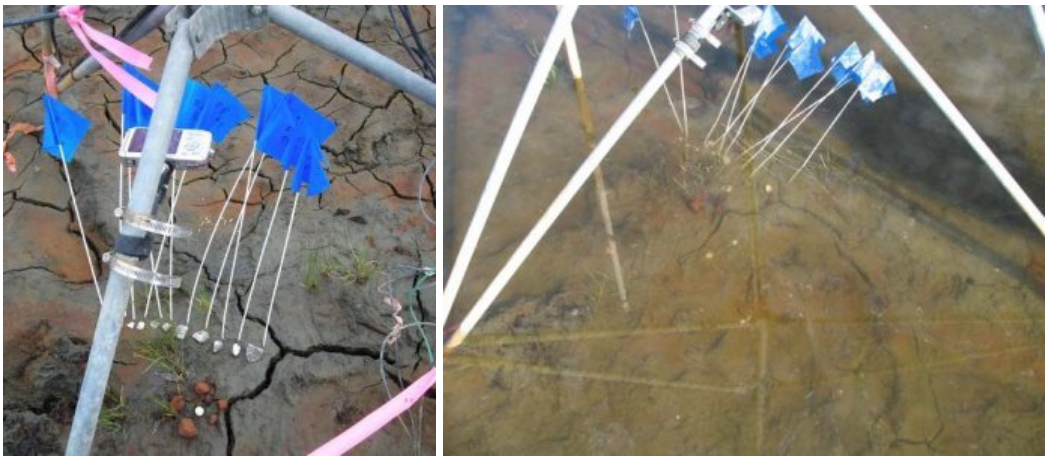

Figure 80. Comp B and C4 pieces as originally placed in June 2007 and underwater in Aug 2007.

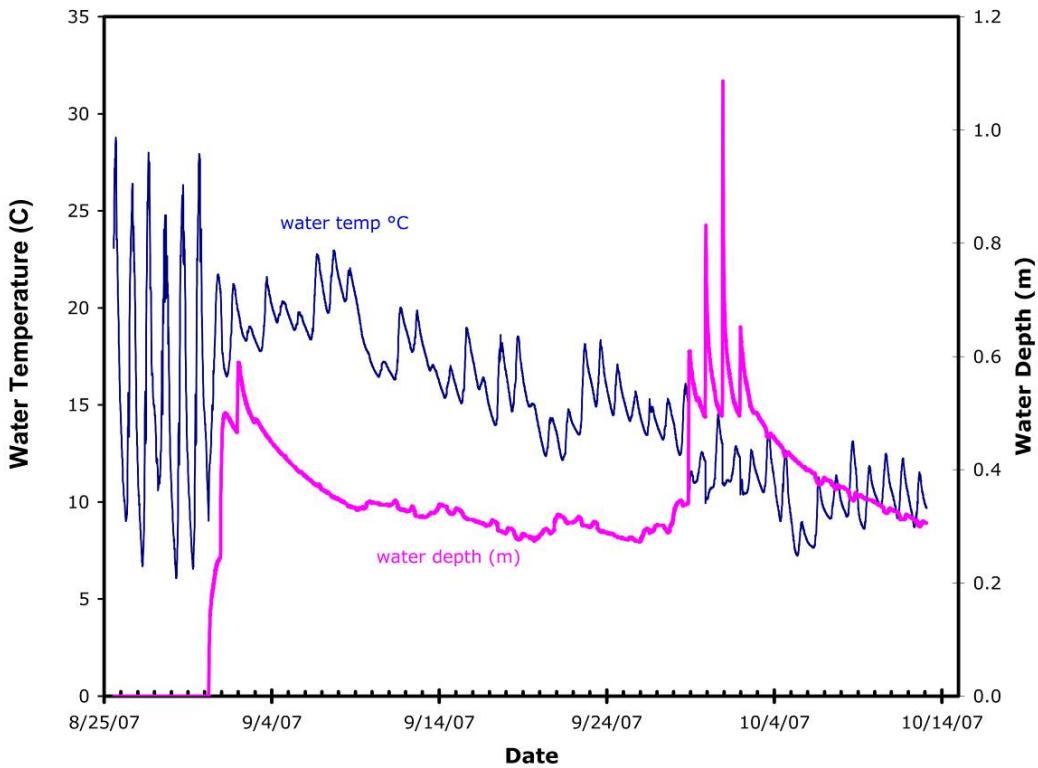

Figure 81. Water temperature (°C) and water depth (m) measurements for Pond 155 at Eagle River Flats, Alaska.

6.2.3 Distribution and weathering of LO detonation residue, ERF, Alaska

6.2.3.1 Description of LO 1:

The crater of LO 1 contained the tail assembly and part of the 120-mm projectile body with Comp B adhered to the metal. There were also large pieces of metal and discrete pieces of Comp B within the crater. The surface of the Comp B was stained a reddish-orange. The chunks appeared to be friable and were easily broken apart to reveal the underlying beige-colored Comp B.

Eighteen discrete deposition points of solid Comp B were found over a 247-m² area, mostly between 13.3–18.3 m east of the crater. Each location had a chunk that was 2–4 cm in the longest dimension, and most deposits had smaller (cm to less than 1 mm) pieces of Comp B. The total mass of centimeter-size Comp B from the 18 locations was 120 g.

6.2.3.2 Description of LO 2 and LO 3

The craters for LO 2 and LO 3 were similar to LO 1 in that they each contained the tail assembly and a portion of the projectile body. The Comp

B residues deposited around the craters ranged from red stains on the surface of the sediment to clusters of millimeter-size particles, to individual Comp B chunks up to 3 cm long (Figure 82a).

At LO 2 in May 2006, we found 81 discrete points with Comp B scattered over a 146 m^2 area, and all the visible residues were stained dark red. We photographed eac of the 14 Comp B deposits (Figure 83). These included 10 chunks of Comp B, 2 disaggregated deposits of solid residues, and 2 red stains with no solid Comp B visible (Table 16). In August 2006, after a series of flooding tides and 180 mm of rainfall, the red stain was gone from all the deposits and the remaining residues were orange-yellow. Of the original 10 chunks, 5 were intact; 4 were broken, roughened or flaking; and 1 was actually a piece of metal surrounded by a stain from Comp B. Two points had deposits of several small particles that were under 2–3 cm of water. No residues were visible at the two remaining points that were originally red surface stains. In May and August 2007, solid Comp B residue was visible at only 7 of the 14 original photo points. Each point with visible residue remaining originally had Comp B pieces at least 2 cm in one dimension. All pieces were dark red in May, appeared friable, and were disaggregating. One deposit had a plant (*Triglochin palustris*) growing through the disaggregating Comp B residue (Figure 84). In 2008, residue was still present at the 7 disaggregated masses.

Figure 82. Crater formed by LO 2 detonation at ERF. On the right is the same area after flooding tides and rainfall in August 2006.

Figure 83. Photos of Comp B chunks dispersed by low-order detonation #2, photographed (l-r) in May and August 2006, and May and August 2007. Missing photographs indicate the loss of HE chunk(s).

Figure 83 (cont'd). Photos of Comp B chunks dispersed by low-order detonation #2, photographed (l-r) in May and August 2006, and May and August 2007. Missing photographs indicate loss of HE chunk(s).

Figure 83 (cont'd). Photos of Comp B chunks dispersed by low-order detonation #2, photographed (l-r) in May 2006, August 2006, May 2007, and August 2007. Missing photographs indicate loss of HE chunk(s).

Table 16. Field observations for Comp B chunks dispersed by LO 2 detonation. Chunks were observed on 24 May 2006, 23 Aug. 2006, 22 May 2007, 24 Aug. 2007, 4 June 2008, 25 Aug.2008, and 14 May 2009.

LO2	May 2006	Aug. 2006	May 2007	Aug. 2007	June 2008	Aug. 2008	May 2009
A	Two larger pieces with several smaller particles 2 x 2 cm	Still present but crumbling	Red, crumbling, 2 x 2 cm area	Crumbling; shedding small particles	Completely disaggregated and hard to see; red	Some planar structure visible in larger piece; several small pieces; orange-red	Looks like a red, rough stain
B	Red stain about 5 x 6 cm; appears disaggregated	Under ~3 cm of water; red stain is gone; several small particles	No particles				
C	Red stain about 3 x 4 cm	Nothing left	Nothing left				
D	Red stain about 8 x 10 cm	Nothing left (no photo)	Nothing left				
E	Red chunk about 1.5 x 2 cm	Intact; no red stain	Getting covered by silt	Not as much silt as in May	Covered with silt	Large disaggregated mass (2 cm); deep red	Mostly covered with silt; red
F	Chunk about 2 x 2-cm, plus smaller piece	Intact	Looks friable.	Still a fairly large piece, but crumbling from surface.	Completely crumbled (2-cm X 3-cm mass). Red.	Disaggregated mass. Red.	Disaggregat ed mass; red.
G	Large chunk about 2.5 x 3 cm	Mostly intact; flaking	Mostly intact	Still a fairly large piece, but crumbling from surface	Large disaggregated mass; red	Large disaggregated mass; red	Appears to be one large, red piece surrounded by small pieces
H	Red chunks about 1.5 x 2.5 cm	Intact	Still intact	Flattening	Disaggregated mass (~3 cm diameter); red	Large disaggregated mass; red	Large, rough, red mass
I	Red chunk about 1 cm x 1 cm	Intact; no red stain	Nothing visible	Nothing visible			
J	Chunk with stain	Large chunk is metal	Metal piece present; all other residue gone				

L02	May 2006	Aug. 2006	May 2007	Aug. 2007	June 2008	Aug. 2008	May 2009
K	Flattened chunk about 1.5 x 2 cm	Under water; two pieces	Nothing visible				
L	Crumbly red area about 2 x 2 cm	Several small particles under water	Nothing visible				
M	Dark chunk with flat side about 2 x 3 cm	Intact; no red	Still present; looks friable	One large piece with three smaller pieces	Disaggregated mass (~3 cm diameter); red	Disaggregated mass	Large red mass
N	Red chunk about 2 x 2 cm	Intact but surface rough; no red	Crumbled	Crumbled with plants growing through HE residue	Completely disaggregated	Disaggregated mass	Red mass almost gone

24 May 2006

23 August 2006

22 May 2007

24 August 2007

4 June 2008

25 August 2008

Figure 84. Images documenting the changes over three summers in one chunk of Comp B at LO 2.

At LO 3 in May 2006, we found 133 discrete points with Comp B scattered over a 378 m² area. In contrast to LO 1 and LO 2, the residues were predominately disaggregating deposits rather than intact chunks of Comp B. We photographed 14 points, of which 7 had chunks, 6 were disaggregating deposits of Comp B, and 1 was a red stain on the surface sediment (Table 17). The LO 3 detonation was close to a drainage channel and may have experienced more frequent inundations than the other 2 sites. In May 2007, solid Comp B residue was visible at only 6 of the 14 photo points, and all the residues were in the form of small, crumbled particles. By August 2008, only 4 deposits remained.

Table 17. Field observations for Comp B chunks dispersed by LO #3. Chunks were observed on 24 May 2006, 23 Aug. 2006, 22 May 2007, 24 Aug. 2007, 4 June 2008, 25 Aug.2008, and 14 May 2009.

LO 3	May 2006	Aug. 2006	May 2007	Aug. 2007	June 2008	Aug. 2008	May 2009
A	Chunk (about 1.5 x 1.5 cm) in shallow, rust-colored drainage channel	Particle gone; no photo taken					
B	Red chunk about 1-cm X 1-cm	Particle gone;no photo taken					
C	Small, disaggregating particle near gully. Vegetation flattened from surface water flow	Particle gone; no photo taken					
D	Large mass of Comp B (5 x 4 cm) with copious red stain	Surface is rough; no red stain	Completely crumbled	Small (~1 mm) red particles	Small (~1-mm) red particles	Several small (mm) particles	Mass of small particles; red
E	Disaggregating mass (2-cm X 3-cm) of Comp B; red	Almost dissolved; no red stain	Nothing left				
F	Flattened chunk of Comp B (about 2 x 1.5 cm)	Separated into several pieces	In three pieces	In three crumbly pieces	No visible residue	Small mass of ~1-2-mm size particles	Indistinct red stain

LO 3	May 2006	Aug. 2006	May 2007	Aug. 2007	June 2008	Aug. 2008	May 2009
G	Small disc-shaped piece of Comp B.	Separated into small pieces. Almost dissolved	Nothing left				
H	Red stain on sediment surface	Nothing left of stain. Standing water	Nothing left				
I	Disaggregated mass of Comp B in wash; copious red stain	Very small pieces plus one larger piece; no red stain	1 small piece	Crumbled flat disc	No visible residue	No visible residue	
J	One large chunk (about 2 x 3 cm) with small chunks; red stain.	Very rough surface; flaking; no red stain.	Crumbling	Crumbly	Crumbly mass 3 x 2 cm: orange	Crumbly mass; orange	Red mass; almost gone
K	Arrowhead-shaped chunk of Comp B (1 cm base); very red	Separated into pieces; no red stain	1 larger piece and 2 small pieces	1 larger piece and 2 small pieces; becoming covered with silt	3 pieces visible; 1 is 6 x 3 mm; 2 are 1 x 1 mm	1 large piece (6 mm) and about 5 small pieces	1 large piece and several small pieces.
L	Rounded, red chunk (diameter about 2 cm)	Appears to have layers; flaking; no red.	Small pieces; looks like the residue may have been crushed (stepped on by others)	Many small pieces; sediment sample core had been removed next to the residue			
M	Flat, red mass of Comp B	Broken apart; no red	Nothing left				
N	Several small (less than 1 cm) red pieces of Comp B	Mostly dissolved; small pieces in standing water	Nothing left				

6.3 Discussion

We documented the persistence of Tritonal and Comp B residues on two military training ranges. Military training ranges are found in a wide variety of environments, from deserts to forests, and from prairie to wetlands (Doe et al. 1999). The settings for our observations were an arid environment and a salt marsh.

Holloman Air Force base is located in an arid environment. During the 6 months that no rain fell, the 10 Tritonal pieces lost between 0–40 mg of TNT (adjusting for the 20% aluminum by mass). A 40 mg loss would be equivalent to the loss rate measured in our outdoor tests at CRREL, where Tritonal chunks lost between 160–520 mg over a three-year period. Since dissolution was not responsible (no rain), we think it likely that the measured 40 mg loss was caused by a piece spalling off the main chunk between the dates of the two mass measurements. During a second 6-month period, however, Holloman experienced significant rainfall. This not only dissolved but also laterally transported the Tritonal chunks, and much higher mass losses were recorded (between 8–580 mg). Although we are less certain about these weights (we might have paired the samples incorrectly), the data suggested that infrequent torrential downpours that transport HE chunks downslope cause larger losses in mass than does dissolution.

Our second location, the ERF salt marsh's mud flat, was subjected to periodic tidal flooding, seasonal freezing and thawing, precipitation in the form of rain and snow, exposure to long hours of sunlight in the summer, and bioturbation by plants and animals. These factors contributed to the physical and chemical transformations of the solid Comp B residues. The appearance of all the Comp B pieces changed substantially in that some crumbed and some disappeared altogether. Because the flow rates are low (<2 cm per second) and the area is flat, we did not think the HE chunks were washed away. Instead, we thought it likely that residence in brackish tidal waters, and freezing and thawing of these particles (either in or out of water) helped to disaggregate the chunks. Chunks of Comp B that were initially large and intact survived better than pieces that were initially small or crumbling. The persistence of the Comp B chunks in the salt marsh environment is much shorter (by orders of magnitude) than would be predicted from dissolution of HE chunks by rainfall in an upland environment (Lever et. al 2005).

The Comp B and C4 placed in Pond 155 at ERF showed that all pieces persisted through the first summer and fall and were not removed by the tide. The C4 piece from the demo 3 site became very friable and could not be reweighed. One of the other C4 pieces likely spalled a piece.

The principal morphological changes in the solid Comp B residues observed for three years were: (a) formation of dark red surface staining that washed off with rain or tidal flooding, and (b) disaggregation of solid chunks into loose masses of crumbled pieces. Disaggregation dramatically increases the surface area of the residue. The formation of dark red surface staining on the Comp B has been documented previously and is due to the phototransformation of TNT. Although the phototransformation of TNT in aqueous solutions has been studied, the compound(s) responsible for the red stain on the solid are just starting to be identified (see Section 4A). If the phototransformation products on the solid are more soluble than TNT, then their formation could be a significant factor that also needs to be included in dissolution models. Because the phototransformation of TNT in aqueous solution produces a complex mixture of highly polar nitroaromatic compounds (Spanggord et. al. 1983; Godejohann et. al. 1998), it is reasonable to assume that the phototransformation products on the solid are also polar.

7 Conclusion

A critical problem facing range managers is to determine whether live-fire training activities are likely to contaminate groundwater under their ranges. Off-base migration of explosive contaminants may trigger federal regulatory actions that can close bases or restrict training. To predict the likelihood of off-base explosive contamination, one needs to know the following:

- mass, type and spatial distribution of explosives on the range
- size distribution of the HE pieces;
- dissolution rates of each HE type as functions of piece size, rainfall and temperature;
- interaction rates of aqueous-phase HE with soil
- characteristics of flow through the vadose zone
- characteristics of groundwater flow under the base

In this study, we focused on the dissolution of explosive particles exposed to rainfall because it was poorly understood, and it initiates aqueous-phase HE transport. Because this dissolution occurs at a particle's surface, we also investigated weathering processes that increase surface area and consequently dissolution rate (e.g., cracking, spalling and splitting). We exposed chunks of TNT, Tritonal, Comp B and C4 to outdoor conditions and analyzed the resulting effluent. These data, along with concurrently collected weather data, constituted a three-year record used to validate dissolution models for HE particles on range soils.

We developed a drop-impingement dissolution model based on laboratory tests and validated it using the outdoor data. The model assumes that raindrops intercepted by HE particles were fully saturated in HE as they dripped off. Particle size, HE type, annual rainfall, and average temperature were key input parameters. Given those parameters, the model we developed offers a simple and accurate method to predict aqueous-phase HE influx into range soils. If the drop-impingement model were coupled to a vadose transport model, one could make a first-order estimate of the HE mass reaching groundwater.

For a known starting population of HE particles, two processes strongly affect the uncertainty of HE influx estimates: fracture of the HE pieces to create additional surface area, and phototransformation of the HE into other compounds. We have made some progress to understand these processes.

Splitting, spalling, and cracking are probably common during the decades-long lifespan for dissolution of gram chunks of HE. During our three-year outdoor tests on 34 HE chunks, 4 split to produce centimeter-size pieces, 14 mm-size pieces spalled off, and 9 of them developed cracks. These events significantly accelerated dissolution by increasing surface area exposed to rainfall. Unfortunately, we do not know how environmental factors influenced fracture of HE particles. Explosives monitored at ERF, an Alaskan tidal salt marsh, disintegrated at a much higher rate than those outside at CRREL or at Holloman AFB, possibly due to submersion in salt water. Freeze-thaw cycling, wet-dry cycling, nearby detonations, and jostling by wind, vehicle, and animal traffic could also have accelerated fracture of HE particles.

Phototransformation appears to be an important mass-loss pathway for HE particles exposed outdoors. For our tests, dissolved TNT mass was only about one-third of the mass lost from the TNT and Tritonal chunks, and dissolved RDX mass was about one-half of the RDX mass lost from Comp B chunks. We think the HE is being phototransformed to compounds not quantified by Method 8330B. For TNT, 2-amino-4,6-dinitrobenzoic acid is found at concentrations similar to those of TNT and could account for much of the missing mass. An unidentified compound, RP 2, is partly responsible for the characteristic red color of photo-degraded TNT. Both of these compounds appear to be stable, highly soluble and elute in the pre-solvent peak area. These results are significant because they suggest that in the presence of moisture, solid TNT readily phototransforms to compounds that are polar, not quantified by Method 8330B. Thus, the influx of transformation products into range soils could exceed that for the HE itself. More work is needed to identify these transformation products, quantify their formation and dissolution rates, and assess their fates.

Probably the largest source of uncertainty in estimating HE aqueous influx into range soils resulted from the poorly quantified starting population of the HE particles on the range. The number and sizes of these particles

depends on many factors including the munitions used, their firing rates, their detonation probabilities (high-order, low-order, or dud) and weathering and mechanical disaggregation.

It is unlikely that the number and sizes of HE particles on ranges can be measured. However, earlier work showed that low-order detonations produced particles sizes that follow a power-law distribution, and HE chunks crushed as part of this work produced power-law distributions of daughter particles. That is, we might be able to make crude estimates for particle numbers and sizes given estimates of total HE mass based on soil sampling or wide-area assessments. Alternatively, we could simulate historical live-fire and blow-in-place activities to “spin up” starting populations of HE particles on ranges. Uncertainties will be high, but estimates may still prove useful to range managers and for guiding future training and cleanup activities.

References

Army Materiel Command. 1971. Engineering Design Handbook: Explosives Series, Properties of Explosives of Military Interest. Army Materiel Command, Alexander, VA.

ATSDR. 1995. Toxicological profile for 2,4,6-trinitrotoluene and RDX. U.S. Department of Health and Human Services, Public Health Service, Agency for Toxic Substances and Disease Registry, Atlanta, GA.

Bear, J. 1972. *Dynamics of Fluids in Porous Media*. Dover Publications, New York.

Bedford C.D, P. S. Carpenter and M. P. Nadler. 1996. Solid-State Photodecomposition of Energetic Nitramines (RDX and HMX), NAWCWPNS TP 8271, Naval Air Warefare Center Weapons Division, China Lake, CA 93555-6001.

Bordeleau, G., R. Martel, G. Ampleman, and S. Thiboutot. 2008a. Environmental impacts of training activities at an air weapons range. *Journal of Environmental Quality,* 37:308–317.

Bordeleau, G., R. Martel, D. Schafer, G. Ampleman and S. Thiboutot. 2008b. Groundwater flow and contaminant transport modelling at an air weapons range. *Environmental Geology,* 55(2):385–396.

Burlinsen, N.E., M.E. Sitzman, L.K. Kaplan and E. Kayser. 1979. Photochemical generation of the 2,4,6-trinitrotoluene anion. *J. Org. Chem,.* 44(2):3695–3698.

Chambre P.L., T.H. Pigford, A. Futjita, T. Kanki, A. Kobayashi, H. Lung, D. Ting, Y. Sato and S.J. Zavoshy. 1982. Analytical performance models for geological repositories, LBL-14842, Lawrence Berkeley Laboratory, University of California, Berkeley, CA.

Chambre, P.L. and T.H. Pigford. 1984. Prediction of waste performance in a geological repository. Mat. Res. Soc. Symp. Proc., Elsevier Science Publishing Co., 26:985–1008.

Clausen, J. L., N. Korte, M. Dodson, J. Robb and S. Rieven. 2007. Conceptual Model for the Transport of Energetic Residues from Surface Soil to Groundwater by Range Activities. ERDC/CRREL TM-06-18.

Clausen, J., J. Robb, D. Curry and N. Korte. 2004. A case study of contaminants on military ranges: Camp Edwards, Massachusetts, USA. *Environmental Pollution,* 129(1):13–21.

Dionne, B.C., D.P. Rounbehler, E.K. Achter, J.R. Hobbs and D.H. Fine. 1986. Vapor Pressure of Explosives. *Journal of Energetic Materials*, 4:447–472.

Doe, W.W., R.B. Shaw, R.G. Bailey, D.S. Jones and T.E. Macia. 1999. Locations and environments of US army training and testing lands: An ecological framework for assessment. *Federal Facilities Environmental Journal,* Autumn, 9–26.

Dontosava, K.M., S.L. Yost, J. Simunek, J.C. Pennington and C.W. Williford. 2006. Dissolution and transport of TNT, RDX, and Composition B in saturated soil columns, *Journal of Environmental Quality,* 35:2043–2054.

DuBois, F.W and J.F Baytos. 1991. Weathering of Explosives for Twenty Years, Los Alamos Report LA-11931.

Environmental Protection Agency. 2008. Region 6 Human Health Medium-Specific Screening Levels. www.epa.gov/Region6/6pd/rcra_c/pd-n/screen.htm

Environmental Protection Agency. 2006. Nitroaromatics, Nitramines and Nitrate Esters by HPLC, SW-846 Method 8330B.

Godejohann M., M. Astratov, A. Preiss, K. Levsen and C. Muegge. 1998. Application of continuous-flow HPLC-proton-nuclear magnetic resonance spectroscopy for the structural elucidation of phototransformation products of 2,4,6-trinitrotoluene, *Analytical Chemistry,* 70:4104–4110.

Grummt, T., H. Wunderlich, A. Chakraborty, M. Kundi, B. Majer, F. Ferk, A.K. Nersesyan, W. Parzefall and S. Knasmueller. 2006. Genotoxicity of nitrosulfonic acids, nitrobenzoic acids and nitrobenzylalcohols, pollutants commonly found in ground water near ammunition facilities, *Environmental and Molecular Mutagenesis,* 47: 95-106.

Hewitt, A.D., T.F. Jenkins, T. Ranney, J. Stark, M.E. Walsh, S. Taylor, M. Walsh, D. Lambert, N. Perron, N. Collins, and R. Karn. 2003. Estimates for Explosive Residue Deposition from the Detonation of Army Munitions. ERDC/CRREL TR-03-16.

Hewitt, A.D., T.F. Jenkins, M.E. Walsh, M.R. Walsh and S. Taylor. 2005. RDX and TNT residues from live-fire and blow-in-place detonations, *Chemosphere,* 61:888–894.

Jenkins, T.J., J.C. Pennington, T.A. Ranney, T.E. Berry Jr., P.H. Miyares, M.E. Walsh, A.D. Hewitt, N.M. Perron, L.V. Parker, C.A. Hayes and E.G. Wahlgren. 2001. Characterization of explosives contamination at military firing ranges. US Army Engineer Research and Development Center, Cold Regions Research and Engineering Laboratory, Hanover, New Hampshire, Technical Report ERDC/CRREL TR-01-5.

Kaplan, D.L. and A.M. Kaplan. 1982. Separation of mixtures of 2,4,6-trinitrotoluene reduction products with liquid chromatography. *Analytica Chimica Acta*, 136: 425-428.

Leggett, D.C, T.F. Jenkins, and R.P. Murrmann. 1977. Composition of vapors evolved from military TNT as influenced by temperature, solid composition, age and source. U.S. Army Cold Regions Research and Engineering Laboratory, Hanover, New Hampshire, Special Report SR-77-16.

Lever J., S. Taylor, L. Perovich, K. Bjella, and B. Packer. 2005. Dissolution of Composition B Residuals. *Environmental Science and Technology,* 39:8803–8811.

Lynch, J.C, K.F. Myers, J.M. Brannon, and J.J. Delfino. 2001. Effects of pH and temperature on the aqueous solubility and dissolution rate of TNT, RDX and HMX. *J. Chem. Eng. Data,* 46:1549–1555.

Lynch, J.C., J.M. Brannon and J.J. Delfino. 2002a. Effect of component interactions on the aqueous solubilities and dissolution rates of the explosive formulations Octol, Composition B and LX-14. *J. Chem. Eng. Data,* 47:542-549.

Lynch, J.C, J.M. Brannon and J.J. Delfino. 2002b. Dissolution rates of three high explosive compounds: TNT, RDX and HMX. *Chemosphere,* 47:725–734.

Lynch, J.C., J.M. Brannon, K. Hatfield and J.J. Delfino. 2003. An exploratory approach to modeling explosive compound persistence and flux using dissolution kinetics. *Journal of Contaminant Hydrology,* 66(3-4):147–159.

Martel, R., M. Mailoux, U. Gabriel, R. Lafebvre, S. Thiboutot and G. Ampleman. 2009. Behavior of energetic materials in ground water at an anti-tank range. *Journal of Environmental Quality,* 38:75–92.

Martel R., M. Mailloux, R. Lefebvre, Y. Michaud, M. Parent, G. Ampleman, S. Thiboutot, S. Jean, and N. Roy. 1999. Energetic materials behavior in groundwater at the Arnhem Anti-Tank Range, CFB Valcartier, Quebec, Canada. INRS - Georesources Report 1999-02.

Matyskiela. 2003. Modeling of Chemical Transport from UXO to surrounding Soil. Final Report submitted to Praxis Environmental Technologies.

Morley, M.C., H. Yamamoto, G.E. Speitel, and J. Clausen. 2006. Dissolution kinetics of high explosives particles in a saturated sandy soil. Journal of Contaminant Hydrology, 85:141–158.

Parmeter, J.E., G.A. Eiceman, D.A. Preston and G.S. Tiano. 1996. Calibration of an explosives vapor generator based on vapor diffusion from a condensed phase. Sandia National Laboratory Technical Report SAN096-2016C.

Pennington, J. C., T.F. Jenkins, G. Ampleman, S. Thiboutot, J.M. Brannon, A.D. Hewitt, J. Lewis, S. Brochu, E. Diaz, M.R. Walsh, M.E. Walsh, S. Taylor, J.C. Lynch, J. Clausen, T.A. Ranney, C.A. Ramsey, C.A. Hayes, C.L. Grant, C.M. Collins, S.R. Bigl, S. Yost and K. Dontsova. 2006. Distribution and fate of energetics on DoD test and training ranges: final report, ERDC TR-06-13.

Phelan J.M., S.W. Webb, J.V. Romero, J.L. Barnett, F. Griffin, and M. Eliassi. 2003. measurement and modeling of energetic material mass transfer to soil pore water- project CP-1227, Sandia Report 2003-0153.

Pruppacher, H.R., and J.D. Klett. 1997. Microphysics of clouds and precipitation. Kluwer Academic Publishers, Boston.

Radtke C.W., D. Gianotto and F.F. Roberto. 2002. Effects of particulate explosives on estimating contamination at a historical explosives testing area. Chemosphere, 46: 3–9.

Ro, K.S., A. Venugopal, D.D. Adrian, D. Constant, K. Qaisi, K.T. Valsaraj, L.J. Thibodeaux, and D. Roy. 1996. Solubility of 2,4,6, -trinitrotoluene (TNT) in water. Journal of Chemical and Engineering Data 41:758–761.

Skelland, A.H.P. 1974. Diffusional mass transfer. Wiley & Sons, New York.

Spanggord R.J., T. Mill, T-W. Chou, W.R. Mabey, J.H. Smith, and S. Lee. 1980. Environmental fate studies on certain munition wastewater constituents- Phase 1 and 11. Contract Report to U.S. Army Medical Research and Development Center.

Spanggord, R. J., W.R. Mabey, T. Mill, T.W. Chou, J.H. Smith, S. Lee, and D. Roberts. 1983. Environmental fate studies on certain munition wastewater constituents, Phase IV – Lagoon model studies. Stanford Research Institute, Menlo Park, CA for U.S. Army Medical Research and Development Command, Fort Detrick, Frederick, MD.

Taylor S., J.H. Lever, B. Bostick, M.R. Walsh, M.E. Walsh, and B. Packer. 2004a. Underground UXO: Are they a significant source of explosives in soil compared to military training on ranges? ERDC/CRREL Technical Report TR-04-23.

Taylor S., A. Hewitt, J. Lever, C. Hayes, L. Perovich, P. Thorne, and C. Daghlian. 2004b. TNT particle size distributions from detonated 155-mm howitzer rounds. *Chemosphere,* 55:357–367.

Taylor S., E. Campbell, L. Perovich, J. Lever, and J. Pennington. 2006. Characteristics of Composition B particles from blow-in-place detonations. *Chemosphere,* 65:1405–1413.

Taylor S., J. H. Lever, J. Fadden, N. Perron, and B. Packer. 2009a. Simulated rainfall-driven dissolution of TNT, Tritonal, Comp B, and Octol particles, *Chemosphere*, 75:1074–1081.

Taylor S., Lever J., J. Fadden, P. Collins, N. Perron, and B. Packer. 2009b. Outdoor Dissolution of TNT and Tritonal, *Chemosphere,* 77:1338-1345.

Thayer, J.R., and R.C. Huffacker. 1980. Determination of nitrite and nitrate by high-pressure liquid chromatography: Comparison with other methods for nitrate determination, *Anal. Biochem*,. 102:110–119.

Walsh, M.E. 1990. Environmental transformation products of nitroaromatics and nitramines, Special Report 90-2, USACRREL.

Walsh, M.R. 2007. Explosives residues resulting from the detonation of common military munitions: 2002-2006. ERDC/CRREL TR-07-2. Cold Regions Research and Engineering Laboratory, Hanover, NH 03755.

Appendix A: Bibliography of ER-1482 Publications

Refereed journal articles

Taylor S., J. H. Lever, J. Fadden, N. Perron, and B. Packer (2009a) Simulated rainfall-driven dissolution of TNT, Tritonal, Comp B, and Octol particles. *Chemosphere*, 75, 1074-1081.

Walsh, M. E., S. Taylor, A. D. Hewitt, M. R. Walsh, C. A. Ramsey, C. M. Collins (2010) Field observations of the persistence of comp b explosive residues in a salt marsh impact area. *Chemosphere*, 78, 467-473.

Taylor S., J. H. Lever, J. Fadden, N. Perron, and B. Packer (2009b) Outdoor weathering dissolution of TNT and Tritonal, *Chemosphere* 77, 1338-1345.

Government documents

Taylor S., J. H. Lever, J. Fadden, M.E. Walsh, N. Perron, S. Bigl, and B. Packer (in prep.), Dissolution rate, weathering mechanics and friability of TNT, Comp B, and Tritonal, ERDC/CRREL Report.

Conference presentations

Lever J.H., S. Taylor, J. Fadden, and B. Packer. 2007. Modeling the outdoor dissolution of exposed chunks of TNT and Tritonal, Partners in Environmental Technology Technical Symposium and Workshop, Washington, D.C.

Lever J.H., S. Taylor, J. Fadden, and B. Packer. 2009. Modeling the outdoor dissolution of TNT, Tritonal and Comp B, Partners in Environmental Technology Technical Symposium and Workshop, Washington, D.C.

Taylor S., J. Fadden, N. Perron, J.H. Lever, and B. Packer. 2007. Outdoor dissolution of Composition B, TNT, and Tritonal. Partners in Environmental Technology Technical Symposium and Workshop, Washington, D.C.

Taylor S., J.H. Lever, J. Fadden, and B. Packer. 2009. Modeling the outdoor dissolution of high explosives, second international dialogue on underwater munitions, Oahu, Hawaii.

Taylor S., J.H. Lever, J. Fadden, and B. Packer. 2009. Dissolution rate and weathering mechanics of TNT, Comp B, Tritonal, and Octol. Seminar at U of Hawaii, Manoa, February 2009.

Taylor S., J. Fadden, N. Perron, J.H. Lever and B. Packer (2008) Friability and its role in outdoor dissolution of high explosives. Partners in Environmental Technology Technical Symposium and Workshop, Washington, D.C.

Walsh M.E., A.D. Hewitt, M.R. Walsh, S. Taylor, C.M. Collins, S.R. Bigl, M.A. Chappell, C.A. Ramsey. 2008. Surface water and sediment sampling adjacent to a low-ordered 120-mm mortar projectile, Partners in Environmental Technology Technical Symposium and Workshop, Washington, D.C.

Walsh M. E., C. M. Collins, S. Taylor, M. R. Walsh, A. D. Hewitt, T. A. Douglas, C. A. Ramsey. 2008. Energetic residues from artillery and mortar live-fire: Studies on Alaskan training ranges. Sixth International Conference on Remediation of Chlorinated and Recalcitrant Compounds, Monterey, California.

Walsh M. E., A. D. Hewitt, S. Taylor, C. A. Ramsey, C. M. Collins. 2007. Persistence of high explosives from low-order detonations within a salt marsh impact area. Partners in Environmental Technology Technical Symposium and Workshop, Washington, D.C.

Appendix B: Photos of Control Chunks and Force vs. Displacement Plots

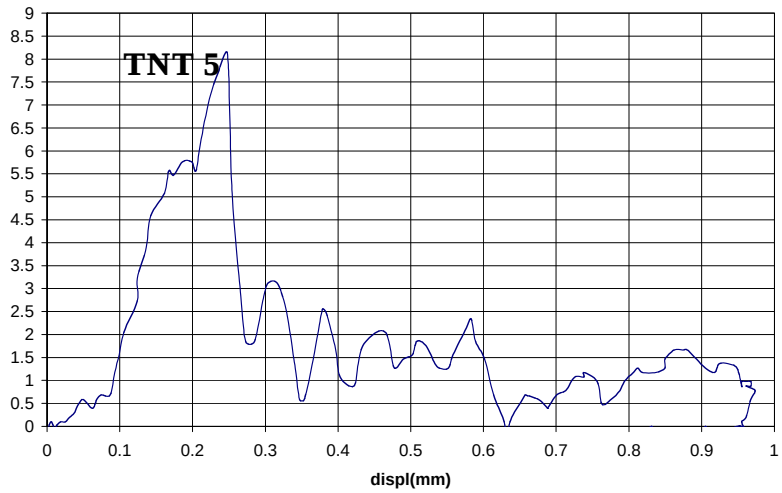

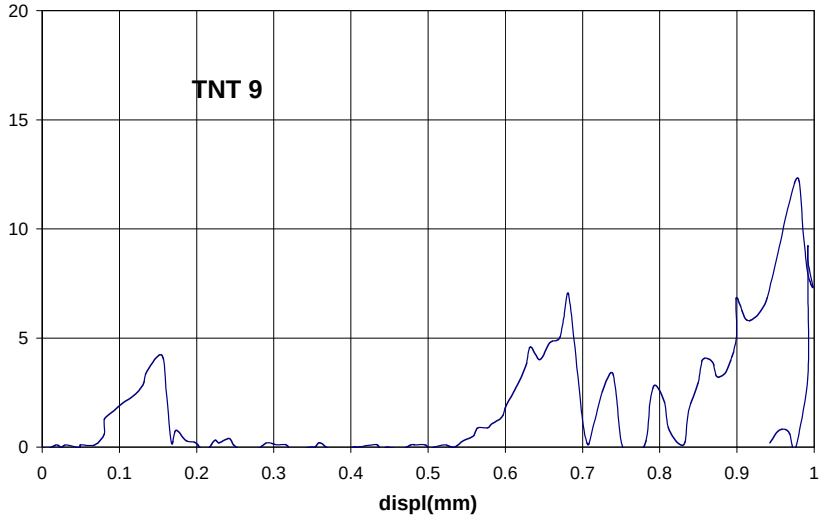

Figure B-1. Force (lb) vs. displacement (mm) plots for TNT chunks that had weathered outdoors for 14 months (TNT 5) and 36 months (TNT 9).

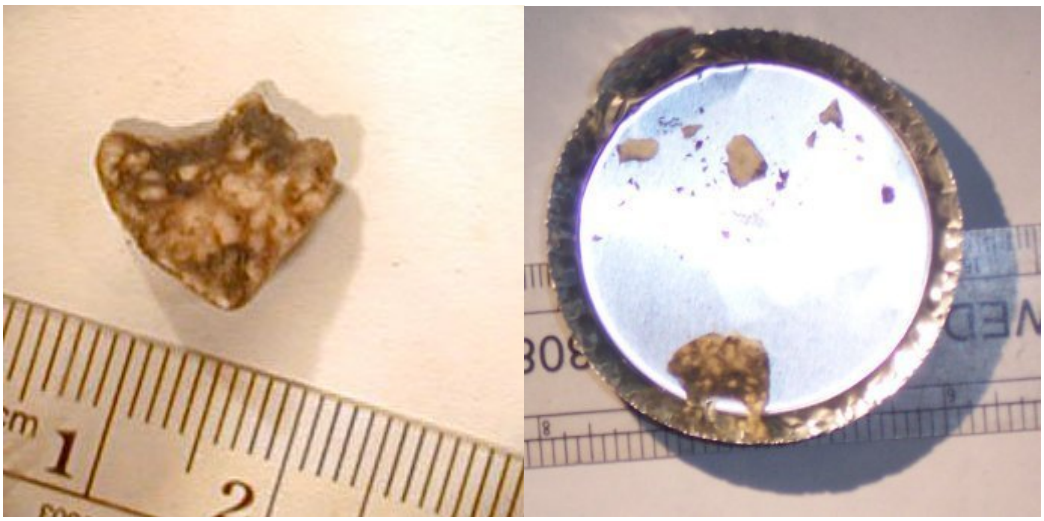

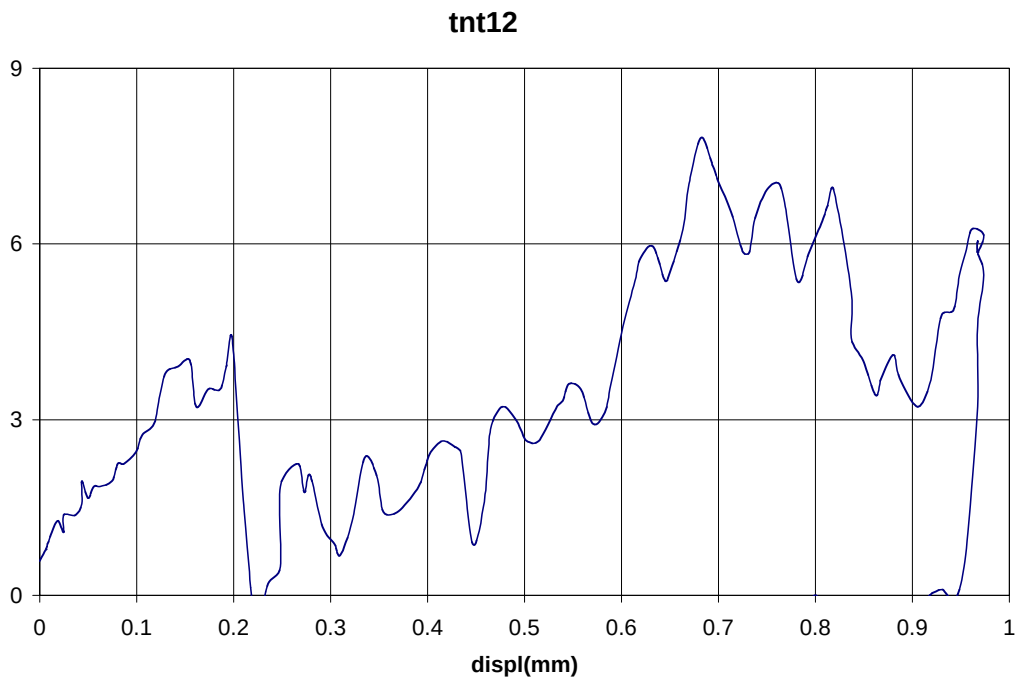

Figure B-2. Images of TNT control chunk 12 before crushing (upper left) and after crushing (upper right), shown along with its force displacement plot (lower).

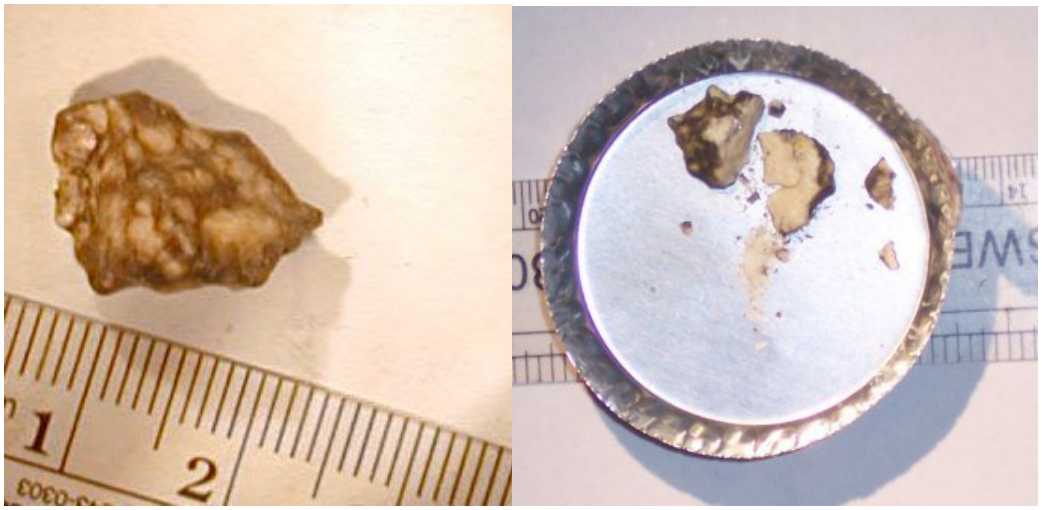

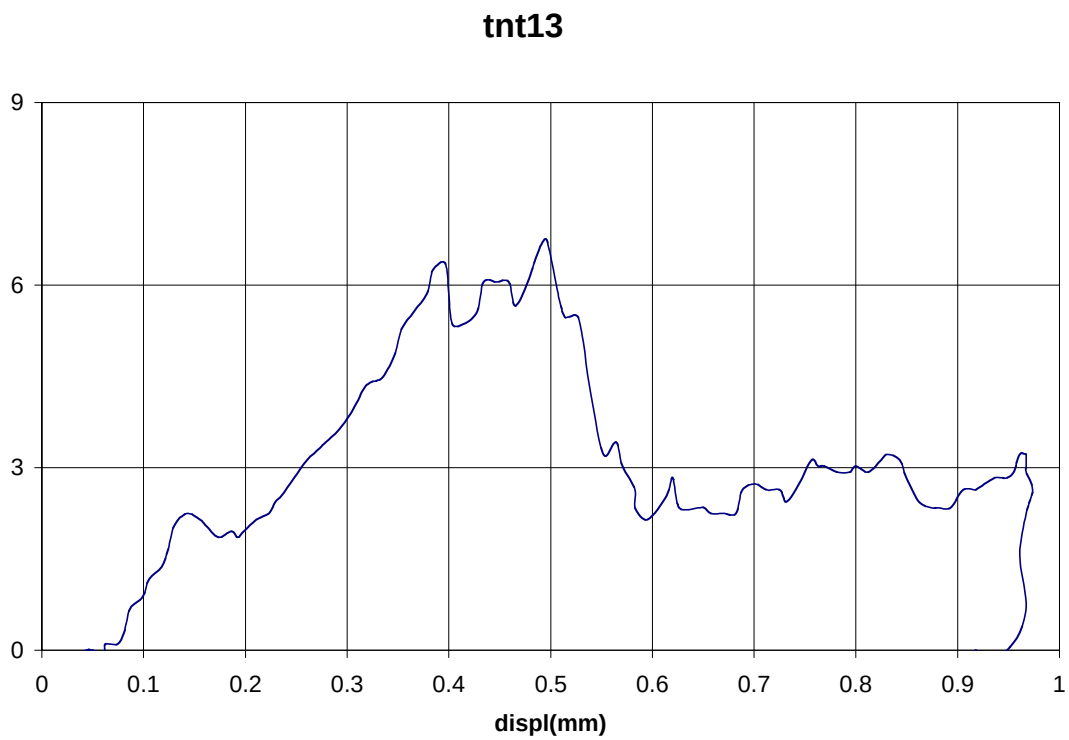

Figure B-3. Control chunk TNT 13, before and after crushing, shown along with its force displacement plot.

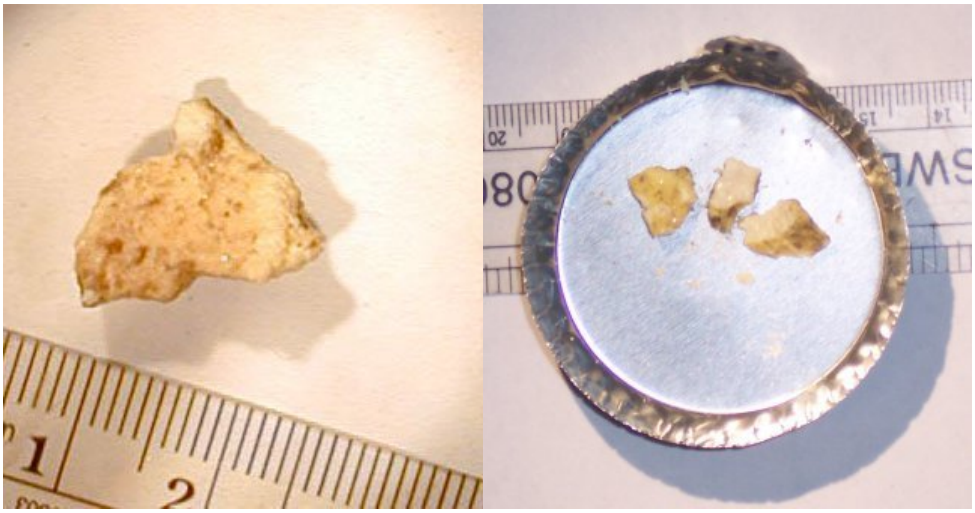

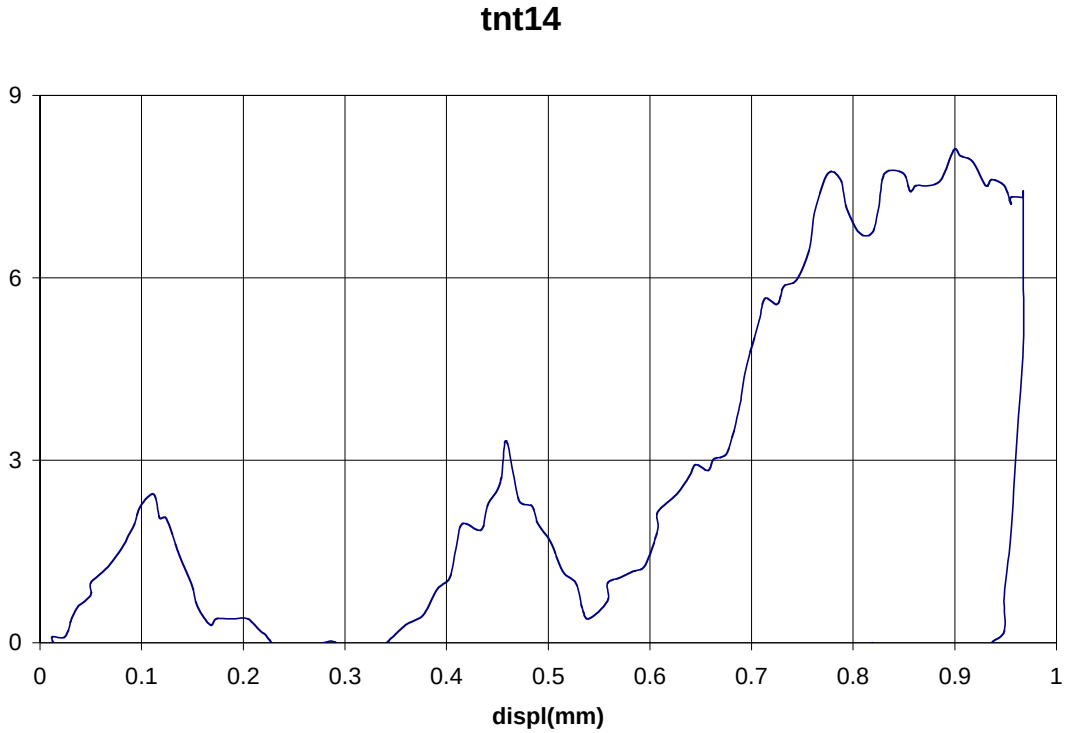

Figure B-4. Control chunk TNT 14, before and after crushing, shown along with its force displacement plot.

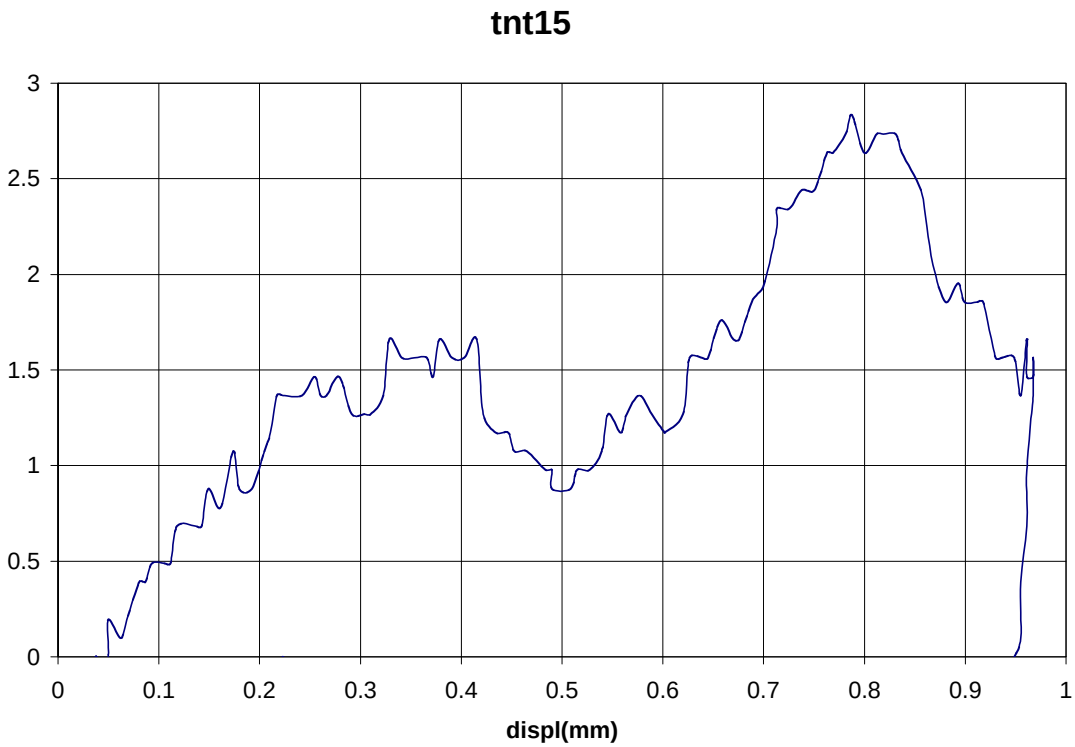

Figure B-5. Control chunk TNT 15, before and after crushing, shown along with its force displacement plot.

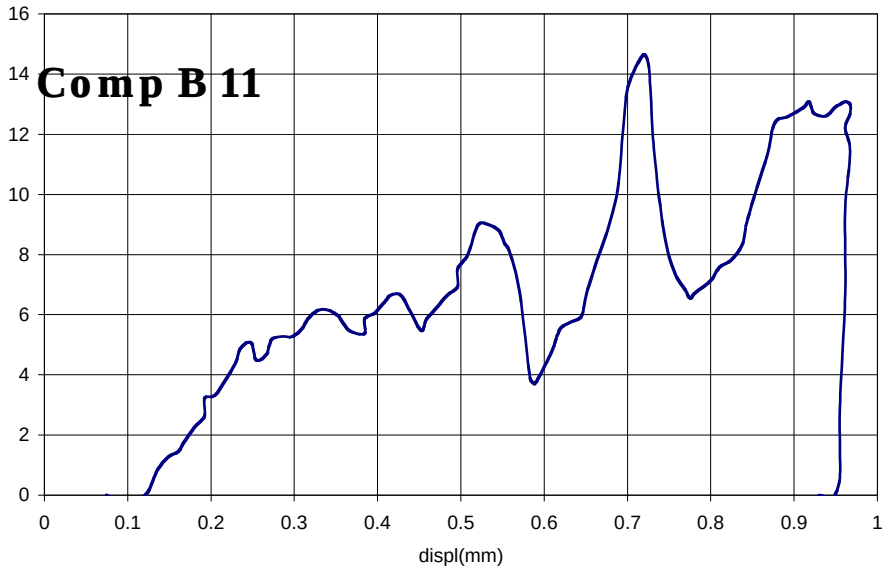

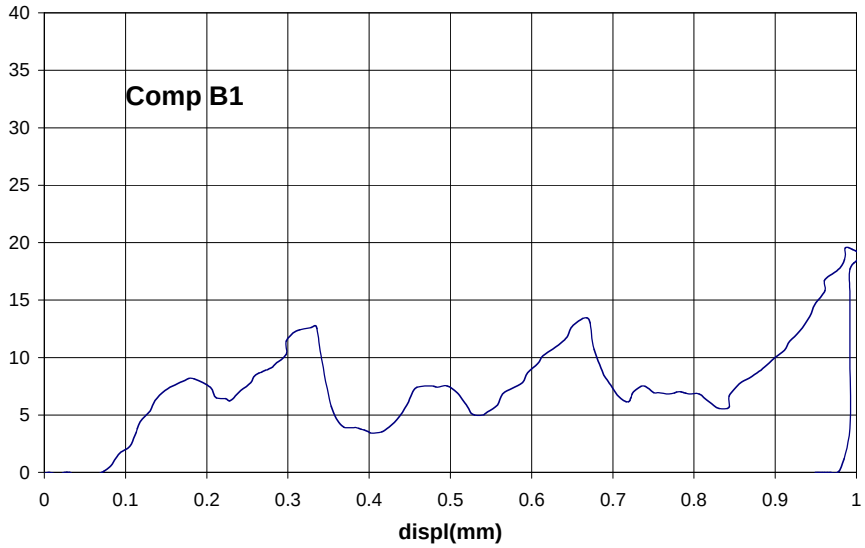

Figure B-6. Force displacement plots for Comp B 11 and Comp B 1. Both these HE chunks were samples in our outdoor dissolution tests.

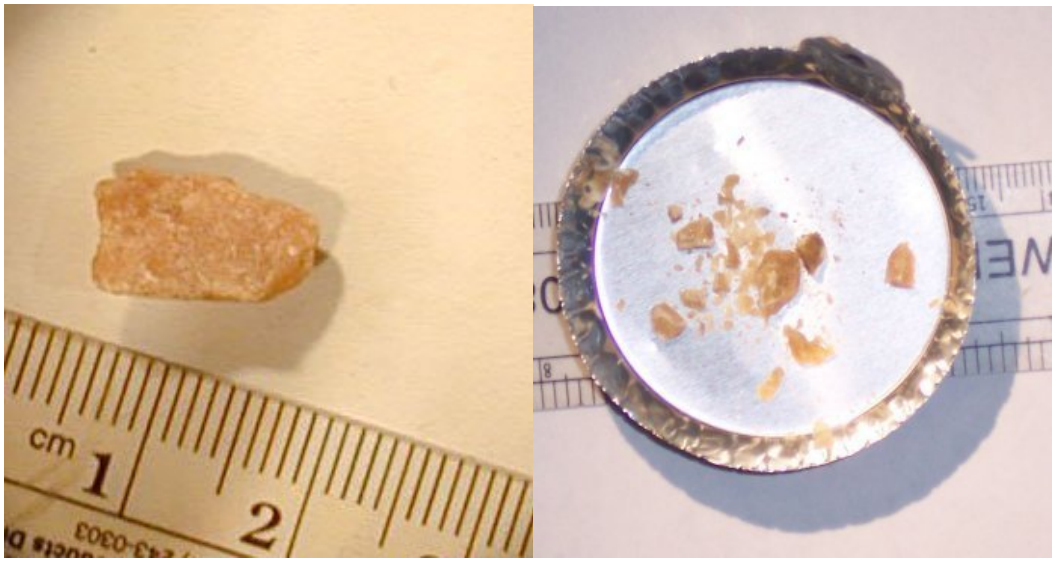

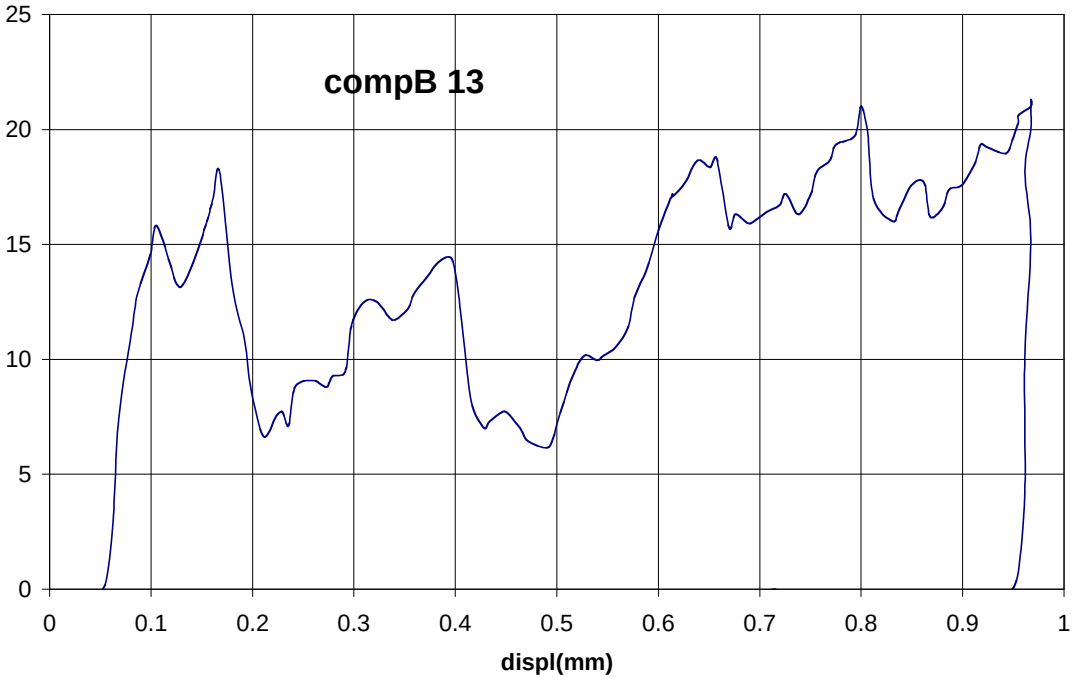

Figure B-7. Control chunk Comp B 13, before and after crushing, shown along with its force displacement plot.

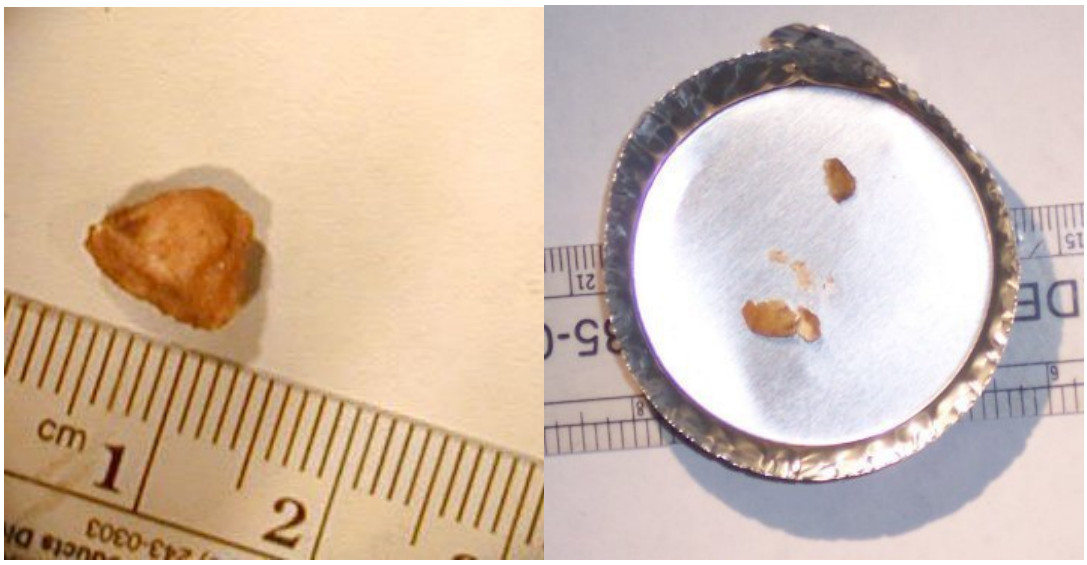

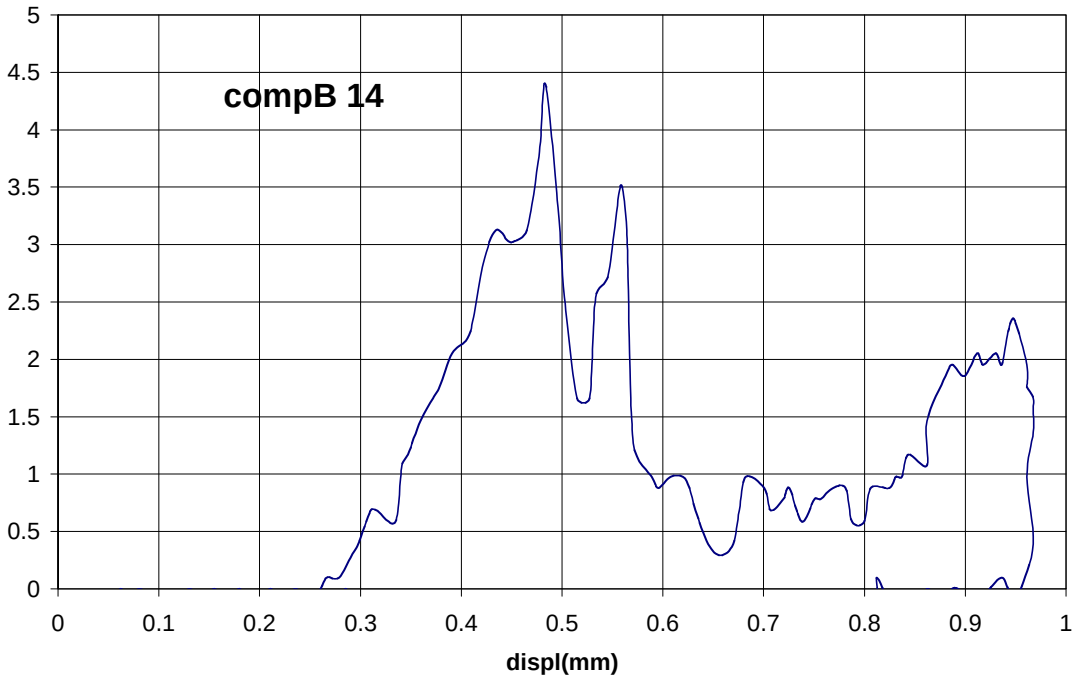

Figure B-8. Control chunk Comp B 14, before and after crushing, shown along with its force displacement plot.

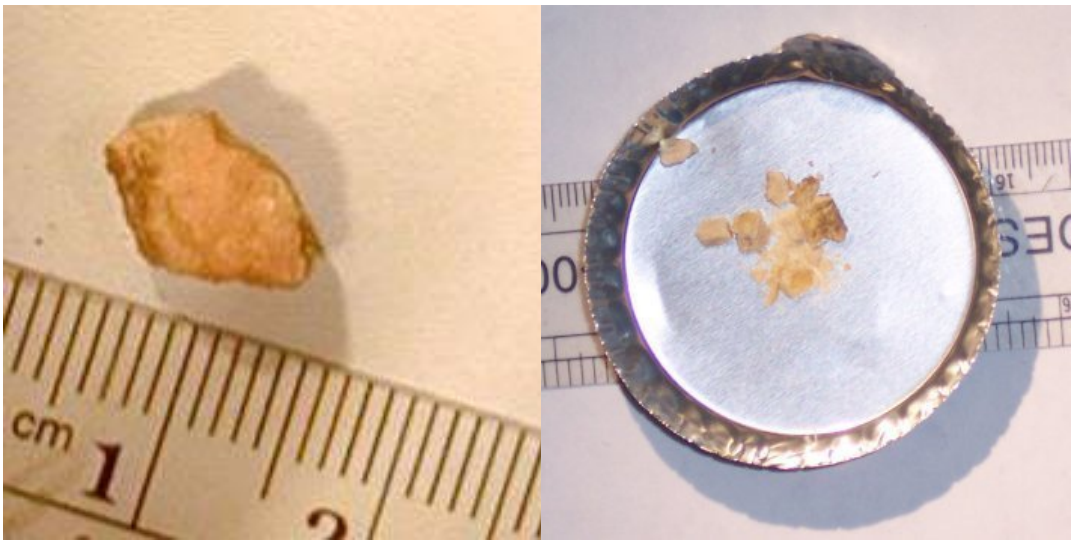

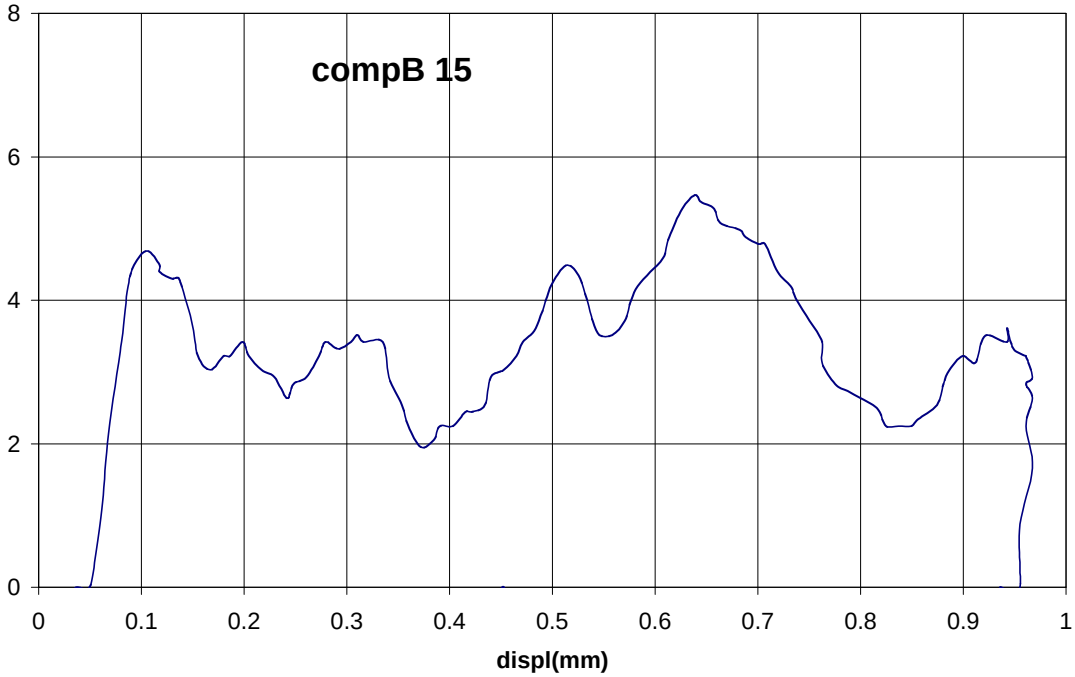

Figure B-9. Control chunk Comp B 15, before and after crushing, shown along with its force displacement plot.

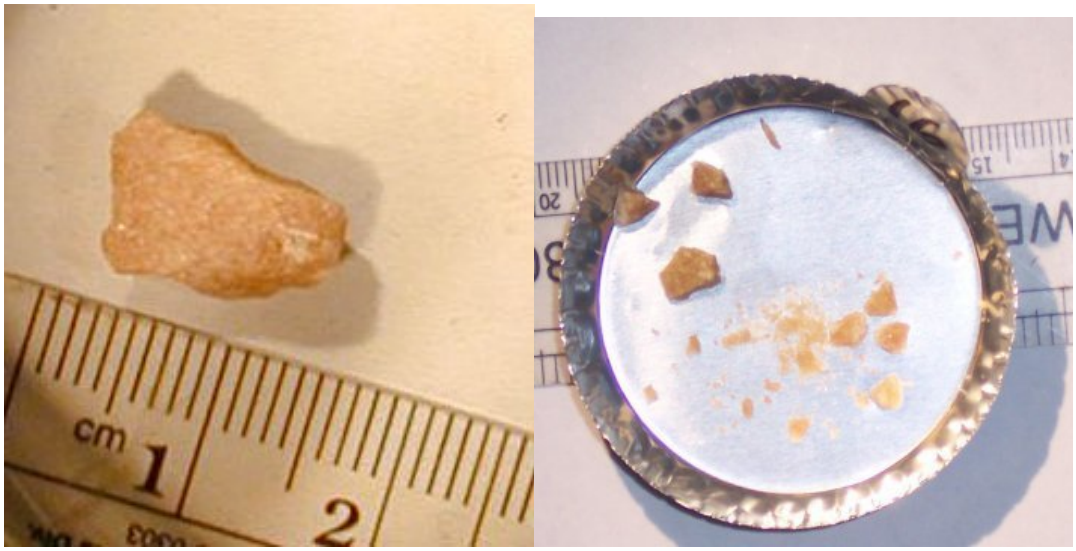

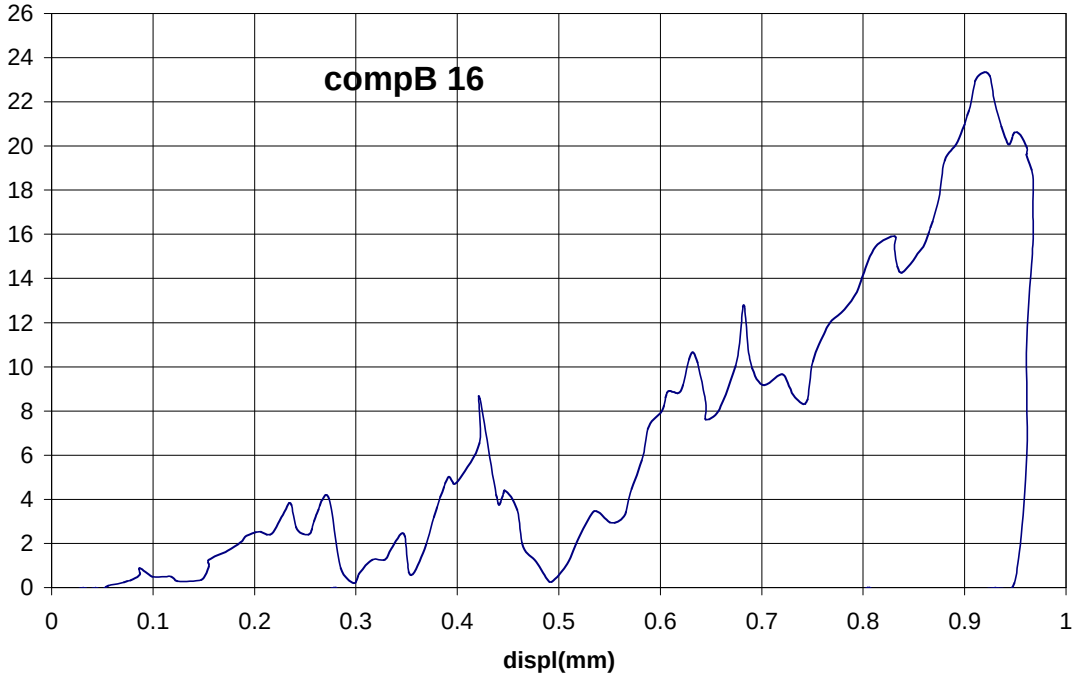

Figure B-10. Control chunk Comp B 16, before and after crushing, shown along with its force displacement plot.

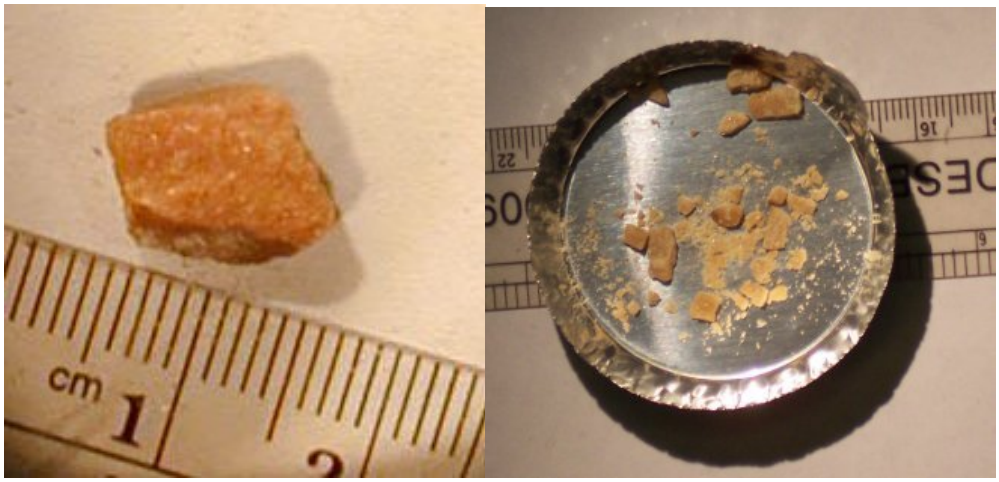

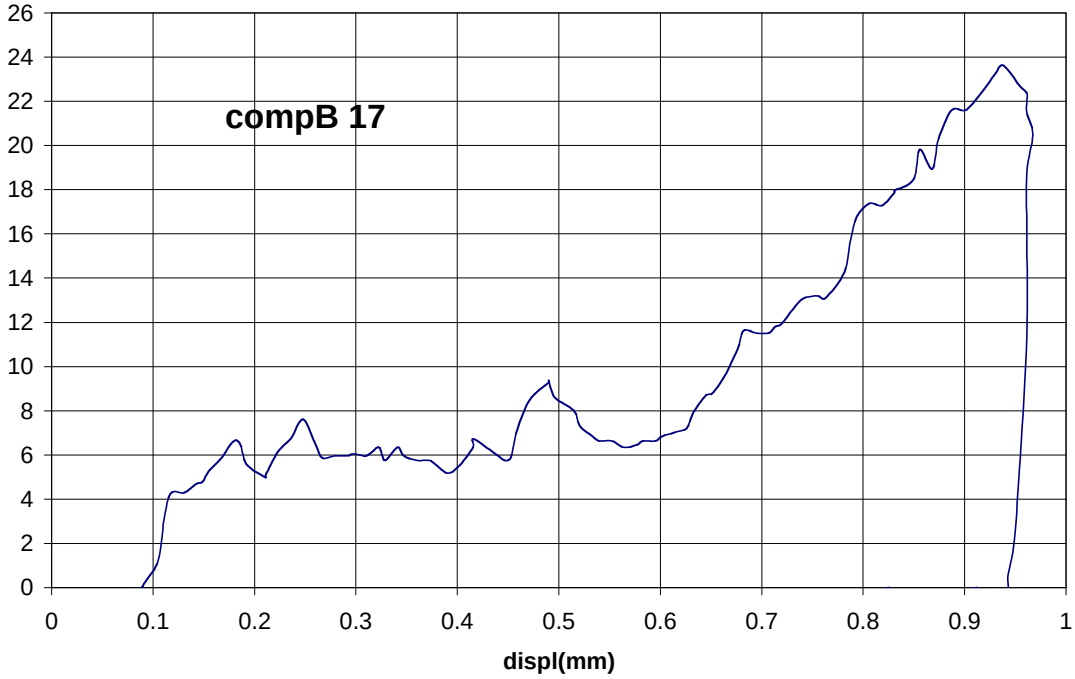

Figure B-11. Control chunk Comp B 17, before and after crushing, shown along with its force displacement plot.

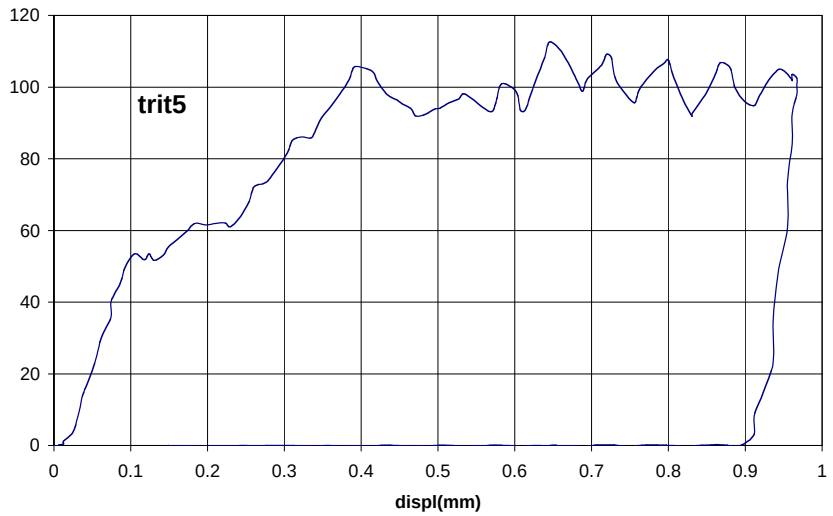

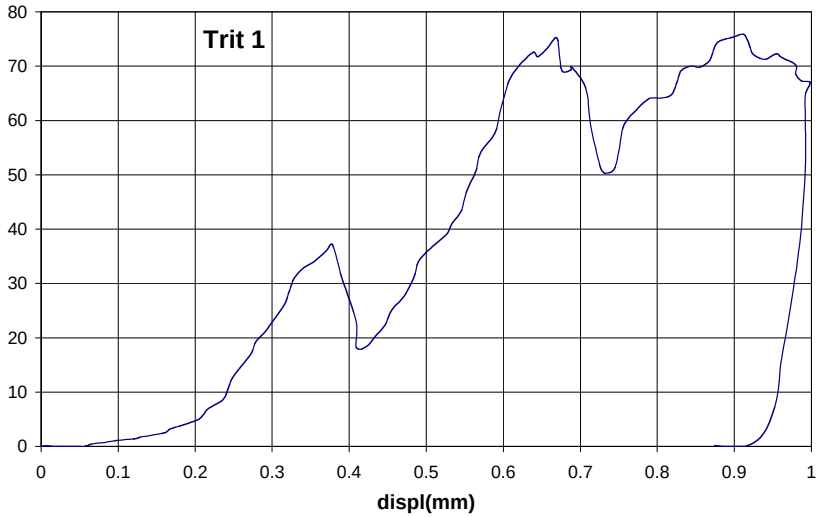

Figure B-12. Force displacement plots for Tritonal 5 and Tritonal 1. Both these HE chunks were samples in our outdoor dissolution tests.

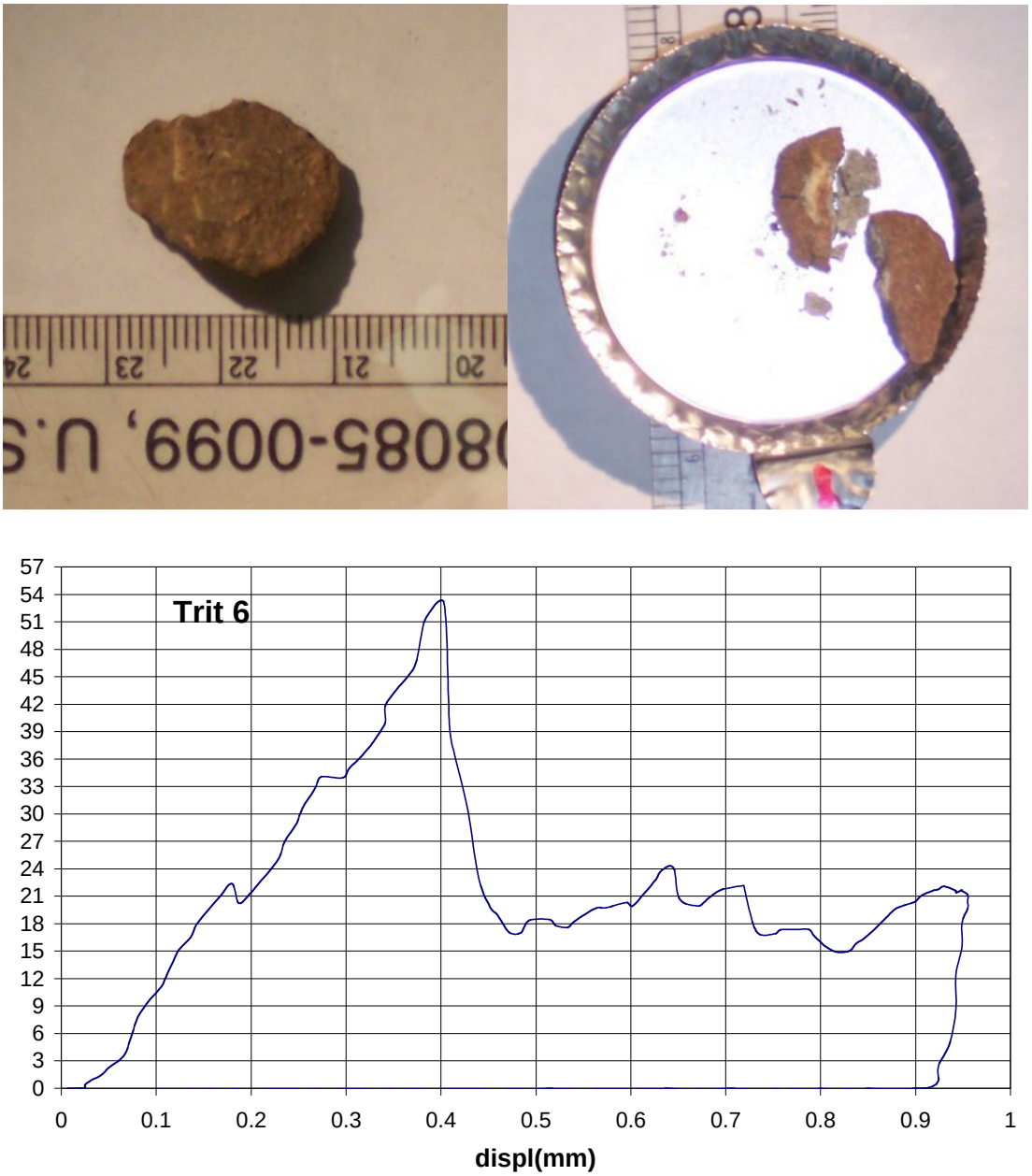

Figure B-13. Control chunk Tritonal 6, before and after crushing, shown along with its force displacement plot.

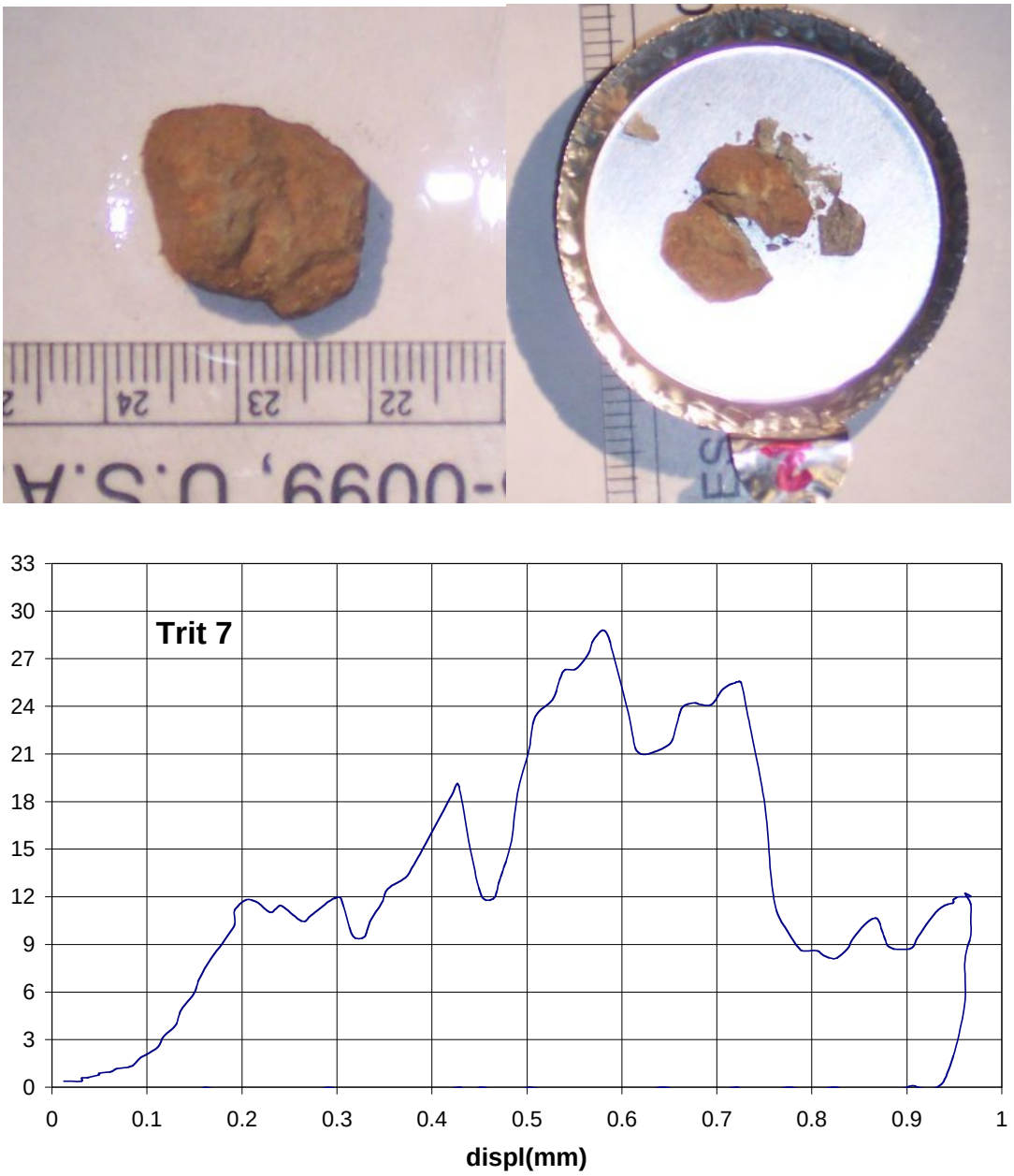

Figure B-14. Control chunk Tritonal 7, before and after crushing, shown along with its force displacement plot.

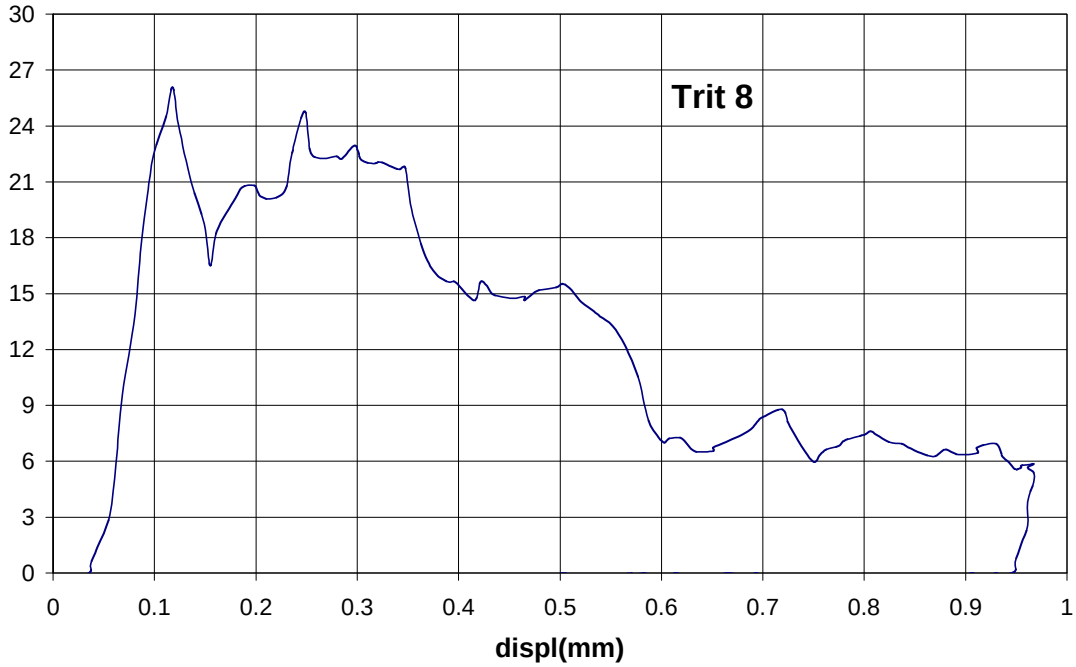

Figure B-15. Control chunk Tritonal 8, before and after crushing, shown along with its force displacement plot.

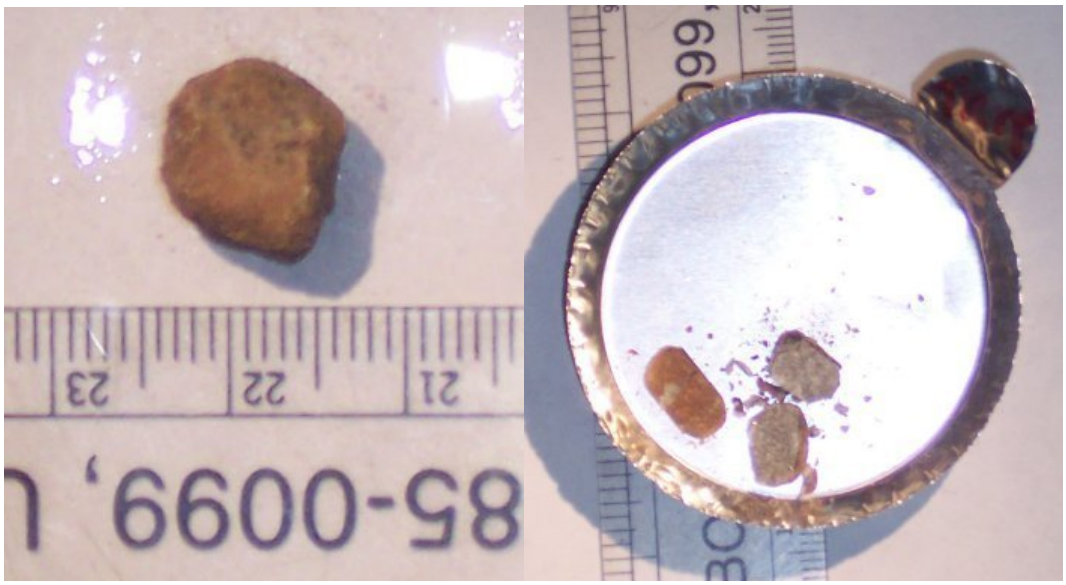

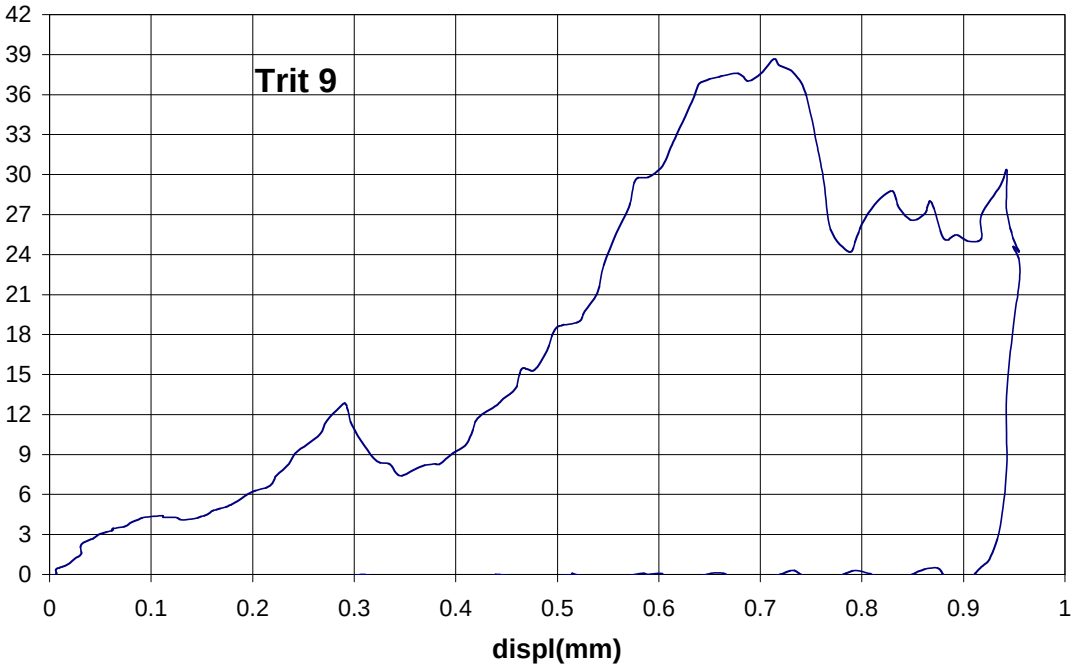

Figure B-16. Control chunk Tritonal 9 before and after crushing, shown along with its force displacement plot.

Table B-1. Change in the number and mass of fragments from TNT 5, Tritonal 5, and Comp B 11. Mass of the dust is shown in red.

# of Particles	TNT 5		Tritonal 5		Comp B 11	
	July-07 Mass (mg)	May-09 Mass (mg)	July-07 Mass (mg)	May-09 Mass (mg)	July-07 Mass (mg)	May-09 Mass (mg)
1	321.7	277.51	1399.8	374.75	176.1	147.1
2	212.3	182.02	214.1	243.35	51.9	20.82
3	40.4		89.4	205.75	39.7	12.69
4	6.2		68.5	89.4	34.2	8.8
5	5.7		65.5	51.76	19.8	3.64
6	0.6		52.1	50.75	5.2	
7	8.7		23.7	50.23	0.4	
8	4.8		17.1	45.65	9.1	
9			16.5	43.81	1.3	
10			13.4	30.51		
11			10.4	27.36		
12			6.6	24.35		
13			8	21.75		
14			7.7	18.06		
15			4	16.67		
16			1.8	16.62		
17			6.2	14.81		
18			2.9	14.64		
19			2.1	12.74		
20			1.3	12.4		
21			0.7	9.47		
22			27.4	9		
23				8.32		
24				7.89		
25				7.6		
26				7.16		
27				5.97		
28				5.12		
29				3.61		
30-90				66.3		
dust				13.81		

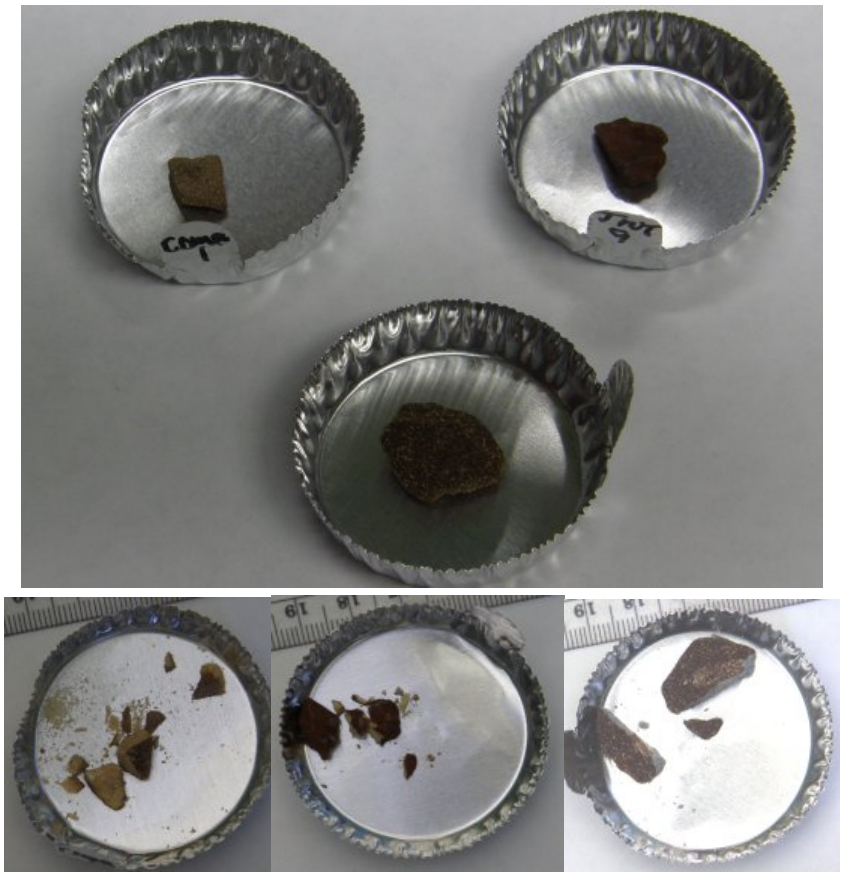

Figure B-17. Grouped images of Comp B 1, TNT 9, and Tritonal 1 before and after crushing in May 2009. These chunks were outdoors for three years.

Table B-2. Mass of fragments and of dust (red) from samples crushed in May 2009.

Comp B 1	TNT 9	Tritonal 1
290.64	294.72	1815.89
182.25	218.08	898.71
85.51	78.58	48.57
20.91	18.62	4.91
12.49	8.14	
13.63	2.82	
7.32	1.81	
5.05	4.65	
1.92		
2.62		
0.98		
1.17		
20.21		

REPORT DOCUMENTATION PAGE

Form Approved
OMB No. 0704-0188

Public reporting burden for this collection of information is estimated to average 1 hour per response, including the time for reviewing instructions, searching existing data sources, gathering and maintaining the data needed, and completing and reviewing this collection of information. Send comments regarding this burden estimate or any other aspect of this collection of information, including suggestions for reducing this burden to Department of Defense, Washington Headquarters Services, Directorate for Information Operations and Reports (0704-0188), 1215 Jefferson Davis Highway, Suite 1204, Arlington, VA 22202-4302. Respondents should be aware that notwithstanding any other provision of law, no person shall be subject to any penalty for failing to comply with a collection of information if it does not display a currently valid OMB control number. PLEASE DO NOT RETURN YOUR FORM TO THE ABOVE ADDRESS.

1. REPORT DATE (DD-MM-YYYY)
February 2010

2. REPORT TYPE
Final

3. DATES COVERED (From - To)

4. TITLE AND SUBTITLE
Dissolution Rate, Weathering Mechanics, and Friability of TNT, Comp B, Tritonal, and Octol

5a. CONTRACT NUMBER

5b. GRANT NUMBER

5c. PROGRAM ELEMENT NUMBER

6. AUTHOR(S)
Susan Taylor, James Lever, Marianne Walsh, Jennifer Fadden, Nancy Perron, Susan Bigl, Ronald Spanggord, Matthew Curnow, and Bonnie Packer

5d. PROJECT NUMBER
ER-1482

5e. TASK NUMBER

5f. WORK UNIT NUMBER

7. PERFORMING ORGANIZATION NAME(S) AND ADDRESS(ES)
U.S. Army Engineer Research and Development Center (ERDC)
Cold Regions Research and Engineering Laboratory
79 Lyme Road
Hanover, New Hampshire 03755-1290

8. PERFORMING ORGANIZATION REPORT NUMBER
ERDC/CRREL TR-10-2

9. SPONSORING / MONITORING AGENCY NAME(S) AND ADDRESS(ES)
Strategic Environmental Research &
Development Program
901 N Stuart Street
Suite 303
Arlington VA 22203

10. SPONSOR/MONITOR'S ACRONYM(S)
SERDP

11. SPONSOR/MONITOR'S REPORT NUMBER(S)

12. DISTRIBUTION / AVAILABILITY STATEMENT
Approved for public release; distribution is unlimited.

13. SUPPLEMENTARY NOTES

14. ABSTRACT

The Army needs live-fire training and testing, but residues from such activity can contaminate nearby groundwater and trigger regulatory actions that restrict training or even close bases. Our three-year project measured the dissolution of TNT, Comp B, Tritonal, Octol, and C4, both in the laboratory and outdoors under conditions that mimic what occurs in the field—dissolution of spatially isolated explosives scattered onto range soils. The resulting data and dissolution models provided insight on environmental factors that affect dissolution, the frequency at which explosive chunks split, and the size of explosive loads on existing ranges. Our drop-impingement model indicated we can use rainfall data and average solubility to calculate the dissolution rate and expected lifespan of explosive pieces. Other findings included learning that the crushing strengths of explosives were low and did not significantly change after three years of outdoor exposure. Also, size distributions of the crushed explosives showed power law distributions, as found for blow-in-place, low-order detonations. This similarity suggests that we can crudely estimate particle size distributions on soils from total mass. Range managers can use the work reported here to guide future training and cleanup activities.

15. SUBJECT TERMS
high explosives, dissolution, friability, dissolution models

16. SECURITY CLASSIFICATION OF:			17. LIMITATION OF ABSTRACT	18. NUMBER OF PAGES	19a. NAME OF RESPONSIBLE PERSON
a. REPORT	b. ABSTRACT	c. THIS PAGE			19b. TELEPHONE NUMBER (include area code)
UU	UU	UU	UU	178	

Standard Form 298 (Rev. 8-98)

Prescribed by ANSI Std. 239.18